A driven two-component BEC: Chaos in a Macroscopic Quantum System

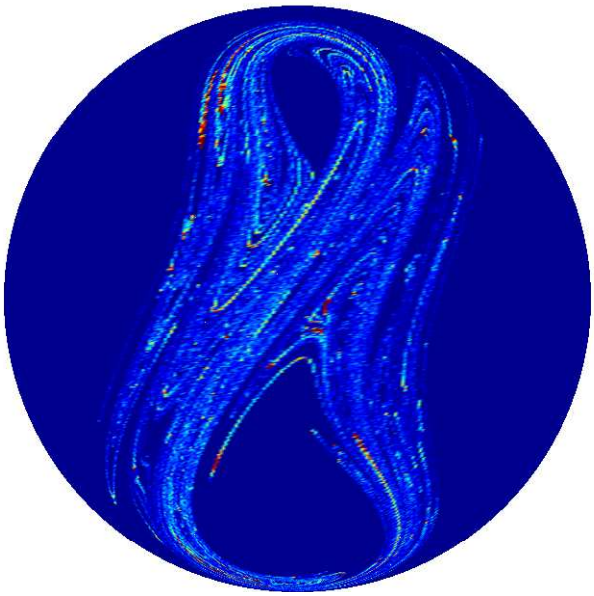

Jiří Tomkovič

2013

Dissertation

submitted to the

Combined Faculties of the Natural Sciences and Mathematics

of the Ruperto-Carola-University of Heidelberg. Germany

for the degree of

Doctor of Natural Sciences

Put forward by

Jiří Tomkovič

born in: Karl-Marx Stadt (today’s Chemnitz), Germany

Oral examination: 05. February, 2014

A driven two-component BEC: Chaos in a Macroscopic Quantum System

Referees: Prof. Dr. Markus K. Oberthaler
Dr. Sandro Wimberger

Abstract

This work discusses the experimental realization of a mixed regular-chaotic phase space in a macroscopic quantum system. The effective Planck's constant of the system can be varied in a large range. Therefore, the semi-classical limit of the system can be studied, where the initial size of the many particle wave packet is much smaller than typical structures of the phase space. Thus, different structures of the phase space can be resolved. In a weakly driven system, the Poincaré-Birkhoff scenario is investigated by the dispersion of the wave packet at a stable or unstable fixed point. In a strongly driven system, different dynamics of a wave packet is found, dependent on preparation in a regular island or the chaotic sea. The time evolution can be described by a classical model, which is in good agreement with experiment as well as the mean field model for the considered observables.
In an independent experiment using an atomic beam setup the generation of motional coherence of a single atom by spontaneous emission of a single photon has been demonstrated.

Zusammenfassung

Diese Arbeit behandelt die experimentelle Realisierung eines gemischt regulär-chaotischen Phasenraumes in einem makroskopischen Quantensystem. Die effektive Planck-Konstante des Systems kann über einen großen Bereich variiert werden. Dies ermöglicht eine Betrachtung des Systems im semi-klassischen Grenzfall, bei dem die anfängliche Größe eines Vielteilchen-Wellenpakets deutlich kleiner ist als typische Strukturen des Phasenraumes. Somit können unterschiedliche Bereiche des Phasenraumes aufgelöst werden. In einem schwach getriebenen System wird das Poincaré-Birkhoff Szenario über das Zerfließen der Wellenpakete an stabilen bzw. instabilen Fixpunkten untersucht. In einem stark getriebenen System zeigt sich eine unterschiedliche Dynamik der Wellenpakete, je nachdem, ob sie in einer regulären Insel oder dem chaotischen Phasenraum gestartet wurden. Die Beschreibung der Dynamik mit Hilfe eines klassischen Modells führt zu einer guten Übereinstimmung sowohl mit den Messdaten als auch einem "Mean-Field" Modell in den betrachteten Observablen.
In einem unabhängigen Experiment mit einem Atomstrahl wird die Erzeugung von Kohärenzen in den Impulszuständen eines einzelnen Atoms durch die spontane Emission eines einzelnen Photons nachgewiesen.

Contents

1. Introduction

The stability of an integrable (and thus regular) system subjected to a perturbation is of wide interest – in classical mechanics as well as in quantum systems. A large class of classical systems can be solved exactly just in a linear approximation, while higher order contributions have to be treated as a perturbation of the integrable system. Arising from the discussion of the stability of certain solutions under perturbation, e.g. the stability of the solar system, a new class of solutions was found for chaotic regions. This opened up the route to structurally different physics, examined by nonlinear dynamics. Such behaviour was found for many different systems, including the rings of saturn, chaotic behaviour of convection, stability of lasers and plasmas, in acoustics and many more [4]. Furthermore, the theory of nonlinear dynamics provided seminal contributions to philosophical aspects of physics, such as the disconfirmation of Laplace's demon [5].

The manifestation of chaos in a quantum system raised some questions, which are closely related to the transition from the quantum to classical regime. For an isolated system in the quantum regime, which is described by a linear Schrödinger equation, the time evolution will be periodic or quasi periodic, even if the classical counterpart behaves chaotic. However, if the effective Planck's constant is decreased towards the semi classical regime, it has to describe the classical chaotic trajectories. Thus, the discussion of the quantum-to-classical transition is inseparably interwoven with the discussion of quantum states located in a classically chaotic region.

Among the first experiments of a quantum system with a classically chaotic counterpart were investigations of the δ-kicked rotor [6], due to its primary role in classical nonlinear dynamics. Exploring the diffusion of particles exposed to periodic kicks resulted in the discovery of quantum resonances [7, 6]. This opens up the route for the observation of quantum accelerator modes [8, 9], using quantum resonances by performing the kicks close to multiples of the Talbot time. The difference of the period of the kicks to the Talbot time is discussed as an effective Planck's constant [10], providing a system for the investigation of quantum to classical transition.

The diffusion of particles in the quantum kicked system exhibits an anomalous behaviour, which has no classical counterpart. Beyond the Heisenberg time, diffusion is almost zero due to dynamical localization [11, 12]. The closely related Anderson localization was also observed in microwave billiards [13] and for Bose-Einstein condensates (BEC) in random potentials [14, 15].

In contrast, the transport of particles in a δ-kicked potential can exhibit quite counterintuitive behaviour even for classical systems. The ratchet effect introduced by Feynman [16], describes the transport of an ensemble against a gradient if the symmetries of the system are broken and diffusion takes place. Substituting the diffusion by transport in the chaotic sea leads to ratchet effects in Hamiltonian systems [17]. The atom optical implementations rely up to date on quantum resonances [18, 19] or dissipation [20, 21, 22]. Furthermore, it was realized in a BEC [23].

A striking feature of quantum mechanics is the existence of tunneling through a barrier, although the energy of the wave packet is well below the barriers height. This is often discussed by means of the most simple system – a double well potential. The periodic driving of such a system can lead to complete suppression of tunneling [24, 25]. At another abstraction level dynamical barriers can arise in the classical mixed phase space. Hence, the quantum counterpart should exhibit tunneling through this dynamical barrier, discussed as dynamical tunneling and chaos assisted tunneling (CAT) for the tunneling between two stable islands moderated by states of the chaotic sea [26]. It was shown theoretically, that CAT will increase the tunneling rate by orders of magnitude and critically depends on the effective Planck's constant [27]. This makes it quite attractive for the quantum optics community, since many particle tunneling could lead to the realization of "cat"-states. An increase due to CAT could raise the tunneling rate to experimental observable times, whereas the typical tunneling times are experimentally not feasible.

For single atoms, chaos assisted tunneling was observed in [28, 29], however it is still challenging for many body systems. A very natural choice for the investigation is a driven double well potential. This can be realized in a BEC in external as well as internal degrees of freedom. The dynamics can be mapped onto a Bloch sphere and is often referred to as driven or kicked top. We will concentrate in the following on the implementation of the driven double well in Fock space (driven Top) in internal degrees of freedom in a BEC.

Chaos assisted tunneling is discussed in the framework of a driven top in several works [30, 27] exhibiting a crucial dependency on the effective Planck's constant. Due to its direct dependency on the atom number in the BEC, the effective Planck's constant can be experimentally varied over

several orders of magnitude Therefore, the system is perfectly suited for studying the quantum-to-classical transition and reaching a semi-classical limit. The prediction of chaos on the Bloch sphere can be found in several theoretical works [31, 32, 33], a realization deep in the quantum regime was reached in [34]. Since the work of [34] relies on internal states of noninteracting atoms, the number of ”spins” is strongly limited yielding in a $\hbar_{\text{eff}}$ larger than typical structures of the phase space. The different sensitivity of states on perturbations is discussed, wether located in regular islands or in the chaotic sea. They find a much larger robustness for the states in stable islands. Furthermore it is suggested, that quantum states located in the classical chaotic sea will exhibit enhanced entanglement [35, 36]. This is of great interest in context of many body systems.

The present investigation builds on the realization of the symmetric undriven top in a spinor BEC in our group [37, 38]. Here we present the realization of a driven top in the semi classical regime. The driving is implemented by altering the coupling strength periodically, experimental details will be given in chapter 3. The derivation of the mean field and a classical model as well as some basic properties of the system will be outlined in the subsequent chapter.
In a weakly driven system, the Poincaré-Birkhoff scenario is investigated in chapter 4 for the most simple system. The generation of elliptic and hyperbolic fixed points due to driving is supported by results of the spreading of the wave packets. A mixed phase space is realized in a strongly driven system in chapter 5 and verified by the different behaviour of the wave packets depending on whether prepared in the chaotic sea or in a regular island. Simulations with a mean field model as well as a classical model fit quite well to the experimental data. This supports the idea to predict some aspects of the behaviour of a wave packet in the driven system by expectations obtained from the structure of the classical phase space.

2. The driven double well system

2.1. Bose-Hubbard Hamiltonian

The complete derivation of the Bose Hubbard Hamiltonian is treated in different works [39, 40, 41, 42, 43], and thus only some key features will be given in the following (see also [38]). The Hamiltonian can be written [44, 45, 46, 41] in the second quantization for a spinor condensate driven by an external field and assuming s-wave scattering as:

$$\hat{\mathcal{H}} = \hat{\mathcal{H}}_0 + \hat{\mathcal{H}}_{coupl} + \hat{\mathcal{H}}_{MF} + \hat{\mathcal{H}}_{inter} \tag{2.1}$$

$$\hat{\mathcal{H}}_0 = \sum_{i=1,2} \int \mathrm{d}^3 r \hat{\Psi}_i^\dagger(\mathbf{r}) \left[-\frac{\hbar^2}{2m}\nabla^2 + V(\mathbf{r}) \right] \hat{\Psi}_i(\mathbf{r}) \tag{2.2}$$

$$\hat{\mathcal{H}}_{coupl} = -\frac{\hbar\Omega_R}{2} \int \mathrm{d}^3 r \left[\hat{\Psi}_1^\dagger(\mathbf{r})\hat{\Psi}_2(\mathbf{r}) e^{i\Delta t} + \hat{\Psi}_2^\dagger(\mathbf{r})\hat{\Psi}_1(\mathbf{r}) e^{-i\Delta t} \right] \tag{2.3}$$

$$\hat{\mathcal{H}}_{MF} = \sum_{i=1,2} \frac{4\pi\hbar^2 a_{ii}}{2m} \int \mathrm{d}^3 r \hat{\Psi}_i^\dagger(\mathbf{r})\hat{\Psi}_i^\dagger(\mathbf{r})\hat{\Psi}_i(\mathbf{r})\hat{\Psi}_i(\mathbf{r}) \tag{2.4}$$

$$\hat{\mathcal{H}}_{inter} = \frac{4\pi\hbar^2 a_{12}}{m} \int \mathrm{d}^3 r \hat{\Psi}_1^\dagger(\mathbf{r})\hat{\Psi}_2^\dagger(\mathbf{r})\hat{\Psi}_1(\mathbf{r})\hat{\Psi}_2(\mathbf{r}) \tag{2.5}$$

with $\hat{\Psi}^\dagger$ ($\hat{\Psi}$) being the creation (annihilation) field operator fulfilling the standard bosonic commutation relations. The form of $\hat{\mathcal{H}}_0$ assumes the same trapping potential $V(\mathbf{r})$ for both spin species. The coupling term $\hat{\mathcal{H}}_{coupl}$ includes a small detuning Δ and is written in the rotating frame approximation. Within the framework of a condensate in an external double well potential [42] this term is equivalent to the hopping term describing the tunneling between the wells. The self interaction of the field associated with the intra-species scattering length a_{ii} leads to an additional term $\hat{\mathcal{H}}_{MF}$, which has some experimental implications treated in Sec. 3.3. The

last interaction term $\hat{\mathcal{H}}_{inter}$ describes the collision of two particles in different spin states. This nonlinearity enables the system to show up a large variety of effects.

In order to obtain a two mode model, the field operators are approximated by:

$$\hat{\psi}_i = \Phi_0 \hat{a}_i \tag{2.6}$$

with Φ_0 as a scalar mode function and the operators $\hat{a}_i^\dagger$ and $\hat{a}_i$ creating or annihilating a particle in spin state i. Throughout the rest of this work, the hyperfine state $|F=1, m_f=+1\rangle = |1\rangle$ will be denoted with index *1* and $|F=2, m_F=-1\rangle$ with index *2*. As both spin species experience the same potential $V(\mathbf{r})$, their functions Φ_0 are assumed to be equal. This assumption[1] is only valid if the system is in the miscible regime [47], but is a good approximation if the trapping potential is very tight as in the considered system. Thus the external degree of freedom is frozen and uncoupled from the internal dynamics. Following [46, 38] the Hamiltonian 2.1 can be written in a two mode model:

$$\hat{\mathcal{H}}_0 = E\left(\hat{a}_1^\dagger \hat{a}_1 + \hat{a}_2^\dagger \hat{a}_2\right) \tag{2.7}$$

$$\hat{\mathcal{H}}_{MF} = \chi_{11}\, \hat{a}_1^\dagger \hat{a}_1^\dagger \hat{a}_1 \hat{a}_1 + \chi_{22}\, \hat{a}_2^\dagger \hat{a}_2^\dagger \hat{a}_2 \hat{a}_2 \tag{2.8}$$

$$\hat{\mathcal{H}}_{inter} = 2\chi_{12}\, \hat{a}_1^\dagger \hat{a}_2^\dagger \hat{a}_1 \hat{a}_2 \tag{2.9}$$

$$\hat{\mathcal{H}}_{coupl} = -\frac{\Omega}{2}\left(\hat{a}_1^\dagger \hat{a}_2 e^{i\Delta t} + \hat{a}_2^\dagger \hat{a}_1 e^{-i\Delta t}\right) \tag{2.10}$$

with the coefficients in the single spatial mode approximation:

$$E = \int \mathrm{d}^3 r \Phi_0^* \left[-\frac{\hbar^2}{2m}\nabla^2 + V(\mathbf{r})\right]\Phi_0 \tag{2.11}$$

$$\chi_{ij} = \frac{4\pi\hbar^2\, a_{ij}}{2m} \int \mathrm{d}^3 r |\Phi_0|^4 \tag{2.12}$$

$$\Omega = \hbar\Omega_R \int \mathrm{d}^3 r \Phi_0^* \Phi_0\ . \tag{2.13}$$

[1] A more detailed analysis is given in [38].

The Hamiltonian can be further simplified by introducing angular momentum operators:

$$\hat{J}_x = \frac{1}{2}\left(\hat{a}_1^\dagger \hat{a}_2 + \hat{a}_2^\dagger \hat{a}_1\right) \tag{2.14}$$

$$\hat{J}_y = \frac{1}{2i}\left(\hat{a}_2^\dagger \hat{a}_1 - \hat{a}_1^\dagger \hat{a}_2\right) \tag{2.15}$$

$$\hat{J}_z = \frac{1}{2}\left(\hat{a}_2^\dagger \hat{a}_2 - \hat{a}_1^\dagger \hat{a}_1\right) \tag{2.16}$$

fulfilling the standard commutation relations for a spin $N/2$ algebra. When neglecting all constant terms (proportional to N and N^2) the two mode Hamiltonian can be written in the form:

$$\hat{\mathcal{H}} = \chi \hat{J}_z^2 - \Omega \hat{J}_x + \delta \hat{J}_z \, . \tag{2.17}$$

The coupling Ω is experimentally well controlled and can be varied in the range of a few Hertz up to $330\,Hz$ (times $2\pi\hbar$). The effective detuning:

$$\delta = \Delta + (2J-1)(\chi_{22} - \chi_{11}) \tag{2.18}$$

depends on the chosen detuning Δ of the coupling and on particle density, thus atom number in the BEC. This term is typically treated as constant. In fact, the detuning changes with time since some atoms are lost during the experimental sequence. The quantification and methods to compensate this are described in Sec. 3.3.

Finally the nonlinearity χ can be written as:

$$\chi = \chi_{11} + \chi_{22} - 2\chi_{12} \tag{2.19}$$

$$= \frac{1}{2}(g_{11} + g_{22} - 2g_{12}) \int \mathrm{d}^3 r |\Phi_0|^4 \tag{2.20}$$

with $g_{ij} = \frac{4\pi\hbar^2 a_{ij}}{m}$. The corresponding term is quadratic in $\hat{J}_z$ leading to nonlinear dynamics and is thus the reason for the system being so attractive for researchers. Absolute value as well as sign of χ can be tuned by changing the inter-species scattering length a_{12} close to a Feshbach resonance (see Sec. 3.2.1 for details).

Scaling the Hamiltonian

It should be noted, that the coefficients Ω, χ and δ are in units of energy. On the other hand these quantities are experimentally determined as frequencies, thus the Hamiltonian will be scaled accordingly. Furthermore for numerical simulation of the dynamics it is favourable to express the Hamiltonian in dimensionless variables, which will be derived in the following.

As a first step, the coefficients will be scaled by $2\pi\hbar$:

$$\tilde{\chi} = \frac{\chi}{2\pi\hbar};\ \tilde{\Omega} = \frac{\Omega}{2\pi\hbar};\ \tilde{\delta} = \frac{\delta}{2\pi\hbar}\ . \tag{2.21}$$

Hence the scaled versions correspond to the experimentally measured frequencies, which are typically in the order of $\chi N \approx 20\,Hz \ldots 35\,Hz$ and $\Omega \approx 10\,Hz \ldots 50\,Hz$. It is common within the semiclassical approximation of this Hamiltonian, to project the dynamics onto an unit sphere. In order to be comparable to classical simulations, also the two mode hamiltonian will be mapped on the unit sphere. Since creation and respectively annihilation operators raise or lower the quanta in steps of one, the scaling has to be introduced in a pre factor in the angular momentum operators. Therefore the scaled angular momentum operators $\hat{\mathcal{J}}$ reads as:

$$\hat{\mathcal{J}}_i = \frac{2}{N}\hat{J}_i \tag{2.22}$$

Expressing the Hamiltonian 2.17 in scaled terms yields in:

$$\begin{aligned} \frac{1}{\hbar}\frac{2}{N}\frac{1}{2\pi\tilde{\Omega}}\hat{\mathcal{H}} &= \frac{1}{2}\frac{\tilde{\chi}N}{\tilde{\Omega}}\hat{\mathcal{J}}_z^2 - \hat{\mathcal{J}}_x + \frac{\tilde{\delta}}{\tilde{\Omega}}\hat{\mathcal{J}}_z \\ \hat{\mathcal{H}}' &= \frac{\Lambda}{2}\hat{\mathcal{J}}_z^2 - \hat{\mathcal{J}}_x + \epsilon\hat{\mathcal{J}}_z \end{aligned} \tag{2.23}$$

with the relative nonlinearity $\Lambda = \frac{\tilde{\chi}N}{\tilde{\Omega}}$ and the scaled detuning $\epsilon = \frac{\tilde{\delta}}{\tilde{\Omega}}$.

The relative nonlinearity Λ plays an important role for the system as it determines the relative strength of the nonlinearity to the coupling. If the coupling exceeds the nonlinearity the system exhibits slightly deformed Rabbi like oscillations [48]. On the other hand, if the nonlinearity is much stronger than the coupling, the dynamics is completely changed. Details of the dynamics will be discussed in Sec. 2.3.
The scaled detuning ϵ influences the system much less as it is chosen to

be smaller than one, $\epsilon \ll 1$ and thus just tilts the axis of the Rabbi oscillations a bit.
The scaling factor $\frac{1}{\hbar}\frac{2}{N}\frac{1}{2\pi\tilde{\Omega}}$ of the Hamiltonian can be divided into several distributions. One of them is the effective Planck's constant of the system. It can be determined by the commutator relations of the angular momentum operators and calculates to :

$$\hbar_{\text{eff}} = \frac{2}{N} \, . \tag{2.24}$$

Therefore the system exhibits the potential of behaving pure quantum mechanically for small, or classically for large N. For instance the experiment in [34] was done with $N = 7$ implying that the effective $\hbar_{\text{eff}}$ and thus a minimal uncertainty state is large compared to typical structures of the classical phase space. On the other hand, with a large atom number almost classical experiments are available. Hence this system is ideally suited for the experimental investigation of quantum to classical transition.

The remaining factor of $2\pi\tilde{\Omega}$ corresponds to a scaling of frequencies and thus times:

$$\tilde{\omega} = \frac{\omega}{2\pi\tilde{\Omega}} \tag{2.25}$$

$$\tilde{t} = 2\pi\tilde{\Omega}t \tag{2.26}$$

and is required for the comparison of numerical and experimental results. The scaled Hamiltonian (Eq. 2.23) can be solved numerically for a moderate atom number up to the order of $\mathcal{O}(1 \times 10^3)$, which is done in Sec. A.2. The scaling apostrophe is omitted throughout the rest of this work.

The Bose-Hubbard Hamiltonian can also be cast into an effective single particle Hamiltonian [49, 50] with a potential being similar to the classical one but a z dependent modification of the effective mass. This is appreciated for deeper insight into the quantum behaviour of the Hamiltonian or if the particle number is too large for the numerical diagonalization. Since one goal of this work is to translate findings from the classical model into the mean field system, primarily the classical approximation and numerical solution of the Bose-Hubbard Hamiltonian will be used.

2.2. Semi-classical approximation

In order to get a feeling for the dynamics described by the Hamiltonian in Eq. 2.17, a semiclassical model is derived. Following the route of [45], the

angular momentum operator $\hat{J}$ is replaced by its expectation values:

$$\hat{J} \rightarrow \frac{N}{2}\begin{pmatrix} \sin\vartheta\cos\varphi \\ \sin\vartheta\sin\varphi \\ \cos\vartheta \end{pmatrix} \tag{2.27}$$

which is the standard form of a unit vector in spherical coordinates with radius $N/2$ (due to dealing with a spin $N/2$ system). It is common to project the dynamics onto a unit sphere with radius one and to express the Hamiltonian in terms of the height z instead of polar angle ϑ. Therefore the angular momentum operators and thus the Hamiltonian will be written in terms of scaled coordinates $z = \cos\vartheta$ and the azimuth angle φ:

$$\hat{J}_x \rightarrow \frac{N}{2}\sqrt{1-z^2}\cos\varphi \tag{2.28}$$

$$\hat{J}_y \rightarrow \frac{N}{2}\sqrt{1-z^2}\sin\varphi \tag{2.29}$$

$$\hat{J}_z \rightarrow \frac{N}{2}z\,. \tag{2.30}$$

Substitution of these into the unscaled Hamiltonian 2.17 leads to:

$$\mathcal{H} = \frac{2\pi\tilde{\chi}N^2}{4}z^2 - \frac{N}{2}2\pi\tilde{\Omega}\sqrt{1-z^2}\cos\varphi + \frac{N}{2}2\pi\tilde{\delta}\,z\,. \tag{2.31}$$

Scaling this semi-classical Hamiltonian by $N2\pi\tilde{\Omega}/2$ equivalently to the mean field system yields:

$$\tilde{\mathcal{H}} = \frac{\Lambda}{2}z^2 - \sqrt{1-z^2}\cos\varphi + \epsilon z \tag{2.32}$$

using the same definitions for relative nonlinearity and detuning.

It should be noted that the presented derivation of the semi-classical model is just a rough ”experimentalists point of view”. For a neat derivation, the Ehrenfest theorem is used to derive the equation of motion for the expectation value of $\langle\hat{J}\rangle$, and to derive an effective Hamiltonian from that [51, 45]. The full analysis was provided by Steffen Löck and yields in the same results [52].

The scaling of the Hamiltonian in Eq. 2.32 is done with the factor of $N2\pi\tilde{\Omega}/2$, thus actually all frequencies would have been scaled with the same factor. This implies a scaling of frequencies by $N/2$ leading to wrong conclusions. The experimental determined frequencies are (in first order) independent of particle number N, hence these behave as a kind of "angular" frequencies. The scaling with $N/2$ on the other hand would lead to

frequencies at the surface of the sphere. Due to that reason and according to the scaling of the mean field model, the factor of $N/2$ has to be omitted leading to same scaling as Eq. 2.25.

2.2.1. Initial states

Although the number state base (see Sec. A.2) is a complete basis of the Bose-Hubbard Hamiltonian in Eq. 2.23, it is not the proper choice for the treatment of the problem. The more appropriate states are the eigenstates of the angular momentum operators with an axis pointing towards (ϑ, φ) [45]. Theses coherent spin states (CSS) can be written as [53, 32]:

$$|\vartheta, \varphi\rangle = \sum_{k=0}^{N} \binom{N}{k}^{\frac{1}{2}} \cos^k\left(\frac{\vartheta}{2}\right) \sin^{N-k}\left(\frac{\vartheta}{2}\right) e^{i(N-k)\varphi} |k, N-k\rangle \tag{2.33}$$

with N being the total atom number and k the number of particles in state $|2\rangle$. It was shown that these states form a complete basis [53]. Coherent spin states are minimal uncertainty states [45]. Experimentally, we can create such states by preparing all atoms in the $|1\rangle$ state, which is shown to be equivalent to a CSS. Since an arbitrary rotation transfers a CSS into another one, we can prepare a CSS at a certain position (ϑ, φ) in phase space by applying a high power coupling pulse onto the $|1\rangle$ state [54].

The CSS has a finite width on the Bloch sphere due to quantum mechanical uncertainty principle, thus classical simulations working with a single point state will differ from the quantum mechanical mean field model. In order to make them comparable to the mean field model, a distribution of points will be used [30, 34] for initial preparation. For large atom numbers N, the binomial distribution of the CSS approaches a Gaussian distribution with mean of (ϑ, φ) and a standard deviation of $\sigma = 1/\sqrt{N}$ [32, 55]. Therefore, we use a Gaussian distribution of points on the Bloch sphere as initial distribution for the classical simulations, with parameters of the CSS. The generation of the distribution is described in Sec. A.1.1. After calculating the time evolution for all points, the mean as well as the variance are obtained for the resulting classical distribution.

2.3. Properties of the undriven system

Although the properties of the symmetrical system have been intensely studied theoretically [44, 56, 41, 49, 50] as well as experimentally [57,

42, 58, 59], some basic properties will be discussed in the following since the undriven system serves as a starting point for the discussion of the driven system.

2.3.1. Symmetrical system

Most of the features of the undriven system can be understood when determining the fixed points of the system, their stability and linearized dynamics around. Since this can be obtained analytically for the symmetrical system with $\epsilon = 0$, we will focus briefly on this case. The full derivation is presented in Sec. A.1.3, a summary of the results will be given in the following.

The symmetrical system exhibits a fixed point at $z_{Pl} = 0; \varphi_{Pl} = 0$ with a frequency of surrounding orbits of $\omega_{Pl} = \sqrt{1+\Lambda}$. This fixed point, labeled with ”plasma”, will remain stable for all values of the relative nonlinearity. On the other side of the Bloch sphere, a second fixed point is located at $z_\pi = 0$; $\varphi_\pi = \pi$ with a frequency of $\omega_\pi = \sqrt{1-\Lambda}$ (all frequencies will be given in scaled units according to Eq. 2.25). This fixed point becomes unstable at a critical value of $\Lambda_* = 1$ and is named "π".

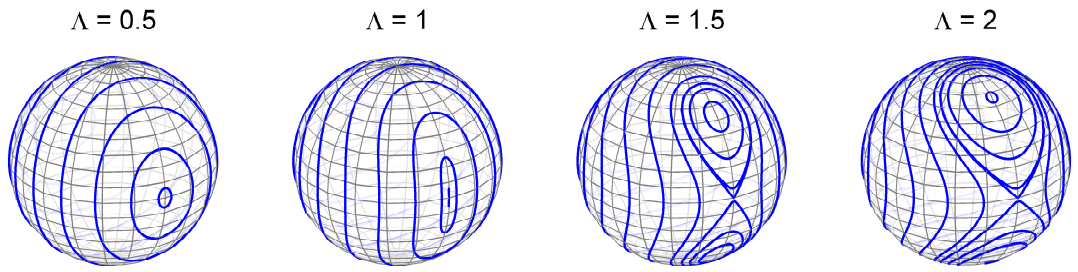

Figure 2.1.: Visualizing the Bifurcation. The phase spaces are plotted for different values of Λ on the Bloch sphere. The bifurcation occurs at a critical value of $\Lambda_* = 1$, at the π-side of the Bloch sphere.

At the same critical nonlinearity $\Lambda_* = 1$, two new stable fixed points appear at $z_\pm = \sqrt{1-\frac{1}{\Lambda^2}}$; $\varphi = \pi$. Orbits close by will oscillate with a frequency of $\omega_\pm = \sqrt{\Lambda^2 - 1}$. Therefore, the system exhibits a scenario at the "π"-side, where one stable fixed point becomes unstable and two new stable fixed points occur – a typical behaviour for a pitchfork [60] or period doubling bifurcation [4]. The bifurcation is depicted in Fig. 2.1 on the Bloch sphere, the fixed points and frequencies of adjacent orbits are depicted in Fig. 2.2,

which is experimentally investigated in [58]. For a comparison, the tilted system is included in the last graph, discussed in detail in Sec. 2.4.

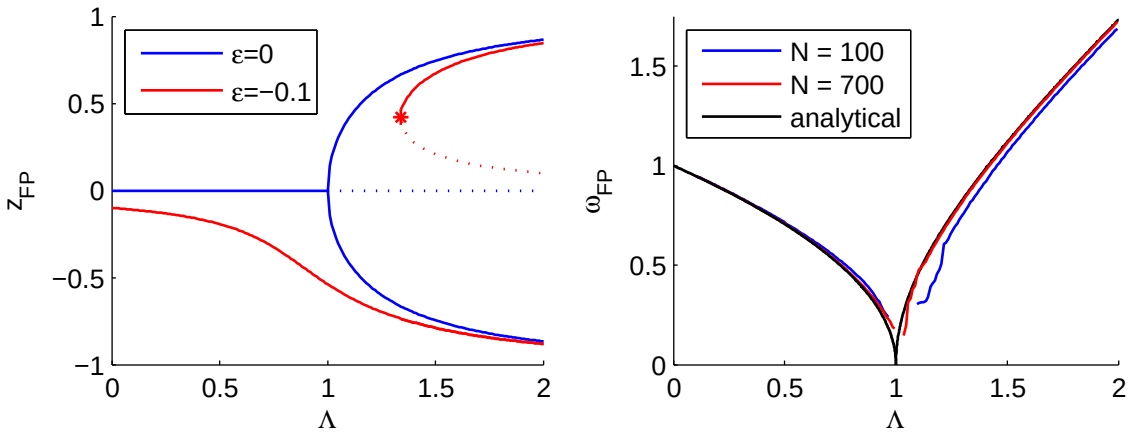

Figure 2.2.: Left: Pitchfork bifurcation for symmetric and tangent bifurcation for asymmetric system. The positions of the stable fixed points are depicted with solid lines, unstable fixed points with dotted ones.
Right: Critical slowdown in the symmetric system. Approaching the critical relative nonlinearity Λ_* frequencies of orbits close to the fixed point tend to zero in the classical approximation. This is contrasted to simulations in the mean field model performed for two different atom numbers and thus $\hbar_{\text{eff}}$. The simulations for large atom numbers follow the classical approximation quite well – just failing in the vicinity of the critical relative nonlinearity. In contrast, small atom numbers deviates even for larger distance to the critical nonlinarity and fails completely close by.

For large relative nonlinearities, the $z_\pm$ fixed points move towards the poles – leading to macroscopic self trapping in the Josephson regime [57, 58].

2.3.2. Critical slowdown

When the relative nonlinearity approaches the critical value of Λ_*, frequencies in the small amplitude approximation tend to zero independent from which direction the limit is done. This critical slowdown is depicted on the right panel of Fig. 2.2 for the analytical model as well as simulations in the mean field regime for two different atom numbers. Regarding large

atom numbers, thus semiclassical behaviour, frequencies of the simulation fit to the analytical model quite well. Close to the critical value Λ_*, the simulation breaks down due to limited $\hbar_{\text{eff}}$. On the other hand, the deviation to theory is much more obvious for larger $\hbar_{\text{eff}}$ in the transition regime. Not only the simulation breaks down for a much larger distance to the critical point, but also the deviation gets more pronounced.
A similar behaviour occurs in the mean field model when approaching the unstable z_π fixed point in the bifurcated system. The difference of eigenenergies, which determine the time evolution of the wave packet, tends to zero close to the unstable fixed point. This is well known behaviour in classical mechanics of orbits close to a separatrix [51].

Would it be feasible to experimentally verify critical slowdown in an experimental system with limited time? Due to atom loss (Sec. 3.2.3) the experimental available time is limited, therefore it is a hard task to measure small frequencies. In order to experimentally confirm the effect, a large atom number should be used and loss effects will have to be compensated. Additionally a trick known from determining trap frequencies of condensates [61] can be used. A wave packet in a harmonic trap breathes with approximate twice of the trap frequency, which can be measured by obtaining variances. Although it is experimentally more time consuming to measure variances, the desired frequencies can be raised by a factor of two with this method. The physics close to the critical point is intensely studied in [47] and references within.

2.3.3. Squeezing at the unstable fixed point

The dynamics close to the unstable fixed point at $z_\pi = 0;\ \varphi_\pi = \pi$ exhibit an interesting feature, especially in conjunction with the underlying many particle system. When the fixed point becomes unstable, the two Lyapunov-exponents $\lambda_\pm = \pm\sqrt{\Lambda - 1}$ get real with opposite sign (see [4] or Sec. A.1.3 and A.1.4). The Lyapunov-exponent with positive sign corresponds to the exponential separation of points along the unstable manifold, the one with negative sign to contraction along the stable manifold. Applying this to the initially prepared distribution, it will be extracted along the unstable axis and contracted along the stable one. Thus the distribution will be (number-) squeezed according to (see Sec. A.1.3):

$$\xi_{\text{N}}^2(\tilde{t}) = -\frac{20}{\ln 10}\sqrt{\Lambda - 1}\,\tilde{t} \tag{2.34}$$

(in [dB]), and be elongated along the axis with angle of $\alpha_{us} = \frac{\pi}{2} - \arctan\left(\sqrt{\Lambda - 1}\right)$ to the φ-axis. This simple model fits quite well to the numerical simulation

depicted in Fig. 2.3 for large atom numbers. A more advanced approach in the quantum regime can be found in [55], the experimental realization in [38, 59]. Squeezing in this kind of system is intensely discussed [45] as it implies many particle entanglement and improvement of interferometric techniques. It was shown for the external [62, 63] as well as the internal system [54, 59, 38] and can be used to improve interferometry [54].

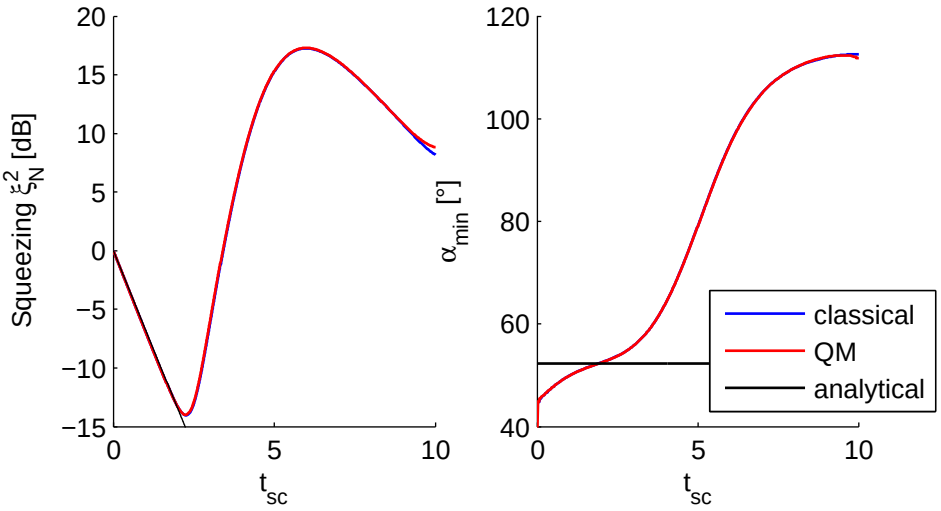

Figure 2.3.: Squeezing at the unstable fixed point for $\Lambda = 1.6$, $\epsilon = 0$ and $N = 700$ atoms.
Left: Number squeezing vs. scaled time. The distribution achieves its best squeezing for $t_{sc} \approx 2.25$, but getting bent afterwards. The simple analytical model fits quite well to numerics.
Right: Angle of axis of best squeezing vs. time [38]. The distribution is elongated along the unstable axis for the time of best squeezing, which fits well with the analytic expression.

The comparison of the simple analytical model with classical and quantum simulations reveals that certain aspects of the system, as mean and variances, can be well described classically even at exceptional points. This requires a semiclassical system with a large atom number, the restriction to short time scales and being not too close to the bifurcation point. The last item can be understood when considering the system at the critical relative nonlinearity Λ_*. Putting a single classical particle close to the fixed point, nothing will happen due to vanishing Lyapunov-exponents. On the other hand, a quantum wave packet will start to diverge and will ”feel” the potential afterwards. Thus time evolution close to the exceptional point is dominated by quantum behaviour even in the small $\hbar_{\text{eff}}$ limit and classical dynamics play a secondary role.

2.4. Tangent bifurcation

The symmetrical system described in the previous section is an exceptional case. Due to experimental noise, the symmetry will be broken in most situations. Although the asymmetric system will merge into the symmetrical case for very small detunings, the question arises, how large the experimental fluctuations are in relation to typical frequencies.

Even with our high precision magnetic field stabilization [38], the shot to shot fluctuations of the magnetic field are in the order of $\Delta B = 50\,\mu G$ equivalent to a detuning of $0.5\,Hz$. Taking into account the nonlinearity of $N\chi \approx 2\pi \cdot 32\,Hz$ (for 700 atoms) and thus a required coupling strength of $\Omega \approx 2\pi \cdot 20\,Hz$ to reach a medium bifurcated system, the magnetic field fluctuations correspond to a scaled detuning of $\epsilon \approx 0.025$. Hence the system would be tilted anyway for different realizations in an arbitrary direction. In order to keep the asymmetry of the system from shot to shot in sign and same order of amplitude, it is required to tilt the system on purpose. The artificial tilt should be much larger than tilt due to fluctuations, thus a value of $\epsilon \approx -0.1$ was chosen throughout the experiments. The negative sign is preferable since the island close to $F = 1$ is enlarged by that. There the atom loss is much less than in the other component (see Sec. 3.2.1).

Due to the tilt, the bifurcation occurs at a larger value of $\Lambda_* = \sqrt{1 + \epsilon^{\frac{2}{3}}}^3$ (see Sec. A.1.3), corresponding to $\Lambda_* \approx 1.3$ for the chosen detuning. Furthermore, atom loss also reduces the relative nonlinearity during time evolution, thus a value significant larger than the bifurcation point Λ_* has to be used. On the other hand one cannot chose quite low values of the coupling strength since this would further reduce the available scaled time. Thus an effective relative nonlinearity of $\Lambda = 1.5$ was chosen for the experiments in the bifurcated regime.

The tilt shifts the fixed points a bit, however the behaviour of the system is changed strongly. By increasing Λ, the stable z_π fixed point evolves continuously into one of the $z_\pm$ fixed points (according to sign of ϵ) but remains stable for all values of Λ. On the other hand, the bifurcation occurs ”out of the blue sky” with the emergence of one stable and one unstable fixed point (see Fig. 2.2). The bifurcation can be roughly understood in the following (refer to Fig. A.1 for details): consider a double well potential which is so strong tilted, that the upper (old) fixed point exceeds the unstable one in the center. Therefore, only the lower fixed point is present. When decreasing the tilt, the rising edge of the stable fixed point in the untilted system becomes zero at a value of Λ_*. At the same value, also the second derivative becomes zero, indicating an inflexion point. Further decrease

of the tilt leads to the emergence of a stable and an unstable fixed point at this inflexion point. Therefore this type of bifurcation is named tangent bifurcation [4].

The experimental verification of the blue sky bifurcation is a quite useful tool to check system parameters independently. The method for determining the nonlinearity via measurement of plasma and π oscillations used in Sec. 3.7 has some disadvantages. On one hand, due to the large coupling strength necessary to remain in the low nonlinearity approximation, the light field shift is different. Thus the measurement of the detuning can not be used in the experiments with much lower Ω. On the other hand, the frequencies of plasma and π oscillations are much larger due to the large coupling strength. Hence the time scale of these measurements is much shorter than the for the final experiments. Thus atom loss plays minor role and the measured nonlinearity appears larger than that seen by the atoms in the temporal mean due to loss.

2.4.1. Experimental realization

A rough summary of methods used to probe the blue sky bifurcation experimentally is given in the following, a more detailed description of experimental methods is given in Sec. 3. For some atom number N the nonlinearity $N\chi$ is fixed[2], however the relative nonlinearity Λ can be tuned over a large range by changing the coupling strength Ω. In order to obtain the same scaled detuning of $\epsilon = -0.1$ for all values of Ω, the absolute detuning $2\pi\delta = 2\pi\epsilon\,\Omega$ has to be adjusted accordingly.

For each parameter set of Ω and δ, the initial preparation is done close to the stable fixed points, thus z_π for $\Lambda < \Lambda_*$ and at each of the stable fixed points $z_\pm$ for the bifurcated system. In order to minimize effects of atom loss (Sec. 3.2.3), the preparation was always carried out within the lower hemisphere (thus at z_- and $-z_+$) and the sign of the detuning was changed instead. Since the bifurcation point as well as position and frequencies of the fixed points depend on detuning, a loss compensation[3] was implemented to avoid an additional time dependent tilt due to mean field shift.

The time evolution of $z(t)$ is obtained by measuring the imbalance of the two spin states by absorption imaging (Sec. 3.6) at different time steps. Subsequently the data is filtered for a certain atom number (typically

[2] for fixed trap geometry and magnetic field

[3] see Sec. 3.3. Parameters for $N = 500$ atoms and mean imbalance of $z = 0$ where used, thus $\tau_{loss} = 200\,ms$ and $\delta_{loss} = 14\,Hz$.

within a ±25 atom range) according to the loss for that atom number and mean imbalance. This results in small amplitude oscillations, where amplitude, offset and frequency can be deduced by a sine fit. The so obtained data is plotted in Fig. 2.4, where the fitted offset is an approximation to the position of the fixed point (left graph), the scaled frequency is depicted on the right panel.

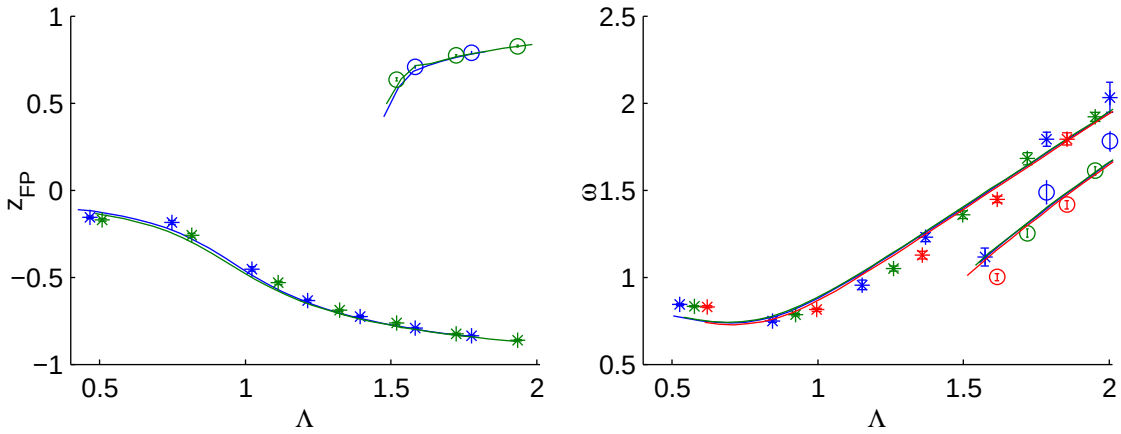

Figure 2.4.: Experimental observation of the bifurcation of the tilted system with $\epsilon \approx -0.1$ for different atom numbers (*550* atoms/blue to *650* atoms/red).
Left: Position of fixed points deduced from mean value of oscillations (asterisk/circle with error bars and fit as solid line).
Right: Scaled frequencies of fast/deep fixed points (asterisk) and slow ones (circle) with fits. The uncertainty of the frequencies obtained by fitting procedure is given as a *95* % confidential interval. The universality of the system is revealed since the curves for different atom numbers lie on top of each other, although they exhibit a different nonlinearity.

For a comparison of the experiment with theory, fixed points as well as frequencies obtained for several coupling strengths are used for fitting. The nonlinearity $N\chi$ and an offset detuning δ_o are treated as free parameters. Since a closed analytical solution for fixed points and corresponding frequencies is hard to derive in the tilted system, the Hamiltonian is approximated by a Taylor expansion (Sec. A.1.3). Solving the Taylor expansion for fixed points, an approximated model can be derived which is used for the fit. Due to strong anharmonicity, the expansion point has to be selected with care.

The results of the fit with the analytical model exhibit a strange behaviour. The nonlinearities for different atom numbers correspond just roughly to

that determined by plasma- and π-oscillations (Sec. 3.7) but are out of error margins of the other measurements. Furthermore the values obtained from the fit of the fixed points and that of the frequencies do not correspond to each other within error bounds.
The behaviour can be explained by a violation of the small amplitude approximation of the analytical model. Due to non vanishing amplitudes of the oscillations in the anharmonic system, a systematic error occurs in positions as well as in frequencies. To circumvent this limitation, a numerical model for the fit was developed regarding the amplitude of the oscillations. This model is included in Fig. 2.4 revealing an excellent agreement with the experiment. Furthermore, the parameters obtained by a fit of position and that of frequencies agree to each other within error bounds and also to plasma- respectively π-oscillations. It should be noted that this numerical model shows some deviation to the optimal case in Fig. 2.2.

Approaching the bifurcation point from the right, the data exhibit a decreasing frequency of the slow fixed point. However a critical slowdown beyond a linear behaviour can not be revealed. Albeit this was not the intention of the experiment.

Comparing the data in scaled units for different atom numbers, all curves fall onto the same universal one. This reveals the validity for the simple model using only two parameters Λ and ϵ as well as the proper scaling behaviour. Consequently the simple semi classical model using two effective parameters is a very well approximation of the considered system besides all the experimental details such as atom loss.

The trapping potential was changed for all other measurements. Therefore, the calibration obtained by the blue sky bifurcation can not be used for the other measurements.

2.5. Driving the system

In this section, different ways to perturb the system and a motivation for the choice of parameters will be discussed. As the overall aim is to reveal that the chosen system exhibits a KAM scenario (see Sec. 4) and a mixed phase space can be realized, solely Hamiltonian systems will be considered, precisely periodically driven ones.

The physics of a periodically driven system is well known since the example of an sinusoidal driven harmonic oscillator is treated in most introductory courses of classical mechanics. When perturbing an undamped

harmonic oscillator one finds resonance phenomena for driving frequencies close to the frequency of the harmonic oscillator with a divergence of amplitudes [64]. As the frequency of an orbit is independent on amplitude, the whole phase space becomes unstable at the same time due to driving.

In contrast, the KAM theorem (see Sec. 4) opens up a route to a mixed phase space. Roughly speaking, it states for small driving amplitudes that orbits with an irrational frequency to driving ratio will survive slightly perturbed. Vice versa one may conclude that the orbit is broken up when a rational frequency ratio is chosen, i.e. the driving frequency is a small multiple of the orbit frequency. For an anharmonic system, the resonance condition will be fulfilled for a small range of orbits, others will remain slightly changed. Thus it is likely to generate a mixed phase space when driving an anharmonic system with a frequency being resonant (or a multiple of that) of some orbits.

To perturb the system in a controlled manner the two parameters Λ and ϵ can be used to drive the system. The detuning ϵ is directly accessible as the detuning of the coupling to the two photon transition and could be changed in time via frequency modulation of the coupling RF or MW fields. As the parameter Λ is the ratio of the nonlinearity to the coupling strength, it could be either changed by driving the coupling strength or the nonlinearity.

2.5.1. The parameters of choice

In all realised experiments throughout this work, the outcome is averaged over many almost equal realizations of the same experiment. Thus a noisy behaviour (with large variances) could not only be caused by time evolution in the chaotic sea, but also by technical noise leading to enhanced shot-to-shot fluctuations. Therefore, it is experimentally quite favourably to preserve a stable, regular part of the phase space even in the driven system, i.e. a stable island of the undriven system is also present in the driven one. On the other hand, as the system parameters are known to some uncertainty it is advantageous to generate a large chaotic sea and large moving islands by driving.

Since the parameter Λ defines the barrier height of the double well potential and the detuning ϵ the tilt, it is expected to perturb the deep islands only slightly when driving the coupling. This is supported by simulations and thus a sinusoidal driving of Λ was chosen through all driven experiments within this work. It can be experimental realized by an amplitude modulation of the coupling RF-field as described in Sec. 3.4.2.

It should be noted, that this choice is not inalienable, the driven experiments could have been done by driving the detuning with minor implications. Albeit the driving amplitude should be kept small for both cases. By varying the coupling strength in a larger range, the light shift [65] will be changed and thus the detuning too. Vice versa by changing the detuning in a larger range, also the effective coupling will be modified. However, this effect can be neglected for small driving amplitudes.

There are two quite different regimes for Λ, both of them were investigated in this work. On one hand, for $\Lambda = 0.7$ the system is still not bifurcated and thus an example of a most simple model. On the other, with $\Lambda = 1.5$ the system is bifurcated and exhibits a double well structure. For both cases, a detuning in the order of $\epsilon = -0.1$ was chosen to break the symmetry of the system. Since our system exhibits an enhanced atom loss in the $F = 2$ manifold (3.2.3), it is favourable to select a negative sign for the detuning and start in the left hemisphere (when looking from $\varphi = \pi$) to constrain the time evolution to negative z-values for short times to minimize loss.

For sake of completeness, it should be mentioned, that also the nonlinearity can driven. On one hand, it can be controlled by changing the inter-species scattering length close to the Feshbach-resonance via time-periodic variation of the magnetic field (see Sec. 3.2.1 for details of the magnetic field stability). On the other hand, the definition of the nonlinearity (see Eq. 3.2) offers a different route for a coherent control due to changing the overlap of the wavefunctions of both atomic states. This method is already implemented in atom chip experiments [66] to modify and control the nonlinearity over several magnitudes [67].

2.5.2. Driving frequency

Day to day experience and knowledge from classical mechanics leads to the conclusion, that driving with the frequency of the orbit will perturb the system most. This is expanded by KAM theorem to all rational frequency ratios. Unfortunately the experimental available time is limited by atom loss (Sec. 3.2.3) to a few cycles of the undriven orbit. Thus the outcome of the experiments relies on perturbation being as fast as possible.

In the following an approximation for the best driving frequency should be derived in the quantum regime (see Sec. A.2.2 for details). Therefore time dependent perturbation theory will be applied. The driven Hamiltonian $\hat{H}(t) = \hat{H}_0 + A_D \hat{W}(t)$ is split into a time constant part $\hat{H}_0 = \Lambda/2 \hat{J}_z^2 - \hat{J}_x + \epsilon \hat{J}_z$ and a time varying part $\hat{W}(t) = -\sin(\omega_D t + \varphi_D) \hat{J}_x$. Then the differential

equations for slow time varying coefficients in the eigenbase of $\hat{H}_0$ are established after separation of fast phase evolution of the undriven system. With the assumption that these coefficients can be written in a power series in the driving amplitude, the differential equations can be uncoupled leading to the solution for the first order perturbation coefficients:

$$b_k^{(1)}(t) = -\frac{iN}{4}\sum_n b_n^{(0)}(J_x)_{kn}\left[\frac{e^{i\varphi_D}\left(1-e^{i(\Delta\omega_{kn}+\omega_D)t}\right)}{\Delta\omega_{kn}+\omega_D} - \frac{e^{-i\varphi_D}\left(1-e^{i(\Delta\omega_{kn}-\omega_D)t}\right)}{\Delta\omega_{kn}-\omega_D}\right]. \tag{2.35}$$

The difference of eigenfrequencies is labeled with $\Delta\omega_{kn} = \omega_k - \omega_n$, the driving frequency with ω_D, the initial occupation of state n with $b_n^{(0)}$ and the matrix element of the driving with $(J_x)_{kn}$. A significant contribution is expected for the case when the denominator becomes small, thus if the driving frequency hits one of the transition frequencies. Since all coefficients and the frequencies depend on the diagonalization of $\hat{H}_0$, which could not be done analytically, the conclusions are not universal and both cases will be discussed separately.

Driving frequency for the bifurcated system

For the bifurcated system, the parameter set $\Lambda = 1.53,\ \epsilon = -0.07$ and as start point $z_0 = 0, \varphi_0 = 2.51$ was chosen, such that the rotational frequency of the unperturbed system is in the order of $\omega_0 = 0.76$ (in scaled units). By numerical diagonalization of $\hat{H}_0$ and a calculation of the coefficients of the eigenstates with a coherent spin state located at z_0, φ_0, a relatively sharp distribution of the zeroth order coefficients $b_k^{(0)}$ (around k) is obtained. Due to the double well structure and the nonlinearity, a nonlinear behaviour of eigenenergies (or frequencies) is expected, however in the region of k the differences of adjacent eigenfrequencies $\Delta\omega_{k,k-1}$ equals the rotational frequency ω_0 with minor linear corrections. In the analogy of the harmonic oscillator, all eigenfrequencies exhibits a frequency difference of ω_0, leading to full rephasing after a time $T_{per} = 2\pi/\omega_0$. The similar occurs in the considered system, however the minor corrections to the frequency difference prevent a complete rephasing of the wave packet.

Since only a few $b_n^{(0)}$ have major contributions to the sum of Eq. 2.35, also the structure of $(J_x)_{kn}$ matters only for these n. For matrix elements close to $n = k$, the significant contributing terms are the main diagonal $(J_x)_{n,n}$ and the ones after the next $(J_x)_{n,n\pm2}$ elements. Terms along the

off-diagonal $(J_x)_{n,n\pm1}$ are suppressed by approximately one order of magnitude. Thus, to achieve a perturbation of the system as fast as possible, it is more convenient to drive the system with twice of the rotational frequency $\omega_{\mathrm{Driv}} \approx \Delta\omega_{n,n-2} \approx 2\Delta\omega_{n,n-1} \approx 2\omega_0$. Driving directly at the rotational frequency would also disturb the system, but the perturbation would need much longer time scale to grow. Since several eigenstates are involved and the difference of their eigenfrequencies differ slightly, the resonance condition is not sharp anymore. This leads to a smearing of resonant driving frequencies over the distribution of eigenfrequency differences of involved states.
Consequently, within all the driven experiments at $\Lambda = 1.53$, the double rotational frequency was chosen as driving frequency.

Driving frequency for the unbifurcated system

In order to reveal the KAM theorem in the most simple system, a parameter set of $\Lambda = 0.7,\ \epsilon = -0.11$ and $z_0 = 0.48,\ \varphi_0 = \pi$ as start point was chosen. Also in this case the difference of eigenfrequencies $\Delta\omega_{n,n-1}$ around the maximal $b_k^{(0)}$ is close to the rotational frequency $\omega_0 = 0.75$ of this orbit. However, the distribution of matrix elements of $(J_x)_{kn}$ has changed. The major contribution is along the main diagonal, but the corresponding terms in the sum are independent of transition frequencies. The off diagonal terms $(J_x)_{n,n\pm1}$ and $(J_x)_{n,n\pm2}$ are in the same order, however an order of magnitude smaller than the main diagonal. Higher contributions become quite small. In contrast to the $\Lambda = 1.5$ system, here the system can be driven with ω_0 or the twice, both choices lead to fast excitations of the system. For the sake of consistency, also this system was driven with twice of the rotational frequency.

To conclude, time dependent perturbation theory can not be consulted to explain small shifts of position and rotational frequency of fixed points for larger amplitudes being known from the classical system. However, the choice of the proper driving frequency can be explained quite well.

3. Realization of a driven two component BEC

The Bose-Hubbard Hamiltonian can be realized in external [62, 68, 57, 42] as well as internal degrees of freedom [58]. The internal implementation has some advantages like an enhanced stability against environmental noise and a direct accessibility to the phase of coupling. Therefore we choose the internal realization.

The measurements were performed at a well-established experimental setup. Hence just a short overview of some technical aspects will be given. The basic apparatus was built by Bernd Eiermann and coworkers, so most design thoughts can be found in his work [69]. The next generation implemented the external Josephson system [70, 71]. A significant improvement of the stability of the experiment was achieved in the works of Christian Gross and Andreas Weller [72, 37] yielding the first experiments in the internal system [54] at this machine. Properties of the symmetric system (Sec. 2.3) and experimental efforts to realize this are intensely studied in [58, 38].

Rubidium^{87} exhibits some features making it the system of choice for realizing the internal system. A Feshbach resonance between the two hyperfine states $|F = 1\rangle$ and $|F = 2\rangle$ arises at low magnetic field of $B = 9.1\,G$ (Sec. 3.2.1), which is experimentally easily accessible. The hyperfine splitting of $\Delta\nu_{HF} \approx 6.8\,GHz$ and the Zeeman splitting of $\Delta\nu_Z \approx 6.3\,MHz$ (at this field [73]) are in a range which can be directly addressed by commercial radio hardware.
Furthermore the almost equal intra-species scattering lengths of the two hyperfine species are experimentally quite favourable. On one hand, this reduces the mean field shift (Sec. 3.3), on the other it is a requirement for establishing the single mode approximation (Sec.2.1).
Additionally, the first order Zeeman shift is equal for the two hyperfine states $|F = 1, m_F = +1\rangle$ and $|F = 2, m_F = -1\rangle$, since the corresponding Landé-g_F factors differ just in sign [74, 75]. Therefore implications of magnetic field fluctuations are vastly reduced and the stability of the experiment is enhanced.

3.1. Basic steps to reach Bose-Einstein condensation

The realization of a Bose-Einstein condensate is a well known task nowadays, being first developed in [76, 77] using different atom optic techniques [65, 43, 78]. In the following a short summary of the basic steps to condense ^{87}Rb will be given described in detail in [69, 72, 58]. In contrast to the first implementation in our lab [69], the condensation is done in the optical dipole trap and not in the magnetic trap by now.

A sample of ^{87}Rb is evaporated in a vacuum chamber and pre cooled and compressed by a funnel (2D magneto-optical trap (MOT) + push beam). This creates an atomic beam which is transferred through a differential pumping stage towards the experimental chamber. There the atoms are trapped in a 3D-MOT and subsequently transferred into a magnetic trap. A compression in phase space density and cooling close to T_c is achieved in a TOP-trap (time orbiting potential) by evaporative cooling. The sample in the $|F = 1, m_F = -1\rangle$ state is subsequently transferred to a crossed dipole trap ("waveguide" at $1030\,nm$), which is far detuned to atomic transitions. Opening of the trap leads to further loss of fast atoms and thus evaporative cooling to achieve condensation. After condensation and loosing all spare atoms, an optical lattice at $820\,nm$ is ramped up to realize a chain of tight confined BEC's. The condensate is subsequently transferred to the $|F = 1, m_F = 1\rangle$ state by an adiabatic passage [79].

Due to large detuning of the dipole traps to the atomic transitions at $780\,nm$ and $795\,nm$ [73], the trapping potential is equivalent for the different components. The waveguide is slightly focussed yielding in a tight trap in transversal direction with $130\,Hz$ trapping frequency, but as low as $2.7\,Hz$ in longitudinal direction. In order to achieve a tight trap in longitudinal direction, a pair of beams forming an optical lattice are superimposed to the waveguide [72, 38] yielding in trapping frequencies of the order of $650\,Hz$.

Using an optical lattice for longitudinal confinement rather than a single focussed beam, has the big advantage of creating many almost equal traps (up to 35 in our system), with a well spacing of at least $5.5\,\mu m$ [38]. The trap depth is large enough to suppress tunneling between adjacent wells within experimentally investigated time scales. Therefore, the condensates of different wells are uncoupled and the same experiment is repeated many times at the same experimental run, enhancing the statistics enormously.

This method introduces some new drawbacks. In order to obtain structurally the same dynamics in all wells, the according parameters have to be the same. Thus, spacial homogeneity of the coupling and the magnetic fields is required. An atom number inhomogeneity is observed due to slight focussing of the wave guide, but can be excluded by post selection. A discussion of inhomogeneities is given in [38], whereas an improvement of the homogeneity of the coupling has been achieved since that.

3.2. Tuning the nonlinearity

According to Eq. 2.20 the nonlinearity χ depends on the difference of intra-species scattering lengths a_{11}, a_{22} to the inter-species scattering length a_{12}. Since these are approximately equal for the investigated hyperfine states of ^{87}Rb [80], the nonlinearity almost vanishes at zero magnetic field.

However, the inter species scattering length between the two hyperfine states $|F, m_F\rangle = |1, +1\rangle$ and $|F, m_F\rangle = |2, -1\rangle$ can be tuned by using a Feshbach-resonance around $B_0 = 9.1\,G$ (first reported in [80]). A general introduction into Feshbach-resonances can be found in [40, 81], the latest data were taken from [82, 37]. Therefore, by tuning the inter species scattering length while retaining the intra particle scattering lengths, the nonlinearity can be tuned over a large range.

3.2.1. Feshbach resonance

The basic idea of Feshbach resonance is the tuning of a molecular bound state (e.g. via a magnetic field) to be close to resonance to an open channel in the scattering process of two atoms $|1\rangle$ and $|2\rangle$. The inter species scattering length a_{12} is modified by a magnetic field according to [83, 81, 37]:

$$a_{12}(B) = a_{12}^0 \left(1 - \frac{\Delta B}{B - B_0 - i\frac{\gamma_B}{2}}\right). \tag{3.1}$$

For the examined resonance between $|F, m_F\rangle = |1, +1\rangle = |1\rangle$ and $|F, m_F\rangle = |2, -1\rangle = |2\rangle$ the parameters were measured to $B_0 = 9.1047\,G$ as the position and $\Delta B = 2.0\,mG$ as the width of the Feshbach-resonance including a loss from the excited state with loss rate $\gamma_B = 4.7\,mG$ and

a background scattering length of $a_{12}^0 = 97.7\,a_0$ [82], with the Bohr radius $a_0 = 5.292 \times 10^{-11}\,m$. The maximal achievable change in scattering length is limited by the loss. The nonlinearity χ calculates in the single mode approximation (Eq. 2.20):

$$\chi = \frac{1}{2}(g_{11} + g_{22} - 2g_{12}) \int \mathrm{d}r |\Phi_0|^4 \tag{3.2}$$

with $g_{ij} = 4\pi\hbar^2 a_{ij}/m$. Thus, while the intra species background scattering lengths $a_{11} = 100.4\,a_0$ and $a_{22} = 95.47\,a_0$ [84, 37] are not affected by the Feshbach-resonance, the nonlinearity χ can be varied in amplitude and sign by tuning the inter species scattering length.

Close to the Feshbach resonance, two body and three body loss is enhanced [80, 85]. This limits on the one hand the time accessible for experiments, on the other it results in a change of system parameters and in decoherence. Thus a compromise between a strong nonlinearity and enhanced loss has to be found. In all experiments a value of $B = 9.12\,G$ was chosen, yielding in a nonlinearity of $N\chi = 2\pi \cdot (31.9 \pm 2.3)\,Hz$ for $N = 700$ atoms and the current trap frequencies.

3.2.2. Temporal magnetic field stability

Fluctuations of the magnetic field alter the detuning due to higher order Zeeman shifts. In order to limit these fluctuations well below the artificial detuning, a strong restriction on typical field fluctuations is required. Therefore, the magnetic field is actively stabilized [37, 38], which ensures a shot to shot stability of $50\,\mu G$, equivalent to a detuning of $\delta = 0.5\,Hz$. Another limit arises due to the narrow width of the Feshbach-resonance of $\Delta B = 2.0\,mG$. To ensure an almost equal nonlinearity for all experiments, the fluctuation of the magnetic field has to be much smaller than this typical order. However, the limit due to detuning is the more stringent condition, and thus the width of the Feshbach resonance is irrelevant for further considerations.

As the $50\,Hz$ signal of the line influence the magnetic field compensation, the high stability could only be achieved by locking the sequence to the phase of the $50\,Hz$ signal. The remaining $50\,Hz$ component on our field can be cancelled using a feed-forward technique to ensure also temporal homogeneity.

In order to calibrate the feed-forward, the influence of the line on detuning has to be determined. This is realized by measuring the outcome of short

time Ramsey sequences [86, 87] at different phases (thus times) of the line. A small shift in the magnetic field shifts also the resonance frequency of the Ramsey. Therefore, amplitude and phase of the additional signal can be adjusted in such a way, that the influence of the line vanishes in the Ramseys during the full *50 Hz* cycle (see Fig. 3.1). Hence the influence of the line can be reduced to the order of our shot-to-shot stability of *50* µ*G*.

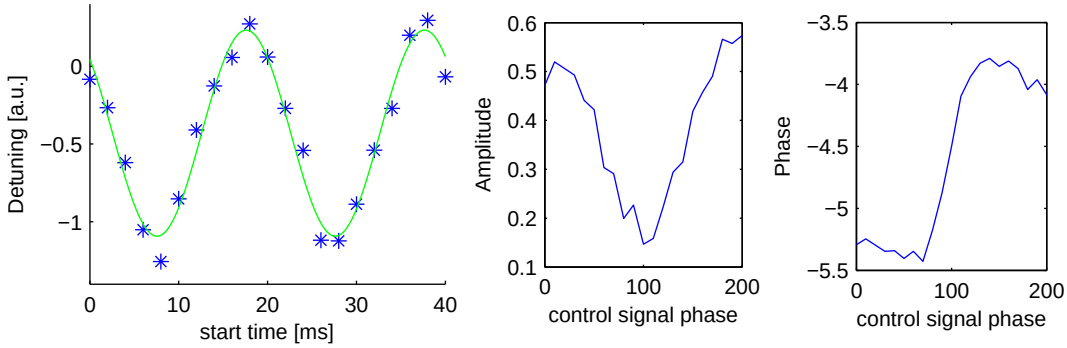

Figure 3.1.: Left: Detuning measured by a Ramsey depending on the start delay to the *50 Hz* trigger, thus the phase of the line. The detuning alternates with *50 Hz*.
Center: Applying the compensation signal. The amplitude (center) and phase (right) of the fitted sine (from the left graph) are plotted for different phases of the compensation signal. Clearly a drop of the amplitude for a compensation phase around *100°* is observed.

Due to long time drifts of the magnetic field stabilization the offset field is calibrated regularly by a Ramsey measurement (typically twice per hour).

3.2.3. Atom loss

The loss of atoms during the experiment has strong implications, since the defining parameters of the experiment $N\chi$ and δ depend directly on the atom number. Therefore, a brief summary of atom loss in our experimental system will be given.

As the lifetime due to background losses and scattering of trap light is in the order of *20 s*, it can be neglected for our experimental time scales of a few *ms*. Furthermore, two different contributions to the loss are of importance. Spin relaxation loss occurs if two atoms collide and one excited atom relaxes to the ground state. The energy released by this process is transferred to kinetic energy and suffice to loose both atoms from the

trap. It is only important for the $|F = 2\rangle$ manifold and proportional to n^2 [81].

Close to a Feshbach resonance, atom loss is strongly enhanced [80, 88, 81], due to 3-body recombination and enhanced two body loss. The basic process of the Feshbach resonance is that the incoming states of the scattering of two atoms are energetically close to a bound molecular state. For 3-body recombination, a third atom contributes to the scattering process, thus a real molecule can be formed and the redundant energy is covered by the third atom. Thus all three atoms are lost in this *3*-body recombination, with a rate proportional to n^3 [81].

Both loss processes depend on density, thus on total atom number. Furthermore loss depends also on densities of each hyperfine species, thus on imbalance z. On the one hand, two body loss is restricted to the $|2\rangle$ state, thus the loss is enhanced for states being close to $z = 1$ in contrast to states close where all atoms are in the absolute ground state of the system at $z = -1$. On the other hand, the probability for the scattering of an atom in state $|1\rangle$ with an atom in state $|2\rangle$ depends on both atom numbers. Thus, considering a fixed total atom number N, this loss process is maximized for equal atom numbers in both spin states $N_1 = N_2$, achieved for $z = 0$.

Loss has some serious implications onto the system, since it changes the system parameters with time and can cause decoherence [38]. On the one hand, the nonlinearity $N\chi$ depends directly on atom number, but also χ has an implicity N dependency via the density. Thus Λ will decrease with time for a fixed coupling strength. On the other hand, the detuning δ of the system is changed due to the modification of the mean field shift (see Sec. 3.3 for details). The implication of atom loss on detuning is the most important one, since it alters the phase space drastically.

However, this effect can be compensated by changing the detuning of the coupling with time (Sec. 3.4.2). For that purpose, the atom loss as well as mean field shift (Sec. 3.3) have to be quantified. To determine the loss rate, we measured the residual atom number after some time t for different initial atom numbers and imbalances for our experimental time scales. We see no deviation from exponential decay for these short times, thus we cannot distinguish between the different loss processes. Therefore, the data set for a certain initial atom number and imbalance is fitted with an exponential $N(t) = N_0 \exp(-\gamma t)$, leading to an imbalance and atom number depending loss rate $\gamma(z, N)$.

Since the parameters of the system depend on atom number, the loss rate has to be included into the post-selection of atoms in order to select these atoms which have undergone the same time evolution (Sec. 3.6.2).

Therefore, it is advantageous to deploy an simple formula for the dependency of atom loss on imbalance and atom number, which is treated with an heuristic model:

$$\gamma(z, N_0) = (az^2 + bz + c)\sqrt{N_0} + d \; . \tag{3.3}$$

This model is in good agreement to the data for a range of $N_0 = 350 \ldots 700$ and $|z| < 0.9$ with the parameters:

$$\begin{aligned} a &= (-0.395 \pm 0.008)\,\tfrac{1}{s} \\ b &= (0.147 \pm 0.004)\,\tfrac{1}{s} \\ c &= (0.547 \pm 0.022)\,\tfrac{1}{s} \\ d &= (-2.54 \pm 0.50)\,\tfrac{1}{s} \; . \end{aligned}$$

For an initial atom number of $N = 700$ and zero imbalance, a decay time of $\tau = 84\,ms$ is obtained.

3.3. Mean field shift

When discussing the dynamics of a BEC within the Gross-Pitaevskii equation [39] the main difference to the Schrödinger equation is a nonlinear term $\propto g_i|\Phi_0|^2$ describing the influence of all other particles as a mean field. Since the Rb-BEC is repulsive and thus the scattering lengths are positive, the zero point energy is shifted upwards for each hyperfine species when adding more particles. In the single mode approximation both spin states share the same spacial mode Φ_0 and are separated by $6.8\,GHz$ in energy. Therefore, if both scattering lengths were equal the mean field shift would lead to a joint shift of energies but transition frequencies would be unchanged. Due to a small difference in the intra species scattering lengths of the $|F = 1\rangle$ and $|F = 2\rangle$ hyperfine states [89] with $a_{11} \gtrsim a_{22}$, the ground state energy of the $|F = 1\rangle$ state is shifted slightly more than the one of the other spin species. Thus the resonant transition frequency is lowered when adding more particles, leading to a negative offset detuning.

The same is obtained when revisiting the formula for the overall detuning δ [90]:

$$\delta \sim \Delta + (g_{22} - g_{11})\,n \; . \tag{3.4}$$

It has to be noted, that the last term depends on density of atoms, thus total atom number and trap geometry (the labelling is interchanged according to the notation of [90]). If the total atom number is considered to

be constant, the term $\Delta\nu = (g_{22} - g_{11})\, n$ can be easily compensated by an external detuning Δ and is thus omitted.

Since we are working close to a Feshbach resonance to enhance the nonlinearity, implying enhanced atom loss, the atom number cannot be treated as constant anymore. By loosing atoms the mean field shift implies a change in overall detuning δ, thus the system is tilted during time evolution. As shown later, the tilt is too large to be neglected. Therefore in this section a method to measure and quantify the mean field shift is presented.

In a fixed geometry, the density n depends in a nonlinear way on the atom number N. Since the atoms interact with each other, by putting in more atoms into a trap, the wavefunction expands. Hence the density grows slower than with N. In the Thomas-Fermi approximation the density depends on atom number as [40]:

$$n \sim N^{\frac{2}{5}} \tag{3.5}$$

Given that the intra species scattering length is slightly larger in state $|1\rangle$ (3.2.1) and the density is positive and real, the detuning due to mean field shift becomes negative. For sake of simplicity the model will be slightly changed to:

$$\Delta\nu = -b\sqrt{N} \tag{3.6}$$

with a positive real number b. In the interesting range of 300 to 700 atoms, the square root model differs in the order of $\mathcal{O}(1 \cdot 10^{-3})$ from the Thomas-Fermi approximation, which is more than sufficient for the current considerations. A numerical solution of the GPE (provided by Eicke Nicklas) supports this approximation.

In order to exclude effects of the mean field shift, we compensate the detuning by changing the coupling frequency accordingly (Sec. 3.4.2). A different approach to compensate the mean field shift is theoretically investigated in [91].

3.3.1. Determination of the mean field shift

As a Ramsey interferometer [86, 87] is perfectly suited to measure such small frequency differences (a few Hz on top of $6.3\,MHz$), it is used to quantify the mean field shift. For the experimental determination of the mean field shift, a magnetic field of $B = 9.2\,G$ (further away from the Feshbach resonance) was chosen to minimise loss and phase diffusion due to

nonlinearity [37]. Since the mean field shift depends only on the density n and on the intra species scattering lengths a_{11} and a_{22}, the different magnetic field should not disturb the measurement of the mean field shift.

The atoms were initially prepared in the $|F, m_F\rangle = |1, +1\rangle$ state and are transferred by a $\pi/2$ pulse (equivalent to a beamsplitter) into an equal superposition of the spin states $|1, +1\rangle$ and $|2, -1\rangle$. After an evolution time of $t_0 = 30\,ms$ an additional $\pi/2$ pulse translates the phase evolution in atom number difference which is measured subsequently by absorption imaging (see Sec. 3.6 for details). The phase of the second $\pi/2$ pulse is chosen to have a $\pi/2$ phase shift according to the resonant atom number N_0 due to a maximal sensitivity there. Thus the measurement for all atom numbers is within the rotating frame of the resonant atom number N_0. Therefore even a small detuning accumulates phase during time evolution and could be detected afterwards.

The detected signal after the Ramsey sequence can be written as:

$$\begin{aligned} z_R = a \cdot \cos(2\pi\nu(N,\delta)t) &= a \cdot \cos(2\pi\nu_0 t_0 + \pi/2 + 2\pi\Delta\nu(N)t_0) \\ &= -a \cdot \sin(2\pi\nu_0 t_0 + 2\pi\Delta\nu(N)t_0) \end{aligned}$$

for the fixed time t_0. Due to technical imperfections the visibility of the Ramsey fringe is reduced which is covered by the additional pre factor a. Close to the Feshbach resonance, the visibility would have been further reduced due to phase diffusion [37]. The frequency depends on the atom number and the detuning δ.

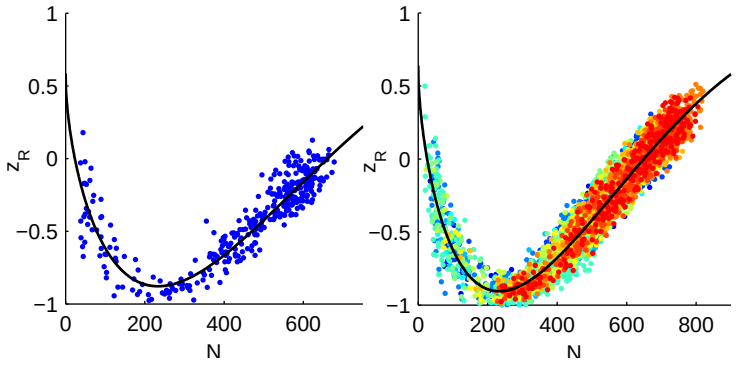

Figure 3.2.: Ramsey signal vs atom number. Left: One scan which is resonant around $N_0 = 650$ atoms, a fit to the data is depicted as a black line. Right: Rescaling all scans (depicted in different colours) according to their offset detuning, all measurements falls onto the same universal curve.

The Ramsey is resonant to the atom number N_0, thus $z_R(N_0, t_0) = 0$. In conclusion, the resonant frequency calculates to $\nu_0 = b\sqrt{N_0}$. Hence the Ramsey signal can be rewritten as:

$$z_R = a \sin\left(2\pi b t_0 \left[\sqrt{N} - \sqrt{N_0}\right]\right). \tag{3.7}$$

By obtaining about 30 independent wells covering different atom numbers within each shot, the Ramsey signal vs. atom number can be measured in a few shots, as done in Fig. 3.2 (left graph). We observe a strong shift of the frequency of the sine with atom number. Furthermore the used model agrees well with the data.

Long term drifts of the magnetic field results in different resonant atom number from scan to scan. To test the model, all bare data from different scans are rescaled in a way, that they are resonant to the same atom number. If the model is correct, then all scaled data points will fall onto the same curve as shown in the right panel of Fig. 3.2. This is a clear indication of an almost correct scaling behaviour. Thus, the parameter b averages over many scans to:

$$b = (0.82 \pm 0.02)\, Hz/\sqrt{N}. \tag{3.8}$$

Linearizing the mean field shift around a certain atom number, e.g. 500 atoms, one obtains a gradient of 55 atoms/Hz.

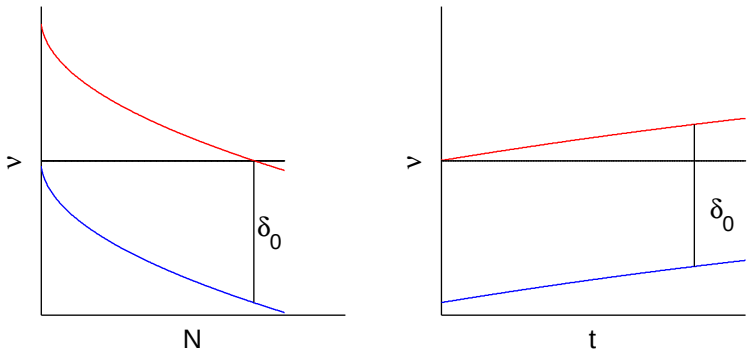

Figure 3.3.: Detuning due to mean field shift.
Left: Detuning vs. atom number. The resonant frequency is depicted in black, the detuning due to mean field shift in blue, which is shifted by an additional detuning δ_0 (red).
Right: Detuning vs. time, assuming a constant offset detuning δ_0. Due to an exponentially decay of the atom number, the detuning is increased. In the large atom limit, the detuning deviates just slightly from a linear increase.

All driven experiments were done with an initial atom number of $N = 700$. However due to atom loss close to the feshbach resonance, more than 350 atoms were lost during the experimental sequence of maximal $60\,ms$, leading to a detuning of about $7\,Hz$. Comparing this to the chosen detuning of about $1.5\,Hz$ (for the $\Lambda = 1.5$ system) it turns out that the system is massively changed by atom loss. Thus an compensation for the detuning due to mean field shift was implemented (see App. 3.4.2).

The decay of atom number behaves exponentially, thus also the detuning rises exponentially, although with twice of the decay time (see Fig. 3.3). To compensate for the mean field shift, the additional detuning has to be exponentially decreasing .

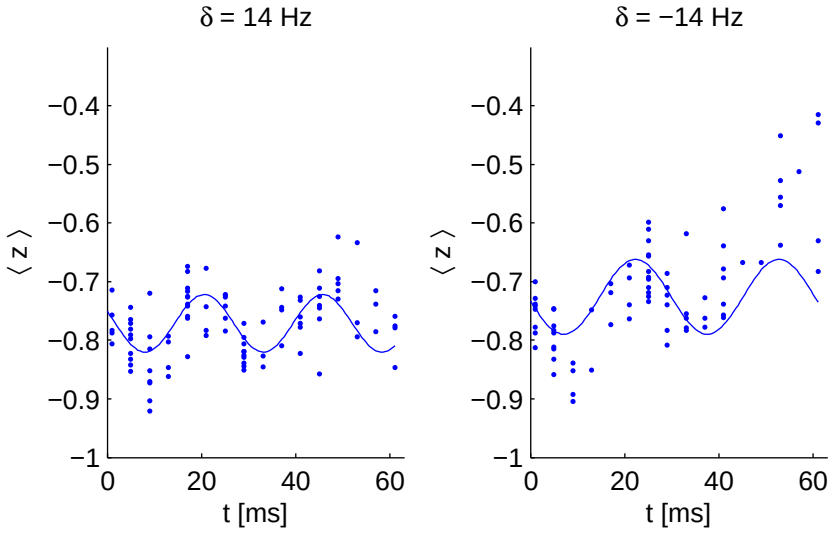

Figure 3.4.: Illustration of the influence of detuning compensation. Left: The detuning compensation is applied with proper amplitude and sign. All points scatter around the sine oscillation almost equally. Right: The compensation is applied with wrong sign, mimicing a twice as large atom loss. An overall shift is visible additional to the oscillation. The effect would be half as strong as on the right side for a measurement without loss compensation.

The technical implementation of the detuning compensation is described in Sec. 3.4.2, an example of the resulting dynamics is given in Fig. 3.4. The effect of loss driven detuning can be directly observed by measuring the time dynamics of an initial preparation close to the stable fixed point (for $\Lambda > 1$). In absence of loss, small oscillations around the fixed point are expected. With loss and thus a time dependent detuning, the position of the fixed point will be altered during time evolution. Therefore the time

evolution resembles a sine with de- or increasing offset accompanied by a change in oscillation frequency. The effect will be much stronger for "weak" traps than for "deep" ones.

The measurement of the mean field shift indicates a dependency of the detuning on the preparation sequence. In order to ensure the same conditions for all experiments, the same preparation sequence[1] was used.

3.4. Linear coupling of two spin states

The relevant level scheme for the discussion of linear coupling of the two hyperfine states is given in Fig. 3.5. The two hyperfine states are separated by $6.834\,GHz$ ($\cdot 2\pi\hbar$) in energy, the linear Zeeman shift leads to separation of adjacent magnetic sublevels of $6.38\,MHz$ [73] for a magnetic field of $9.12\,G$.

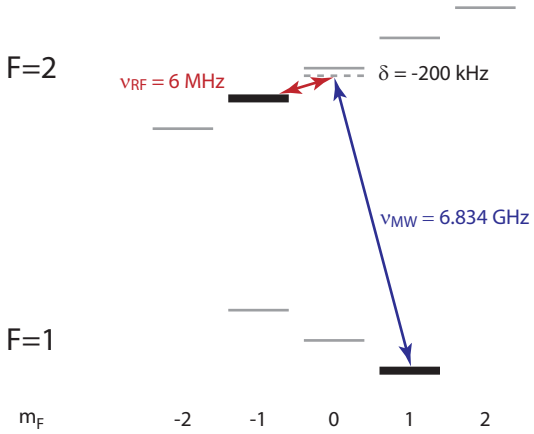

Figure 3.5.: Level scheme of the relevant hyperfine states. The utilized states $|1\rangle$ and $|2\rangle$ are accentuated in black. The relevant transition frequencies [73] are sketched not to scale. Furthermore the levels are shifted due to light field shift of the off-resonant couplings, which is omitted in the plot as it is much smaller.

The direct transition between $|1\rangle$ and $|2\rangle$ is forbidden in the dipole approximation due to a difference of $\Delta m_F = 2$. Therefore, the linear coupling is realized by a two photon transition via an intermediate level $-200\,kHz$ detuned to the $|F = 2, m_F = 0\rangle$ state. Thus, the coupling pulse consists of a microwave at $\nu_{MW} = 6.834\,GHz$ and a RF pulse at $\nu_{RF} \approx 6\,MHz$ (the exact

[1] with a fixed value of PWGBEC

value has to be determined according to light field shift). The large detuning of the intermediate state to the $|F = 2, m_F = 0\rangle$ besides the relative low field strength is sufficient to avoid populating the $|F = 2, m_F = 0\rangle$ state. The single photon Rabi frequencies are typically in the order of $10\,kHz$ for both the RF and the MW coupling, yielding in a two photon Rabi frequency of several hundreds of Hertz.

The detuned single photon coupling of both RF as well as MW result an AC-Stark shift [74]. Thus, the energy levels are slightly shifted, yielding in an additional detuning depending on the power of RF and MW fields. The light field shift is in the order of a hundred Hertz for the combined RF and MW pulses at full power. Since several pulses are involved in the experimental sequence, which require different power, the frequency of each pulse has to be adjusted accordingly.

Compared to the nonlinearity of about $30\,Hz$, the maximal linear coupling suffices to realize almost clean $\pi/2$-pulses (or less) for preparation. The influence of the nonlinearity in this regime is negligible. A residual small phase offset can be compensated by the phase of the next pulse.

An important difference of one- to two photon transitions is the dependency of the coupling strength on amplitude of the coupling field. For (real) two photon processes the coupling scales quadratic with amplitude rather than linear for a single photon transition [92]. However, since the intermediate level is close to an atomic state, the system is quite similar to a detuned Λ-system [92], often discussed in conjunction with STIRAP [93]. Applying their findings to the considered case of a large detuning of the intermediate state compared to the single photon Rabi frequencies, a linear dependency of the two photon Rabi frequency on the amplitude of the coupling fields is expected, which is good agreement with experimental findings. The dependency of the overall Rabi frequency on amplitude is important, since the driving of the system is accomplished by driving the amplitude of the coupling.

3.4.1. Tuning the relative nonlinearity Λ

As derived in Sec. 2.1, the interaction of particles can be described by the dimensionless relative nonlinearity Λ. Since it is defined as the ratio of the nonlinearity $N\chi$ to the coupling Ω, it can be tuned either by changing the magnetic field or trapping frequencies, or the amplitude of the coupling.

All experiments within this work were done at the same magnetic field and thus a fixed nonlinearity χ. We choose to change the coupling instead for the following reasons. On one hand, the coupling is experimentally much

better and faster to control than the magnetic field. This is of importance for the experimental sequence, where different regimes of the relative nonlinearity are required ($\Lambda \ll 1$ for preparation and $\Lambda > 1$ for the experiments). On the other, atom loss depends on the magnetic field, but should be the same for all experiments. Therefore, the coupling is changed for reaching different regimes of the relative nonlinearity.

3.4.2. Modulating the coupling

The coupling is restricted to provide the driving on one hand (Sec. 2.5.1) and to be resonant at all times on the other, thus the frequency has to be adapted during time (Sec. 3.3). Since a two photon transition is used and the coupling depends linearly on both amplitudes (Sec. 3.4), either the MW or the RF could be used for realizing the driving. In the microwave regime, this is a hard task, but it can be easily done on the radio frequency by using an arbitrary waveform generator. An Agilent 33522 A waveform generator is perfectly suited for this task when using the high precision clock (OCXO, oven controlled crystal oscillator). The high precision oscillator is required in order to minimize jitter in the sampling rate.

For the driving, we alter the coupling strength periodically, which is proportional to the amplitude of the RF signal. Thus by amplitude modulation of the RF, arbitrary driving sequences can be implemented. We also modulate the frequency of the RF to compensate for the detuning due to mean field shift. This corresponds to a frequency modulation with an exponential slow down. As this is no standard task being covered by built in functions, the AWG is used in the arbitrary waveform modus and the waveform is calculated by a computer and sent to the AWG afterwards. Even with the largest sampling rate of 250 mega samples per second, the maximal desired sequence length of $60\,ms$ fits into the memory of the AWG, when using the extended memory of 16 mega-samples.

Frequency modulation

The calculation of the frequency modulation will be outlined in the following. As a basic idea, the current frequency is the derivative of the phase

in respect to time [94]:

$$\omega(t) = \frac{\mathrm{d}\varphi}{\mathrm{d}t}$$

$$\varphi(t) = \int_0^t \omega(\tilde{t})\,\mathrm{d}\tilde{t} + \varphi_0$$

Since the detuning scales with the square root of the atom number which decays exponentially, the detuning also decays exponentially but with twice of the decay time:

$$\delta = -\Delta\nu = b\sqrt{N} = b\sqrt{N_0 \exp\left(-\frac{t}{\tau}\right)} = \Delta\nu_0 \exp\left(-\frac{t}{2\tau}\right)$$

with $\Delta\nu_0 = b\sqrt{N_0}$. Hence the frequency has to fulfil:

$$\omega(t) = 2\pi\left[\nu_0 + \Delta\nu_0 \exp\left(-\frac{t}{2\tau}\right)\right]$$

Integrating this equation leads to the time evolution of the current phase:

$$\varphi(t) = 2\pi\left[\nu_0 t - \Delta\nu_0\, 2\tau \exp\left(-\frac{t}{2\tau}\right) + \Delta\nu_0\, 2\tau\right]$$

where the last term is required to obtain the phase $\varphi(t = 0) = 0$. This is the argument of the sine, whereas the amplitude modulation is achieved by a subsequent multiplication of the signal with $[1 + A_{\mathrm{Driv}} \sin(\omega_{\mathrm{Driv}} t)]$. For the sake of convenience all offset phases are omitted in the equations.

The value of $\Delta\nu_0$ can be calculated by evaluating equation 3.6 for examined atom number $N_0 = 700$ to $\Delta\nu_0 = 21.6\,Hz$ (this detuning is on top of the $6.3\,MHz$ signal). Although the decay time depends on the imbalance, and thus on the particular time evolution, a fixed decay time was chosen. The value for zero imbalance, and hence of $\tau = 86\,ms$ was used for all experiments. As the detuning decays with twice of that, it is specified in the experimental data (in the appendix) as $2 \cdot 86\,ms$ as the loss compensation decay time.

3.5. Experimental sequence

In the following section, the experimental sequence will be summarized briefly. Subsequently to condensation and ramping of the trapping potentials to their desired values, a magnetic offset field is ramped up to the specific value to activate the nonlinearity. A high power pulse around J_x transfers the atoms from the $|1\rangle$ state to the desired start value of z. Due to the large Rabi frequency of this pulse ($\approx 310\,Hz$), the nonlinearity almost vanishes but yields in a small error in phase. Subsequently, the coupling power is reduced (and therefore the frequency has to be adjusted) and the phase of the coupling pulse is adjusted according to the desired φ preparation.

The phase shift of the coupling can be intuitively grasped by revisiting the dynamics in the frame of the coupling. Thus the coupling always leads to a rotation around $-J_x$. For sake of simplicity we assume a desired start value of $z = 0$. The first pulse transfers the atoms from $(0, 0, -1)$ to $(0, -1, 0)$. A subsequent time dynamics (without pulse and nonlinearity) leads to a rotation of the atoms along the equator, with the frequency of the coupling pulse. When the atoms have acquired a phase of φ, the attenuated coupling pulse is switched on again and time dynamics according to the desired Hamiltonian will start.

The frequency of the coupling is adjusted according to loss during time evolution, the driving is implemented by amplitude modulation as described in the previous section. The complete pulse is calculated by a computer in advance and replayed by the AWG.

The measurement is achieved by absorption imaging of the atoms. Thus, the only outcome is the number of atoms in state $|1\rangle$ and $|2\rangle$, and therefore each measurement of the system projects the wavefunction onto the z-axis. In order to obtain phase information, e.g. to get full information about the position in phase space, an additional tomography pulse has to be applied. Since almost all investigated dynamics is at the π side of the sphere, a $\pi/2$ pulse around $-J_x$ was chosen for tomography. The imbalance obtained after this pulse is equivalent to $-y$ data.
The phase of the tomography pulse has to be selected with care. The dynamics is always within the rotating frame of the resonant coupling. Due to atom loss, the frequency slightly changes, thus also the rotating frame is changed. Therefore, the phase of the tomography pulse has to include a phase offset according to atom loss.

3.6. Detection and data processing

The atom numbers for spin up and spin down are detected by high-intensity absorption imaging [78, 95], which projects the wave packet onto the z-axis.

3.6.1. Imaging

The imaging involves the simultaneous detection of the two spin states [38, 96], which requires several steps to obtain a good signal. Although it can be done at high magnetic fields, it is found more reliable at low fields due to the negligible Zeeman shift between the levels. Since atom loss is enhanced in the $F = 2$ manifold and the magnetic field ramp needs some time, the $|F = 2, m_F = -1\rangle$ atoms are transferred by a microwave pulse to the $|F = 1, m_F = -1\rangle$ state. Subsequently, the magnetic field is ramped down.

The imaging laser is on resonance to the ^{87}Rb D2 line at $780\,nm$ [73] of the transition from the $|F = 2\rangle$ to the $|F = 3\rangle$ manifold. Therefore, the atoms have to be transferred by a repumper to $|F = 2\rangle$ state before imaging. In order to distinguish different magnetic sublevels, a Stern-Gerlach field (with a magnetic field gradient) is applied and when the atoms are released from the trap. The subsequent time-of-flight of $1.3\,ms$ leads to spacial separation of magnetic sublevels on one hand and a lowering of densities on the other. The resonant imaging laser is shined onto the atoms, and imaged onto a CCD.

The signal is imaged by a high numerical aperture objective onto a CCD. The resolution of the optical system of $1.1\,\mu m$ [97] is well below the separation of adjacent wells. Design thoughts of the imaging optics are given in [97]. Details of our imaging besides a careful calibration and analysis of noise sources are published in [96].

3.6.2. Data processing

The imaging analysis yields in atom numbers for $|F = 1\rangle$ and $|F = 2\rangle$. Hence the total atom number $N = N_1 + N_2$ and the imbalance $z = \frac{N_2 - N_1}{N_2 + N_1}$ can be determined directly. Before investigating the measurement data, some post selection and filtering has to be applied to the data.

Post selection

Since both system parameters Λ and ϵ depend on atom number, different experiments are comparable if and only if the atom number matches. In the experiment, fluctuations of atom numbers both from well to well and from shot to shot are always present. Therefore, a post selection of atom numbers is mandatory.

Due to loss, atom number decreases with time. However, in order to compare experiments for different times, the system parameters should match. Therefore, the atom number for a certain time step has to be selected according to the loss, thus $N(t) = N_0 \exp(-t/\tau)$ for a given time t. Adjacent atom numbers give almost same dynamics, thus a range of atom numbers (typically ± 25) is selected to enhance statistics. The range of atom numbers at a certain time is calculated according to the loss for both boundaries. Throughout this work, if a reference to a certain atom number is given, the value N_0 without loss is meant.

The situation becomes more complicated due to atom number and imbalance dependency of the loss rate $1/\tau(N_0, z)$. The atom number dependency can be easily resolved since the fit of the loss rate (Sec. 3.2.3) involves the same initial atom number N_0 as the experiment.
For handling the imbalance dependency, a running average filter over the time evolution of the mean z is used to determine the loss rate up to a certain time. The atom number of the subsequent time step is filtered according to this loss rate.

Detecting outliers

Due to the complex preparation procedure, a small error in one technical component can lead to "false" results. Most likely, this will result in measuring no atoms which can easily be removed in data analysis. However, some imperfections can lead to "false" results in a single shot or a whole scan which is not detected by bare eye or imaging statistics. Therefore, it is required to remove such outliers on a statistical basis without altering the statistics of the "real" results.

All experiments are repeated several times per parameter set (typically 6 to 8 times) for a certain experimental time. A huge advantage arises from the fact the same experiment is done in parallel in different wells within the same shot. In each shot 6 to 10 of the lattice sites contain atom numbers in the post-selected range. Hence, a modification of a Z-Score test [98] can be used to evaluate if a certain shot i is an outlier according to all other measurements or not.

For a certain parameter set and time, the mean and standard variation are calculated for all measurements, however shot i is excluded. Assuming normal distribution of the N measurements (including n values of shot i), approximately $M = 0.045 \cdot N$ values should be out of a 2σ neighbourhood to the mean. This is a quite good approximation for a state close to gaussian state, e.g. at small times or within a stable island. It is clearly violated for a state after some time evolution in the chaotic sea, however the chosen method yields not in an increase of outliers in these cases.
The shot i consists of n measurements, whereat k values are out of the 2σ neighbourhood. In a standard Z-score test, all points exceeding a fixed threshold are rejected. Thus, a large threshold has to be chosen to avoid altering the statistics due to removing rare events which belong to the ensemble.

In contrast, the information of obtaining k outliers out of n can be used to set up a more advanced threshold. If shot i is an outlier due to technical reasons, it is more likely to get many values which are out of the 2σ neighbourhood within this shot. The joint probability of obtaining k outliers out of M, by choosing n values out of N, is given by the hypergeometric distribution[2] [99]:

$$P(k) = \frac{\binom{M}{k}\binom{N-M}{n-k}}{\binom{N}{n}} \,. \tag{3.9}$$

This probability is above $60\,\%$ [3] if shot i belongs to the normal distribution of this measurement. Contrary, the shot i is treated as an outlier with all of its values if this probability is less than one percent. Although this is a quite conservative limit, it suffices to exclude outliers due to technical reasons but does not effect broad distributions, e.g. in the chaotic sea. A large majority of the such detected outliers correlates with a jump in the offset values of the magnetic field, which could have been excluded by different methods.

Tomography data

The determination of φ from tomography data is done in the following way. After the time evolution (driven or undriven), a $\pi/2$ tomography pulse is applied, corresponding to a rotation around $-J_x$. Therefore, the measured imbalance $\tilde{z}$ corresponds to $-y$ of the original distribution. In conjunction

[2] The calculation fails if k exceeds M, thus k is set to $k = M$ for these cases.
[3] This limit applies for our typical number of measurements but is not valid in general.

with the imbalance data z, the phase is determined by:

$$\varphi = -\arcsin\left(\frac{\tilde{z}}{\sqrt{1-z^2}}\right) . \tag{3.10}$$

The variance σ_φ is calculated according to Eq. A.49. It should be noted, that the variances plotted in the flat phase spaces are not normalized according to Eq. A.47. The normalization is done to obtain variances being independent on mean z and φ values, thus they represent the variance on the surface of the sphere. In contrast, the flat phase space plot is an projection of the data, therefore the variances have to depend on mean values and must not be normalized.

3.7. Determining system parameters

Nonlinearity

The relative nonlinearity Λ can be obtained by small amplitude oscillations close to stable plasma and π fixed points. We achieve this with strong coupling pulses in order to enter the small relative nonlinearity regime. In the linear approximation, the (unscaled) frequencies calculate to $\omega_{Pl} = 2\pi\Omega\sqrt{1+\Lambda}$ for the plasma fixed point and $\omega_\pi = 2\pi\Omega\sqrt{1-\Lambda}$ for the π one (see Sec. A.1.3). Thus the relative nonlinearity can be determined by:

$$\Lambda = \frac{\omega_{Pl}^2 - \omega_\pi^2}{\omega_{Pl}^2 + \omega_\pi^2} \tag{3.11}$$

even if the coupling strength is unknown. An independent check of the coupling can be achieved by comparing the experimentally chosen value to the measured one of $\Omega = \sqrt{\frac{1}{2}(\omega_{Pl}^2 + \omega_\pi^2)}$. The experimental determination gives a value of $N\chi = (31.9 \pm 2.3)\,Hz$ for $N = 700$ atoms.

This method has some drawbacks since it measures the nonlinearity at a shorter time scale compared to the driven experiments due to the large coupling strength (see also Sec. 2.4). Thus, the altering of $N\chi$ due to atom loss is less important. As an independent check one can measure the position of fixed points and frequencies of small amplitude oscillations in the bifurcated regime for a small coupling and compare this to numerical values. This can be done for same parameter and time scales as in the driven system. Since position as well as frequency depends on amplitude of the oscillation due to nonlinearity, it is typically required to obtain the dynamics of several start points in order to get a reliable value of Λ.

Detuning

The detuning ϵ can also be determined by position and frequency of fixed points in the same manner as the nonlinearity. In fact, a more sensitive and much faster method exists to symmetrize the system. When preparing a wave packet at the unstable π fixed point in the bifurcated regime, after a short time the distribution is squeezed in one direction and thus spreads in the other (Sec. 2.3.3). The spreading is symmetric if and only if the system is symmetric. Thus, the symmetry of the system can be verified within a few shots by looking at the symmetry of the spreading in short time dynamics.

Since the detuning depends quite sensitive on the magnetic field, long time drifts of the magnetic field yields in different detunings for larger time scales. Although the magnetic field is actively stabilized (Sec. 3.2.2), long term drifts remain, e.g. due to temperature sensitivity of electronic circuits and sensors. Therefore the magnetic field is calibrated regularly to accomplish a zero offset detuning. This is realized by a two-photon Ramsey sequence [86, 87], which detects the detuning exactly on the experimental transition. During the measurements, after every two experimental runs, a few shots of a Ramsey sequence were performed to obtain the offset detuning and calibrate the magnetic field.

4. Poincaré-Birkhoff Scenario

When an integrable Hamiltonian system is perturbed slightly, the question arises, in which way the solution of the driven Hamiltonian differs from the undriven one. This is a quite natural question, e.g. the gravitational two body system is exactly solvable, but the solar system with some more planets is not. In fact, the stability of the solar system was of moving spirit behind the exploration of nonlinear dynamics [4]. A first answer to the problem was given by Poincaré in the 19th century, however the more general solution was found more than half a century later by Kolmogorov, Arnold and Moser [100, 101] with the KAM theorem. It basically states, that the non-resonant orbits[1] of an integrable system exposed to a small periodic perturbation, will survive slightly deformed [4, 51]. In contrast, the tori being resonant to the driving will be disturbed.

The KAM theorem states which tori will survive the perturbation and which will not. But it does not predict the behaviour of non-surviving tori. This is discussed by the Poincaré-Birkhoff theorem [102], which will be outlined briefly according to [4].
In the vicinity of a resonant orbit, there will be non-resonant tori with higher or lower energy. These tori will remain close to the undriven dynamics, thus the direction of rotation within the Poincaré map will be preserved. One of these will rotate clockwise, the other one counterclockwise. Thus, there has to be a line of points in between, which will be mapped just in radial direction under the action of the driving. Applying the mapping at these points, the image will be another line of points. Since the map is area preserving, these two lines have to intersect in an even number of points. The intersection points are the fixed points of the map, half of them being stable (elliptic), the other half unstable (hyperbolic). Generally, there must be $2nq$ fixed points (with n being a natural number and the driving hits a $r : q$ resonance).
The manifestation of the Poincaré-Birkhoff theorem in quantum mechanics has been shown theoretically for different systems [103, 104] and is briefly discussed for a system similar to our investigated one in [105].

[1] Non resonant in the sense, that the ratio of eigenfrequency to driving is not a ”simple” rational number with small denominator.

4.1. A simple model system

For a first test of the Poincaré-Birkhoff scenario in a macroscopic quantum system we choose the system parameters such, that the system exhibits a quite simple phase space in the undriven case. In the non-bifurcated regime, for parameters $\Lambda = 0.7$, $\epsilon = -0.114$ the system offers two stable fixed points associated to plasma- and π-oscillations, and otherwise regular motion (see Fig. 4.1). The small detuning ϵ was chosen to break the symmetry of the system. It is remarkable that there is a slight anharmonicity in the system leading to smaller frequencies for trajectories closer to the stable fixpoint (at $\varphi = \pi$) and faster time evolution for trajectories further away (see Fig. B.1).

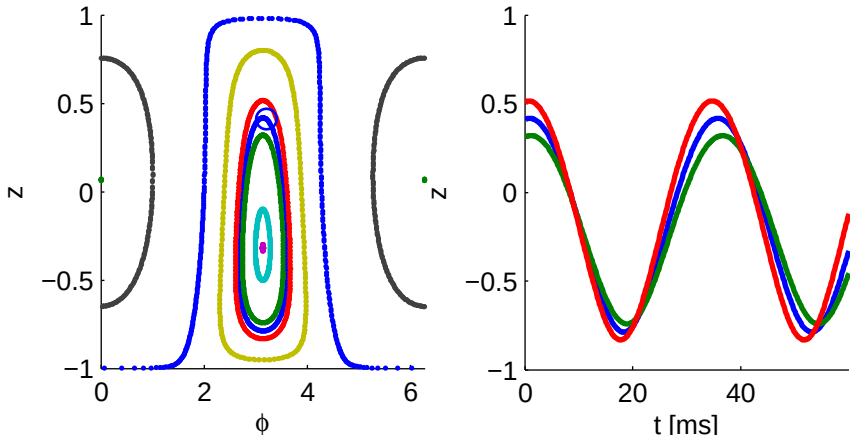

Figure 4.1.: Left: Phase space plot of the undriven system for the chosen parameter set (obtained by classical numerics). The starting point used in the experiments is marked with a circle. All phase spaces within this work will have φ as x-axis and z as y-axis, however the labels will be omitted due to lack of space. Right: Time evolution of the z-projection of 3 adjacent starting points. The blue curve belongs to trajectories resonantly driven by the external driving later. Due to anharmonicity of the system, trajectories located close to the stable fixpoint evolve slower, whereas trajectories located farther outside will evolve faster than the driven one.

In the undriven case, by increasing Λ into the bifurcated regime, interesting phase space structures will arise on the π-side. We will concentrate on this side and center the phase spaces around $\varphi = \pi$. Trajectories at the π-side rotate counterclockwise around the π-fixed point. It should be noted that the Poincaré-Birkhoff scenario can also be realised on the plasma-side without fundamental changes.

4.2. Driving

The question arises how the system behaves after applying a small perturbation due to external harmonic driving. The classical driven hamiltonian reads as:

$$H(z,\varphi) \;=\; \frac{\Lambda}{2}z^2 - \Big(1 + A_{\text{Driv}}\sin\left(\omega_{\text{Driv}}t + \varphi_{\text{Driv}}\right)\Big)\sqrt{1-z^2}\cos\left(\varphi\right) + \epsilon z \tag{4.1}$$

where the driving occurs due to the $A_{\text{Driv}}\sin(\omega_{\text{Driv}}t + \varphi_{\text{Driv}})$-term and can be experimentally controlled by changing the coupling strength. Following the KAM-theorem "non-resonant" orbits (i.e. with irrational frequency to driving ratio, or at least not too close to simple rational ratios) will survive slightly deformed, orbits with a rational frequency to driving ratio will be destroyed. The driving frequency ω_{Driv} is chosen to hit a $1:2$ resonance of the undriven system, so the double of the natural frequency of the selected starting point in Fig. 4.1. According to the Poincaré-Birkhoff theorem this orbit breaks up into $2n\cdot 2,\ n\in\mathbb{N}$ fixed points [102, 4, 51], i.e. at least 4 fixed points. Half of these fixed points show stable (elliptic), the other half unstable (hyperbolic) behaviour.

The system's behaviour is best shown in a Poincaré map, where the time evolution of a starting point is plotted for times being multiples of the driving period in a phase space (Fig. 4.2).
Such a Poincaré map for the undriven system at the same times would result in two points for the resonant trajectory[2]. All trajectories towards the fixed point will result in points rotating clockwise (because the time evolution is slower than the resonant one due to anharmonicity), a trajectory located more outside will rotate counterclockwise due to its higher frequency.

With this in mind, one can easily understand the location of the stable respectively unstable manifolds emerging from the unstable fixed point when the phase space is just slightly deformed by driving (compare to [51]). In the detail plot of Fig. 4.2 points on the manifold a) are outside the resonant one, so they move counterclockwise, points on the manifold c) are closer to the center so they move clockwise, implying axis 1) is the direction of the unstable manifold. The same arguments hold for the other axis, so b) is rotating clockwise towards the unstable fixed point, d) is rotating counterclockwise, i.e. also towards the unstable fixed point. Thus line 2) is depicting the stable axis to the manifold.

[2] For the blue line in Fig. 4.1, the driving period is the half of the period of the orbit, resulting in two points for this trajectory

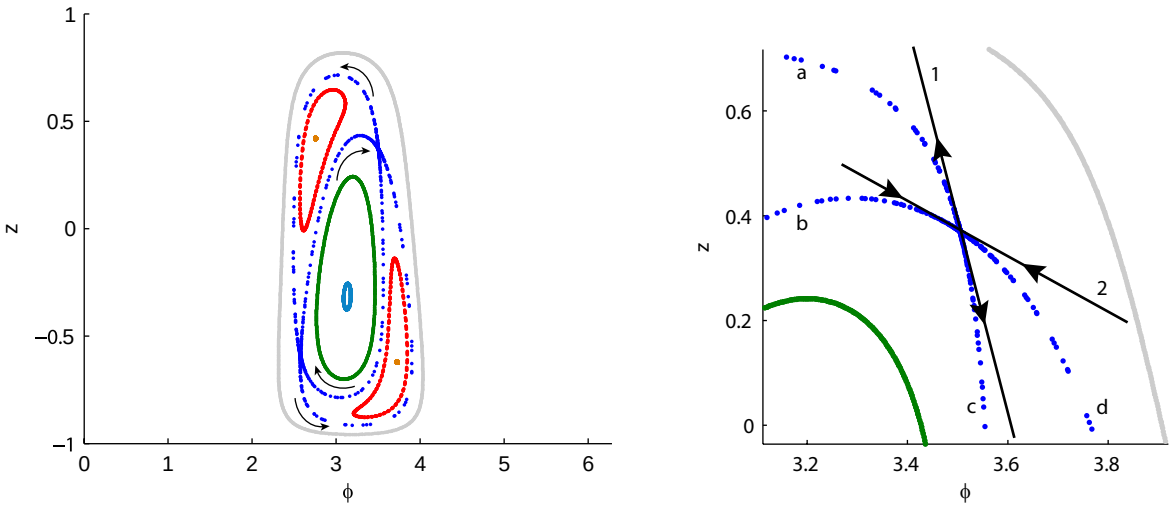

Figure 4.2.: Poincaré map for the driven system with $\Lambda = 0.7$, $\epsilon = -0.114$, $A_{\text{Driv}} = 0.03$, $\omega_{\text{Driv}} = 1.477$
left: Two new stable fixed points (in orange) are created by driving, just as well as two unstable fixed points (on the crossing of the blue manifolds). The arrows depict the rotation direction of points within the Poincaré map.
right: Zoom into upper right unstable fixed point

The thereby - dynamically - generated phase space has some features similar to the undriven bifurcated system[3] for $\Lambda > 1$ [58], notably the unstable fixed points with corresponding manifolds. In context of macroscopic quantum systems unstable fixed points are intensely discussed as a source of entanglement [45], so controlling the properties of an unstable fixed point could be the key ingredient for generation of many particle entanglement.

As a major difference to the undriven system these unstable fixed points can be generated dynamically even in systems, which don't exhibit a bifurcation at all[4]. The properties of the unstable fixed point can be modified by controlling the driving - which could be experimental more accessible. One should note that the unstable fixed point will not rest in place during time evolution, as the Poincaré map does not show full trajectories. In fact it will move close to the orbit of the same starting point in the corresponding undriven system. Associated to this also the stable/unstable manifolds will wind through the phase space.

[3] Only valid for $\epsilon = 0$, a detuned system bifurcates according to Eq. A.30 at the different value of $\Lambda = (1 + \epsilon^{2/3})^{3/2}$.

[4] This scenario only requires an anharmonic system which can be resonantly driven.

4.3. Measurement

In the numerical analysis of a mixed phase space, several methods are known for an investigation of the time dynamics in different regimes in phase space. Among these are the direct plot of the Poincaré map, calculation of the autocorrelation function or fourier analysis of trajectories, the calculation of local Ljapunov exponents for closely adjacent starting conditions or using of delay coordinates [4]. Experimentally the maximal evolution time is limited by atom loss to a few driving periods (Sec. 3.2.3). For these short time scales a plot of experimental data in a Poincaré map is pointless. Furthermore experimental noise could lead to superpositions in fourier spectra. So we will focus on different methods.

Considering the many particle system with a finite $\hbar$, the initial preparation in phase space is not a single point but rather a wave packet with finite size approaching a gaussian distribution with a standard deviation of $\sigma = 1/\sqrt{N}$ for larger atom numbers [45]. Retranslating this to the classical numerical simulations, one should rather start with a bunch of gaussian distributed points than a single one. So for short times it's natural to extend the concept of Ljapunov exponents, which describes how fast two infinitesimal adjacent points are separated by looking at the time evolution of the variance of the distribution. Constraining to short times is necessary since the variance will be no good measure if the distribution becomes far from gaussian.

4.4. Review of time evolution in the undriven system

We shortly remind ourselves of the time evolution of such a wave packet in the undriven system using the classical picture. Consider the system for $\Lambda = 0.7$ and the preparation of a distribution at the initial points marked in Fig. 4.1, all points of the distribution located at the blue line will oscillate with the same frequency. The part of the distribution which is closer to the center will oscillate slower, the fraction away from center will have a faster time evolution. Additional to the joint rotation of all points around the center, this will lead to a shearing and dispersion of the distribution as shown in Fig. 4.3.

This behaviour is experimentally confirmed in Fig. 4.4. The mean oscillates around the stable fixed point whereas the variance grows with time. Since the long axis of the distorted distribution is rotated during one period of

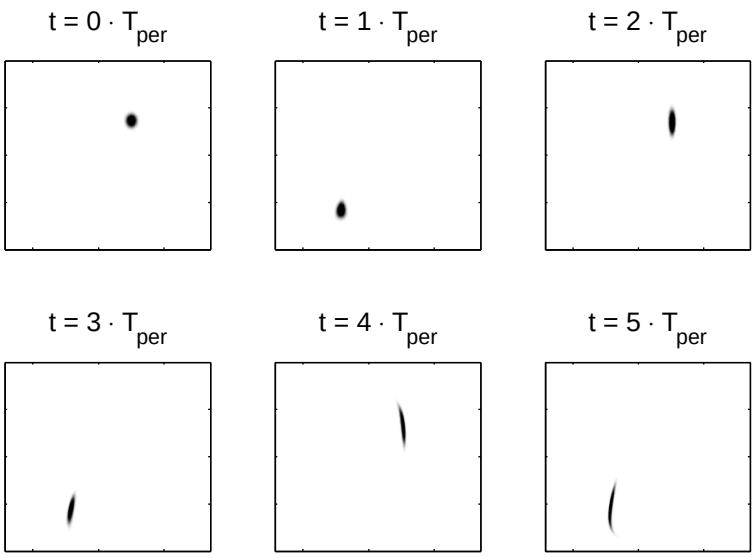

Figure 4.3.: Classical simulation of time evolution in the undriven system for $\Lambda = 0.7,\ \epsilon = -0.114$.
The distribution with a size corresponding to $N = 700$ atoms was initialized at the position of the unstable fixed point in Fig. 4.2 and is plotted for multiples of the driving period, even though in this case the amplitude of the driving was zero. A divergence of the distribution occurs even in undriven system due to its anharmonicity. The plot of the distribution is done accordingly to sec. A.1.2 as for all simulated distributions. A click on the picture starts a video, a detailed plot can be found in Fig. B.3.

the mean, the variance shows an extra oscillatory behaviour due to different projection to measurement axis. Although the measured variance exceeds the calculated one owing to the influence of experimental noise and imperfections, a qualitative similar behaviour is observed.
The experimental data were used to determine more accurate values for Λ and ϵ by a fit with the classical and the quantum model. Furthermore, these values are used for the simulation of the time evolution in the driven systems.

In contrast, preparing the distribution at the stable fixed point will lead to a slight wobbling of the distribution but it remains overall at the position of the fixed point. This is consistent with what would be expected from the corresponding quantum system. For the chosen large atom numbers, the CSS is quite narrow, so the initial distribution samples only a small part in the vicinity of the minima of the potential and thus experiences the

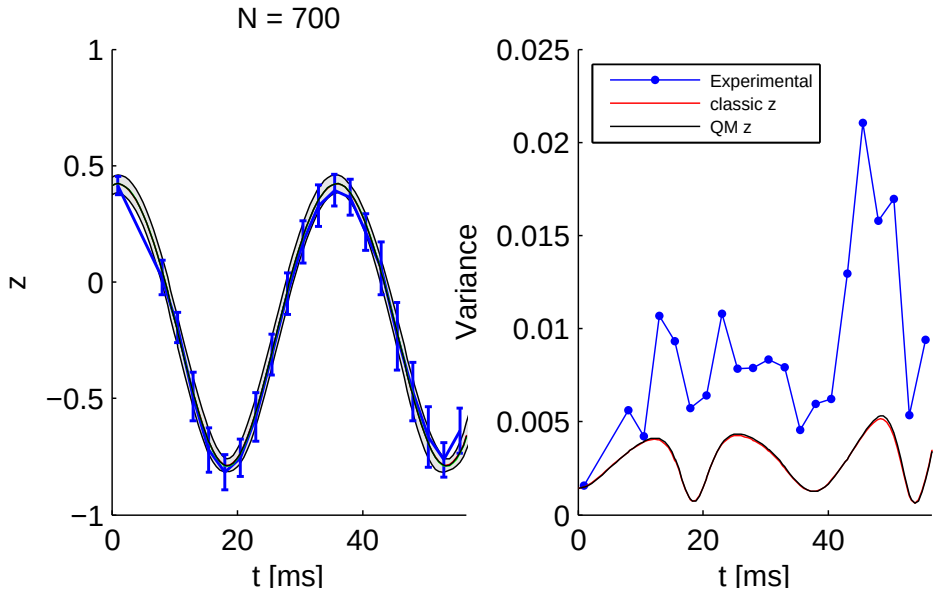

Figure 4.4.: Experimental data and simulation for the starting point $z = 0.41$, $\varphi = 3.21$ in the undriven system with $\Lambda = 0.7$, $\epsilon = -0.114$, $N = 700$
left: For the experimental data, the mean as well as the standard deviation (as errorbars) in z were plotted in blue, the simulation for the fitted parameter is plotted with the standard deviation as a gray band
right: Plot of the measured variance in z in contrast to the simulations, which were done classically as well as quantum mechanically. The different simulation methods lie on top of each other.
During one oscillation period of the mean, the variance also oscillates due to tilt of the long axis of the distribution according to the measurement axis (compare to Fig. B.3), leading to an extra oscillatory behaviour of the variance during one period. An overall increase of the variance is observed.

anharmonicity of the potential (compare to Fig. B.1) just slightly. This leads to a large overlap of the initial distribution with the ground state of the potential of approximately 97%. Since only the higher excited states lead to some additional time dynamics, wobbling will be strongly suppressed.

A much more interesting case is the preparation of a wave packet at an unstable fixed point, as can be done in the undriven case for $\Lambda > 1$ (Fig. 4.5). In the classical picture the distribution will be squeezed along the axis of the stable manifold and diverge along the unstable manifold axis for small

times. For larger times, the distribution will resemble the vicinity of the unstable manifold [38, 45]. The time evolution shown in Fig. 4.5 exhibits

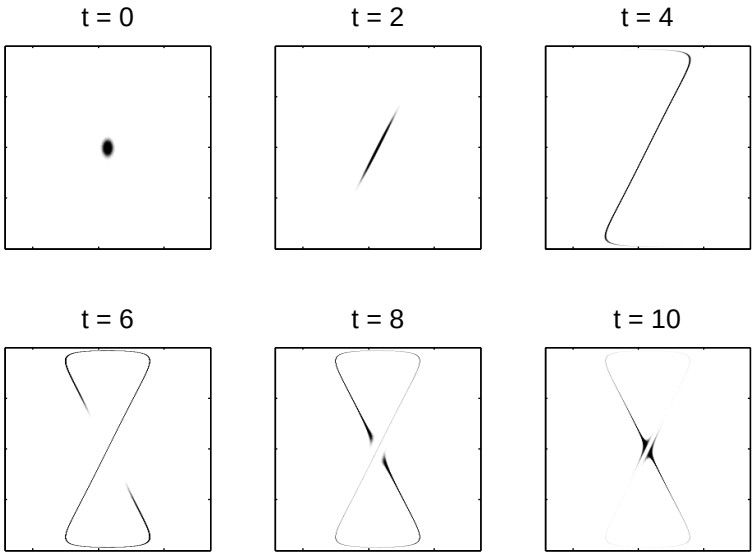

Figure 4.5.: Classical simulation of time evolution for preparation at an unstable fixed point in the undriven system with $\Lambda = 1.6,\ \epsilon = 0$. It should be noted that due to the projective character of the measurement process, even for short times beyond the turning points interferences between two parts of the wave packet for same z values could occur. These cannot be resembled by classical simulations which limits the usage of the classical analog to short times. A click on the picture starts a video.

two distinct features. For short times, the distribution achieves its best squeezing at $t = 2.25$ (see Fig. 2.3). On the other hand, the wave function exhibits a highly non-gaussian state for $t \gtrsim 4$. These states are expected to exhibit many particle entanglement, which can be important for the enhancement of quantum interferometry [54, 59].

To conclude, the previous examples in the undriven systems reveal that one can understand the short time behaviour of a distribution (or even a wave packet when neglecting interference) from the underlying Poincaré map, even though for quite different timescales. The other way around, time evolution of mean and variances of a distribution can be directly connected to the underlying phase space. So measuring variances experimentally is a tool (additional to the time evolution of mean) to confirm the phase space structure.

4.5. Time evolution in the driven system

The aim of this chapter is to test experimentally for a phase space structure emerging due to driving according to Poincaré-Birkhoff theorem (see Fig. 4.2). For that a preparation at different points in phase space has to be implemented.

The plotted Poincaré map shows the phase space for multiple times of the driving period. This map can also be plotted with an additional time offset which is equivalent to a driving with a driving phase φ_{Driv}. For a time offset from $t_{\mathrm{Offset}} = 0$ to $t_{\mathrm{Offset}} = t_{\mathrm{per}}$ (equally to $\varphi_{\mathrm{Driv}} = 0 \ldots 2\pi$) the phase space is rotated by $180°$ around the centered stable fixed point (see Fig. B.2) such that the upper left stable fixed point is transferred to the lower right one. Throughout this chapter the term stable/unstable fixed point is used solely for the moving fixed points created by driving.

For the experimental realization, it is quite favourable to prepare the system at the same point initially and change the driving phase. Otherwise by

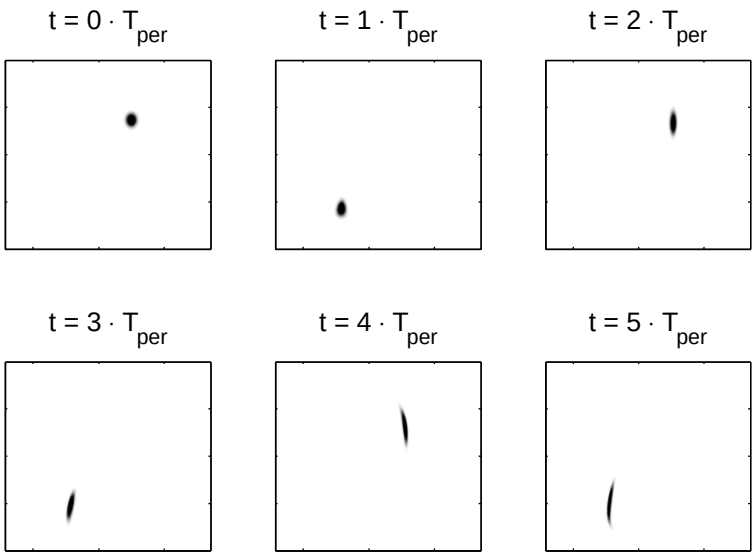

Figure 4.6.: Classical simulation of time evolution at the stable fixed point. The distribution was initialized at $z_0 = 0.37$, $\varphi_0 = 3.50$, $A_{\mathrm{Driv}} = 0.03$, $\omega_{\mathrm{Driv}} = 1.477$ and driven with $\varphi_{\mathrm{Driv}} = \pi$, so it is initially close to the stable fixed point. During the first oscillation periods, the distribution slowly broadens but get refocussed for very long times (visible in the video), revealing the expected dynamics of a wave packet in a weak trap. A click on the picture starts a video, a detailed plot can be found in Fig. B.4.

preparing at different points, these different trajectories will experiencing different loss rates (see Sec. 3.2.3) leading to complications in the data analysis. By changing the driving phase[5] the system offers the possibility to prepare always at the same point but to rotate the whole phase space instead to reach different regimes. It is worth reminding that the position of stable and unstable fixed points are not transferred exactly into each other by changing the driving phase, therefore a small preparation error will occur due to this method.

In the following, some numerical results in the driven system will be compared to the dynamics in the undriven system, before the experimental data will be discussed in Sec. 4.5.1.

By now the results of the time evolution at the stable fixed point in the undriven system (see Sec. 4.4) can be translated to the moving stable

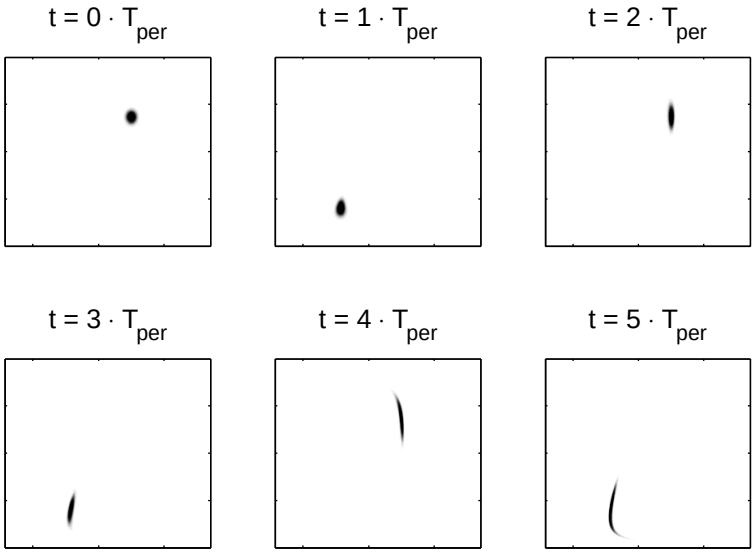

Figure 4.7.: Classical simulation of the time evolution at the unstable fixed point $z_0 = 0.37,\ \varphi_0 = 3.50,\ A_{\mathrm{Driv}} = 0.03,\ \omega_{\mathrm{Driv}} = 1.477$. Preparing the distribution at the unstable fixed point initially, the long axis broadens much faster than for the stable fixed point as well as in the undriven system (Fig 4.3). For longer times the distribution winds along the unstable manifold and diverges furthermore in contrast to the stable fixed point. A click on the picture starts a video, a detailed plot can be found in Fig. B.5

[5]The driving phase can be experimentally controlled much better than the initial preparation.

fixed point created by driving the system. When preparing a distribution at the stable fixed point it will remain there, although the stable fixed point itself is rotating in the phase space during time evolution. Due to the 2 : 1 resonance the original position will be retained after two driving periods. A closer look at the classical picture shows that a point slightly displaced from the moving stable fixed point will oscillate around it (within the Poincaré map) with a much slower frequency than an oscillation around the stable fixed point in the undriven system will require. Accordingly in the quantum picture the dynamically generated local trap will be very shallow, so preparing a wave packet at the minimum of the potential will lead to some overlap with the ground state aside with some excitations of higher states[6]. This leads to slow breathing of the wave packet within the dynamically created trap as revealed in Fig. 4.6.

In contrast preparing the system at the unstable fixed point will also lead to a rotation within the phase space for shorter times but an additional squeezing of the distribution along the axis of the stable manifold and a divergence along the unstable manifold will occur. For longer times the distribution will wind along the unstable manifold thus the mean cannot follow the time evolution of the unstable fixed point anymore as shown in

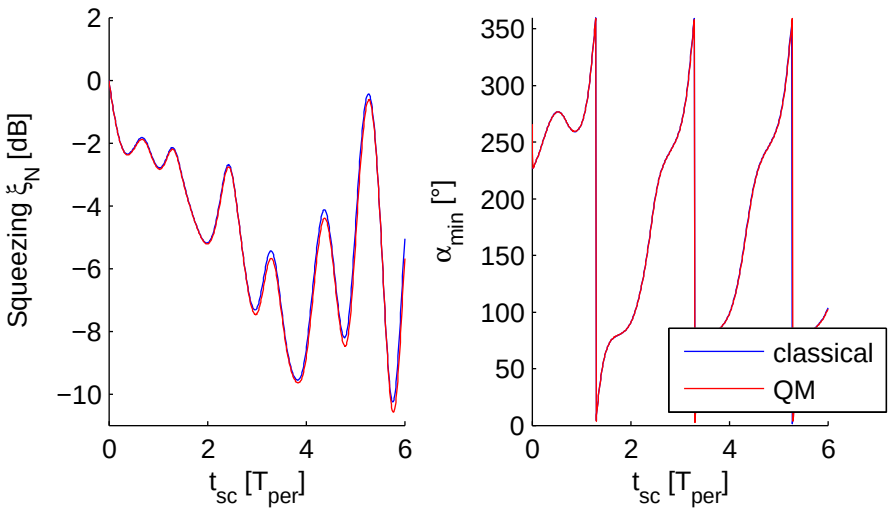

Figure 4.8.: Simulation of squeezing for a preparation at the unstable fixed point, where the distribution is faster and deeper squeezed than for the stable fixed point (compare to Fig. B.7). Oscillations of the squeezing during one period are not related to projection of the variance to the measurement axis as in Fig. 4.4.

[6]The form of the potential is rather elliptic than circular, so no perfect overlap of an initial coherent spin state with the ground state of the local potential is expected

Fig. 4.7. Even for a few driving periods and very weak driving ($A = 0.03$), the distribution diverges along the long axis faster than in the stable fixed point or the undriven system. This should be experimentally observable in an increased variance along the long axis.

The contraction along the axis of the stable manifold leads to a faster squeezing of the distribution than in the undriven system or within the stable fixed point (see Fig. 4.8, Fig. B.7). By comparing how fast the distribution is squeezed, numerical simulations indicate that the characteristics of the unstable fixed point can be directly modified by changing driving parameters. Thus the distribution is faster squeezed for higher driving amplitudes and short times, but the squeezing quickly vanishes after shorter times due to winding along unstable manifold or inset of chaotic behaviour (depending on driving amplitude).

4.5.1. Experimental results of stable fixed point preparation

For an experimental check of the expected behaviour within the stable island a weak driving with $A_{\mathrm{Driv}} = 0.03$ or strong driving with $A_{\mathrm{Driv}} = 0.2$ was chosen. As the initial system parameters are known just to some uncertainties the position of the stable fixed point could vary to certain degree. To ensure preparation within the island it is favourable to choose a preparation close to $\varphi_{\mathrm{Driv}} = 3/2\pi$ and $\varphi_0 = \pi$ due to a ”larger size” of the island in phase space.
However, the time evolution at an unstable fixed point is much more sensitive to the initial preparation than for the stable fixed point. Therefore the preparation for the stable fixed point was done at the same position as the unstable fixed point but a different driving phase. The position of the unstable fixed point was estimated numerically for both driving amplitudes and preparation was done there ($z_0 = 0.41, \varphi_0 = 3.21$ for $A_{\mathrm{Driv}} = 0.03$ and $z_0 = 0.5, \varphi_0 = 3.21$ for $A_{\mathrm{Driv}} = 0.2$) .

The experimental results of the time evolution for a driving phase $\varphi_{\mathrm{Driv}} = 0.7 \cdot 2\pi$ are shown in Fig. 4.9 for about 3 driving periods (raw data included in appendix C.1). The maximal measuring time is limited by loss in the vicinity of the Feshbach resonance. For better comparability the time evolution in the driven system is contrasted to the undriven dynamics, also the corresponding phase spaces for the fitted parameter are plotted. Due to the mentioned uncertainties in system parameters the preparation was rather outside the center of the island. This should induce some additional time dynamics in long time regime.

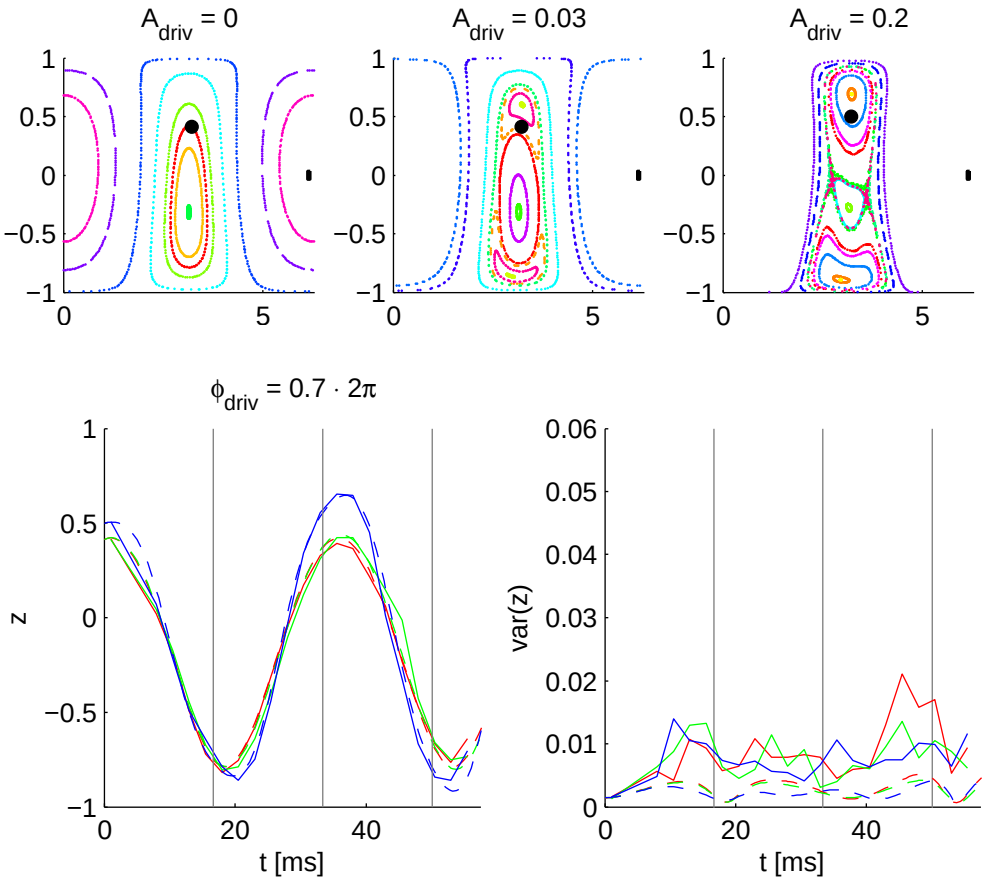

Figure 4.9.: Experimental data for a preparation in the vicinity of the stable fixed point for $\Lambda = 0.7,\ \epsilon = -0.114,\ \varphi_{\mathrm{Driv}} = 0.7 \cdot 2\pi,\ \omega_{\mathrm{Driv}} = 1.477,\ N = 700$
upper: Classical phase spaces for different driving amplitudes. The initial experimental preparation is marked with a dot, the rectangle at $\varphi = 2\pi, z = 0$ indicates the size of the effective Planck's cell.
lower: Experimental data (solid lines) and classical simulations (dotted lines) for different driving amplitudes (red: no driving, green: $A_{\mathrm{Driv}} = 0.03$, blue: $A_{\mathrm{Driv}} = 0.2$), vertical lines indicate full driving periods. The time evolution of the mean is plotted left, the corresponding variances right.

For the weakly driven system the mean $\langle z \rangle$ follows the undriven system quite well[7]. The difference to the strong driven regime is quite obvious. Besides a larger amplitude (which is partly induced by the different starting point) a slight shift in frequency is observed which is fully recovered

[7]The jump in the mean between $t = 0ms$ and $t = 8ms$ in the guide to the eye occurs due to omitting of two measurement points to save measuring time.

by classical simulations. This can be understood when rethinking the original system. The system parameter Λ is the ratio of the nonlinearity to the coupling strength. So by changing the coupling by about 20% (as done for a driving amplitude of $A_{\mathrm{Driv}} = 0.2$) the system temporarily has a different Λ leading to faster/slower time dynamics (according to actual phase) within short times compared to the undriven system.

The situation is much more interesting looking at the time dynamics of the variances in z. The simulation for the undriven case (red) exhibits the oscillatory behaviour due to projection to z-axis and is growing quite slowly. The weakly driven system (green) follows this behaviour with marginal differences due to a preparation too far from the stable fixed point to reveal the expected trapping of the distribution. In contrast the strongly driven (in blue) system indicates a suppression in variances (as in the middle of the second and third driving period).

Although the measured variances exceeds the simulation a qualitative related behaviour is observed. At least at the end of the third driving period a suppression of variance in the strong driven regime compared to the undriven one is detected, indicating the creation of a moving trap (close to the stable island) due to driving. This is a first hint, that the system can be stabilized by driving.

4.5.2. Preparation at the unstable fixed point

The preparation for the experiments at the unstable fixed point is the same as for the stable one except the driving phase was set to $\varphi_{\mathrm{Driv}} = 0.2 \cdot 2\pi$. Thus the unstable fixed point is initially localized close to the zenith. As plotted in the phase spaces of Fig. 4.10, the preparation in the weak driven system is aside from the unstable fixed point. Thus its influence to the time dynamics might be quite small. Due to inset of chaos around the unstable fixed point in the strongly driven regime besides a ”better preparation”, the initial point is located quite well at the unstable fixed point for this case.

Comparing the time evolution of the mean to the situation in the stable fixed point (Fig. 4.9), only slight differences are visible. The weakly driven system follows the undriven one quite well, as in the other case. However in the strongly driven regime the signal appears to be shifted in phase. A closer look to the stable fixed point (Fig. 4.9) reveals more differences. There, the signal is slower than the undriven one at full periods of the driving (where the actual phase of driving is around $3/2\pi$, thus the coupling is smaller than in the undriven system). On the other hand, it is faster for

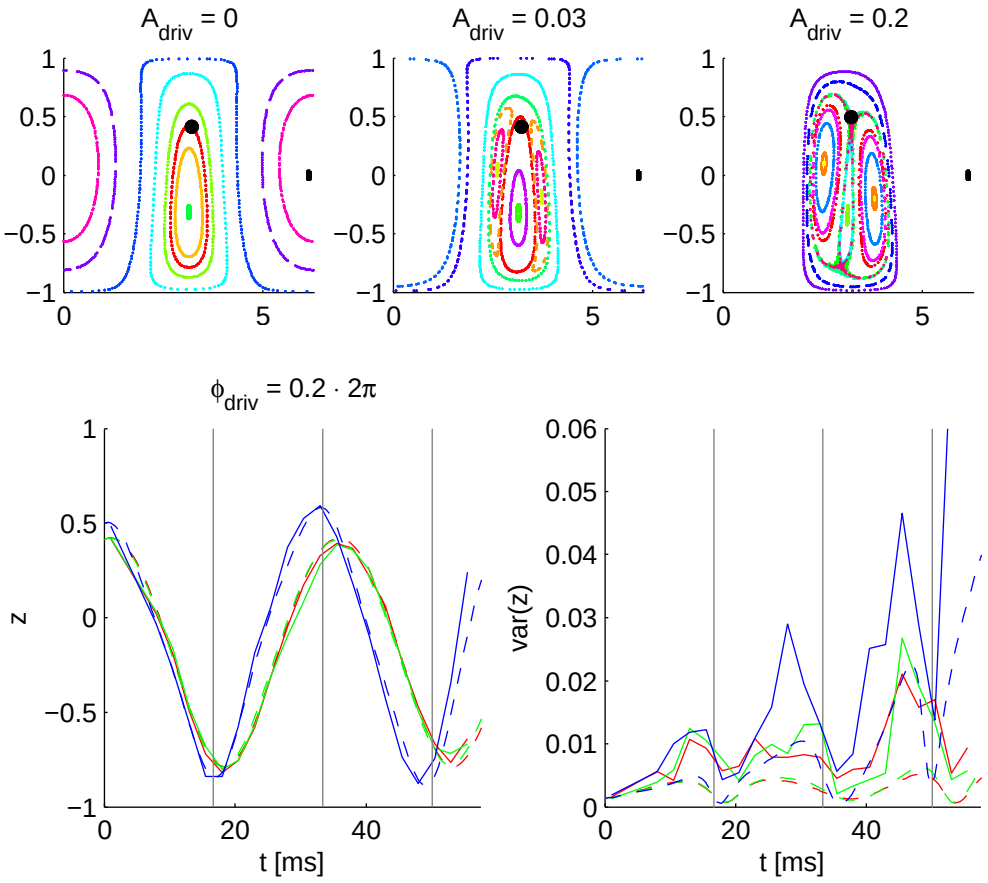

Figure 4.10.: Experimental data for a preparation in the vicinity of the unstable fixed point for $\Lambda = 0.7,\ \epsilon = -0.114, \varphi_{\text{Driv}} = 0.2 \cdot 2\pi,\ \omega_{\text{Driv}} = 1.477,\ N = 700$. The colourcode is corresponding to Fig. 4.9

half driving periods (slope is steeper than the undriven one). The situation is inverted for the unstable fixed point in Fig. 4.10, there the strong driven system is faster around full periods of driving and slower in between, which is consistent with the temporal coupling strengths. Starting with a large coupling strength for the unstable fixed point also implies a smaller amplitude than for the stable one, which is experimentally confirmed.

In contrast, the difference is obvious when looking at the time evolution of the variances in z. In the numerical simulations the weakly driven system exhibits the same behaviour as the undriven one, as expected by the wrong preparation. The measured variances for both cases exceed the numerical one clearly, but as for the stable fixed point a similar qualitative behaviour as in the simulations is obvious. Also the difference in variance between weak driving and the undriven system is within experimental un-

certainties.

The situation dramatically changes for the strongly driven regime. Within the first driving period, both numerical simulations and the experiment follow the undriven one well. Subsequently the variance is enhanced within each driving period, but gets refocussed for full driving periods again. The peaks in the variance within the last driving period exceeds the undriven one by a factor of two. This shows the faster divergence along the unstable manifold created by driving.

The ultimate test for the expected behaviour at an unstable fixed point would be the realization of enhanced squeezing along the stable manifold. When looking at the variance in z, the axis of the stable manifold has to be perpendicular to z-axis. This is the case for times where the distribution reaches zenith respectively its lowest position. However the distribution is strongest bent at these points. Squeezing is a sensitive measure for such effects, so even numerically only slight squeezing is expected with this measuring method. To be able to measure an enhanced squeezing due to driving, the initial preparation (together with a properly chosen driving phase) has to be in a way, that for the time of best squeezing the wave packet achieves a position in phase space with minimized bending (e.g. the mean in z should be at the position of the undriven stable fixed point). The squeezing parameter of the state can be quantified by a tomographic readout. In the presented experiments, we restricted the analysis to two perpendicular measurement axes. However, squeezing analysis might be a further step for analysis of the system.

To conclude, a clear effect of the driving for the variances in z could be observed leading to focussing for a stable fixed point and an enhanced divergence for an unstable one as expected by classical theory.

4.6. Preparation between stable and unstable fixed point

Also of interest is the question, in which way the dynamics is changed, when shifting the initial preparation from the unstable fixed point towards the stable one. With the preparation method described in the previous chapter, this task can be fulfilled easily. The preparation is done at the position of the unstable fixed point for a certain driving phase and the experiment is repeated for a bunch of different driving phases.

As seen in Fig. 4.7 the distribution (or wave packet) is rotating in the phase space during time evolution. Thus at each time step the long axis is projected to the measurement axis along z slightly different such that the measured variance is not meaningful for comparison of different times. The problem could be solved by a subsequent tomography after the time evolution. This is experimentally quite ”expensive”, so we will follow a different route.

The situation could be compared to the preparation at an unstable fixed point in the undriven system (Fig. 4.5), where the distribution mainly diverges along the unstable manifold. There, for short times the angle of the long axis of the distribution is slightly tilted to the axis of the unstable manifold, reaching the axis exactly for the moment of best squeezing and getting bent afterwards. Thus to look for the maximum variance in that system, it's best to make a tomography such that the axis of the unstable manifold is parallel to the measurement axis.

In the driven system, we get this for free. As the phase space is rotated during time evolution, the measurement of the variances has to be done at these times when the axis of the unstable manifold is parallel to the measurement axis. Wether this will work is a matter of time scales - the rate of ”diffusion” along the unstable manifold to the rotational frequency of the unstable fixed point. Due to stronger bending of the unstable manifold, this will only work for short times. The phase space is slightly asymmetric, therefore the times will differ a bit for the upper and lower unstable fixed point. As size and shape of the stable fixed point will vary for different driving amplitudes, also the position of the unstable manifold changes, but this is a smaller effect. A numerical analysis for $A_{\mathrm{Driv}} = 0.05,\ \varphi_{\mathrm{Driv}} = 0.2 \cdot 2\pi$ gives the times for the unstable axis being parallel to z as $t = 14.3\,ms,\ t = 47.6\,ms$ for the lower fixed point and $t = 28.8\,ms$ for the upper one. These times are close to the maximum of the simulated variances for strong driving in Fig. 4.10.

The measured variances in the long axis are plotted in Fig. 4.11 for different driving phases and these special times, compared to simulations. For short times of $t = 13\,ms$ just a slight dependency of the variance from driving phase is detected which is within the experimental uncertainties. For subsequent driving periods the situation changes: a strong dependency of the variance from initial preparation is detected in the strongly driven regime. The maximum of the measured variance is around $\varphi_{\mathrm{Driv}} = 0.3 \cdot 2\pi$ with the initial preparation at an unstable fixed point. It also exceeds the variance in the undriven system revealing the generation of an unstable axis due to driving. On the other side, around $\varphi_{\mathrm{Driv}} = 0.7 \cdot 2\pi$ a minimum is detected much smaller than in the undriven system. This indicates the

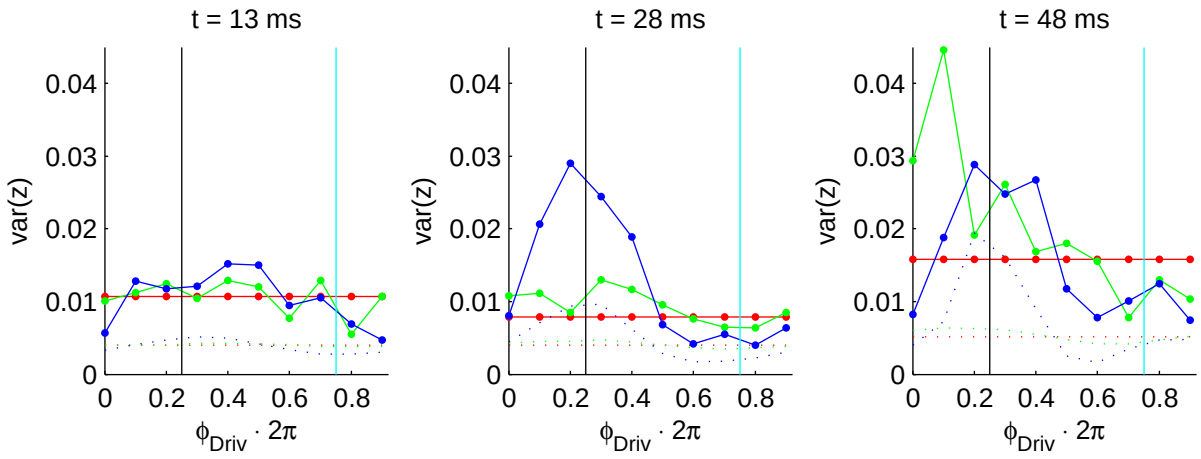

Figure 4.11.: Dependency of the variance from the initial preparation in experiment (solid lines) and classical simulation (dotted lines).
red: undriven, green: slightly driven with $A_{Driv} = 0.03$, blue: strongly driven with $A_{Driv} = 0.2$. The undriven system is independent on driving phase, thus the result of a single measurement is given for that case.

occurrence of a moving island around the stable fixed point in the driven system.

In this chapter the breakup of the regular phase space due to driving accordingly to the Poincaré-Birkhoff theorem was experimentally investigated. The resonantly driven trajectory breaks up into a chain of stable and unstable fixed points together with according manifolds. The experiments reveal a similar behaviour at these fixed points as in the undriven system for different parameters. Thus driving the system opens up the route to the creation of special structures in phase space which could be inaccessible in the undriven system. The behaviour of a wave packet initially prepared at an unstable fixed point is widely discussed, but driving the system is an additional tool to create such a scenario.
For stronger driving the Poincaré-Birkhoff theorem together with the KAM-theorem can be applied subsequently to describe a cascade of bifurcations leading to chaos. Our experiments are the first step of such a cascade and thus a first cornerstone towards chaos in macroscopic quantum systems.

5. Exploring Bloch sphere chaos in a mixed system

Up to now, the influence of weak driving onto the system was investigated. However, stronger driving alters the system beyond the creation of elliptic and hyperbolic fixed points according to Poincaré-Birkhoff theorem. Considering the dynamics close to an elliptic fixed point, which is created by driving. Some of the orbits close by will also be resonant to the perturbation according to KAM theorem [4, 51]. Therefore, these orbits will break up yielding in a series of bifurcations on finer and finer scales. Hence, a fine layer of chaotic states arises between the remaining stable tori. However, this is of limited interest for an quantum system with finite $\hbar_{\text{eff}}$, since it could not sample details on smaller scales than this fundamental limit. Therefore, the perturbation is increased in order to obtain a large chaotic sea.

Theoretical investigation of the driven system can be found in [32, 30, 33], the kicked version is discussed in [27]. The experimental realization of [34], which is deep in the quantum regime, was already discussed in the introduction.
A similar model is discussed in literature as Duffing oscillator [51], where the perturbation is equivalent to the driving of the detuning in our system. It should be noted that the Duffing oscillator can be much better approximated by a harmonic oscillator close to the undriven stable fixed points than the investigated system.

5.1. Basic system properties

In chapter 4 the mechanism of Poincaré-Birkhoff was investigated. To explore a mixed system with a larger chaotic sea, why not just drive this system at $\Lambda = 0.7$ harder? As can be seen in Fig. 4.9, due to the large anharmonicity, the system behaves quite stable for most of the phase space even for a large driving amplitude of $A = 0.2$, where just a small chaotic layer occurs. When recalling that Λ is the ratio of the nonlinearity to the coupling strength, by driving the coupling with an amplitude more than

$A = 0.3$ the system is not slightly changed but temporarily driven into a completely different region. Particulary the system would bifurcate for a short time. Thus additional effects are expected for very strong driving. To avoid this, we choose to work deep in the bifurcated regime to circumvent this effect.

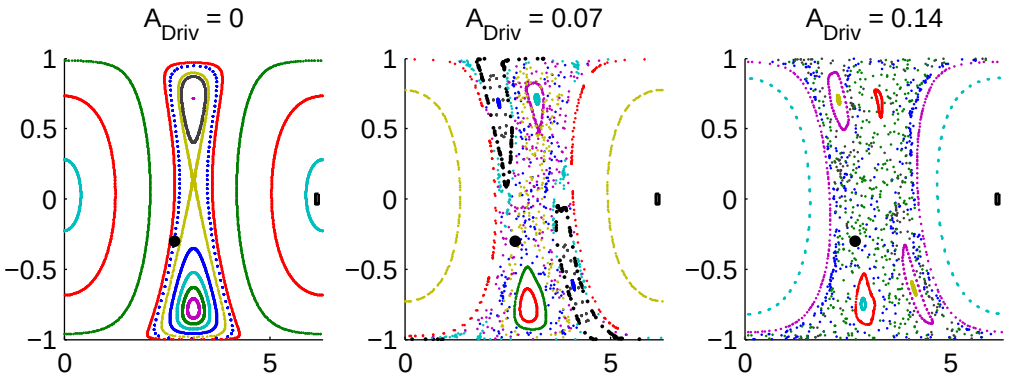

Figure 5.1.: Phase space of the investigated system with $\Lambda = 1.53$, $\epsilon = -0.07$, $\omega_{\text{Driv}} = 1.5867$.
Left: In the undriven system, a double well structure typical to the bifurcated system appears. Due to the tilt in ϵ the phase space is asymmetric in z.
Center: Driving with $A_{\text{Driv}} = 0.07$, $\varphi_{\text{Driv}} = 0$. The two stable fixed points of the undriven system survive slightly altered, additional two moving islands are created by driving (black). In between, a large chaotic sea arises.
Right: Phase space for strongly driven system. Both the two stable islands and the moving island shrink and the chaotic sea becomes more dominant.

We set the parameters to $\Lambda = 1.53$ and $\epsilon = -0.07$, a phase space plot can be found in Fig. 5.1. For these settings, on the π-side of the Bloch sphere two stable fixed points exist at $z_+ = 0.72$, $z_- = -0.79, \varphi_\pm = \pi$ together with an unstable one at $z_{us} = 0.13$ in between (see Sec. 2.3). The different regime can be entered by changing the coupling strength from $40.6\,Hz$ (for $\Lambda = 0.7$) to $20.7\,Hz$. However this implies some drawbacks as the driving frequency and the scaled time also scale with the coupling strength (Sec. 2.1), but the maximal experimental time is restricted by loss. Thus, roughly half of the driving periods are experimentally accessible. For a more accurate determination of the driving frequency, the local frequencies of the bifurcated system have to be considered.

The dynamics in the undriven bifurcated system were intensely studied in [58, 38, 59, 45], where especially the dynamics in the quantum regime for

a preparation at the unstable fixed point (see also Fig. 4.5) raised some attention. For this work a few measurements in the undriven system were performed for the same initial conditions as in the driven case. Additionally to other calibration measurements (see. 3.7), the time evolution of different start points within the undriven system serves on one hand to obtain system parameters under realistic conditions, on the other as a reference for comparing the dynamics in the driven regime.

The time evolution for some of the measured start points and selected times is plotted in Fig. 5.2 in comparison to simulations. Measurements for all start points with the simulation can be found in Sec. C.2.1. Besides the z-data also the y-data (equivalent to φ) was acquired by an additional tomography pulse after the time evolution, so the resulting mean values can be plotted within the phase space with their variances. The classical phase space is included in light gray and a simulation of the time dynamics of a distribution as a density plot (see Sec. A.1.2).

When comparing the time evolution of different start points, a difference not only in the mean, but also in the width of the distributions is observed. Within the stable islands (as red and cyan) the distributions rotate around the stable fixed points and variance remains small. In contrast, by starting close to (but not at) the separatrix (blue and green) the distributions are ripped apart quickly. A qualitatively similar behaviour between experiment and simulation is observed also in the variances.

Of particular interest is the blue curve, as this is the starting point of most of the other investigations. A simulation of the time evolution of the distribution is plotted in Fig. 5.3. The distribution follows the classical trajectory but disperses along it on a fast time scale. For the driven cases, the system was driven at a $2:1$ resonance compared to the frequency of this orbit such that the stable and unstable fixed points created by the driving are located close by.

A fit of the experimental data with classical respectively mean field model serves as a calibration of the parameters Λ and ϵ. Due to the time evolution under realistic conditions, thus long times and same parameter range, the determination of the parameter is more accurate than by plasma- and π-oscillations. The fitted parameters are used for all simulations in the driven regime. We observe a deviation of the start points of simulation and theory. Even if the influence of the loss to the detuning is almost avoided, it alters also the nonlinearity, thus the effective Λ. In contrast, the model system of the simulation deals with constant nonlinearity and detuning, thus acting as an effective model. These effects could be included into the simulation, but then the theoretical description by Poincaré-plot and fixed points will fail. Thus a time periodic model without loss is used and the starting conditions in the simulation have to be altered according to

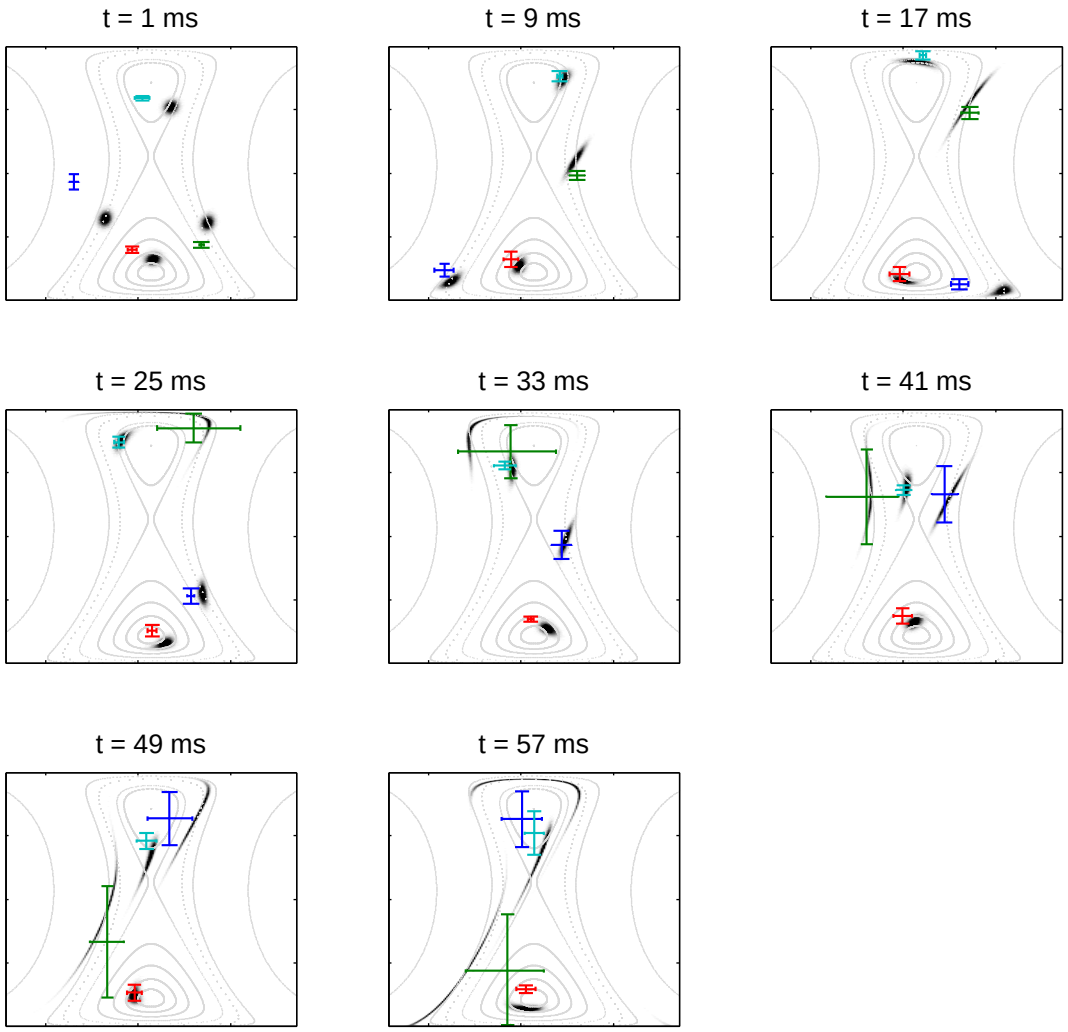

Figure 5.2.: Comparison of the time evolution in experiment and simulation for different starting points in an undriven system. Classical phase space is plotted in light gray, the simulated distributions are shown as in the other plots. The experimental data is plotted for each starting point with measured error bounds as coloured crosses. The experimental variances are not normalized according to A.50 (since the phase space plot shows a projection).

the experimental ones to obtain a satisfactory agreement in the time evolution between experiment and simulation.

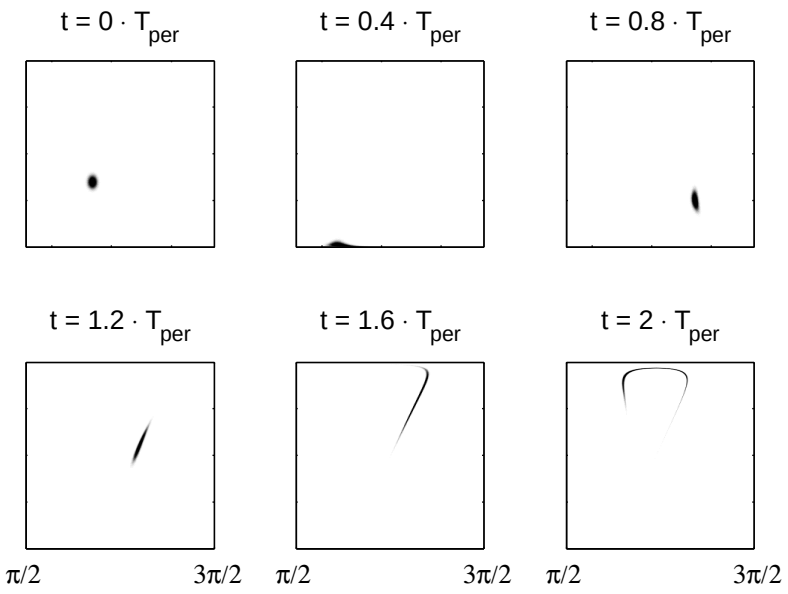

Figure 5.3.: Classical simulation of the time evolution in the undriven system prepared at $z_0 = -0.3$, $\varphi_0 = 2.68$ with $\Lambda = 1.53$, $\epsilon = 0.07$. Even in the undriven system the distribution spreads on a short time scale for this preparation.

5.1.1. Driven system

The phase spaces for the driven system with medium ($A_{\text{Driv}} = 0.07$) and strong driving amplitude ($A_{\text{Driv}} = 0.14$) are also included in Fig. 5.1. The driving frequency was chosen to $\omega_{\text{Driv}} = 1.5867$ at a $2:1$ resonance to the trajectory of the blue starting point in Fig. 5.2 and was kept constant for all experiments within this chapter.

The two stable fixed points of the undriven system survive slightly altered, additionally a stable moving fixed point (or period 2 orbit) is created for medium driving. This is visible as two black islands at $z = 0.68,\ \varphi_{\text{Driv}} = 2.28$ and $z = -0.61,\ \varphi_{\text{Driv}} = 4.09$. By changing the driving phase (equivalent to looking at a different time), these moving fixed points rotate through the phase space close to the trajectory of the undriven system and pass into each other after one driving period. Besides the moving stable fixed point an unstable one is created at $z = 0.63,\ \varphi_{\text{Driv}} = 3.98$ and $z = -0.56,\ \varphi_{\text{Driv}} = 2.21$. In the vicinity of the moving stable fixed points, dynamics will be regular in the rotating frame of the fixed point. Thus an stable island is created close to each stable fixed point. In contrast, the separatrix is broken up and a larger part of the phase space becomes chaotic.

Considering the fitted start point from the reference measurement in Fig. 5.2, the stable fixed point is closest to our initial preparation point for a driving phase of approx. $\varphi_{\mathrm{Driv}} = 0.38 \cdot 2\pi$, the unstable for $\varphi_{\mathrm{Driv}} = 0.9 \cdot 2\pi$.

For stronger driving with $A_{\mathrm{Driv}} = 0.14$ the stable moving island shrinks and the chaotic sea becomes larger. Furthermore adjacent points in the chaotic sea are ripped apart faster from each other than in the medium driven case. This is confirmed by numerical investigation of Lyapunov exponents (Fig. A.2) for different starting points in the phase space.

5.2. Time evolution at a stable/unstable fixed point

The phase space of the driven bifurcated system in Fig. 5.1 exhibits on the one hand some similar features as the system for $\Lambda = 0.7$ (in chapter 4), such as a stable moving island. On the other hand the unstable fixed point is deep within the chaotic sea and from a simple point of view it could be expected that a distribution is ripped apart faster than for the unbifurcated system.

In close analogy to chapter 4 the behaviour of a distribution initially prepared at an unstable respectively stable fixed point will be investigated in the following.

5.2.1. Stable island

For all investigated driving amplitudes, the preparation is done at the same start point as in the undriven system at $z_0^{exp} = 0,\ \varphi_0^{exp} = 2.51$ and the driving phase is chosen in a way that the stable fixed point is close to the initial preparation. Due to the deviation of the fitted start point to the experimental one, the optimal driving phase at which the stable island is close by, differs for experimental respectively fitted start point. Since the experimentally obtained time evolution in the undriven system fits best for the fitted start point, the proper driving phase should be chosen accordingly to the fitted start point of $z_0 = -0.3,\ \varphi_0 = 2.68$ rather than the experimental one. This implies a slight different value for hitting the stable island.

The experimental data of the time evolution in mean and variance is included in Fig. 5.4, the raw data for all measurements within this chapter can be found in C.2. Beneath the undriven reference, measurements

for increasing driving amplitude from slightly driven system $A_{\text{Driv}} = 0.035$ (red) to strong driven system with $A_{\text{Driv}} = 0.14$ (green) are included. The corresponding classical simulation with $N = 700$ is plotted as a dotted line. Since classical and quantum simulation coincides for the desired times, the quantum simulation is omitted for better readability.

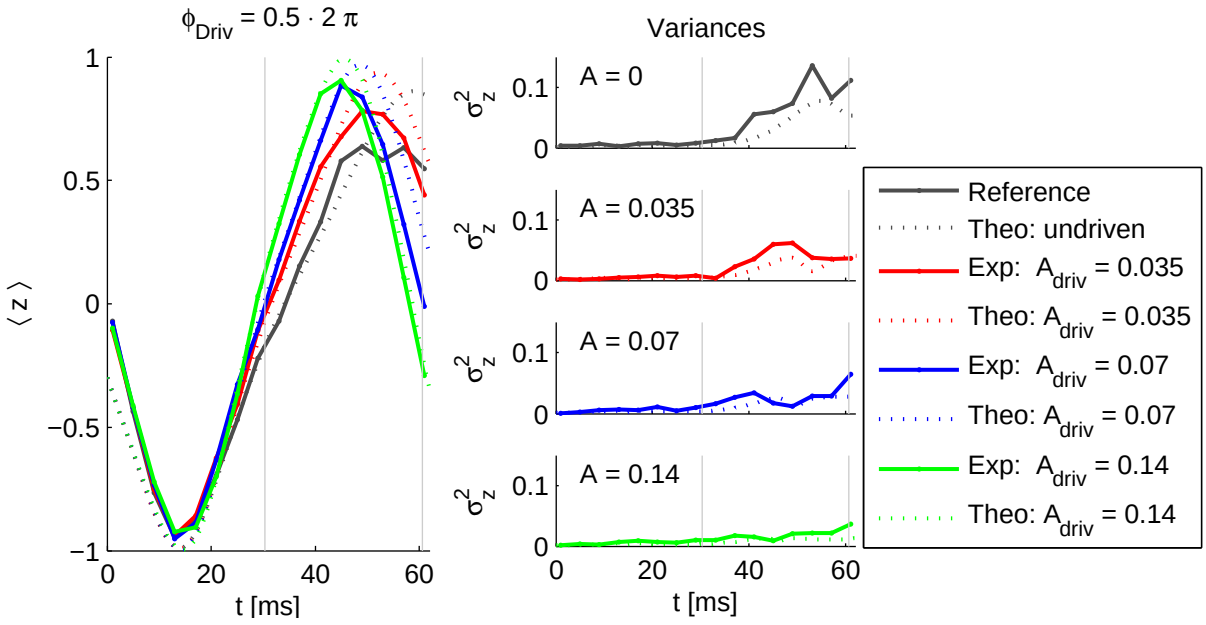

Figure 5.4.: Experimental and theoretical time evolution $\langle z \rangle$ (left) and variance in z (right) for different driving amplitudes and preparation close to the stable fixed point ($\varphi_{\text{Driv}} = 0.5 \cdot 2\pi$). The driving alters the mean due to preparation slightly off the center of the island. Thus, the time evolution of the mean is a bit faster. For variances stronger driving implies a slower growth, thus a stabilisation of the distribution is achieved. For strong driving the data is plotted for the deviating driving phase of $\varphi_{\text{Driv}} = 0.45 \cdot 2\pi$.

Comparing the evolution of the mean in z (left column), the driven system follows the undriven one during the first driving period well. Subsequently a shift in frequency is observed. For increasing driving amplitude the time evolution becomes faster, which is also reproduced by simulations. In the experiment, the preparation is not perfectly at the center of the island, but rather at the boundary. This leads to the observed frequency shift - for a preparation in the center of the island, this would not occur.

Another interesting point is the comparison of variances on the right (with increasing driving amplitude from top to down). For later times, the vari-

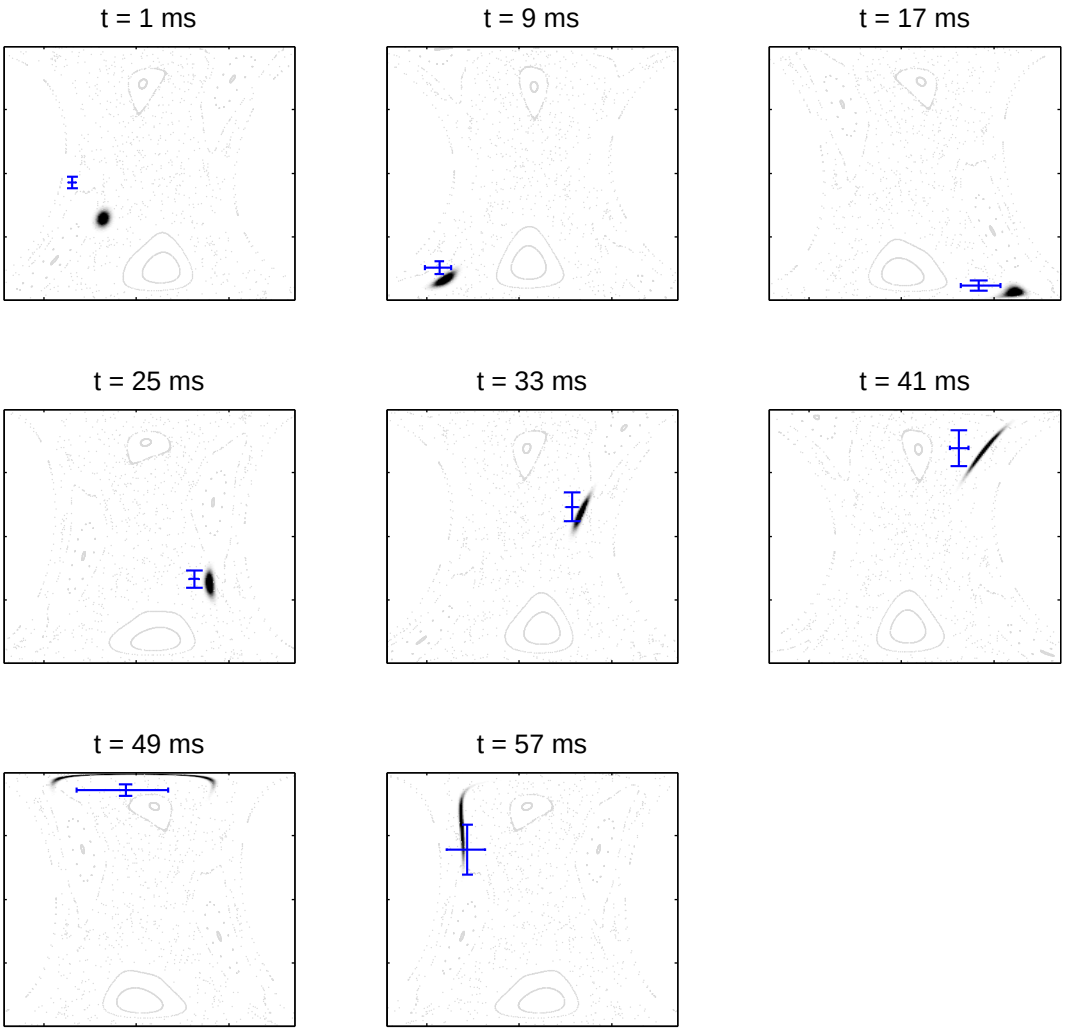

Figure 5.5.: Comparison of the time evolution in the experiment (blue) and the simulation close to the stable moving island. The initial state is prepared at $z_0 = -0.3$, $\varphi_0 = 2.68$ and $A_{\mathrm{Driv}} = 0.07$, $\omega_{\mathrm{Driv}} = 1.59$, $\varphi_{\mathrm{Driv}} = 0.5 \cdot 2\pi$, for the classical simulation a distribution of $N = 700$ atoms is used.
Even though the preparation is not perfectly at the center of the moving island, the distribution broadens just slowly. A click on the picture starts a video, a detailed plot can be found in Fig. B.8.
The video was calculated for optimal start conditions in the moving island with $\varphi_{\mathrm{Driv}} = 0.4 \cdot 2\pi$. Apart from the oscillation around both stable fixed points, a breathing of the distribution within the moving island is observed.

ance is largest for the reference measurements and decreases with increasing driving amplitude, in qualitative agreement with the simulation. This is the expected behaviour when preparing within a stable island, where the island becomes deeper with increasing driving amplitude.

For the medium driven system with $A_{\mathrm{Driv}} = 0.07$ both the z data and φ data was measured. Hence the time evolution in the experiment can be plotted within the phase space (see Fig. 5.5). The classical phase space for each time is plotted in light gray in the background. A classical simulation of a distribution of $N = 700$ atoms is included as a density plot, the experimental data is plotted with the corresponding variances as blue crosses.

The time evolution starts at the boundary of the stable island, however due to the investigated short time scales the sticky region around the stable island serves as an effective enlargement of the island. Thus the distribution follows it through the phase space during time evolution quite well. Compared to the reference measurement in Fig. 5.2, respectively Fig. 5.3, it is obvious that the distribution broadens more slowly in the driven than in the undriven system. Except the first point, the experimental data qualitatively agrees well with simulations - also the variances are comparable.

Additionally the simulation with finer time steps is included in the appendix in Fig. B.8. In the digital version of this work, a click on Fig. 5.5 starts a video of the simulated time evolution started at the center of the moving island ($z_0 = -0.29,\ \varphi_0 = 2.39$) with appropriate driving phase $\varphi_{\mathrm{Driv}} = 0.38 \cdot 2\pi$. One can see, that the distribution is trapped within the moving stable island for a long time. Besides, a breathing of the distribution within the island appears. The breathing frequency is connected to the trap depth [61]. Therefore, the dynamically created trap is much deeper here, due to its much faster breathing than in the $\Lambda = 0.7$ system (Fig. 4.6). Since the shape of the moving island is changed during its way through the phase space – which is equivalent to different initial driving phases – the overlap of a prepared CSS with the ground state of the island changes for different driving phases. Thus the amount of breathing depends on the initial driving phase.

5.2.2. Unstable fixed point

Changing the driving phase by π to $\varphi_{\mathrm{Driv}} = 0$, the same starting condition is close to a moving unstable fixed point, which is deep within the chaotic sea. In Fig. 5.6 the time evolution of mean and variance for different driving amplitudes is plotted.

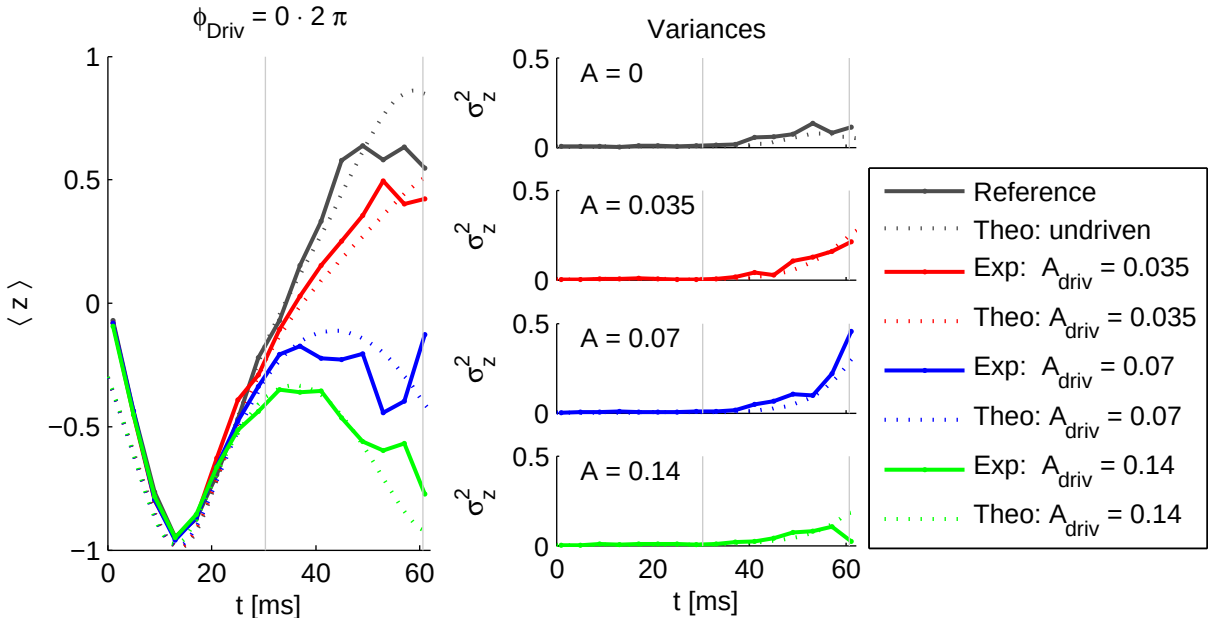

Figure 5.6.: Comparison of the experimental time evolution of means and their respective variances and simulations for a preparation close to the unstable fixed point ($\varphi_{\text{Driv}} = 0$). For stronger driving the time evolution of the mean is drastically changed. The variances exhibit a strong growth for a weak and medium driven system. Thus the unstable fixed point becomes more "unstable" with higher driving amplitude. In the strongly driven regime, the variance seems to grow not as fast as in the other cases but this is due to the time evolution of the mean being close to the south pole. The experimental points have to scatter symmetrically around the mean. Thus, if the mean is close to the boundary in a confined system, this implies a restriction for the variance. For strong driving the data is plotted for a driving phase of $\varphi_{\text{Driv}} = 0.95 \cdot 2\pi$.

In contrast to the stable island in Fig. 5.4 the mean is not only slightly altered compared to the undriven system. Rather the mean of the driven system follows the reference for barely one driving period but diverges completely from it subsequently.

The variances exhibit a strong growing tendency with a faster rate for stronger driving. This is in qualitative agreement with the Lyapunov exponents in Fig. A.2 (Sec. A.1.4). However, the Lyapunov exponent is the averaged separation rate of adjacent points determined in the long time limit. Thus it is not directly comparable to our measurements with a finite $\hbar_{\text{eff}}$ in the short time limit.

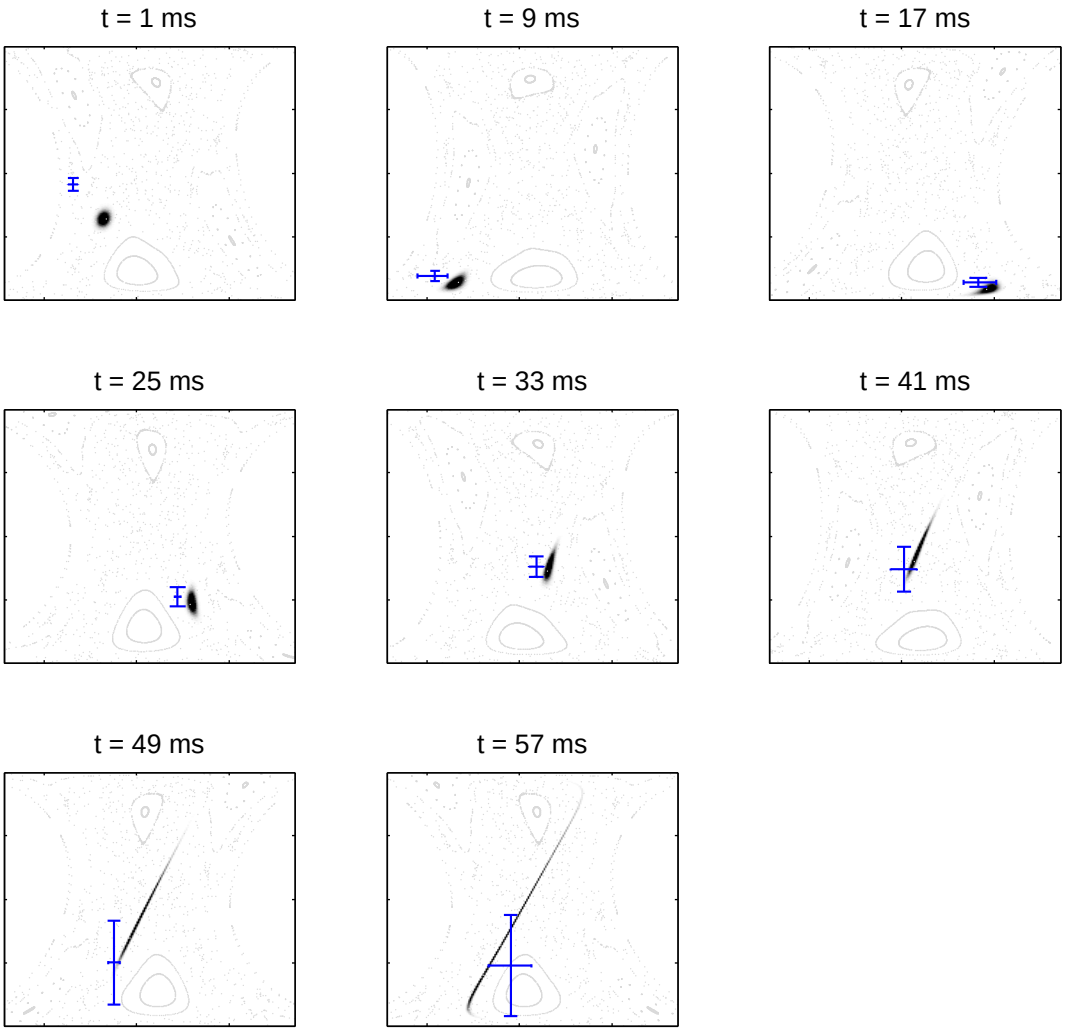

Figure 5.7.: Comparison of experimental time evolution and simulation close to an unstable fixed point deep in the chaotic sea. The preparation is done at $z_0 = -0.3$, $\varphi_0 = 2.68$ and $\varphi_{\text{Driv}} = 0 \cdot 2\pi$, $\omega_{\text{Driv}} = 1.59$, a medium driving amplitude of $A = 0.07$ and $N = 700$ atoms for the classical simulations.
Within the first driving period the system follows the undriven system quite well, but gets ripped apart soon evolving into a non-gaussian state. A click on the picture starts a video, a detailed plot can be found in Fig. B.9.

In the strongly driven regime the variance seems to behave differently. Although, when comparing the raw data in appendix C.2.5, it becomes obvious that the distribution becomes very broad but close to the south pole. Since the dynamics is restricted onto the sphere, the variance in z

cannot reach large values for a mean close to the poles.

Just as for the stable island, the time evolution in phase space is plotted for the medium driven system in Fig. 5.7. This illustrates the mechanism leading to a fast ripping apart of the distribution. During the first driving period, it follows the undriven one, but gets catapulted towards the unstable fixed point of the undriven system. Subsequently it gets stretched in the direction of the unstable manifolds of the undriven system, whose impact is noticable in short time dynamics.

The experiment exhibits a qualitatively comparable behaviour to the simulation, not only in the mean, but also in the variances. Mind that the simulation looks a bit broader than it actually is due to nonlinear plot (A.1.2). The variance grows much stronger than for the stable island indicating the expected behaviour at an unstable fixed point or in the chaotic sea.

5.2.3. Comparison of stable and unstable fixed point

A direct comparison of the variances in z and y is included in Fig. 5.8. The variances in z (depicted on the left) were measured twice, once with additional $90°$ tomography rotation (dark blue/red), once without but with enhanced statistics (light red/blue). Simulation is included as a dotted line. In the vicinity of the stable island the width of the distribution in z grows very slowly. In contrast for a start point in the chaotic sea it is rapidly growing and reaches values about one order of magnitude larger than in the stable island. The dip in the blue curve around $50\,ms$ occurs because the distribution reaches the turning point in z.

The variance in y (so basically in φ) is depicted on the right. It exhibits a slow growing tendency for both preparations on a completely different scale than the variances in z. As above, the peak in the blue curve around $50\,ms$ is due to reaching the turning point. In result for times around $2\,T_{per} \approx 61\,ms$ the variances in y are comparable although the variance in z is much larger for starting in the chaotic sea. Without the information about the variance in y and the simulations, the behaviour of the variance in z could have be explained by a squeezed state, which is rotated in the phase space such that once the long axis and in the other case the short axis is measured. However the similar behaviour of variances in y for larger times in conjunction with the huge difference in z variances, clearly shows that the distribution is ripped apart in the chaotic sea in contrast to the behaviour within the stable island.

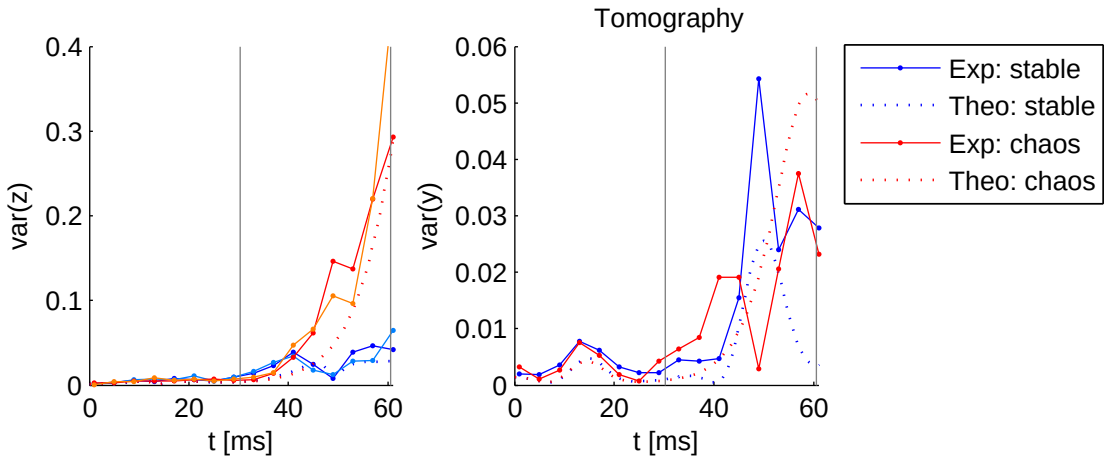

Figure 5.8.: Comparing time evolution of variances for a medium driving amplitude of $A = 0.07$ and different driving phases. red: $\varphi_{\text{Driv}} = 0 \cdot 2\pi$, blue: $\varphi_{\text{Driv}} = 0.5 \cdot 2\pi$. Light red and light blue are corresponding measurements from a different run with higher statistics.
Left: variances in z. The different behaviour in the stable island (blue) and in the chaotic sea (red) is obvious.
Right: variances in y (so basically in φ), attention should be paid to the different axes. The variances in y behave roughly similar for both driving phases.

5.3. Preparations from chaotic sea to stable island

So far, the behaviour of a distribution started in a stable island or deep in the chaotic sea were presented. Thus the question arises, in which way the resulting variance depends on different preparations within the phase space. For experimental reasons, the route from chapter 4 is followed to initially prepare always at the same point and rotate the phase space instead by changing the driving phase. Due to the analogy of driving phase to evolution time, this is equivalent to a fixed phase space and preparing the distribution on different points along one trajectory, e.g. the blue dotted one in the left part of Fig. 5.1. Thus by changing the driving phase from 0 to 2π the transition from stable island via the boundary to deep within the chaotic sea can be studied.

Since the variance in z exhibits a maximum for both extreme cases (stable and unstable fixed point) for times around $2\,T_{per}$ and the stable island is approximately elongated along z for quite a while, the dependency can be

evaluated at time $t = 2\,T_{per}$. Thus an analysis of the best evolution time as in chapter 4 can be omitted.

For a medium driven system with $A = 0.07$ the dependency of variance in z and y (after applying a tomography pulse) on the driving phase is depicted in Fig. 5.9. For z data (upper left) two different measurements as in sec. 5.2.3 were available, the numerical simulation is included as a dotted line. In the lower part simulated distributions for two extreme cases can be found which reveal on one hand the trapping by the island (right) on the other the fast diffusion in the chaotic sea (left).

A strong dependency of the variance on the driving phase is observed in z. The maximum is close to the position where the unstable fixed point is expected, the minimum close to the position of the stable island. The transition from unstable to stable is quite steep and appears a bit later than expected by a simple argument based on the distance of the starting point to the stable island in the phase space. Also, the variance rests on a low level for a larger range in driving phase, as the stable island is hit in the preparation. The variance remains not only small within the stable island, in fact it stays on the level also within the sticky region around the stable island for short times.

The steepness is also shown by the Lyapunov exponents (see Fig. A.2), where the start point is either within the stable island with vanishing Lyapunov exponent or in the chaotic sea with a finite value. Since the sticky region serves as a partial barrier [106, 107] being overwhelmed after finite time, it is not reflected in the Lyapunov exponents calculated on a much larger time scale. Furthermore, due to finite size of the initial distribution depending on $\hbar_{\mathrm{eff}}$, the transition should occur in minima at the order of the initial distribution, although it is much smaller than the observed steepness in the examined case.

The variance in y exhibits a weak dependency on the driving phase. The distribution in the stable island is elongated almost vertically and even in the chaotic sea this is the main direction at the time $t = 2\,T_{per}$. Thus the y variance exhibits a weak dependency on driving phase and is not the inverse of the z-data. This confirms, that the observed increase in z-variance can be directly connected to the spreading of the initial gaussian distribution in the phase space.

A comparison of the same dependency for different driving amplitudes is included in Fig. 5.10. The reference measurement is depicted in gray, and as it is independent of driving phase it is measured once and plotted as a reference for all phases. It should be mentioned that the reference is measured with less statistics.

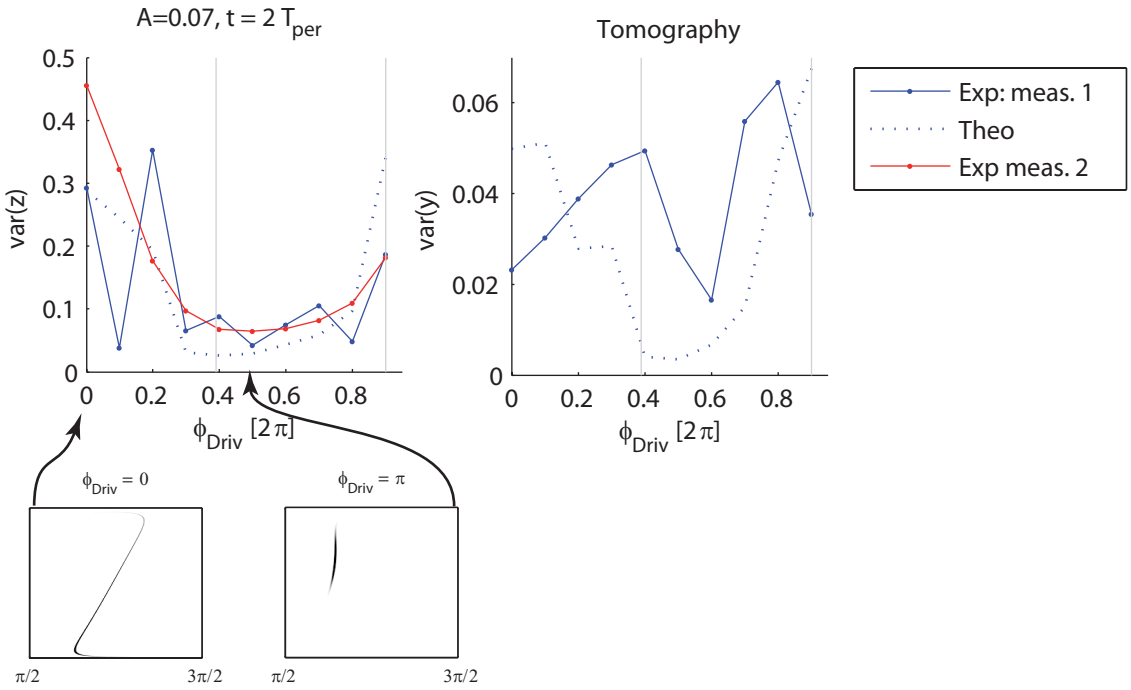

Figure 5.9.: Dependency of variances in z (left) and y (right) for a fixed time evolution of $t = 61\,ms$ ($\equiv 2.013 \cdot T_{per}$) on driving phase for an amplitude $A = 0.07$. Red and blue are two different measurement runs with same parameters, the red with higher statistics. The vertical lines indicate the position of the stable/unstable fixed point.
Upper-left: Variance in z, a strong dependency on the driving phase is observed. Experimental data exhibits a qualitatively similar behaviour as simulation. Upper-right: Variances in y measured after applying a $\pi/2$ pulse (corresponding to variances in φ). The data in y exhibits a much weaker dependency on the driving phase and is not the inverted signal of z-data.
Lower: Simulated distribution for a driving phase $\varphi_{\text{Driv}} = 0$ (chaotic sea) on the left and for $\varphi_{\text{Driv}} = \pi$ (vicinity of stable fixed point) on the right.

However comparing the minimal variances of weak and medium driven system to the reference, they exhibit a much narrower width in z than in the undriven system indicating the trapping in the stable island. From simulation it is expected that the medium driving creates a deeper trap than in the weakly driven system, thus the variance should remain smaller for the medium driven system. Due to preparation at the border of the island, the weakly driven system exhibits a slightly smaller variance instead. On

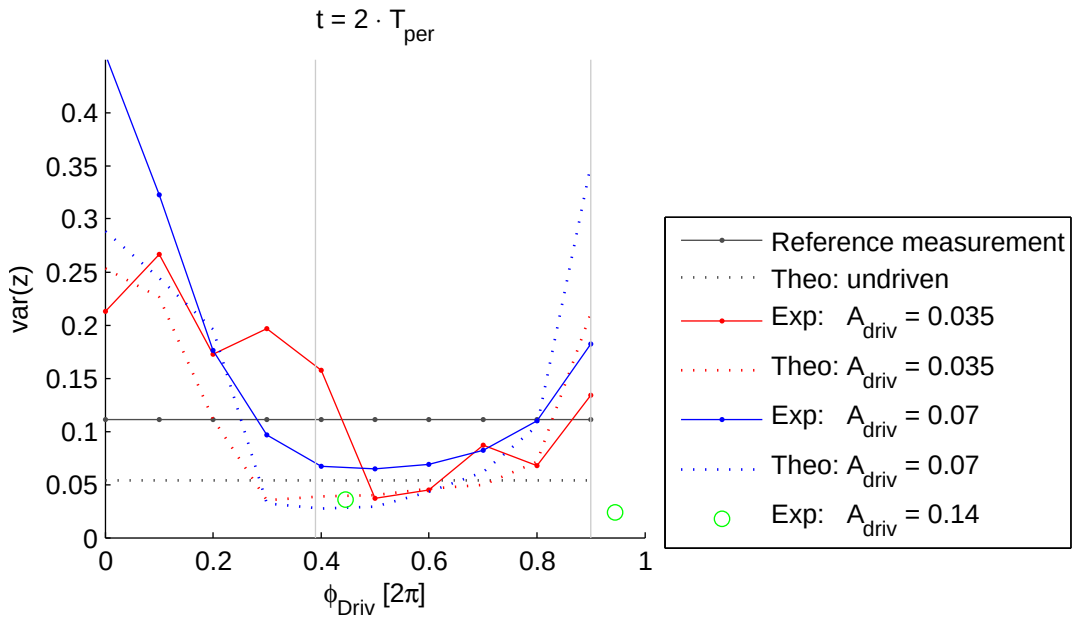

Figure 5.10.: Variance after a time evolution of $t = 61\,ms$ ($\equiv 2.013 \cdot T_{per}$) for different driving phases and amplitudes.
The reference was measured only once (no driving phase dependency), but the statistics is not as good as for the driven cases. The medium driven system is already discussed in Fig. 5.9. The slightly driven system shows a qualitatively similar behaviour, although a bit shifted. However the variance grows not as fast as in the medium driven case for a preparation close to the unstable fixed point.
For the strongly driven system, just the two preparation phases for stable island or chaotic sea were measured. Although the variances appear to be in the same order of magnitude, the raw data in Sec. C.2.5 exhibits qualitatively different behaviour.

the other hand, in the chaotic sea the weakly driven system is growing less than the medium driven system as expected by the Lyapunov exponents (A.2).

5.3.1. Phase space mapping

Up to now, the different behaviour of starting in the chaotic sea or the stable island is mainly deduced by the development of variances. To directly visualize the entirely different behaviour, we plot the time evolution

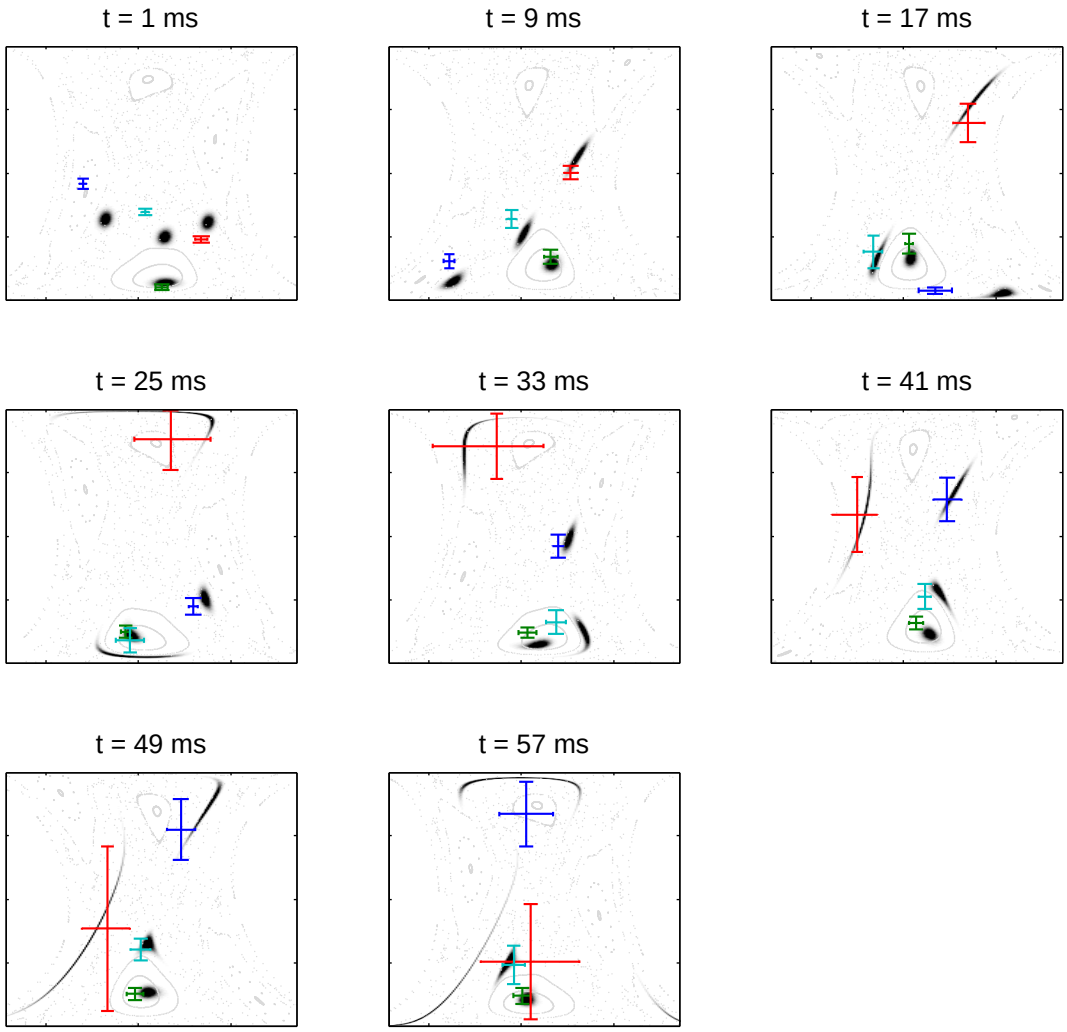

Figure 5.11.: Time evolution for different initial start points in the phase space with parameters $A_{\text{Driv}} = 0.07$, $\varphi_{\text{Driv}} = 0.3 \cdot 2\pi$. The different behaviour, whether the start point is located within a stable island or in the chaotic sea is clearly visible in the variances.

of different starting points with their variances in phase space (Fig. 5.11). The experimental data is compared to a classical distribution.

The same start points as in the phase space plot of the undriven system (Fig. 5.2) were used. The different regimes were sampled in the following way: the blue one is located close to the moving island, the green one inside the stable non-moving island, the cyan in the sticky region around the stable fixed point, and the red one in the chaotic layer between moving and non-moving islands.

Within the stable non-moving island, the distribution rotates around the stable fixed point and variance remains on a low level, as confirmed by experiment (green). In the vicinity of this island – at the sticky region – the distribution also rotates around the stable island (cyan) however the variance becomes larger than deep in the island. The behaviour of the distribution close to the moving stable island was already explored in Fig. 5.5, but for a different driving phase and thus a preparation closer to the stable fixed point. Here, the behaviour differs not much, except the variance grows a bit faster than in Fig. 5.5. Compared to the reference measurement in Fig. 5.2, the distribution remains smaller in the driven regime. Finally, starting in the chaotic sea, the distribution rips apart fast as confirmed by the experiment (red).

In conclusion, the examples show that by using a distribution of points rather than a single one the structure of a mixed phase space can be directly confirmed even in the short time limit.

5.4. Sensitivity on initial conditions

One key ingredient of chaos is the exponential separation of close adjacent points, thus extreme sensitivity on initial conditions. This is reflected by a positive Lyapunov-exponent, which is a measure for the separation rate. In contrast, in a quantum mechanical system the initial preparation is uncertain in the order of $\hbar_{\text{eff}}$. Hence a quantum preparation occupies a phase space area which is not transported as a whole by the Hamiltonian mapping. In this section we will shortly focus on the question how the dependency on initial preparation manifest itself in the examined quasi classical system. The arguments can be found in the books [4, 51].

As the classical system is Hamiltonian, the Liouville theorem states that a phase space volume is preserved in time [4]. Thus, as one Lyapunov exponent is larger than zero (see sec. A.1.4) the other[1] has to be the negative of the first one to fulfill Liouvilles theorem. This is equivalent to the stretching of an area element in one direction and shrinking it in the other. The bounded phase space and the appearance of all coordinates of the ODE inside trigonometric functions – thus periodic boundaries apply – acts as a form of folding.

The concept of stretching and folding is widely discussed in the context of maps, where it leads to mixing. In the framework of Hamiltonian systems it implies the existence of fractal basins within the chaotic regions of phase

[1] In a 2 dimensional phase space there are 2 Lyapunov exponents [4].

space [4]. In the examined system, consider a small area in the vicinity of the unstable fixed point of the undriven system. In the driven system, it is stretched till it reaches the vicinity of both poles and evolves then back towards the ”center”. As the unstable axis is continuously changing in time, it doesn't reach the origin perfectly and a second cycle starts. Repeated application of this stretching and folding leads to an interweaving net of the image of the initial area. As the system is ergodic within the chaotic sea, the image of the initial area covers the whole chaotic sea, although the total area does not change.

As our model system is the classical version of a quantum mechanical system, the initial preparation has the size of $1/\sqrt{N}$ (Sec. 2.2.1). The stretching and folding of a gaussian distribution covering this area is depicted in Fig. 5.15, where indications of a fractal structure can be seen. In the experiment, the measurement process will always be afflicted with some error (the readout uncertainty amounts roughly to $\Delta z = 0.02$ in the actual system), but also in simulation uncertainties occur. In this coarse grained picture, the fractal image appears to fill the whole chaotic sea. On the other hand, by measuring coarse grained, one cannot distinguish to which basin the outcome belongs. This implies that an outcome cannot be related to a certain start point - the memory of the system is erased by coarse graining. Transferred to the experiment it follows that different starting points within the chaotic sea will lead to the same results after some time.

We will discuss the experimental data in the following. As in most other measurements, instead of choosing different starting points the preparation was done at $z_0 = 0,\ \varphi_0 = \pi$ (close to the unstable fixed point of the undriven system) and the driving phase was changed to mimic different start points in phase space. A comparison of the time evolution for different initial preparations is shown in Fig. 5.12. The time evolution is plotted as a histogram of all obtained z-values for each time step and is normalized to the maximum to provide better visibility. On the left side, the time evolution for a preparation at the position of the stable/unstable fixed point is plotted. In this case, the driving phase determines whether the preparation is within the stable island or close to the unstable fixed point. Thus a huge difference is observed.

In contrast, by starting in the chaotic sea for all driving phases (depicted on the right side), only slight differences are noticeable, e.g. the diagonal hole shifts a little bit. This holds also for the other driving phases plotted in Sec. C.2.7 which were omitted in Fig. 5.12 due to lack of space.

An attempt to quantify the similarity of the distributions after approximately $60\,ms$ of time evolution is given in Fig. 5.13. There the variance for the obtained distributions is plotted for all different driving phases.

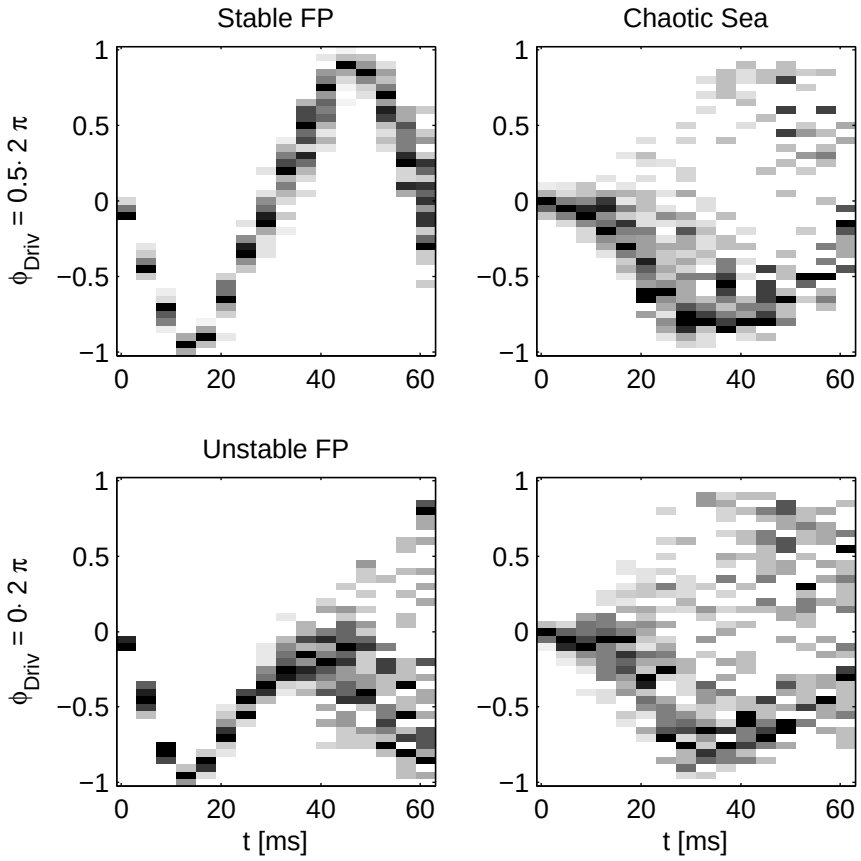

Figure 5.12.: Comparing time evolution for starting at the stable/unstable fixed point or within the chaotic sea for different driving phases. For each time step a measured histogram is plotted. For a better visibility the histograms are normalized to the maxima.
Left: starting close to the stable/unstable fixed point at $z_0 = 0; \varphi_0 = 2.5$ (experimental parameters). The driving phase was chosen to prepare close to the stable fixed point in the upper ($\varphi_{\text{Driv}} = 0.5 \cdot 2\pi$) and close to the unstable fixed point ($\varphi_{\text{Driv}} = 0 \cdot 2\pi$) in the lower graph.
Right: starting at $z_0 = 0; \varphi_0 = 3.1$ in the chaotic sea for same driving phases. For a preparation deep in the chaotic sea just slight dependency on the driving phase is observed.

The distributions are quite broad, thus some rare events contribute much more to the variance in lack of high statistics for a single time. Therefore, the distributions were summed over the last two time steps. This is justified due to small changes in histograms for these times.

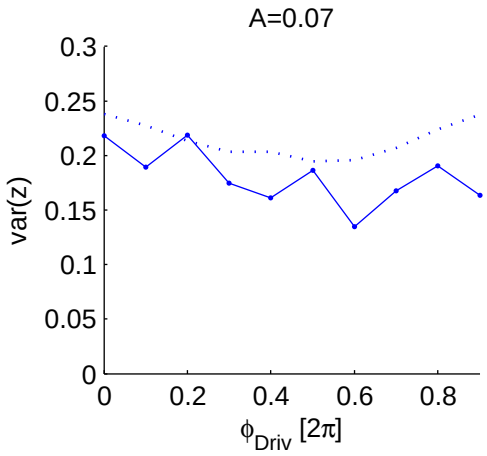

Figure 5.13.: Approaching ergodicity: Variance vs driving phase for starting in the chaotic sea at $z_0 = 0; \varphi_0 = 3.1$ and driving amplitude $A = 0.07$ (solid line: experiment; dotted line: simulation). The variances are averaged over the last two time steps, from $t = 57\,ms$ to $t = 61\,ms$ to avoid outliers due to bad statistics. This is justified as the distribution differs barely for the last time steps.

We find a weak dependency of the variance on the driving phases, whereupon the systematic dependency is on the order of measurement noise. This should be contrasted to the case in Fig. 5.10 for a preparation close to stable/unstable fixed points with about one order of magnitude variation. The obtained almost equal variances for all different driving phases, and thus different preparations in phase space is a hint for an equalization of distributions even for this short times.

A comparison of histograms for different driving phases is plotted in Fig. 5.14, where the histograms were summed over the last three time steps. The results for a preparation close to stable respectively unstable fixed point at $z_0 = -0.3,\ \varphi_0 = 2.68$ and different driving phases were plotted on the left column. This is contrasted by the results for a preparation in the chaotic sea at $z_0 = 0.08,\ \varphi_0 = 3.13$ for the same driving phases at the right.

Although the peaked signal of the stable fixed point is smeared out a bit on the left, a different behaviour is observed. A strong dependency on the driving phase can be observed, not only in the position of the distribution, but also in the shape. Close to the unstable fixed point the distribution is spread all over the whole z-range, it's quite broad there. Close to the stable fixed point for $\varphi_{\text{Driv}} = 0.4 \cdot 2\pi$ the distribution gets peaked and rel-

atively thin. Due to summation over several times, the plotted histogram is broader than a realization for a single time would be.

In contrast, only slight differences are noticeable on the right. For almost all driving phases a very broad distribution appears and only the position of a small peak on top varies. The time scales of the experiment do not allow the measurement of long time dynamics to completely verify ergodicity in the system. Also a full tomography to reconstruct the distribution in phase space is experimentally too costly. Therefore a foresight in long time dynamics is numerically investigated in Fig. 5.15.

A distribution is initialized in the chaotic sea and time evolution plotted for multiples of the driving period. Even for relatively short times at $t = 8T_{per}$ the distribution occupies almost the whole area of the chaotic sea and fills it completely for larger times. This is only part of the truth since the area of the initial preparation is conserved in a Hamiltonian system. Thus the distribution fills the phase space along a thin net, approaching a fractal structure. As a potential measurement process is always coarse grained, the fractal structure could not be resolved and the same result would be obtained independent where the initial preparation has been done (as long as done in the chaotic sea).

In conclusion the experiment exhibits a very weak dependency on initial conditions for a preparation in the chaotic sea as expected for a chaotic system. Although the time scales of the experiment do not allow for a complete verification of ergodicity, the fast equalizing of distributions for different starting conditions supports the assumption of an ergodic system.

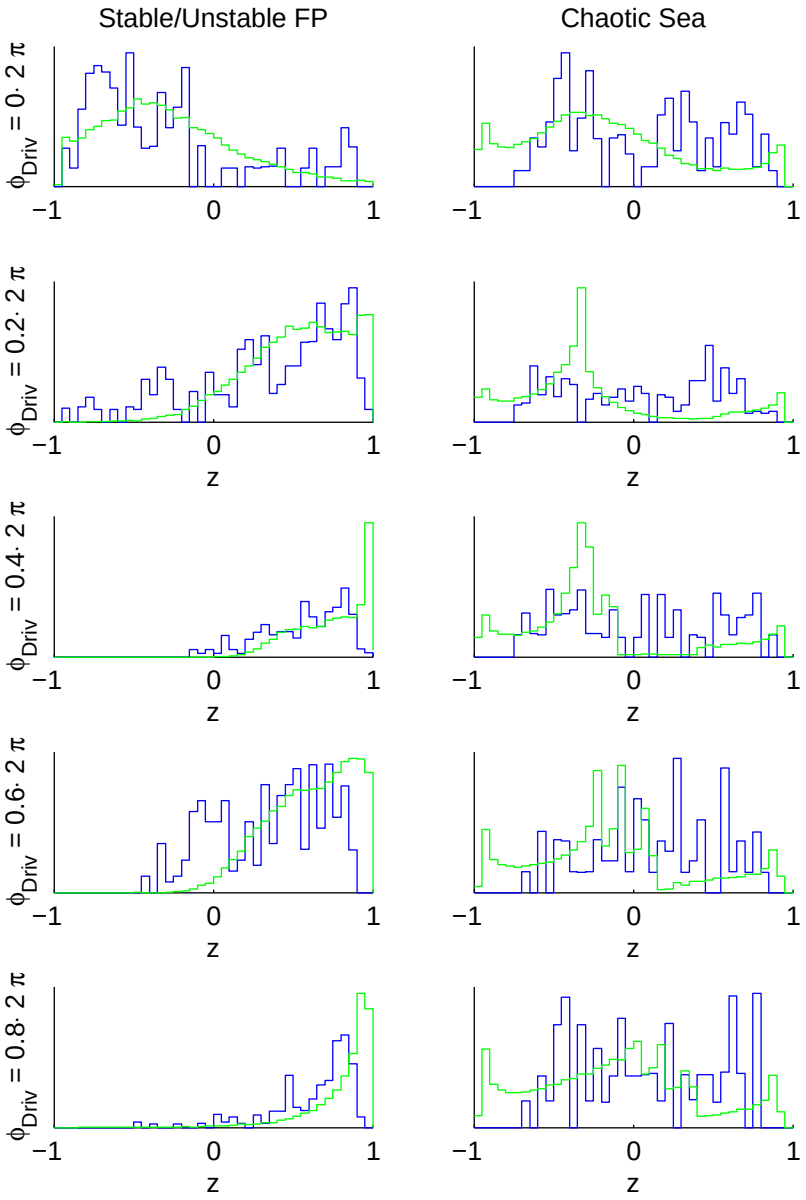

Figure 5.14.: Histograms for different preparation, combined data obtained for times from $t = 53\,ms$ to $t = 61\,ms$. Blue: measured histograms, simulation is plotted in green.
Left: preparation close to the stable/unstable fixed point at $z_0 = -0.3,\ \varphi_0 = 2.68$ for different driving phases.
Right: preparation in the chaotic sea at $z_0 = 0.085, \varphi_0 = 3.13$ for same driving phases.
For a preparation in the chaotic sea, much smaller sensitivity on initial conditions is observed.

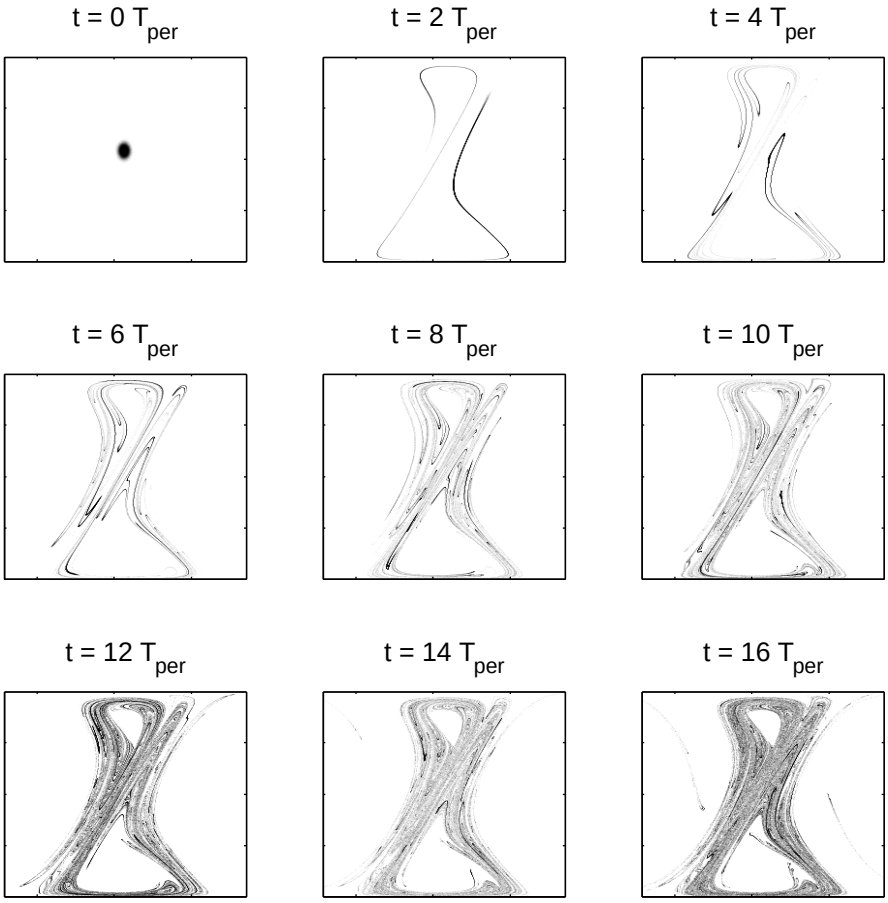

Figure 5.15.: Classical simulation of the time evolution of a distribution prepared at $z_0 = 0.085;\ \varphi_0 = 3.13$ for $N = 700$ atoms. Even for short times at $t = 2T_{per}$ the distribution is bent around the stable fixed points multiple times and encloses a larger part of the phase space. For larger times the chaotic sea is gradually filled by the distribution. In a quantum simulation the result would be different due to interference effects. Due to finite size of $\hbar_{\text{eff}}$ in a real world experiment one cannot sample fine details created by folding and stretching (a video for quantum system can be found here).

6. Single photon beam splitter

In an unrelated experiment the generation of motional coherence of a single atom by spontaneous emission of a single photon is examined, performed at a different experimental setup. The work was published in [108], therefore just a brief introduction will be given. A more general introduction and a subsumption of this topic can be found in [109].

Coherent superpositions are at the heart of quantum mechanics, creating them requires that the splitting process cannot distinguish between the different outgoing states. Processes which give information about the individual quantum states making them distinguishable lead to decoherence. A paradigmatic example is spontaneous emission which destroys coherence if the photon can carry information about the superposition state [110, 111, 112]. We present a situation where spontaneous emission induces coherence between motional atomic quantum states. In our setup an atom spontaneously emits a single photon in front of a mirror. The indistinguishability of emission directions towards and away from the mirror results in a coherent superposition between the corresponding correlated atomic motion. This coherence is revealed in direct interferometric measurements which are in quantitative agreement with an intuitive as well as with a full quantum mechanical model. This is a paradigm example that spontaneous emission per se is coherent and only in the limit of free space it leads to full decoherence.

A reprint of [108] is given on the next pages, where Martin Kiffner contributed the quantum mechanical description. Technical details can be found in the supplementary information of [108] or in [127], where also the calibration methods are described. A more general description of the experimental setup can be found in [128].

DOI:10.1038/NPHYS1961

Single spontaneous photon as a coherent beamsplitter for an atomic matterwave

Jiří Tomkovič,[1, a)] Michael Schreiber,[2] Joachim Welte,[1] Martin Kiffner,[3] Jörg Schmiedmayer,[4] and Markus K. Oberthaler[1]

[1)] *Kirchhoff-Institut für Physik, Universität Heidelberg, Im Neuenheimer Feld 227, 69120 Heidelberg, Germany*

[2)] *Ludwig-Maximilians-Universität, Schellingstr. 4, 80799 München, Germany*

[3)] *Physik Department I, Technische Universität München, James-Franck-Straße, 85747 Garching, Germany*

[4)] *Vienna Center for Quantum Science and Technology, Atominstitut, TU Wien, 1020 Vienna, Austria*

(Dated: 3 April 2011)

In spontaneous emission an atom in an excited state undergoes a transition to the ground state and emits a single photon. Associated with the emission is a change of the atomic momentum due to photon recoil[1]. Photon emission can be modified close to surfaces[2,3] and in cavities[4]. For an ion, localized in front of a mirror, coherence of the emitted resonance fluorescence has been reported[5,6]. In free space experiments demonstrated that spontaneous emission destroys motional coherence[7–9]. Here we report on motional coherence created by a single spontaneous emission event close to a mirror surface. The coherence in the free atomic motion is verified by atom interferometry[10]. The photon can be regarded as a beamsplitter for an atomic matterwave and consequently our experiment extends the original recoiling slit Gedanken experiment by Einstein[11,12] to the case where the slit is in a robust coherent superposition of the two recoils associated with the two paths of the quanta.

We consider an atom passing by a mirror which spontaneously emits a single photon (see Fig. 1a). As a result of the photon momentum the atom receives a corresponding recoil kick in the direction opposite to the photon emission. In the absence of the mirror the observation of the emitted photon direction implies the knowledge of the atomic momentum resulting from the photon-atom entanglement[8]. In the presence of the mirror the detection of a photon in a certain direction does not necessarily reveal if it has reached the observer directly or via the mirror. For the special case of spontaneous emission perpendicular to the mirror surface the two emission paths are in principle indistinguishable for small atom-mirror distances $d \ll c/\Gamma$, where c is the speed of light and Γ the natural linewidth. This general limit is always fulfilled in our experiments. Thus the atom after this emission event is in a superposition of two motional states.

This is also true for the more general case of tilted emission, as revealed in Fig. 1b for emission close to the mirror surface. One expects residual coherence for emission angles where the optical absorption cross section of the atom and the mirror atom observed by a fictitious observer in the emission direction still overlap. This is visualized in Fig. 1b, where the corresponding cross-sections are indicated with the bars. The overlap as a function of emission direction is depicted on the sphere (blue no coherence, red full coherence). The result on the atomic motion is indicated for one special trajectory which starts with an atom moving parallel to the mirror surface and a single photon emission under an angle to the mirror normal. This case leads to an imperfect coherent superposition of two momentum states separated by less than two photon momenta $\hbar k_0$. The spatial distribution of the atoms at the position of the detector is shown, where the color corresponds to the degree of coherence. In Fig. 1c we contrast this to the case of larger distance to the mirror, where the portion of coherent atomic momentum is strongly reduced.

It is important to keep in mind that a single particle detector cannot distinguish between coherent superpositions and mixtures but only gives the probability distribution. Thus an interferometric measurement[13] has to be applied to reveal the expected coherent structure (see Fig. 2). For that, the two momentum states of interest have to be overlapped and the coherence i.e. well defined phase difference, is verified by observing an interference pattern as function of a controlled phase shift applied to one of the momentum states. The two outermost momentum states are expected to show the highest coherence. Their recombination can be achieved by a subsequent Bragg scattering off an independent standing light wave (see Fig. 2b) with the suitable wavelength[10,14]. The relative phase ϕ_B is straightforwardly changed shifting the probing standing light wave. This is implemented by moving the retroreflecting mirror by distance L. The upper graph depicts the results obtained for large distances ($> 54\mu m$) of the atom to the mirror i.e. a free atom. In this case no interference is observed, and thus spontaneous emission induces a fully incoherent modification of the atomic motion. For a mean distance of

[a)] E-Mail: single-photon@matterwave.de

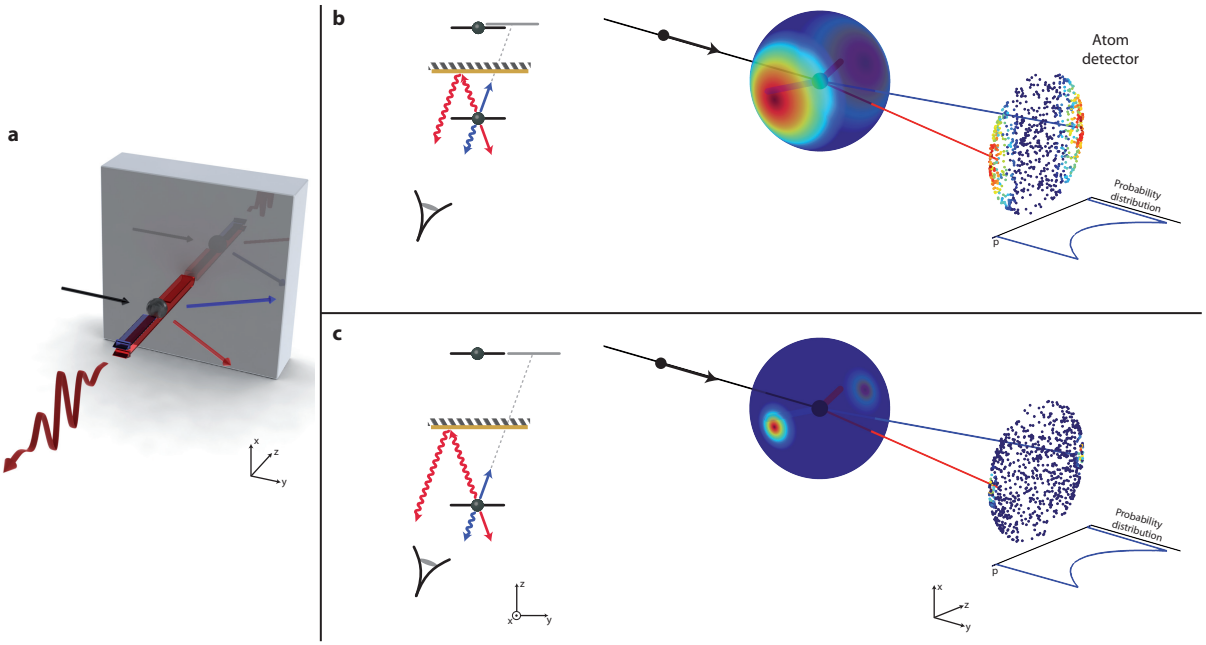

FIG. 1. Motional coherence generated by a single spontaneous emission event. (a) The situation of interest is depicted – an atom in front of a mirror spontaneously emits a single photon. For emission perpendicular to the mirror surface an observer can in principle not distinguish if the photon has been reflected or not. Momentum conservation in the atom-photon system implies that the atom after the emission is in a coherent superposition of two different momentum states separated by twice the photon recoil. (b) Indistinguishability is also given for more general emission directions. With the spatial extension of the atom corresponding to the optical absorption cross section, indistinguishability can be estimated by the projected overlap of atom and its mirror-image. This overlap is represented colorcoded on a sphere for all emission directions (red: full coherence, blue: no coherence). Repeating the experiment – single atom emits a single photon – leads to the indicated pattern at the atom detector. The colorcode indicates the probability generating a coherent superposition for the corresponding event (red: full coherence, blue: no coherence). (c) In the case of large distances to the mirror the coherent portion drastically reduces, approaching the limit of vanishing coherence in free space.

$2.8\mu m$ clear interference fringes are observed demonstrating that a single spontaneous emission event close to a mirror leads to a coherent superposition of outgoing momentum states.

In the following we describe the essential parts of experimental setup shown in Fig. 2b, lower graph. Further details are provided in the supplementary information. Since the effect critically depends on the distance between atom and mirror a well collimated and localized beam of ^{40}Ar atoms in the metastable $1s_5$ state is used. In order to ensure the emission of only a single photon we induce a transition $1s_5 \rightarrow 2p_4$ ($\lambda_E = 715nm$). From the excited state $2p_4$ the atom predominantly decays to the metastable $1s_3$ state via spontaneous emission of a single photon ($\lambda_{SE} = 795nm$) (branching ratio of $1s_5/1s_3 = 1/30$). The residual $1s_5$ are quenched to an undetectable ground state with an additional laser. Choosing the appropriate polarization of the excitation laser the atomic dipole moment is aligned within the mirror plane leading to the momentum distribution after spontaneous emission shown in Fig. 2a. The interferometer is realized with a far detuned standing light wave on a second mirror. Finally the momentum distribution is detected by a spatially resolved multi channel plate (MCP) approx. $1m$ behind the spontaneous emission enabling to distinguish between different momenta.

For systematic studies of the coherence we analyze the probability for finding a particle in a coherent superposition of momentum states as a function of atom-mirror distance d. This is done by analyzing the final momentum distribution for different phases ϕ_{B} within the interferometer and fit for each resolved momentum ($\approx 1/8$ of a photon momentum) an interference pattern given by

$$N = N_0 + N_A \cos(\phi_{\mathrm{B}} + \phi_0). \qquad (1)$$

In Fig. 3 we plot the visibility $V = N_A/N_0$ (with N_0 the constant atom number, N_A the oscillatory part) revealing that the coherence vanishes within distances of a few micrometers to the mirror.

For a basic understanding of the physics behind the experimental observation we use a simple semiclassical model. We follow the picture of an atom and its image by Morawitz[15] and Milonni, Knight[2] and assume a two level system with ground state $|g\rangle$ and excited $|e\rangle$. In order to deduce the indistinguishability between the atom and its mirror atom, i.e. the photon emission towards and away from the mirror, we attribute to the atom a size corresponding the optical absorption cross section

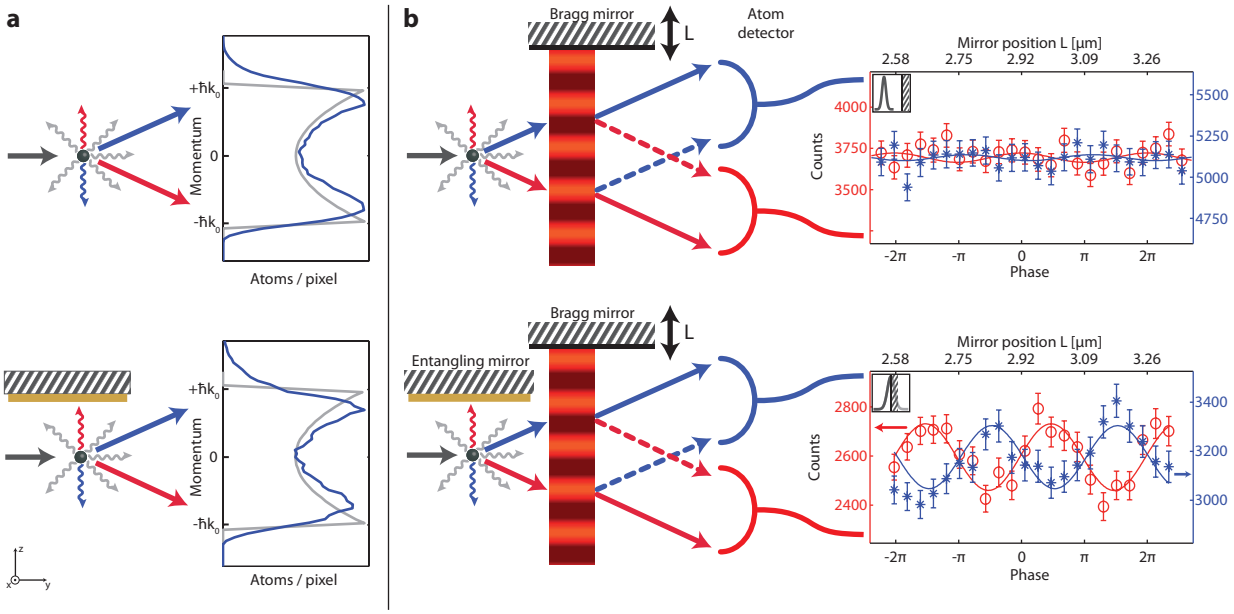

FIG. 2. Experimental confirmation of coherence induced by spontaneous emission. (a) Experimental observation of momentum distribution does not reveal the coherence. In both cases - close to and far from the mirror - the momentum distribution is the same (blue line). In order to compare the observed momentum distribution after spontaneous emission with theory (light gray) the data has been deconvoluted by the initial momentum distribution. The deviation results from a residual filtering of high spatial frequencies. (b) The coherence is revealed if the spontaneous emission event is employed as the first beamsplitter of an atom interferometer. The recombination is accomplished by Bragg scattering from a standing light wave. The relative phase of the two paths can be changed by moving the "Bragg" mirror as indicated. In the case of a mean distance of 54 μm between atoms and "entangling" mirror (upper graph, error bars indicate poisson noise) no interference signal is observed confirming the free space limit. The inset depicts the position of "entangling" mirror to the atomic beam. For a mean distance of 2.8 μm (lower graph) the two complementary outputs of the interferometer reveal an interference pattern with a maximal visibility of $5.9\% \pm 1.1\%$.

($\sigma = 3\lambda^2/2\pi$). In the direction perpendicular to the mirror an observer can not distinguish atom and mirror atom in principle and thus a coherent superposition of momentum states is emerging $|\psi\rangle = 1/\sqrt{2}(|+\hbar k_0\rangle + |-\hbar k_0\rangle)$ with the photon momentum $p_{rec} = \hbar k_0$. For emission directions other than perpendicular the probability P for generating $|\psi'\rangle = 1/\sqrt{2}(|+\hbar k'\rangle + |-\hbar k'\rangle)$ can be estimated by the overlap region of atom and mirror atom with the assigned effective size as shown in Fig. 1b. This overlap depends on the distance between atom and mirror and on the observation angle (for details see supplementary information). In order to quantitatively compare with the experimental data the finite resolution of momentum detection has to be taken into account leading to an integration over different observation directions. Further averaging due to the finite extension of the atomic beam (width in transverse direction of $10\mu m$) and the initial momentum distribution results in a reduction of the visibility V. The prediction within this model is shown as solid blue line in Fig. 3.

The comprehensive quantum mechanical model (for details see supplementary information) takes into account the modified mode structure of the electromagnetic field due to the presence of the mirror[16]. We derive a master equation for the internal degrees of freedom of the atom and its center of mass motion perpendicular to the mirror surface. It is found that the quantum state of the atomic center of mass motion after spontaneous emission can be written as

$$\hat{\varrho}_{gg}(t=\infty) = \alpha \frac{3}{8} \int_0^1 \mathrm{d}u \left(|\psi_s\rangle\langle\psi_s| + u^2 |\psi_p\rangle\langle\psi_p| \right), \quad (2)$$

where

$$|\psi_s\rangle = \left(r_s^* e^{ik_0 u\hat{z}} + e^{-ik_0 u\hat{z}} \right) |\psi_0\rangle, \quad (3)$$

$$|\psi_p\rangle = \left(-r_p^* e^{ik_0 u\hat{z}} + e^{-ik_0 u\hat{z}} \right) |\psi_0\rangle. \quad (4)$$

The operators $e^{\pm ik_0 u\hat{z}}$ in Eqs. (3) and (4) describe the transverse recoil momentum $\pm\hbar k_0 u$ transferred to the atom by the spontaneously emitted photon. The Fresnel coefficient r_s (r_p) accounts for the reflection of the transversal electric (transversal magnetic) mode at the mirror and $|\psi_0\rangle$ describes the motional state of the atom before spontaneous emission. The normalization is ensured by the normalization constant α. For a quantitative comparison with the experiment we assume that

$$|\psi_0\rangle = \int \mathrm{d}p f(p,d) e^{\frac{i}{\hbar}pd} e^{i\phi_f(p)} |p\rangle \quad (5)$$

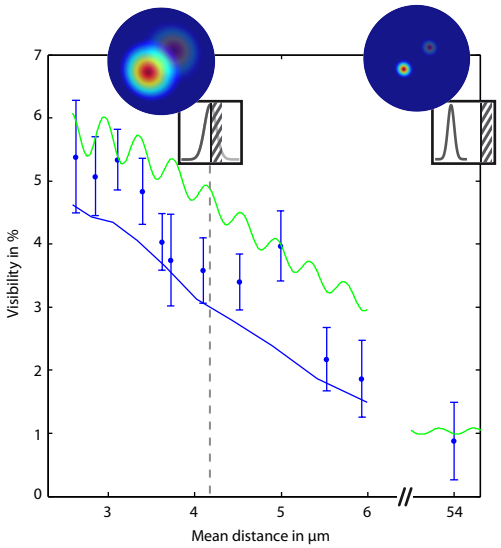

FIG. 3. Dependence of visibility on the mean atom-mirror distance. Measured data is depicted as blue points. The mean distance is calculated from the position of the "entangling" mirror with respect to the center of the atomic beam as indicated in the insets. The error bars indicate a 95% confidential interval resulting from the fitting procedure to the interference pattern. The expectation from the simple cross section overlap model is shown with the blue line. The quantum mechanical treatment is depicted as green line. One finds good agreement between theory and experiment by including details such as initial spatial and momentum distribution, averaging over all distances, details of Bragg scattering and the final spatial resolution of the atom detector. The mean atom-mirror distance is adjusted by the position of the "entangling" mirror with respect to the collimation slit of the atomic beam.

is a coherent wave packet. The quantity $|f(p,d)|^2$ represents the initial momentum distribution of atoms and is inferred from an independent measurement of the momentum distribution. The description of the initial atomic state by a pure state is a sensible assumption since the width of the slit collimating the atoms is chosen to be close to the diffraction limit. The phase $\phi_f(p)$ determines the shape of the wavefunction in position space. The Bragg grating is modeled as a beamsplitter with a momentum dependent splitting ratio determined from experimental measurements. After free evolution of the atom we determine the probability to detect the atom within the given resolution of the detector. The result of this calculation is shown as green line in Fig. 3 where only the phase $\phi_f(p)$ of the wavefunction in front of the first mirror cannot be fully reconstructed acting as a free parameter. The uncertainty of this phase explains a smaller visibility and the asymmetry between different diffraction orders (see Fig. 4).

So far we have discussed the maximum coherence observed in the experiment. In Fig. 4 the momentum dependence of the coherence is shown for a mean distance of $3.3\mu m$ from the mirror. This reveals that only the outermost parts of the momentum distribution are in a coherent superposition which is consistent with the simple picture of atom and mirror atom. It is important to note that Bragg scattering itself exhibits a momentum dependence (Bragg acceptance). For the chosen short interaction length the Bragg acceptance is indicated by the gray line in Fig. 4. Since the observed coherence decays significantly within the Bragg acceptance we can experimentally confirm that only the most extreme emission events i.e. perpendicular to the mirror surface, lead to a significant generation of coherence. This angular dependence is similar for all investigated mirror distances since it is essentially given by the coherent momentum spread of the strongly confined initial atomic beam.

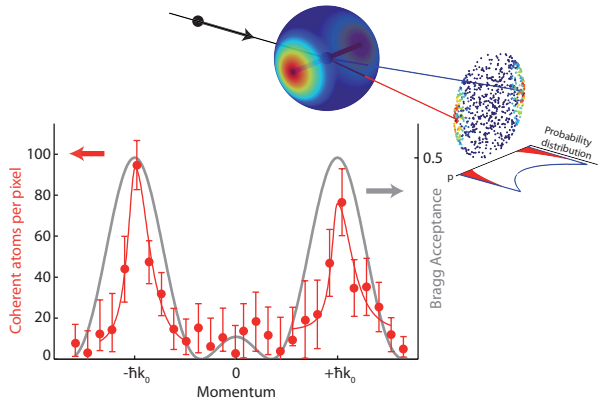

FIG. 4. Observation of angular dependence of coherence. The schematics show an idealized case of coherent momenta for an atom in a fixed distance and an initial momentum parallel to the mirror (red area within the momentum distribution). Due to finite momentum distribution of the atomic beam, the narrow coherent momenta is smeared out in the experimental realization. The measured width of coherent momenta (red points) is smaller than the angle-acceptance of the Bragg-crystal (gray line), revealing that mainly atoms with momenta of $\pm\hbar k_0$ are in a coherent superposition. The data is shown for a mean distance of 3.3 μm (in contrast to Fig. 2b (lower graph), where the atom is much closer to the mirror). Error bars are defined accordingly to Fig. 3.

Finally we would like to point out the differences to other experiments where the connection between spontaneous emission and coherence is investigated. For example the experiment in[8] shows that the spontaneous photon carries away information from the atom about its position, and therefore destroys the coherence when the two paths can be distinguished. The experiment[5] on the other hand provides direct proof for the coherence of photons emitted in the resonance fluorescence of a laser-driven ion in front of a mirror. The observed interference pattern can be regarded as indirect evidence for the motional coherence of the trapped ion, well within the Lamb-Dicke limit[6]. A different example in the context of laser cooling is velocity selective coherent population trapping[17] where spontaneous emission populates motional dark states. Here the direction of the emitted

photon is indistinguishable since it is emitted in the direction of a macroscopic classical field that drives the atom. The most salient feature of our experiment is that a single spontaneous emission event in front of a mirror creates a coherent superposition in freely propagating atomic matter waves, without any external coherent fields involved. The emission directions of the spontaneous photon become indistinguishable due to the mirror.

In the work by Bertet et al.[12] photons from transitions between internal states are emitted into a high finesse cavity. Their first experiment reported in[12] demonstrates the transition from indistinguishability when emission is into a large *classical* field to distinguishability and destruction of coherence between the internal atomic states when emission is into the vacuum state of the cavity. In their second experiment[12] they show that, using the same photon for both beamsplitters in an internal state interferometer sequence, coherence can be obtained even in the empty cavity limit. In our experiment the photon leaves the apparatus. We observe coherence only when the photon cannot carry away which-path information. This implies that the generated coherence in motional states is robust and lasts. In this sense it is an extension of Einstein's famous recoiling slit Gedanken experiment[11]. The single photon is the ultimate light weight beamsplitter which can be in a robust coherent superposition of two motional states. In free space the momentum of the emitted photon allows to measure the path of the atom. This corresponds to a well defined motional state of the beamsplitter i.e. no coherence. Close to the mirror the reflection renders some paths indistinguishable realizing a coherent superposition of the beamsplitter. The large mass of the mirror ensures that even in principle the photon recoil cannot be seen. Thus the atom is in a coherent superposition of the two paths. We measure this generated coherence by matterwave interference.

REFERENCES

[1] Milonni, P. W. *The quantum vacuum* (Academic Press, Boston [u.a.], 1994).

[2] Milonni, P. W. & Knight, P. L. Spontaneous emission between mirrors. *Optics Communications* **9**, 119 – 122 (1973).

[3] Drexhage, K. H. IV Interaction of light with monomolecular dye layers. vol. 12 of *Progress in Optics*, 163 – 192, 192a, 193–232 (Elsevier, 1974).

[4] Goy, P., Raimond, J., Gross, M. & Haroche, S. Observation of cavity-enhanced single-atom spontaneous emission. *Phys. Rev. Lett.* **50**, 1903 (1983).

[5] Eschner, J., Raab, C., Schmidt-Kaler, F. & Blatt, R. Light interference from single atoms and their mirror images. *Nature* **413**, 495–498 (2001).

[6] Eschner, J. Sub-wavelength resolution of optical fields probed by single trapped ions: Interference, phase modulation, and which-way information. *The European Physical Journal D* **22**, 341–345 (2003).

[7] Pfau, T., Spälter, S., Kurtsiefer, C., Ekstrom, C. R. & Mlynek, J. Loss of spatial coherence by a single spontaneous emission. *Phys. Rev. Lett.* **73**, 1223–1226 (1994).

[8] Chapman, M. S. *et al.* Photon scattering from atoms in an atom interferometer: Coherence lost and regained. *Phys. Rev. Lett.* **75**, 3783–3787 (1995).

[9] Kokorowski, D. A., Cronin, A. D., Roberts, T. D. & Pritchard, D. E. From single- to multiple-photon decoherence in an atom interferometer. *Phys. Rev. Lett.* **86**, 2191–2195 (2001).

[10] Oberthaler, M. *et al.* Dynamical diffraction of atomic matter waves by crystals of light. *Phys. Rev. A* **60**, 456–472 (1999).

[11] Bohr, N. *Albert Einstein: Philosopher Scientist* (Library of Living Philosophers, Evanston, 1949). Reprinted in Quantum Theory and Measurement (eds Wheeler, J. A. & Zurek, W. H.) 9-49 (Princeton Univ. Press, Princeton, 1983).

[12] Bertet, P. *et al.* A complementarity experiment with an interferometer at the quantum-classical boundary. *Nature* **411**, 166–170 (2001).

[13] Cronin, A. D., Schmiedmayer, J. & Pritchard, D. E. Optics and interferometry with atoms and molecules. *Rev. Mod. Phys.* **81**, 1051–1129 (2009).

[14] Martin, P., Oldaker, B., Miklich, A. & Pritchard, D. Bragg scattering of atoms from standing light-wave. *Phys. Rev. Lett.* **60**, 515–518 (1988).

[15] Morawitz, H. Self-coupling of a two-level system by a mirror. *Physical Review* **187**, 1792 (1969).

[16] Di Stefano, O., Savasta, S. & Girlanda, R. Three-dimensional electromagnetic field quantization in absorbing and dispersive bounded dielectrics. *Phys. Rev. A* **61**, 023803 (2000).

[17] Aspect, A., Arimondo, E., Kaiser, R. , Vansteenkiste, N. & Cohen-Tannoudji, C. Laser cooling below the One-Photon Recoil Energy by Velocity-Selective Coherent Population Trapping. *Phys. Rev. Lett.* **61**, 826 (1988).

ACKNOWLEDGMENTS

We wish to thank Florian Ritterbusch for assistance throughout the preparation of this manuscript.

We gratefully acknowledge support from the Forschergruppe FOR760, Deutsche Forschungsgemeinschaft, the German-Israeli Foundation, the Heidelberg Center of Quantum Dynamics, Landesstiftung Baden-Württemberg, the ExtreMe Matter Institute and the European Commission Future and Emerging Technologies Open Scheme project MIDAS (Macroscopic Interference Devices for Atomic and Solid-State Systems).

M. K. acknowledges financial support within the framework of the Emmy Noether project HA 5593/1-1 funded by the German Research Foundation (DFG).

J. S. acknowledges financial support through the Wittgenstein Prize.

ADDITIONAL INFORMATION

The authors declare that they have no competing financial interests. Supplementary information accompanies this paper on `www.nature.com/naturephysics`. Reprints and permissions information is available online at `http://npg.nature.com/reprintsandpermissions`. Correspondence and requests for materials should be addressed to single-photon@matterwave.de .

7. Conclusion

In this work a mixed phase space is realized in a driven macroscopic quantum system. Different behaviour of the time evolution of a many particle wave packet is found, whether it is initially prepared at a stable island or in the chaotic sea. In previous works, classical dynamics in the undriven system [58] and quantum behaviour at an unstable fixed point were investigated [38]. The existing setup has been extended to compensate for loss effects and to provide driving in order to investigate the time dynamics in a system described by a mixed phase space.

In a most simple system, featuring just an anharmonicity in the undriven case, the Poincaré-Birkhoff scenario was investigated by weak driving. Due to the driving, resonant orbits have been destroyed and stable and unstable fixed points occur. The time evolution of a wave packet prepared at these points is found to be similar to the dynamics at a stable respectively unstable fixed point of the undriven system. Therefore driving can stabilize the system for a preparation in a stable island or destabilize it at an unstable fixed point.
Furthermore, a mixed phase space is realized, exhibiting regular dynamics within a chaotic sea. Preparing the wave packet at different points along the perturbed orbit, the time dynamics in a stable island and in chaotic sea are studied. The experimental results reveal the expected behaviour obtained from classical phase space, although the time scales are different. Furthermore, the dynamics within the chaotic sea exhibit little dependency on initial parameters and the wave packets spreads much faster than on the unstable fixed point in the Poincaré-Birkhoff scenario.

Extending the classical model by using a distribution of points instead of a single one, classical simulations fit well to experimental data as well as the mean field model for certain observables and short times. Beyond the dynamics of the mean, also the qualitative behaviour of the variances can be reproduced in simulations. Expectations obtained from the classical phase space picture are used to develop an intuitive picture to understand the time dynamics in the driven system. Although the time scales of Poincaré map and experiment are rather different, the results are found to be compatible. Thus the dynamics in the driven mean field model can be predicted by simple arguments using the classical Poincaré map without having to do full quantum simulations.

With the first realization of a mixed phase space for an interacting many body system in the semi-classical regime, the route opens up for the investigation of several aspects, being of importance for both, the chaos and the quantum optics community.

Future prospects might involve the study of the transition from quantum to semi-classical regime. Since the effective Planck's constant of the system depends directly on atom number, it can be varied over a large range. Thus $\hbar_{\mathrm{eff}}$ dependent effects can be investigated – like flooding of islands [129, 130] or regular to chaotic tunneling [131, 132]. The investigation of these effects is beyond the scope of this work. Due to loss, the experimental accessible time scales in the current system are too short for the investigation of tunneling processes in phase space. Further optimization, e.g. fine tuning of $\hbar_{\mathrm{eff}}$ according to the size of the stable island, could tune the system towards the realization of these effects.

The closely related chaos assisted tunneling (CAT) would open up the route to a very interesting field of physics. In this scenario, the tunneling process between two stable islands is moderated by states of the chaotic sea and thus could be enhanced by orders of magnitude [133, 26]. The regular tunneling between two stable islands is experimentally not observable in the undriven system, due to huge tunneling times even for moderate particle numbers. In the context of macroscopic quantum systems, the enhancement of the tunneling rate due to CAT could result in experimentally observable many body tunneling. However, the occurrence of CAT depends critically on the symmetry of the system [134], which is experimentally hard to realize. Candidates to circumvent this problem are the moving period *2* islands investigated in this work. Since these islands are created by perturbation of one orbit, they must have the same energy in principle and thus at least the symmetry of these islands is ensured.

Furthermore, the tunneling rate in a CAT scenario depends critically on the effective Planck's constant [27], hence it could result in the investigation of odd/even effects in a loss-free system. In order to detect these differences, the detection noise in particle number has to be less than one. An enhanced detection is work in progress in our group and first promising results were obtained [135].

With that, the current experiment is directly connected to "coherent destruction of tunneling" [24], where I started my research. We realized the "single photon beam splitter" [108] afterwards with the same apparatus. Finally I switched to the BEC experiment in order to move forwards to chaos assisted tunneling.

A. Technical details

A.1. Numerical treatment of the classical Hamiltonian

It is well known to establish the equation of motion out of a classical Hamiltonian. In the considered case, some numerical problems arise due to the bounded phase space which will be discussed in the following.

Since the problem also arises in the undriven Hamiltonian, the solution is shown for that case for simplicity. For the driven system, the solution can be directly transferred. The undriven Hamiltonian including a detuning ϵ reads as:

$$\mathcal{H} = \frac{\Lambda}{2} z^2 - \sqrt{1-z^2}\cos\varphi + \epsilon z \tag{A.1}$$

resulting in the equation of motion:

$$\begin{aligned} \dot{z} &= -\frac{\partial \mathcal{H}}{\partial \varphi} = -\sin\varphi\sqrt{1-z^2} \\ \dot{\varphi} &= \frac{\partial \mathcal{H}}{\partial z} = \Lambda z + z\frac{\cos\varphi}{\sqrt{1-z^2}} + \epsilon \end{aligned} \tag{A.2}$$

Although a solution to A.2 can be found in [56] the main interest is in solutions to the driven system where no analytical solutions exist. Thus the set of coupled ODE's will be solved numerically. Just as the undriven system, also the driven version of eq. A.2 can be solved as an initial value problem with standard Runge-Kutta solving techniques [136].

When solving the equation of motion with standard Matlab ODE solver, for certain time and starting condition a complex solution will occur, even with small error tolerances and different ODE-solvers. The problem appears when the solution comes close to the poles. As the algorithm takes a linear approximation between two steps, it is in principle possible that the approximated z-value is out of bounds $[-1, 1]$. This implies complex value for the derivative as the square root in A.2 becomes complex.

In Matlab, no ODE solvers for an initial value problem with bounded solutions are known. Expressing equation A.2 in terms of z and φ implies also another numerical problem, which becomes obvious when considering plasma oscillations for small Λ in the untilted system with $\epsilon = 0$. Starting at $z_0 = -1,\ \varphi_0 = \pi/2$ and applying the Hamiltonian A.1, the system undergoes Rabbi-oscillations [48] with a constant angular velocity from $z = -1$ to $z = 1$ and back. In equation A.2 the velocity will depend on z, thus the error in each step within the Runge-Kutta algorithm will differ for several positions in phase space.

To circumvent both problems, equation A.2 will be rewritten with a transformation of coordinates, where z is substituted by $z = \sin\vartheta$:

$$\begin{aligned} \sqrt{1-z^2} &= \cos\vartheta \\ \dot{z} &= \frac{\partial z}{\partial \vartheta}\dot{\vartheta} = \cos\vartheta\,\dot{\vartheta} \end{aligned}$$

yielding in an ODE in the new coordinates:

$$\begin{aligned} \dot{\vartheta} &= -\sin\varphi \\ \dot{\varphi} &= \Lambda\sin\vartheta + \tan\vartheta\cos\varphi + \epsilon\ . \end{aligned} \tag{A.3}$$

Instead of substituting z by $\sin\vartheta$ also $z = \cos\vartheta$ could be used leading to structurally similar ODE's with minor changes. The corresponding driven version reads as:

$$\begin{aligned} \dot{\vartheta} &= -\sin\varphi \\ \dot{\varphi} &= \Lambda\sin\vartheta + [1 + A_{\mathrm{Driv}}\sin(\omega_{\mathrm{Driv}}t + \varphi_{\mathrm{Driv}})]\tan\vartheta\cos\varphi + \epsilon\ . \end{aligned} \tag{A.4}$$

For all classical simulations, the start point $z_0,\ \varphi_0$ is translated to $\vartheta_0,\ \varphi_0$, the time evolution is numerically calculated with the equations A.3 respectively A.4, and the solution is retranslated to $z,\ \varphi$.

A.1.1. Generation of a Gaussian distribution

For the comparison of the quantum with classical simulations the input state for the classical simulation should match the quantum one. In quantum calculations, the input is given in form of a coherent spin state (Eq. 2.33), approaching a normal distribution with $\sigma = 1/\sqrt{N}$ for larger atom numbers. To obtain normally distributed points around mean values $z_0,\ \varphi_0$ on a sphere the polar method [137] was used.

That's how it works: choose two equally distributed random variables v_1, v_2 in the interval $[-1, 1]$. Than calculate $r = v_1^2 + v_2^2$ and reject the points if $r = 0$ or $r \geq 1$. With $\sigma = 1/\sqrt{N}$ and

$$s = \sqrt{-2\frac{\ln r}{r}}$$

the desired coordinates calculate as:

$$x_1 = \sigma \cdot v_1 \cdot s$$
$$x_2 = \sigma \cdot v_2 \cdot s$$

In a flat geometry the resulting points would be shifted to the desired mean values subsequently. In our case all points are rotated to the desired $z_0,\ \varphi_0$ by usual rotation matrices in $\mathbb{R}^3$.

A.1.2. Plot of distributions

To visualize the time evolution of an initial gaussian distribution the following approach was chosen. A set of gaussian distributed points (typically 10^5 to $1.5 \cdot 10^5$) is evolved in time according to the considered Hamiltonian so one obtains the set (z_i, φ_i). Then a regular grid on the surface of a sphere is calculated (typically 500×500 sites), the number of all points (z_j, φ_j) within a site is counted and the result for all sites is plotted either on a 3D sphere or the flat phase space. The regular grid has to be chosen carefully to provide an equal area for each site over the whole sphere as described in [138, 139]. Otherwise the result would look disturbed.

Especially for the distributions in the chaotic sea a normalization of the colormap to the maximal density would be quite unsatisfying due to large fluctuations of the maxima even for small time steps. Instead of normalization, a histogram of all densities is calculated which follows an exponential decay function (except for gaussian distributions). Than the maximum in the colormap is set to twice of the "decay time" thus only a few very high densities are above the threshold and structure within them is lost. On the other side this enhances the visibility in mean densities.

Afterwards, to provide a better visibility, the contrast is enhanced by a gamma correction with $\gamma = 2$ [140].

A.1.3. Stationary points

Some basic insight into the system can be gained by obtaining its fixed points and determining their dependency on system parameters. In the following, the investigation of fixed points and a stability analysis will be presented.

It is required for a fixed point that all first derivatives vanishes [141] to be constant in time. Thus, we are looking for solutions of the ODE A.2:

$$\begin{aligned} \dot{z}_{FP} &= -\sin\varphi\sqrt{1-z_{FP}^2} \\ \dot{\varphi}_{FP} &= \Lambda z_{FP} + z_{FP}\frac{\cos\varphi_{FP}}{\sqrt{1-z_{FP}^2}} + \epsilon \end{aligned} \tag{A.5}$$

fulfilling $\dot{z}_{FP} = 0$ and $\dot{\varphi}_{FP} = 0$.

Fixed points of the symmetrical system $\epsilon = 0$

For the symmetrical system with $\epsilon = 0$ some investigations can be done in a closed analytical manner without any approximations, whereas approximations have to be applied for the tilted system with $\epsilon \neq 0$. Therefore the basic features will be shown for the symmetrical system.

One pair of solutions of Eq. A.5 can be directly given: $\varphi_{FP} = 0; \pi$ and $z_{FP} = 0$. Since these fixed points play an important role, they will be labeled according to:

$$z_{Pl} = 0;\ \varphi_{Pl} = 0 \longrightarrow \text{Plasma} \tag{A.6}$$

$$z_{\pi} = 0;\ \varphi_{\pi} = \pi \longrightarrow \pi\ . \tag{A.7}$$

A motivation for this naming convention will be given shortly. Besides this trivial solution two other fixed points occurs for $\varphi_{FP} = \pi$. The first equation in A.5 vanishes for this choice of φ_{FP}, the second one leads to the solution:

$$\begin{aligned} 0 &= \Lambda z_{FP} - \frac{z_{FP}}{\sqrt{1-z_{FP}^2}} \\ z_{\pm} &= \pm\sqrt{1-\frac{1}{\Lambda^2}}\ . \end{aligned} \tag{A.8}$$

Yet these fixed points are real if and only if the relative nonlinearity fulfills $\Lambda \geq 1$. Furthermore for the critical value of $\Lambda = 1$ the fixed points z_π and $z_\pm$ coincides but differ for larger values of Λ. Hence the system exhibits a bifurcation at $\Lambda = 1$.

Further analysis requires the knowledge of the stability of the fixed points, which will be determined according to [4]. Therefore the coupled ODE's:

$$\begin{pmatrix} \dot{z} \\ \dot{\varphi} \end{pmatrix} = \mathbf{F}(z, \varphi) = \begin{pmatrix} -\sin\varphi\sqrt{1-z^2} \\ \Lambda z + z\dfrac{\cos\varphi}{\sqrt{1-z^2}} + \epsilon \end{pmatrix} \tag{A.9}$$

will be linearized for an orbit close to the stable fixed point z_{FP}. The linearization of the equation of motion is obtained by the Jacobian matrix of $\mathbf{F}$:

$$\mathbf{DF} = \begin{bmatrix} \dfrac{\partial \mathbf{F}_1}{\partial z} & \dfrac{\partial \mathbf{F}_1}{\partial \varphi} \\ \dfrac{\partial \mathbf{F}_2}{\partial z} & \dfrac{\partial \mathbf{F}_2}{\partial \varphi} \end{bmatrix} = \begin{bmatrix} \dfrac{z\sin\varphi}{\sqrt{1-z^2}} & -\cos\varphi\sqrt{1-z^2} \\ \Lambda + \dfrac{\cos\varphi}{\sqrt{1-z^2}^3} & -\dfrac{z\sin\varphi}{\sqrt{1-z^2}} \end{bmatrix}_{\substack{z=z_{FP} \\ \varphi=\varphi_{FP}}} \tag{A.10}$$

evaluated at the desired fixed point. By determining eigenvalues and eigenvectors of $\mathbf{D}F$, the behaviour close to the fixed point can be predicted. If the eigenvalues are solely imaginary, the fixed point will be stable with regular orbits around. On the other hand, if one eigenvalue is real and larger than zero, a point close-by will be exponential separated from the fixed point along the corresponding eigenvector. Contrary if the eigenvalue is real and smaller than zero an adjacent point will exponentially approach the fixed point.

The eigenvalues of $\mathbf{DF}$ can be determined to:

$$\lambda_\pm = \pm\sqrt{\frac{z^2\sin^2\varphi - \cos^2\varphi}{1-z^2} - \Lambda\cos\varphi\sqrt{1-z^2}}\,. \tag{A.11}$$

If the fixed point is stable, the angular frequency of a closed by orbit is determined by the imaginary part of the eigenvalue [4]:

$$\omega = \Im(\lambda) \tag{A.12}$$

On the other hand the eigenvalue coincides with the Lyapunov-exponent for an unstable fixed point. This definition of the Lyapunov-exponent is solely applicable at fixed points of the system, a numerical determination

for a more general case is given in Sec. A.1.4. The eigenvectors of **DF** for real eigenvalues corresponds to the stable respectively unstable manifold/axis.

Evaluating the eigenvalue Eq. A.11 at the plasma fixed point $z_{Pl} = 0, \varphi_{Pl} = 0$ one obtains:

$$\lambda_{\pm}^{Pl} = \pm\sqrt{-\Lambda - 1} \tag{A.13}$$

which is complex for all values of the relative nonlinearity since Λ is always larger than zero. This indicates, that this fixed point is stable for all values of Λ. The frequency of a surrounding orbit reads in scaled units as:

$$\omega_{Pl} = \Im(\sqrt{-1-\Lambda}) = \sqrt{1+\Lambda}\,. \tag{A.14}$$

A similar approach to derive small amplitude oscillations close to the plasma/π fixed points is given in [56] leading to same results.

The fixed point at the π side shows a different behaviour, which is determined by its eigenvalue:

$$\lambda_{\pm}^{\pi} = \pm\sqrt{\Lambda - 1}\,. \tag{A.15}$$

If the relative nonlinearity is smaller than one $\Lambda < 1$, the eigenvalue is solely imaginary, indicating stable behaviour of adjacent orbits. The corresponding frequency in the small amplitude approximation calculates to:

$$\omega_{\pi} = \sqrt{1-\Lambda}\,. \tag{A.16}$$

Therefore the frequency of the plasma fixed point is larger than on the π side, which is indicated by the naming convention.

The two fixed points $z_{\pm}$ occurring at $\Lambda = 1$ are stable since the eigenvalue $\lambda_{\pm}^{\pm} = \pm\sqrt{1-\Lambda^2}$ is imaginary for $\Lambda \geq 1$. The frequency of orbits close to these new fixed points can be linearized by:

$$\omega_{\pm} = \sqrt{\Lambda^2 - 1} \tag{A.17}$$

which fits perfectly with numerics and findings from the effective single particle Schrödinger like equation in [49, 50].

Linearized dynamics at the unstable fixed point

When Λ is larger than one, the eigenvalues of z_{π} become real. Thus the fixed point z_{π} becomes unstable at $\Lambda = 1$, the same value where the other

two fixed points $z_\pm$ occur. Therefore the system undergoes a pitchfork or period doubling bifurcation [4, 50] at $\Lambda = 1$.

Since the considered system is Hamiltonian, phase space volumes will remain unchanged. Thus the real eigenvalues appear in pairs with different sign. The Lyapunov exponent $\lambda_+ = \sqrt{\Lambda - 1}$ with positive sign leads to an exponential separation of adjacent points located at the unstable axis with a rate of $e^{\lambda_+ t}$. The unstable axis is determined by the eigenvector:

$$\begin{pmatrix} \frac{1}{\sqrt{\Lambda - 1}} \\ 1 \end{pmatrix} . \tag{A.18}$$

The angle of the unstable axis to the φ axis calculates[1] to:

$$\alpha_{us} = \arctan\left(\frac{1}{\sqrt{\Lambda - 1}}\right) = \frac{\pi}{2} - \arctan\left(\sqrt{\Lambda - 1}\right) . \tag{A.19}$$

On the other hand, the Lyapunov exponent with negative sign:

$$\lambda_- = -\sqrt{\Lambda - 1} \tag{A.20}$$

corresponds to a contraction of points of the stable manifold. The stable axis:

$$\begin{pmatrix} -\frac{1}{\sqrt{\Lambda - 1}} \\ 1 \end{pmatrix} \tag{A.21}$$

encloses an angle to the φ axis of:

$$\alpha_s = \arctan\left(-\frac{1}{\sqrt{\Lambda - 1}}\right) = \arctan\left(\sqrt{\Lambda - 1}\right) - \frac{\pi}{2} \tag{A.22}$$

In general stable and unstable axis are not orthogonal to each other, except for a value of $\Lambda = 2$.

The rate of squeezing

The initially prepared coherent spin state has the same uncertainty in all directions. When prepared at the unstable fixed point, the state will be stretched along the unstable manifold and squeezed along the stable one. The rate of squeezing of a state will be calculated in the following.

[1] Note that in standard plots the φ axis corresponds to x and the z-axis to y.

The Lyapunov exponent defined in Eq. A.20 describes the exponential separation of points, thus the smallest standard deviation σ of the state will shrink by the rate $\sigma(\tilde{t}) = \sigma_0 \exp\left(\lambda_\pm \tilde{t}\right)$. Contrary the number squeezing[37] is defined by the time evolution of variances σ^2 thus an additional factor of two appears in the rate (in logarithmic scale):

$$\xi_N^2(\tilde{t}) = 10 \log_{10}\left(\frac{\sigma^2(\tilde{t})}{\sigma_0^2}\right) \tag{A.23}$$

$$= \frac{10}{\ln 10} 2\lambda_- \tilde{t} \tag{A.24}$$

Finally the number squeezing can be described by the time evolution in scaled units:

$$\xi_N^2(\tilde{t}) = -\frac{20}{\ln 10}\sqrt{\Lambda - 1}\ \tilde{t}\ . \tag{A.25}$$

The best squeezing is obtained along the stable axis at an angle determined by Eq. A.22. At same time, the state rips apart along the unstable axis. This approximation holds for short times as long as the small amplitude approximation is valid and quantum effects are negligible. This is fulfilled for large N and not too close to the bifurcation point of $\Lambda = 1$, since quantum dephasing is dominating over the classical dynamics close to the bifurcation. A more detailed analysis of squeezing in the quantum system is given in [55].

In a typical experimental scenario for using squeezing, one aims to achieve a fast as possible squeezing. The nonlinearity $N\chi$ is limited in our case, e.g. by loss, but the coupling Ω can be chosen (almost) arbitrary. Since the coupling is not only involved in the relative nonlinearity but also in the scaling of the time $\tilde{t} = 2\pi\Omega t$ (Eq. 2.26), an optimal value should be found. Therefore, the squeezing will be expressed in real time:

$$\xi_N^2(t) = -\frac{20 \cdot 2\pi}{\ln 10}\sqrt{N\chi\Omega - \Omega^2}\ t\ . \tag{A.26}$$

The gradient achieves its maxima for $\Omega = \frac{1}{2}N\chi$. Thus a relative nonlinearity of $\Lambda = 2$ leads to squeezing being as fast as possible (for a time constant Hamiltonian). A scheme for faster squeezing due to pre squeezing is proposed in [45].

Tilted system

Prior to determining the fixed points of the tilted system with $\epsilon \neq 0$, the value of the relative nonlinearity should be determined, where the bifurcation occurs. Since the detuning ϵ adds a tilt to the system, one fixed point of the bifurcated system is shifted upwards and one downwards in energy (see Fig. A.1). Thus the downwards shifted island is getting more stable and is named deep island, the upshifted island is called "weak".

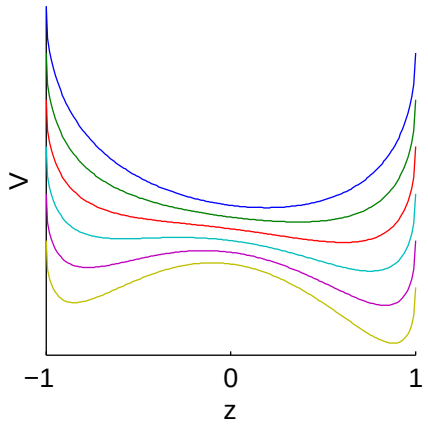

Figure A.1.: Schematic sketch of the inverted pseudo potential at $\varphi = \pi$ for different values of Λ and a fixed tilt ϵ. The relative nonlinearity is increased from blue to yellow. The potentials for different Λ coincide at $z = 0$, however a small offset was added to provide better readability. The tangent bifurcation occurs between red and cyan lines, therefore a new fixed point is created with $z_{FP} < 0$.

When increasing the tilt, the rising edge of the left fixed point becomes more shallow, and reaching zero for some value. Therefore, the left fixed point becomes unstable and coincides with the unstable fixed point in the center for this choice of parameters. In order to obtain the bifurcation point, additionally to the condition of a vanishing derivative for a fixed point

$$0 = \mathbf{F}_2 = \left.\frac{\partial \mathcal{H}}{\partial z}\right|_{\varphi=\pi} = \Lambda z - \frac{z}{\sqrt{1-z^2}} + \epsilon \tag{A.27}$$

also the second derivative has to vanish [141]:

$$0 = \frac{\partial \mathbf{F}_2}{\partial z} = \Lambda - \frac{1}{\left(1-z^2\right)^{\frac{3}{2}}} \,. \tag{A.28}$$

These equations can be established for a value of $\varphi = \pi$ since the condition for $\dot{z} = 0$ is not changed by the tilt. The second equation gives a value for the position z_* of the bifurcation:

$$z_* = \pm\sqrt{1 - \frac{1}{\Lambda_*^{\frac{2}{3}}}}\,. \tag{A.29}$$

Inserting this into Eq. A.27 yields in the condition for a bifurcation of the system at a value of:

$$\Lambda_* = \sqrt{1+\epsilon^{\frac{2}{3}}}^{3}\,. \tag{A.30}$$

The tilt changes the system just slightly, however the position of the fixed points is shifted a bit. For fitting experimental data, it is useful to have an analytical approximation of the position of fixed points. Since the condition of Eq. A.27 cannot be solved directly for a non vanishing tilt, an approximation will be developed.

As we saw in the untilted system, the interesting dynamics occurs at the π side of the Bloch sphere. Thus we will concentrate at the $\varphi = \pi$ fixed points and omit the one at $\varphi = 0$. In order to obtain approximations for the fixed points, taylor expansion of the hamiltonian will be applied around appropriate start points. When the condition of a vanishing first derivative can be solved for the approximated Hamiltonian and an approximation of z_{FP} is obtained.

For the π-fixed point and $\Lambda < \Lambda_*$ a second order taylor expansion around $z = 0$ yields in the fixed point:

$$z_\pi^{(2)} = \frac{\epsilon}{1-\Lambda}\,. \tag{A.31}$$

This deviates remarkably to the numerics, thus the fourth-order taylor expansion of the Hamiltonian:

$$\mathcal{H}|_{\substack{z=0\\ \varphi=\pi}} \approx -\frac{z^4}{8} - \frac{1}{2}(1-\Lambda)z^2 + \epsilon z + 1 \tag{A.32}$$

will be used instead. Differentiate with respect to z leads to the much better approximation of:

$$z_\pi = \left(\epsilon + \sqrt{\epsilon^2 + \tilde{\Lambda}^3}\right)^{\frac{1}{3}} - \frac{\tilde{\Lambda}}{\left(\epsilon + \sqrt{\epsilon^2 + \tilde{\Lambda}^3}\right)^{\frac{1}{3}}} \tag{A.33}$$

with $\tilde{\Lambda} = \frac{2}{3}(1-\Lambda)$ and $\varphi_\pi = \pi$.

The fixed points $z_\pm$ for the bifurcated system with $\Lambda > \Lambda_*$ can be obtained by taylor expansion of $\mathcal{H}$ around the fixed points of the untilted system $z_0 = \pm\sqrt{1-\frac{1}{\Lambda^2}}$. Even when using higher order taylor expansion, the resulting approximation does not fit well with numerics due to large anharmonicity of the Hamiltonian. A much better result can be obtained by fourth order taylor expansion around the points:

$$z_\pm^{(0)} = \pm\sqrt{1-\frac{(1\mp\epsilon)^2}{\Lambda^2}}\,. \tag{A.34}$$

The formula can be solved analytically e.g. by computer algebra, but is too long to be displayed here and does not lead to further insight into the behaviour. It fits quite well with numerics.

A.1.4. Lyapunov-exponents

The Lyapunov-exponent for a Hamiltonian systems describes the rate by that two adjacent points are separated in time. We follow the route of [51, 142] to numerically calculate the largest Lyapunov-exponent using the rescaling method. The basic idea is the following: one starts with two adjacent points $\vec{x}_0$ and $\vec{y}_0 = \vec{x}_0 + \vec{\delta}_0$ separated by a small amount $|\vec{\delta}_0|$ in an arbitrary direction. Subsequently the time evolution of both points is calculated for a small time τ, thus $\vec{x}_\tau, \vec{y}_\tau$ leading to the new displacement $\vec{\delta}_\tau = \vec{y}_\tau - \vec{x}_\tau$. For the next iteration, the direction of the displacement is kept, but the amount is rescaled to the original value, thus the new start points is $\vec{x}_\tau$ and $\vec{x}_\tau + \frac{\delta_0}{\delta_\tau}\vec{\delta}_\tau$. The largest Lyapunov exponent is when calculated according to:

$$\lambda_L = \lim_{N\to\inf}\frac{1}{N\tau}\sum_i^N \ln\left(\frac{\delta_i}{\delta_0}\right)$$

The basic idea of this procedure is that the most unstable axis is dominating over all other axes. Thus two adjacent points will diverge mostly along the unstable axis and with the rescaling in each step, the axis is remained but the distance is rescaled to stay in close vicinity of the desired point.

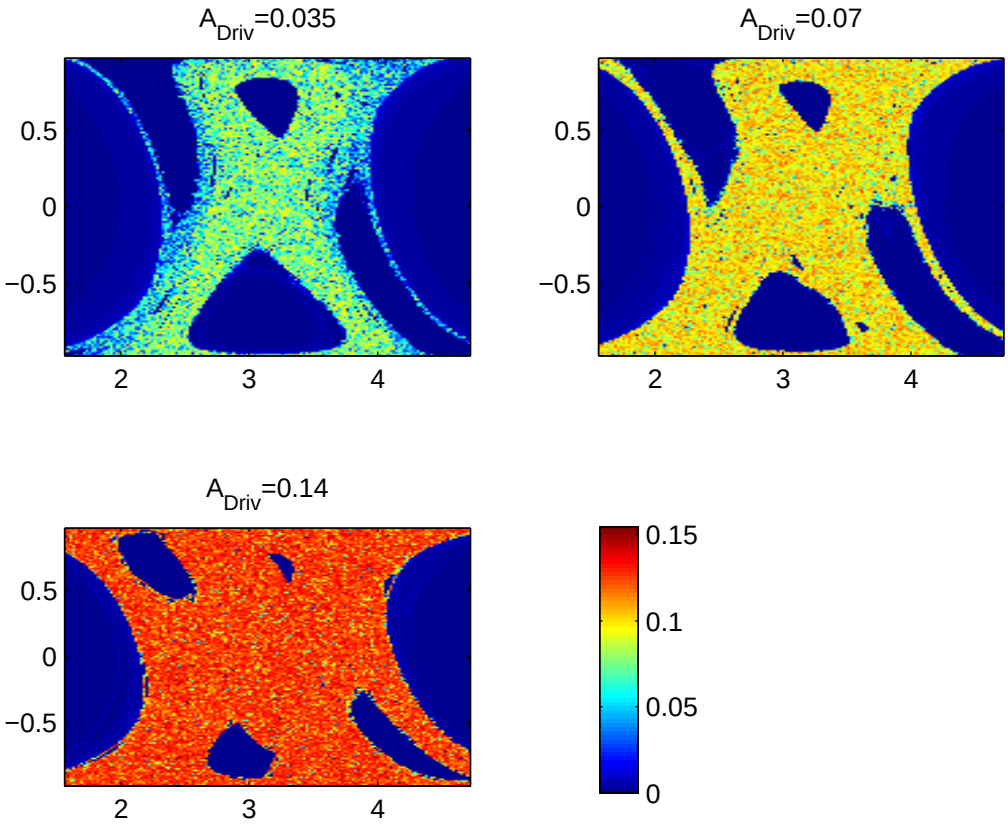

Figure A.2.: Lyapunov exponents of the driven system at $\Lambda = 1.53$ for different driving amplitudes. The calculation is done for many start points in the phase space and plotted according to the same colormap from blue to red.

A.2. Numerical methods to solve the Bose-Hubbard Hamiltonian

In this part, the numerical treatment of the Hamiltonian will be addressed shortly. The (undriven) scaled Bose-Hubbard Hamiltonian for a spin-$N/2$ system including a detuning ϵ reads as [49, 42, 44, 45]:

$$\hat{\mathcal{H}}_0 = \frac{\Lambda}{2}\hat{\mathcal{J}}_z^2 - \hat{\mathcal{J}}_x + \epsilon\hat{\mathcal{J}}_z. \tag{A.35}$$

A.2.1. Numerical diagonalization

Following standard text books [75, 143] the Hamiltonian A.35 will be rewriten in terms of creation and annihilation operators and diagonalized in the number state basis. With the creation and annihilation operators $\hat{a}_1^\dagger$ and $\hat{a}_1$ of one quanta in state $|F=1\rangle$ (and corresponding operators $\hat{a}_2^\dagger$ and $\hat{a}_2$ for state $|F=2\rangle$), the spin-$N/2$ operators can be written in the form [44, 45]:

$$\hat{\mathcal{J}}_x = \frac{1}{N}\left(\hat{a}_2^\dagger \hat{a}_1 + \hat{a}_1^\dagger \hat{a}_2\right) \tag{A.36}$$

$$\hat{\mathcal{J}}_y = \frac{1}{iN}\left(\hat{a}_2^\dagger \hat{a}_1 - \hat{a}_1^\dagger \hat{a}_2\right) \tag{A.37}$$

$$\hat{\mathcal{J}}_z = \frac{1}{N}\left(\hat{a}_2^\dagger \hat{a}_2 - \hat{a}_1^\dagger \hat{a}_1\right) \tag{A.38}$$

where a different normalization was chosen to obtain a Bloch sphere with radius of 1, such that the results of the quantum simulation are direct comparable with classical ones. By calculating some commutation relations of the operators $\hat{\mathcal{J}}$, the value of the effective Planck's constant is given by $2/N$ (see Eq. 2.24). In order to preserve the mapping of the operators $\hat{a}_i$ to state $|F=i\rangle$ and to assign the expectation value of $\langle\hat{\mathcal{J}}_z\rangle \equiv -1$ to all particles being in state $|F=1\rangle$, the labelling of term is swapped according to [44].

The number state basis (equivalent to Fock basis [32]) for a fixed total number N of particles (or spins) is composed by vectors:

$$|\varphi_k\rangle = |k, N-k\rangle \tag{A.39}$$

where k denotes the number of particles in state $|F=2\rangle$ and $N-k$ the number of particles with $|F=1\rangle$. It should be noted the operator $\hat{a}_2$ is acting on the first component of $|\varphi_k\rangle$ within this notation. Thus each state can be decomposed into:

$$|\psi\rangle = \sum_{k=0}^{N} c_k \, |k, N-k\rangle \tag{A.40}$$

with coefficients c_k. By expressing the Hamiltonian A.35 in the number state basis, an equivalent to the Schrödinger equation for the coefficients c_k is derived. The base vector $|k, N-k\rangle$ is assigned to the vector $(\ldots, 1, \ldots)$

with a 1 at the k'th position. To obtain the matrix form of the the spin-$N/2$ operators, their action on a base state is calculated:

$$\begin{aligned}\hat{\mathcal{J}}_z |\varphi_k\rangle &= \frac{1}{N}\left(\hat{a}_2^\dagger \hat{a}_2 - \hat{a}_1^\dagger \hat{a}_1\right)|k, N-k\rangle \\ &= \frac{1}{N}\left(\sqrt{k}\sqrt{k} - \sqrt{N-k}\sqrt{N-k}\right)|k, N-k\rangle \\ &= \left(\frac{2k}{N} - 1\right)|k, N-k\rangle\end{aligned}$$

thus $\hat{\mathcal{J}}_z$ is equivalent to the matrix in number state base NB:

$$\left(\hat{\mathcal{J}}_z\right)_{NB} = \frac{2}{N}\begin{pmatrix} 0-N & 0 & 0 & \dots \\ 0 & 1-N & 0 & \\ 0 & 0 & 2-N & \\ \vdots & & & \ddots \end{pmatrix} \tag{A.41}$$

where the brakets around $\hat{\mathcal{J}}_z$ indicates the matrix form of the operator in the number state base. A verification of the expectation value of $\langle 0, N|\hat{\mathcal{J}}_z|0, N\rangle = -1$ confirms the identification of the first component with the $|F = 2\rangle$ manifold. For $\hat{\mathcal{J}}_x$ follows:

$$\begin{aligned}\hat{\mathcal{J}}_x |\varphi_k\rangle = \frac{1}{N}\big(&\sqrt{k}\sqrt{N-k+1}\,|k-1, N-k+1\rangle + \\ &\sqrt{k+1}\sqrt{N-k}\,|k+1, N-k-1\rangle \big)\end{aligned}$$

which is equivalent to the matrix:

$$\left(\hat{\mathcal{J}}_x\right)_{NB} = \frac{1}{N}\begin{pmatrix} \ddots & & & & \\ & \sqrt{k}\sqrt{N-k+1} & 0 & \sqrt{k+1}\sqrt{N-k} & \\ & & \uparrow_{k+1} & & \ddots \end{pmatrix} \leftarrow k+1$$

where the central 0 is in the $k+1$'th column and row (the $+1$ is due to the start with indice $k = 0$).

Although the matrix form of the operator $\hat{J}_y$ is not directly required to develop the matrix form of the Hamiltonian, in the calculation of the expectation value of φ it is needed. Therefore, it calculates as:

$$\begin{aligned}\hat{\mathcal{J}}_y |\varphi_k\rangle = \frac{1}{iN}\big(&-\sqrt{k}\sqrt{N-k+1}\,|k-1, N-k+1\rangle + \\ &\sqrt{k+1}\sqrt{N-k}\,|k+1, N-k-1\rangle \big)\end{aligned}$$

and thus:

$$\left(\hat{\mathcal{J}}_y\right)_{NB} = \frac{1}{iN}\begin{pmatrix} \ddots & & & & \\ & -\sqrt{k}\sqrt{N-k+1} & 0 & \sqrt{k+1}\sqrt{N-k} & \\ & & & & \ddots \end{pmatrix}.$$

Henceforth the matrix form of the Hamiltonian (A.35) can be obtained by substituting the operators by their matrix counterpart to obtain a $N+1 \times N+1$ matrix:

$$\left(\hat{\mathcal{H}}_0\right)_{NB} = \frac{\Lambda}{2}\left(\hat{J}_z\right)^2_{NB} - \left(\hat{J}_x\right)_{NB} + \epsilon\left(\hat{J}_z\right)_{NB} \tag{A.42}$$

which can be diagonalized (as it is hermitian) to obtain eigenenergies E_k and eigenvectors $|\tilde{\varphi}_k\rangle$. For the typically investigated particle numbers below 1000 atoms the diagonalization is numerically feasible. Thus each input state can be decomposed into the new base:

$$|\psi_0\rangle = \sum_k \tilde{c}_k \, |\tilde{\varphi}_k\rangle$$

and its time evolution can be directly written as:

$$|\psi(t)\rangle = \sum_k \tilde{c}_k \exp\left(-itE_kN/2\right) |\tilde{\varphi}_k\rangle \tag{A.43}$$

where the factor $2/N$ serves as an effective Planck constant [49]. The additional factor of 2 is due to the different normalization of the radius of the Bloch sphere.

On the other hand, the time evolution can be calculated numerically without diagonalization by solving the $N+1$ coupled ODE in the c_k's:

$$\begin{pmatrix} \vdots \\ \dot{c}_k \\ \vdots \end{pmatrix} = -i\frac{N}{2}\left(\hat{\mathcal{H}}\right)_{NB} \begin{pmatrix} \vdots \\ c_{k-1} \\ c_k \\ c_{k+1} \\ \vdots \end{pmatrix} \tag{A.44}$$

Numerical treatment of the driven system

The driven system can be treated analogous when including the explicit time dependency of the driving into the matrix form of the Hamiltonian A.42:

$$\left(\hat{\mathcal{H}}(t)\right)_{NB} = \frac{\Lambda}{2}\left(\hat{\mathcal{J}}_z\right)^2_{NB} - \left[1 + A_{\text{Driv}} \sin\left(\omega_{\text{Driv}}t + \varphi_{\text{Driv}}\right)\right]\left(\hat{\mathcal{J}}_x\right)_{NB} + \epsilon\left(\hat{\mathcal{J}}_z\right)_{NB} \tag{A.45}$$

leading to an explicit time dependency in the coupled ODE's of the coefficients c_k. This can be directly solved by a Runge-Kutta solver, however it's not the best way numerically. In our experiments, the initial state will be a coherent spin state (CSS, see Sec. 2.2.1), which is a superposition of many number states. Since none of the number states is an eigenstate of the Hamiltonian, the occupation will vary rapidly leading to an enhanced error in the numerical treatment.

Following the basic principle of time dependent perturbation theory (Sec. A.2.2 or [75]), the mentioned problem will be circumvented. The idea is for small perturbations that the perturbed state will evolve similar to an unperturbed one (an eigenstate of the Hamiltonian) plus some correction in the order of the perturbation in terms of the eigenbase of the Hamiltonian. Thus all operators within the Hamiltonian will be rewritten in the eigenbase of the Hamiltonian (which is numerically known after diagonalization):

$$\begin{aligned} \left(\hat{\mathcal{J}}_x\right)_{NB} &\rightarrow \left(\hat{\mathcal{J}}_x\right)_{EH} \\ \left(\hat{\mathcal{J}}_z\right)_{NB} &\rightarrow \left(\hat{\mathcal{J}}_z\right)_{EH} \end{aligned}$$

where EH denotes the eigenbase of the Hamiltonian. Thus the matrix form of the driven Hamiltonian can be deployed by substituting in equation A.45 the representations of all operators in the number state base by their pendant in the eigenbase. This representation of the Hamiltonian

$$\begin{aligned} \left(\hat{\mathcal{H}}\right)_{EH} &= \frac{\Lambda}{2}\left(\hat{\mathcal{J}}_z\right)^2_{EH} - \left[1 + A_{\mathrm{Driv}} \sin\left(\omega_{\mathrm{Driv}} t + \varphi_{\mathrm{Driv}}\right)\right]\left(\hat{\mathcal{J}}_x\right)_{EH} + \epsilon\left(\hat{\mathcal{J}}_z\right)_{EH} \\ &= \left(\hat{\mathcal{H}}_0\right)_{EH} - A_{\mathrm{Driv}} \sin\left(\omega_{\mathrm{Driv}} t + \varphi_{\mathrm{Driv}}\right)\left(\hat{\mathcal{J}}_x\right)_{EH} \end{aligned} \tag{A.46}$$

is diagonal for $\omega_{\mathrm{Driv}} t + \varphi_{\mathrm{Driv}} = 2\pi\mathbb{N}$, and in general close to diagonal with small time dependent entries in the off diagonals (for small A_{Driv}). It can be numerically integrated in analogy to equation A.44.

A comparison of both methods can be done for the undriven Hamiltonian, as the quasi analytical solution is known. By calculating the overlap of the wavefunctions obtained by analytical and numerical methods, an estimation of the error of the numerical method exists. The error depends slightly on the start point, but usually the error for the ODE in the number state base is more than an order of magnitude higher than for the ODE in the eigenbase. Although this comparison is somehow weak as the off-diagonal terms are neglected.

Separation of the fast phase evolution in Eq. A.46 and rewriting the ODE in slow varying terms according to Eq. A.56 of the time dependent perturbation theory leads to no further speed improvements. Thus all simulations

in the mean field picture were done with the ODE's in the eigenbase according to Eq. A.46.

Expectation values and variances

For a quantitative comparison of the experiment and the predictions of the simulations, besides the expectation values in z and φ the corresponding variances σ_z^2 and σ_φ^2 were required. In the classical simulations these values are obtained for free, as the results are calculated in z, φ for a distribution of points and mean and variances can be calculated as mean respectively variance over the whole distribution.

In quantum mechanics expectation values and variances for a state ψ and an operator $\hat{O}$ can be calculated by:

$$\begin{aligned} \langle \hat{A} \rangle &= \langle \psi | \hat{A} \psi \rangle \\ \sigma_A^2 &= \langle \psi | \hat{A}^2 \psi \rangle - \langle \hat{A} \rangle^2 \end{aligned} \tag{A.47}$$

where an operator equivalence is used in the last row. For φ no direct operator exists, so σ_φ^2 is derived from the variances in x, y, z. From quantum to classical correspondence, the expectation value $\langle \hat{J}_x \rangle$ corresponds to x (accordingly for the other coordinates and variances). The coordinates transform as:

$$\begin{aligned} x &= \sqrt{1-z^2}\cos\varphi \\ y &= \sqrt{1-z^2}\sin\varphi \end{aligned}$$

Utilizing the gaussian error propagation [99] for variances

$$\sigma_i^2 = \left(\frac{\partial x_i}{\partial \varphi}\right)^2 \sigma_\varphi^2 + \left(\frac{\partial x_i}{\partial z}\right)^2 \sigma_z^2$$

yielding to:

$$\begin{aligned} \sigma_x^2 &= \left(1-z^2\right)\sin^2\varphi\,\sigma_\varphi^2 + \frac{z^2\cos^2\varphi}{1-z^2}\sigma_z^2 \\ \sigma_y^2 &= \left(1-z^2\right)\cos^2\varphi\,\sigma_\varphi^2 + \frac{z^2\sin^2\varphi}{1-z^2}\sigma_z^2. \end{aligned} \tag{A.48}$$

Adding both equations and some minor transformations lead to the formula for the variance in φ:

$$\sigma_\varphi^2 = \frac{\sigma_x^2 + \sigma_y^2}{1-z^2} - \frac{z^2\sigma_z^2}{\left(1-z^2\right)^2} \tag{A.49}$$

Thus with expectation values and variances for all 3 operators $\hat{J}_x, \hat{J}_y, \hat{J}_z$ according to equation A.47 the variance in φ can be obtained.

Normalization of variances

A coherent spin state (CSS) should always have a variance of $1/N$, with N the number of atoms/spins [45]. When calculating the variance for an CSS prepared at $z = 0$ either with the mean field or the classical model, this result is obtained. But then rotating the same state towards the poles, the measured variance in z shrinks due to projection. For an investigation in the dynamics on the Bloch sphere, it would be much more appropriate to uncouple the evolution of the variance from that of the mean, so that a change in variance gives a direct hint if the distribution shrinks or broadens. Thus all variances will be normalized to live on the surface of the sphere according to:

$$\begin{aligned} P &= \frac{z}{2} + \frac{1}{2} \\ \tilde{\sigma}_z^2 &= \frac{\sigma_z^2}{4P(1-P)} \\ \tilde{\sigma}_\varphi^2 &= \sigma_\varphi^2 \cdot 4P(1-P) \end{aligned} \tag{A.50}$$

where the corrected/normalized variances are denoted with a tilde. The factor $4P(1-P) = 1 - z^2 = (\sin\vartheta)^2$ (with ϑ being the angle of spherical coordinates) can be derived by simple geometric considerations. All experimental and simulated variances within this thesis (except the phase space plots like Fig. 5.11) are normalized according to A.50.

A.2.2. Time dependent perturbation theory

In order to gain some insight into short time dynamics beyond pure simulations, time dependent perturbation theory will be applied to the driven system. Structurally the considered driven system is quite similar to a

two level atom subjected to an electro magnetic field in the dipole approximation, as treated in many text books of atomic physics [75, 74, 92]. As the system consists of much more energy levels and is initially not in an eigenstate of the Hamiltonian, the considerations will be slightly modified. The following route is mainly excerpted from [75], but will be given here to ensure the proper definition of terms.

In order to shorten some terms, within this section the driving Amplitude A_{Driv} will be abbreviated with A, the driving frequency with ω_D and the driving phase with φ_D. The driven Hamiltonian can be written as:

$$\hat{\mathcal{H}}(t) = \hat{\mathcal{H}}_0 + A\hat{W}(t) \tag{A.51}$$

with $\hat{\mathcal{H}}_0$ as the undriven Hamiltonian and a perturbing part $\hat{W}(t)$:

$$\begin{aligned} \hat{\mathcal{H}}_0 &= \frac{\Lambda}{2}\hat{\mathcal{J}}_z^2 - \hat{\mathcal{J}}_x + \epsilon\hat{\mathcal{J}}_z \\ \hat{W}(t) &= -\sin(\omega_D t + \varphi_D)\hat{\mathcal{J}}_x \,. \end{aligned} \tag{A.52}$$

Denoting the eigenvectors of $\hat{\mathcal{H}}_0$ with $|\varphi_n\rangle$, an arbitrary state can be written as

$$|\psi\rangle = \sum_n c_n(t)\,|\varphi_n\rangle \tag{A.53}$$

with time dependent expansion coefficients $c_n(t)$ in the eigenbase of $\hat{\mathcal{H}}_0$. The following considerations will all be done in the eigenbase of $\hat{\mathcal{H}}_0$. Since it can't be diagonalized analytically for an arbitrary choice of parameters Λ and ϵ and more than a few atoms, the conclusions can't be done in a strong analytical way. This holds even in the approximation of time dependent perturbation theory and some coefficients have to be obtained numerically. Therefore predictions can be given for a certain set of parameters and starting values merely.

The coefficients $c_k(t)$ have to fulfill the coupled differential equations:

$$i\hbar\frac{\mathrm{d}}{\mathrm{d}t}c_k(t) = E_k c_k(t) + A\sum_n c_n(t)W_{kn}(t) \,. \tag{A.54}$$

This is equivalent to the coupled ODE's for the numerical treatment of the driven Hamiltonian in Eq. A.46. Obviously, in this representation the diagonal terms are in the order of E_k whereas the off-diagonal terms are in the order of the driving amplitude, so typically much smaller. The matrix elements of $\hat{W}$ are denoted with $W_{kn}(t)$:

$$W_{kn}(t) = \langle\varphi_k|\,\hat{W}(t)\,|\varphi_n\rangle = -\sin(\omega_D t + \varphi_D)\cdot\left(J_x\right)_{kn} \,. \tag{A.55}$$

Thus the perturbation term is proportional to the representation of $\hat{\mathcal{J}}_x$ in the eigenbase of $\hat{\mathcal{H}}_0$. The first term of Eq. A.54 leads to the fast phase evolution of the undriven system. Therefore it is more convenient to separate the fast time evolution $c_k(t) = b_k(t)\exp(-i\omega_k t)$ and examine the time evolution of slowly varying terms $b_k(t)$. For the undriven system, these terms are time independent and completely determined by the initial preparation.

Applying the separation of different orders in time into Eq. A.54, the (exact) ODE for the b_k's can be derived:

$$i\hbar\frac{\mathrm{d}}{\mathrm{d}t}b_k(t) = A\sum_n W_{kn}(t)e^{i\Delta\omega_{kn}t}b_n(t) \tag{A.56}$$

with the eigenfrequency difference $\Delta\omega_{kn} = \omega_k - \omega_n$. In order to dissolve the dependency of coupled ODE's, perturbation theory makes the assumption that the $b_k(t)$ can be written in a power series in the driving amplitude:

$$b_k(t) = \sum_i A^i b_k^{(i)}(t)\ . \tag{A.57}$$

Inserting this into Eq. A.56 and comparing the same orders in A, one obtains:

$$i\hbar\frac{\mathrm{d}}{\mathrm{d}t}b_k^{(i)}(t) = \sum_n b_n^{(i-1)}(t)W_{kn}(t)e^{i\Delta\omega_{kn}t}\ . \tag{A.58}$$

This implies that the time evolution of the coefficient in the (i) order is completely determined by the (known) time evolution of the $(i-1)$ coefficients. Therefore the differential equations were uncoupled.

Particularly one obtains for the zeroth order coefficients:

$$\frac{\mathrm{d}}{\mathrm{d}t}b_k^{(0)} = 0\ . \tag{A.59}$$

Thus the $b_k^{(0)}$ are constant (likewise in the undriven system) and as the perturbation is switched on at $t = 0$, they are equal to the $c_k(0)$, hence determined by the input state $|\psi(0)\rangle$. The first order correction term calculates as:

$$\begin{aligned} i\hbar\frac{\mathrm{d}}{\mathrm{d}t}b_k^{(1)}(t) &= \sum_n b_n^{(0)}W_{kn}(t)e^{i\Delta\omega_{kn}t} && \text{(A.60)}\\ &= -\sin(\omega_D t+\varphi_D)\sum_n b_n^{(0)}\left(J_x\right)_{kn}e^{i\Delta\omega_{kn}t} && \text{(A.61)}\\ &= -\frac{1}{2i}\sum_n b_n^{(0)}\left(J_x\right)_{kn}\left[e^{i(\Delta\omega_{kn}+\omega_D)t+i\varphi_D} - e^{i(\Delta\omega_{kn}-\omega_D)t-i\varphi_D}\right] && \text{(A.62)} \end{aligned}$$

Since all coefficients on the right hand side are constant in time, Eq. A.62 can be directly integrated:

$$b_k^{(1)}(t) = -\frac{iN}{4}\sum_n b_n^{(0)}\left(J_x\right)_{kn}\left[\frac{e^{i\varphi_D}\left(1-e^{i(\Delta\omega_{kn}+\omega_D)t}\right)}{\Delta\omega_{kn}+\omega_D} - \frac{e^{-i\varphi_D}\left(1-e^{i(\Delta\omega_{kn}-\omega_D)t}\right)}{\Delta\omega_{kn}-\omega_D}\right] \tag{A.63}$$

by using $\hbar = 2/N$ (see Eq. A.43). In case of the atomic two level system, the driving frequency is close to resonance $\omega_D \sim |\Delta\omega_{kn}|$. Therefore, if $\Delta\omega_{kn} > 0$, the denominator $\Delta\omega_{kn} + \omega_D \sim 2\omega_D$ becomes quite large besides a fast phase evolution of the corresponding term. Hence, such terms are neglected in the so called rotating wave approximation [92]. The same argument holds for the second term if $\Delta\omega_{kn} < 0$.

The similar can be done in the investigation of the driven system in Eq. A.63. A remarkable contribution is expected for driving frequencies approaching one of the transition frequencies $\Delta\omega_{kn}$. Since several eigenstates are involved in the time evolution of an initially prepared coherent spin state, the range of the driving frequency for hitting a resonance is much larger here. For energies above the double well in the $\Lambda = 1.5$ system one obtains numerically $\Delta\omega_{kn} \sim \mathcal{O}(k-n)$ by solving Eq. A.42, thus being positive for $k > n$ and vice versa. Therefore the first term can be dropped for $k > n$ and the second one for $k < n$. On the other hand, the contribution of each term is determined by the product $b_n^0 \cdot \left(J_x\right)_{kn}$. If it vanishes, the term does not contribute even at resonance, equivalently to forbidden transitions in the atomic system.

In order to provide further conclusions, the structure of the coefficients b_n^0 as well as the matrix elements $\left(J_x\right)_{kn}$ have to be investigated in detail. The distribution of the $b_n^{(0)}$ depends on system parameters and the initial preparation and has typically significant contributions for a subset of eigenstates. Thus the coupling strength depends on the local structure of a small subset of the matrix elements of $\left(J_x\right)$, such that the global structure of $\left(J_x\right)$ can be omitted.

To deviate remarkably from the undriven system, it is necessary to get considerable contributions in the first order coefficients $b_k^{(1)}$, since the zeroth order coefficients are constant in time. Furthermore by revisiting the differential equations for the $b_k^{(i)}$ (Eq. A.58) it can be directly deduced that higher contributions can grow not until the contribution of lower order $b_k^{(i-1)}$ becomes significant. Therefore, as long as the first order coefficients remain small, the system remains close to the undriven one. On the other hand, even if first and higher order coefficients becomes large, it does not

imply that the system has to deviate significantly from the undriven one in terms of measuring mean or variances. This depends on all involved coefficients and a cancellation of different contributions could occur.

Hence, the growth of the first order coefficients is a mandatory condition to enable a deviation of the driven system from the undriven one, but it is not sufficient. Therefore, the point of strong growing first order coefficients gives a minimal time for the perturbation to act on the system leading to significant changes.

The analysis is done in section 2.5.2 for the special cases of $\Lambda = 1.5$ and $\Lambda = 0.7$ treated within this work. The consideration can not be generalized to an arbitrary choice of parameters or even different start points.

B. Supplementary information for the unbifurcated system

B.1. Anharmonicity of the potential

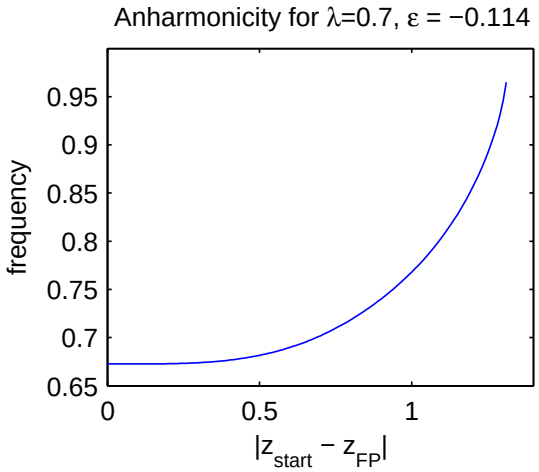

Figure B.1.: Anharmonicity of the system for $\Lambda = 0.7,\ \epsilon = -0.114$
The x-axis shows the distance of the starting point to the fixed point (corresponding to the amplitude of resulting oscillation), the y-axis the scaled frequency.

B.2. Phase space for different times

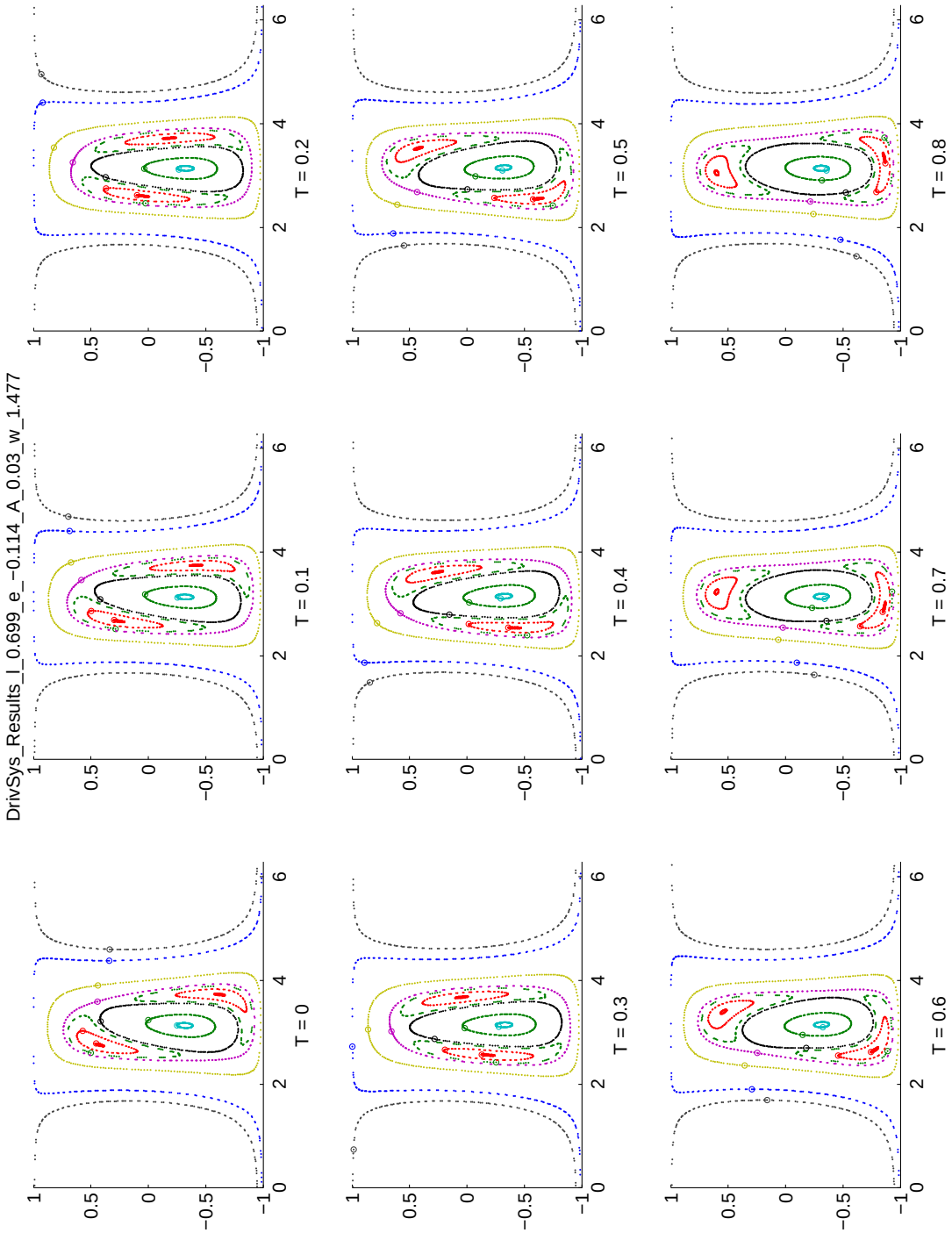

Figure B.2.: Poincaré plot for different time offset (or driving phases) $\Lambda = 0.7$, $\epsilon = -0.114$, $A_{\text{Driv}} = 0.03$
The time is given in units of the driving period.

B.3. Time evolution of distributions

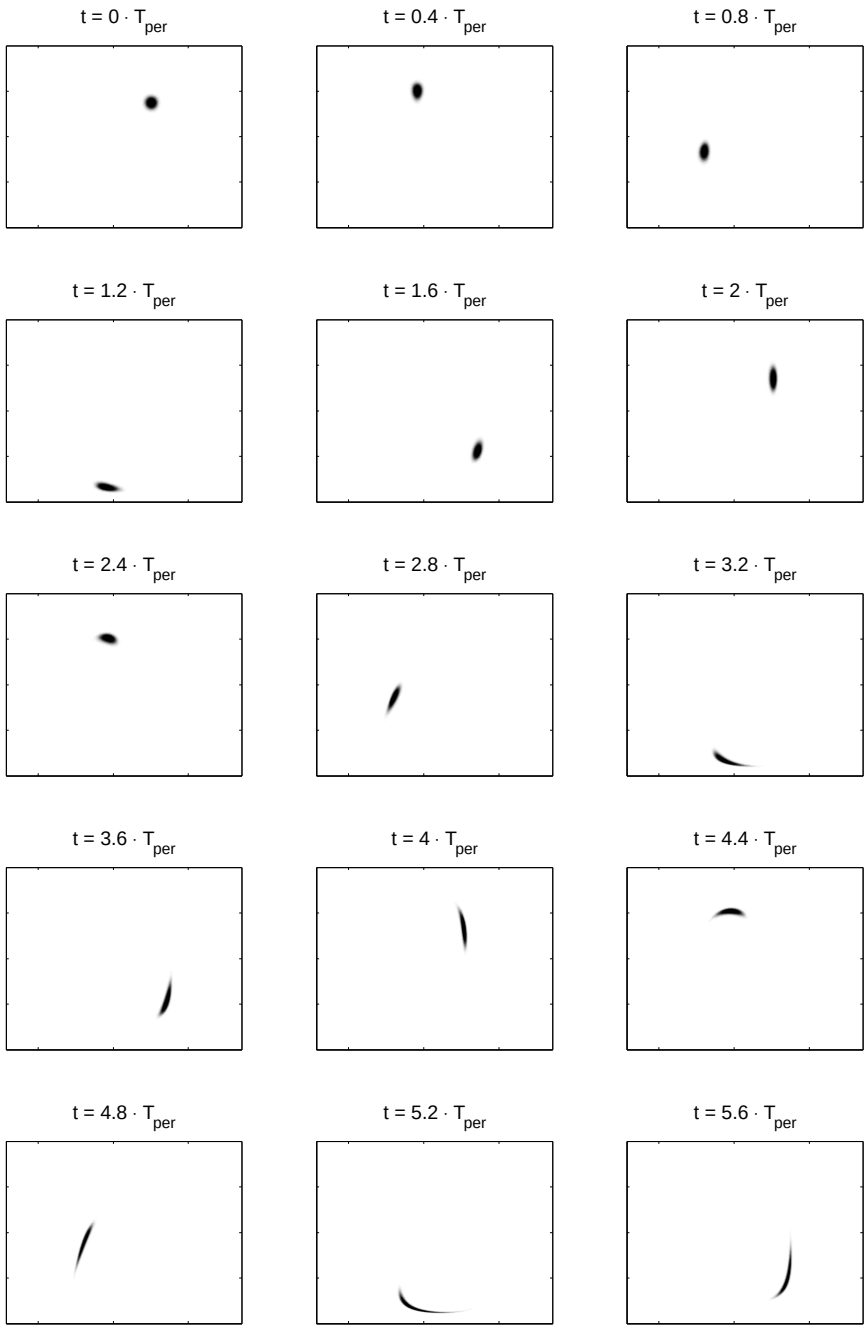

Figure B.3.: Classical simulation of time evolution in the undriven system for $\Lambda = 0.7,\ \epsilon = -0.114$
The time is given in units of the driving period although the system is not driven.

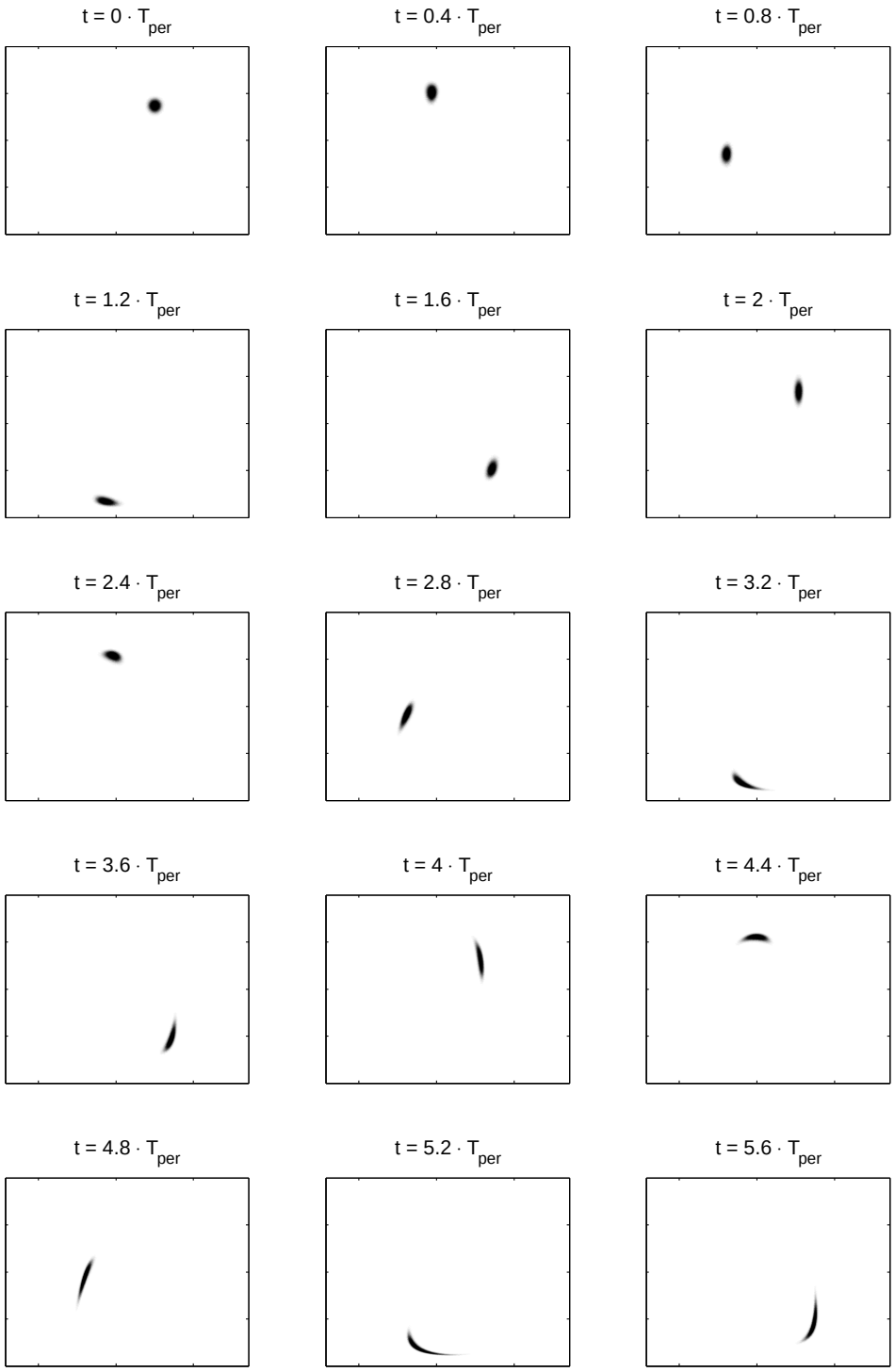

Figure B.4.: Classical simulation of time evolution in the driven system for an initial preparation in the vicinity of the stable fixed point with $\Lambda = 0.7,\ \epsilon = -0.114, A_{\mathrm{Driv}} = 0.03,\ \omega_{\mathrm{Driv}} = 1.477,\ \varphi_{\mathrm{Driv}} = \pi$, preparation at $z_0 = 0.37,\ \varphi_0 = 3.50$ (unstable fixed point for $\varphi_{\mathrm{Driv}} = 0$) The time is given in units of the driving period.

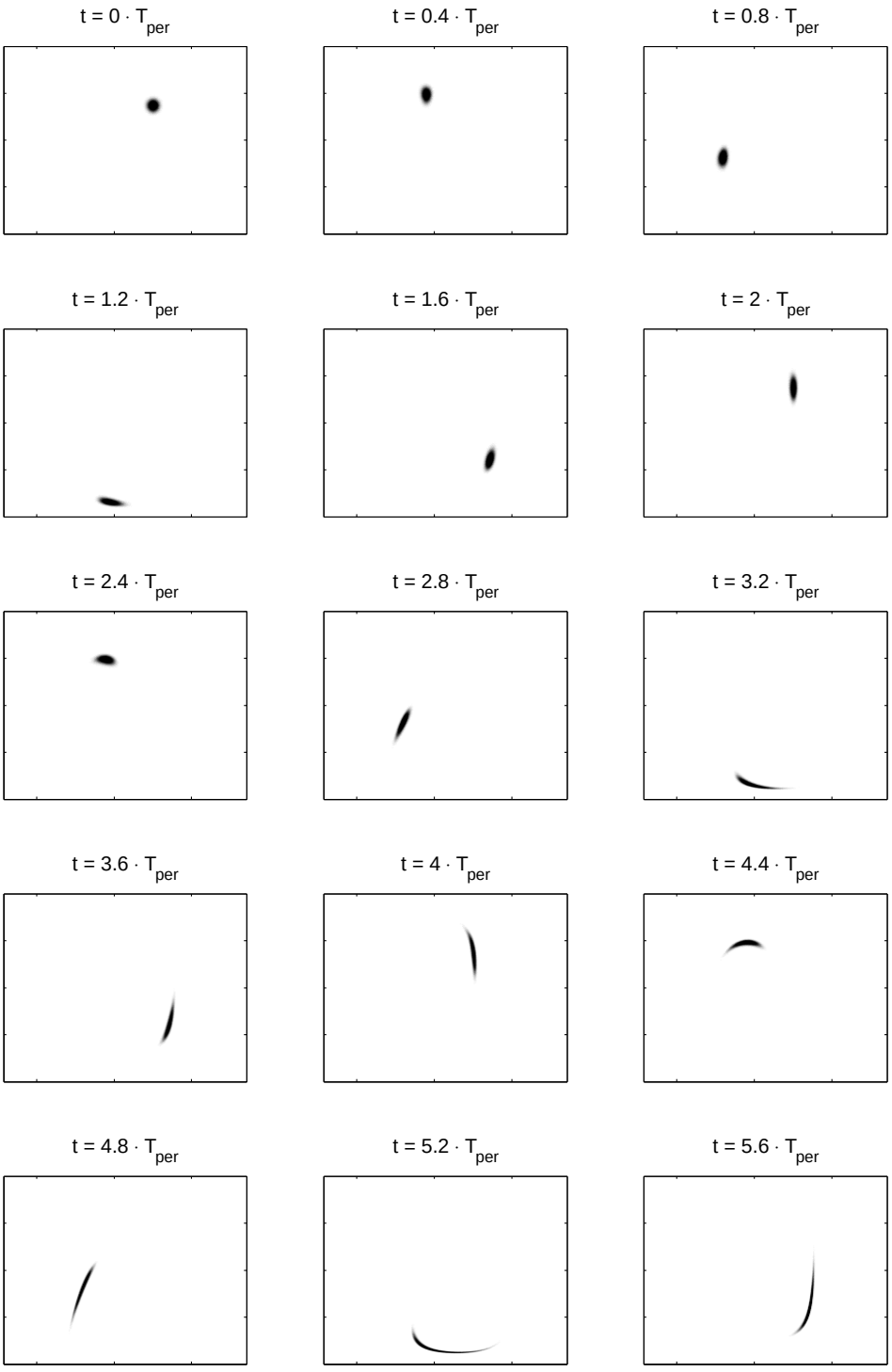

Figure B.5.: Classical simulation of time evolution in the driven system for the unstable fixed point with $\Lambda = 0.7$, $\epsilon = -0.114, A_{\text{Driv}} = 0.03$, $\omega_{\text{Driv}} = 1.477$, $\varphi_{\text{Driv}} = 0$, preparation at $z_0 = 0.37$, $\varphi_0 = 3.50$ The time is given in units of the driving period.

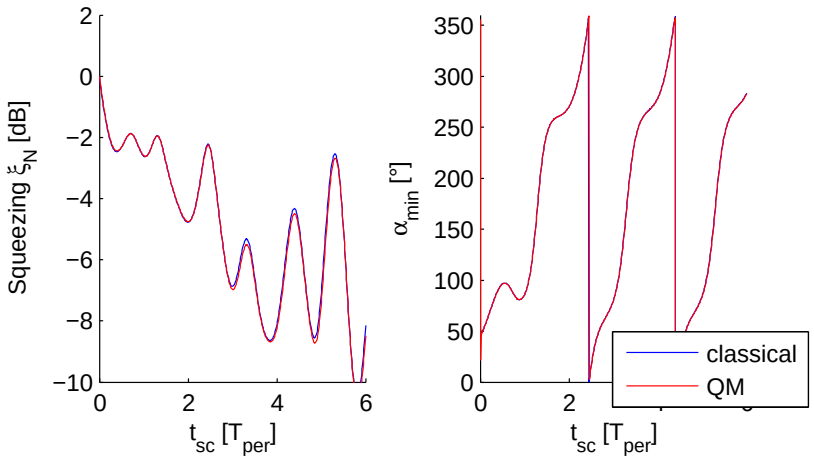

Figure B.6.: Squeezing of a distribution in the undriven system for $\Lambda = 0.7$, $\epsilon = -0.114$, $z_0 = 0.37$, $\varphi_0 = 3.50$.
Even in the regular system in absence of an unstable fixed point, slight squeezing is generated for larger times due to anharmonicity of the system. right: angle of the short axis of the distribution.

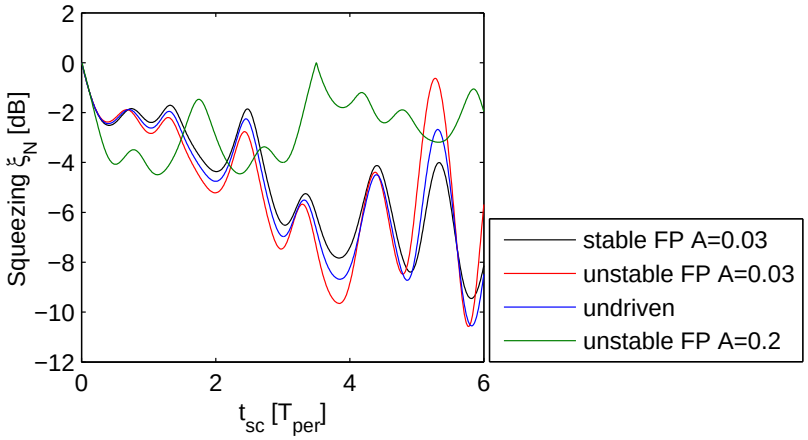

Figure B.7.: Comparison of number squeezing in the driven system for different preparation to the undriven system (QM simulation).
For weak driven system ($A_{\mathrm{Driv}} = 0.03$) the unstable fixed point preparation is a bit faster and deeper squeezed than the undriven one, in contrast to the dynamics at the stable fixed point which is less squeezed. Contrary, the dynamics is faster and more squeezed at the unstable fixed point in the strong driven regime.

B.4. Time evolution in the bifurcated regime

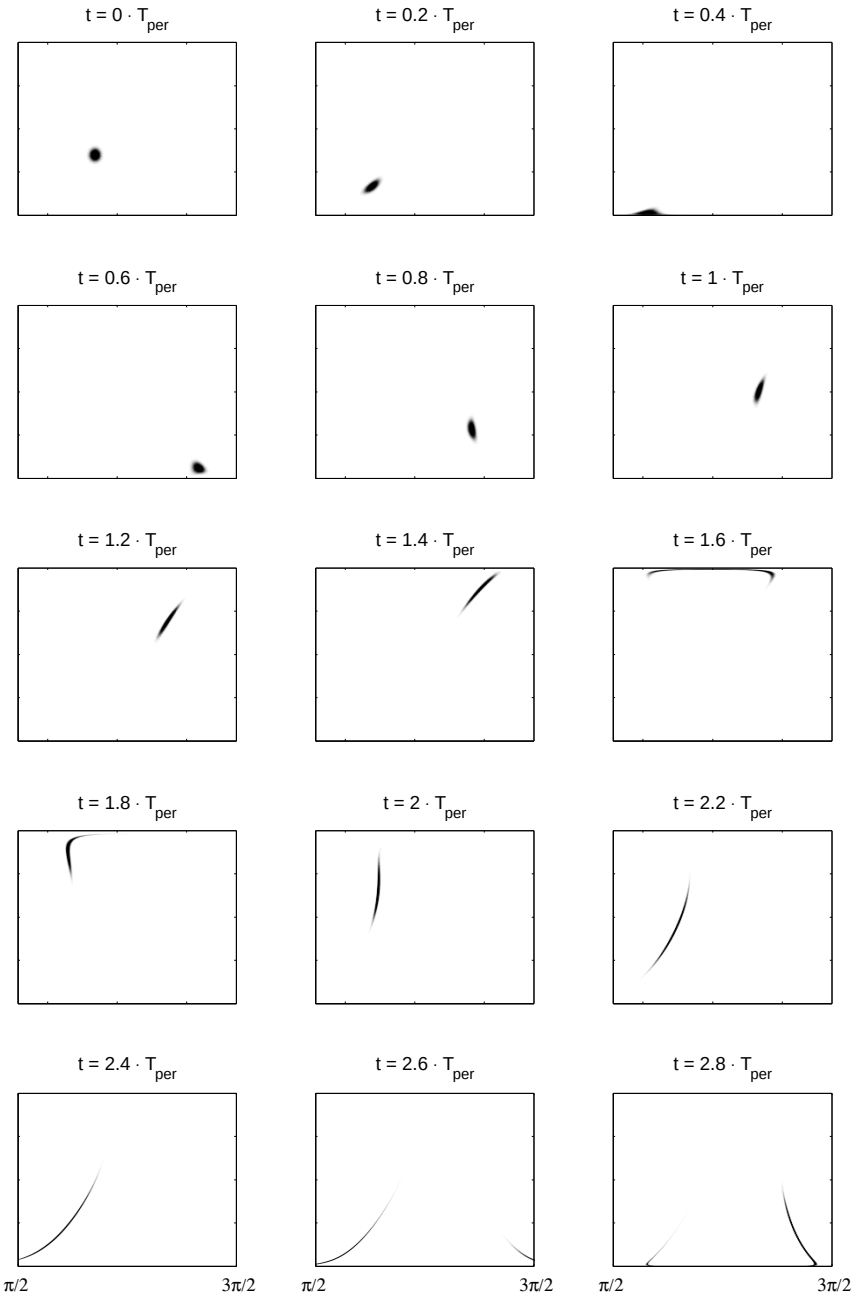

Figure B.8.: Classical simulation of time evolution in the driven system for $\Lambda = 1.53$, $\epsilon = -0.07$, $A_{\text{Driv}} = 0.07$ prepared close to the stable moving island.
The time is given in units of the driving period.

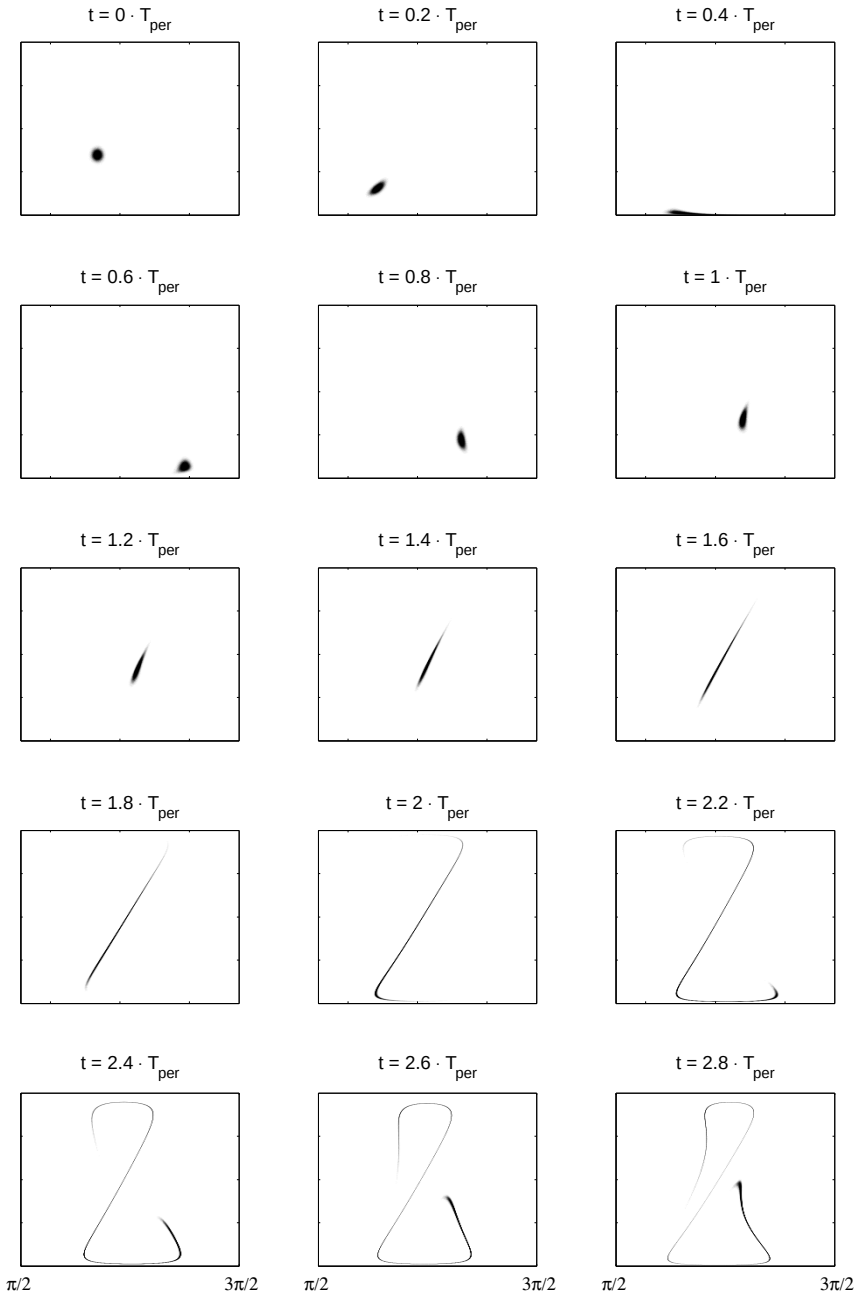

Figure B.9.: Classical simulation of time evolution in the driven system for $\Lambda = 1.53,\ \epsilon = -0.07,\ A_{\text{Driv}} = 0.07$ prepared close to the unstable period 2 orbit.
The time is given in units of the driving period.

C. Raw-data

C.1. Raw-data for measurements at $\Lambda = 0.7$

C.1.1. Reference measurement of the undriven phase space

$$\begin{aligned} \Omega &= 40.6\ Hz\ (*2\pi) \\ \epsilon_{\text{set}} &= -0.1 \\ \epsilon_{\text{fit}} &= -0.114 \end{aligned}$$

Start points:

		set	from fit
z_0	=	0.48	0.41
φ_0	=	π	3.21

Loss compensation

$$\begin{aligned} \tau_{Loss} &= 2 \cdot 86\ ms \\ A_{Loss} &= 21.6\ Hz \end{aligned}$$

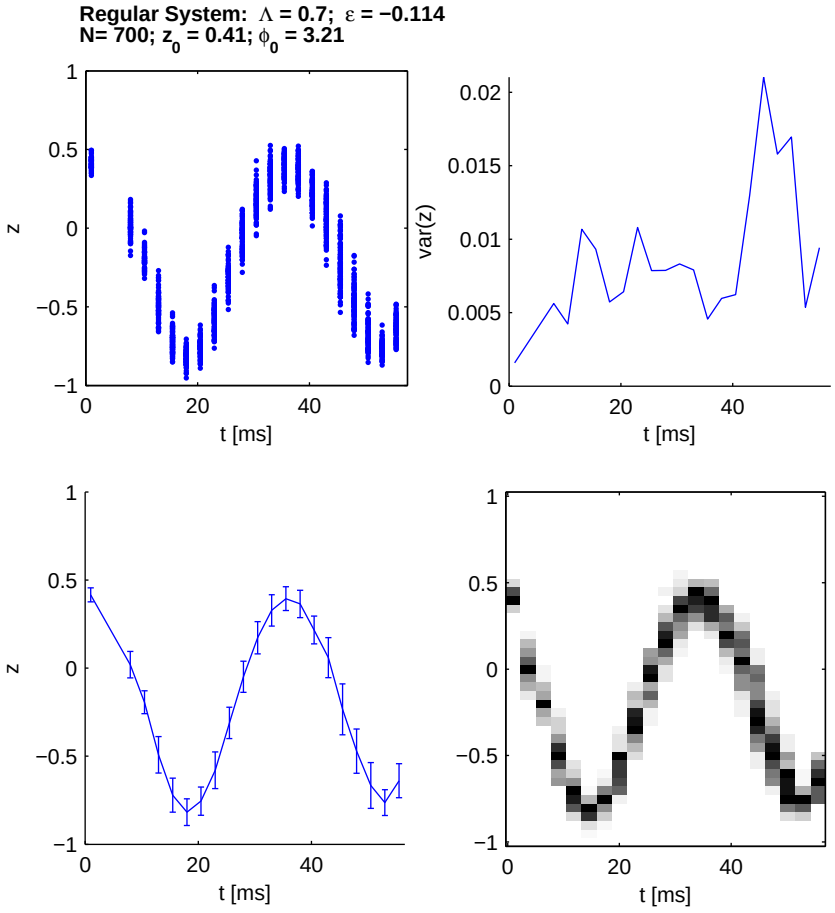

upper left: raw data, each point is one measurement, selected for an atom number of $N = 700$, loss included, outliers removed.
upper right: time evolution of variances
lower left: time evolution of mean including standard-variation as error-bars
lower right: histograms for raw-data. The histogram for each time step is normalized to the maxima.

Next figure: Fit to experimental data including variances for range of atomnumbers from $N = 500$ to $N = 800$.

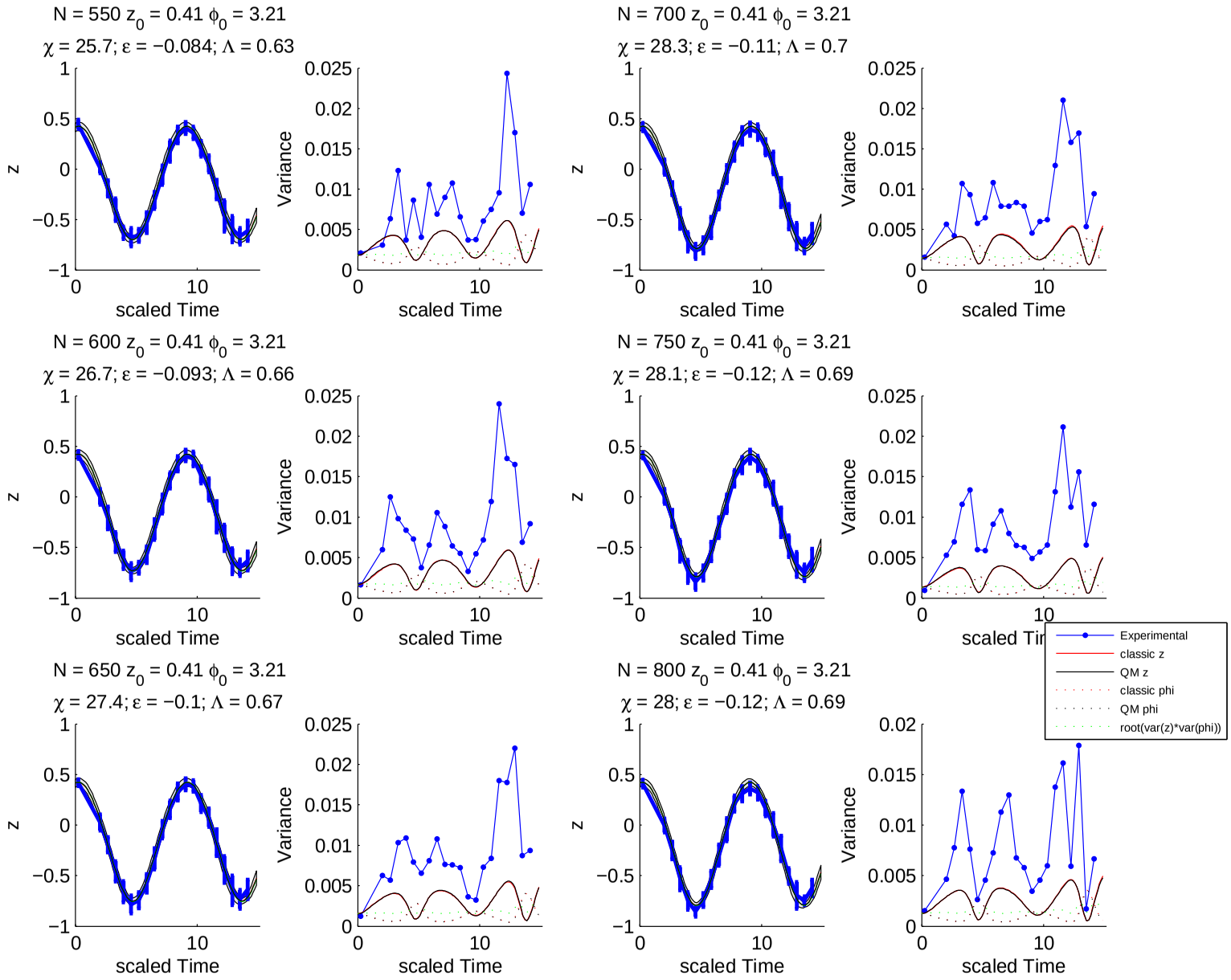
N = 550 z0 = 0.41 ϕ0 = 3.21
χ = 25.7; ε = −0.084; Λ = 0.63
N = 700 z0 = 0.41 ϕ0 = 3.21
χ = 28.3; ε = −0.11; Λ = 0.7
N = 600 z0 = 0.41 ϕ0 = 3.21
χ = 26.7; ε = −0.093; Λ = 0.66
N = 750 z0 = 0.41 ϕ0 = 3.21
χ = 28.1; ε = −0.12; Λ = 0.69
N = 650 z0 = 0.41 ϕ0 = 3.21
χ = 27.4; ε = −0.1; Λ = 0.67
N = 800 z0 = 0.41 ϕ0 = 3.21
χ = 28; ε = −0.12; Λ = 0.69
z
Variance
scaled Time
Experimental
classic z
QM z
classic phi
QM phi
root(var(z)*var(phi))

C.1.2. Small driving amplitude $A = 0.03$

$$\begin{aligned} \Omega &= 40.6\ Hz\ (*2\pi) \\ \epsilon_{\text{set}} &= -0.1 \\ \epsilon_{\text{fit}} &= -0.114 \end{aligned}$$

Driving:

$$\begin{aligned} A_{\text{Driv}} &= 0.03 \\ \omega_{\text{Driv}} &= 59.9\ Hz \\ \omega_{\text{Driv}}^{scaled} &= 1.47 \\ \varphi_{\text{Driv}} &= [0\ \pi/5\ 2/5\pi\ 3/5\pi\ 4/5\pi\ \pi 6/5\pi\ 7/5\pi/8/5\pi\ 9/5\pi] \end{aligned}$$

Start points:

		set	from fit
z_0	=	0.48	0.41
φ_0	=	π	3.21

Loss compensation

$$\begin{aligned} \tau_{Loss} &= 2 \cdot 86\ ms \\ A_{Loss} &= 21.6\ Hz \end{aligned}$$

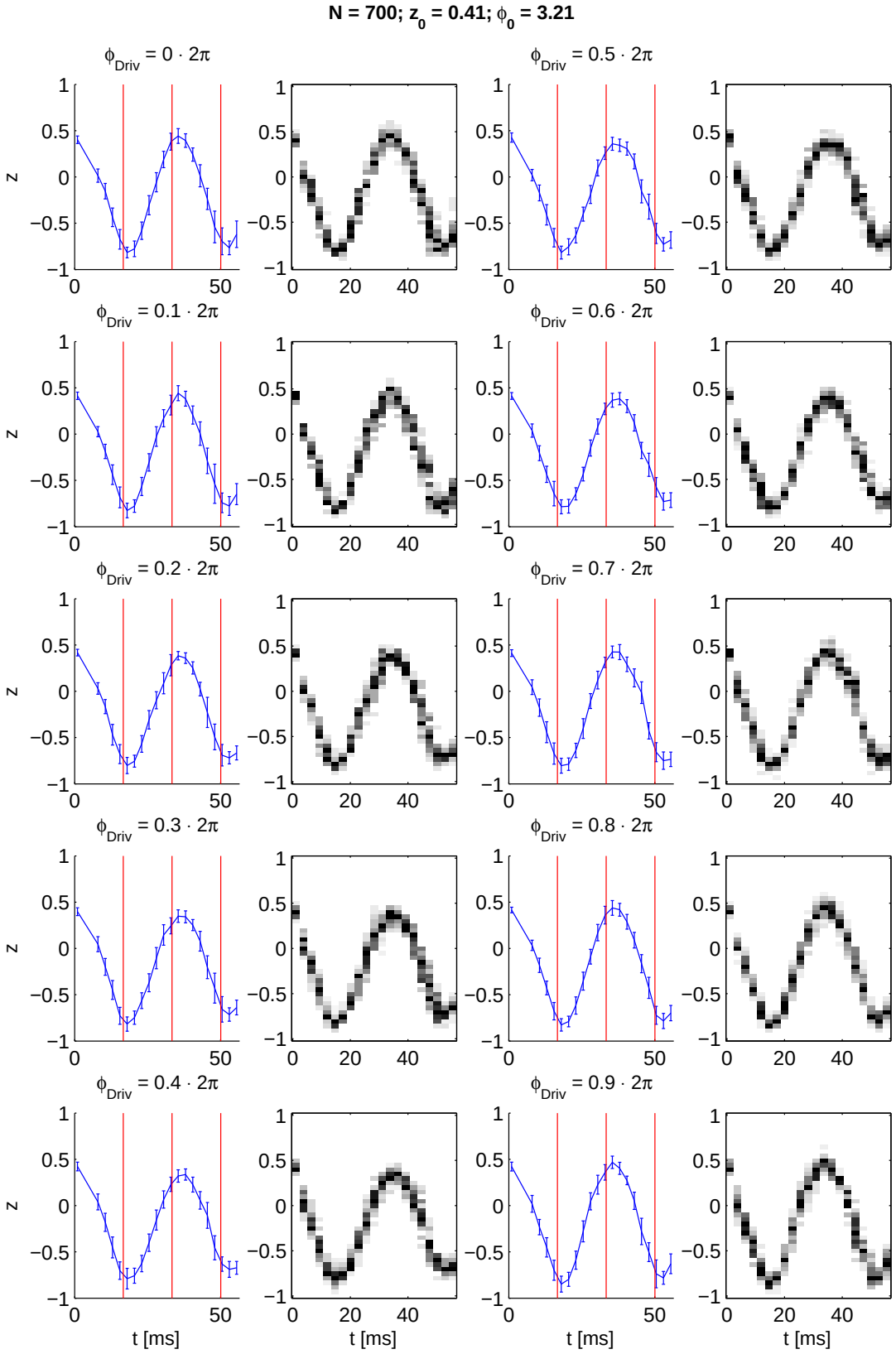
N = 700; z0 = 0.41; ϕ0 = 3.21
ϕDriv = 0 · 2π
ϕDriv = 0.5 · 2π
ϕDriv = 0.1 · 2π
ϕDriv = 0.6 · 2π
ϕDriv = 0.2 · 2π
ϕDriv = 0.7 · 2π
ϕDriv = 0.3 · 2π
ϕDriv = 0.8 · 2π
ϕDriv = 0.4 · 2π
ϕDriv = 0.9 · 2π
z
t [ms]

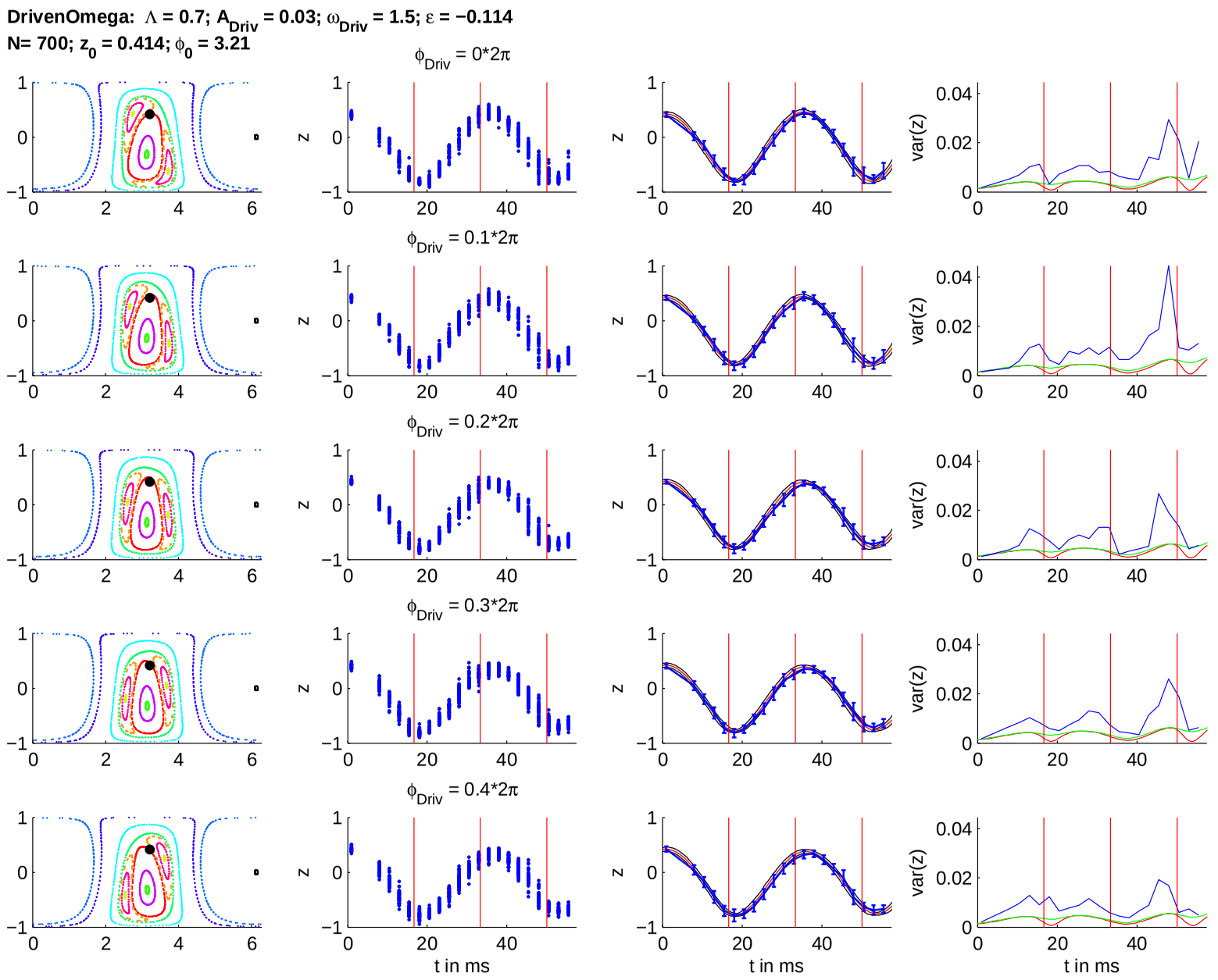
DrivenOmega: Λ = 0.7; A_Driv = 0.03; ω_Driv = 1.5; ε = −0.114
N= 700; z_0 = 0.414; φ_0 = 3.21
φ_Driv = 0*2π
φ_Driv = 0.1*2π
φ_Driv = 0.2*2π
φ_Driv = 0.3*2π
φ_Driv = 0.4*2π
z
var(z)
t in ms

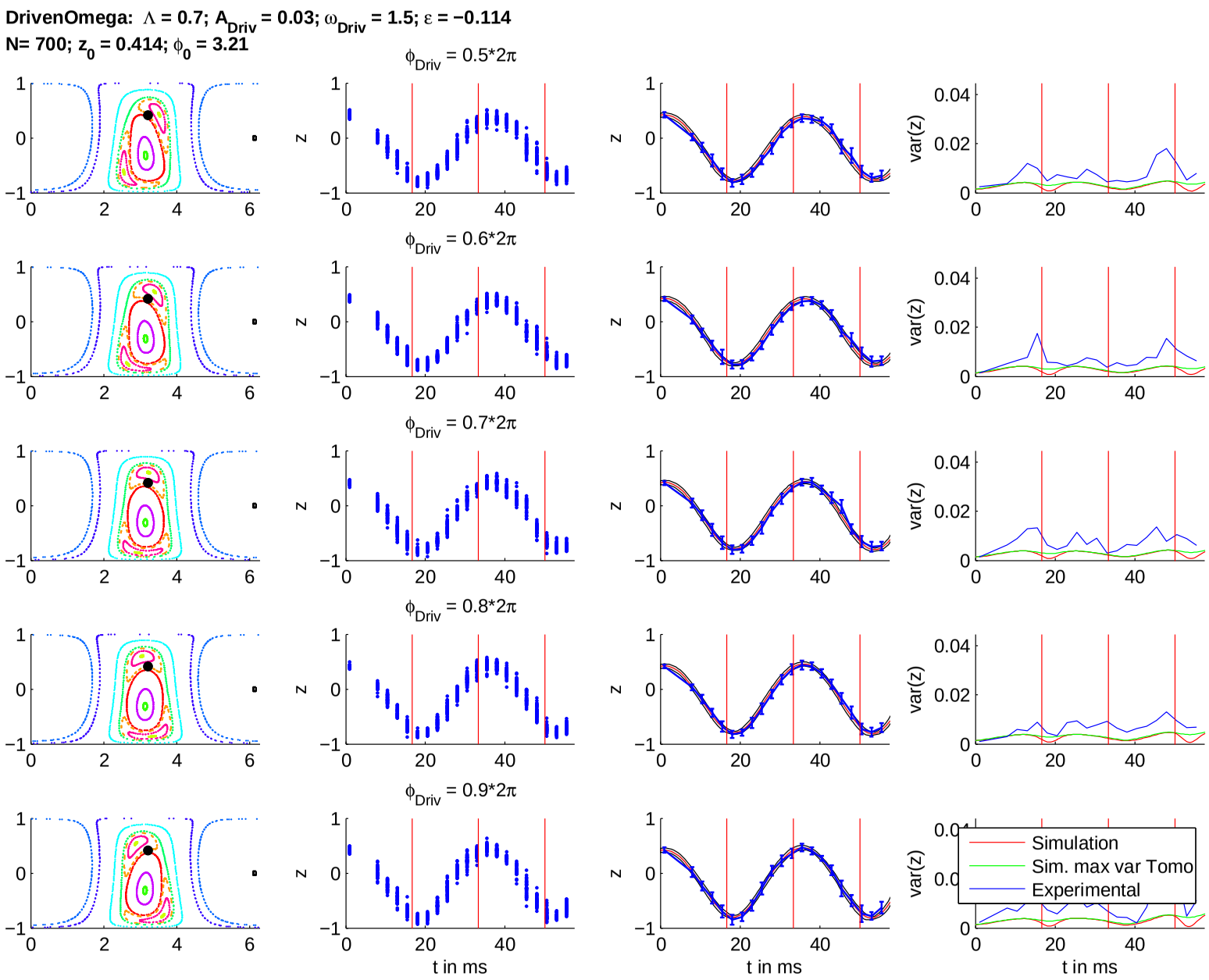
DrivenOmega: Λ = 0.7; A_Driv = 0.03; ω_Driv = 1.5; ε = −0.114
N= 700; z_0 = 0.414; ϕ_0 = 3.21
ϕ_Driv = 0.5*2π
ϕ_Driv = 0.6*2π
ϕ_Driv = 0.7*2π
ϕ_Driv = 0.8*2π
ϕ_Driv = 0.9*2π
z
var(z)
t in ms
Simulation
Sim. max var Tomo
Experimental

C.1.3. Median driving amplitude $A = 0.2$

$$\begin{aligned} \Omega &= 40.6\ Hz\ (*2\pi) \\ \epsilon_{\text{set}} &= -0.1 \\ \epsilon_{\text{fit}} &= -0.114 \end{aligned}$$

Driving:

$$\begin{aligned} A_{\text{Driv}} &= 0.2 \\ \omega_{\text{Driv}} &= 59.9\ Hz \\ \omega_{\text{Driv}}^{scaled} &= 1.47 \\ \varphi_{\text{Driv}} &= [0\ \pi/5\ 2/5\pi\ 3/5\pi\ 4/5\pi\ \pi 6/5\pi\ 7/5\pi/8/5\pi\ 9/5\pi] \end{aligned}$$

Start points:

		set	from fit
z_0	=	0.55	0.5
φ_0	=	π	3.21

Loss compensation

$$\begin{aligned} \tau_{Loss} &= 2 \cdot 86\ ms \\ A_{Loss} &= 21.6\ Hz \end{aligned}$$

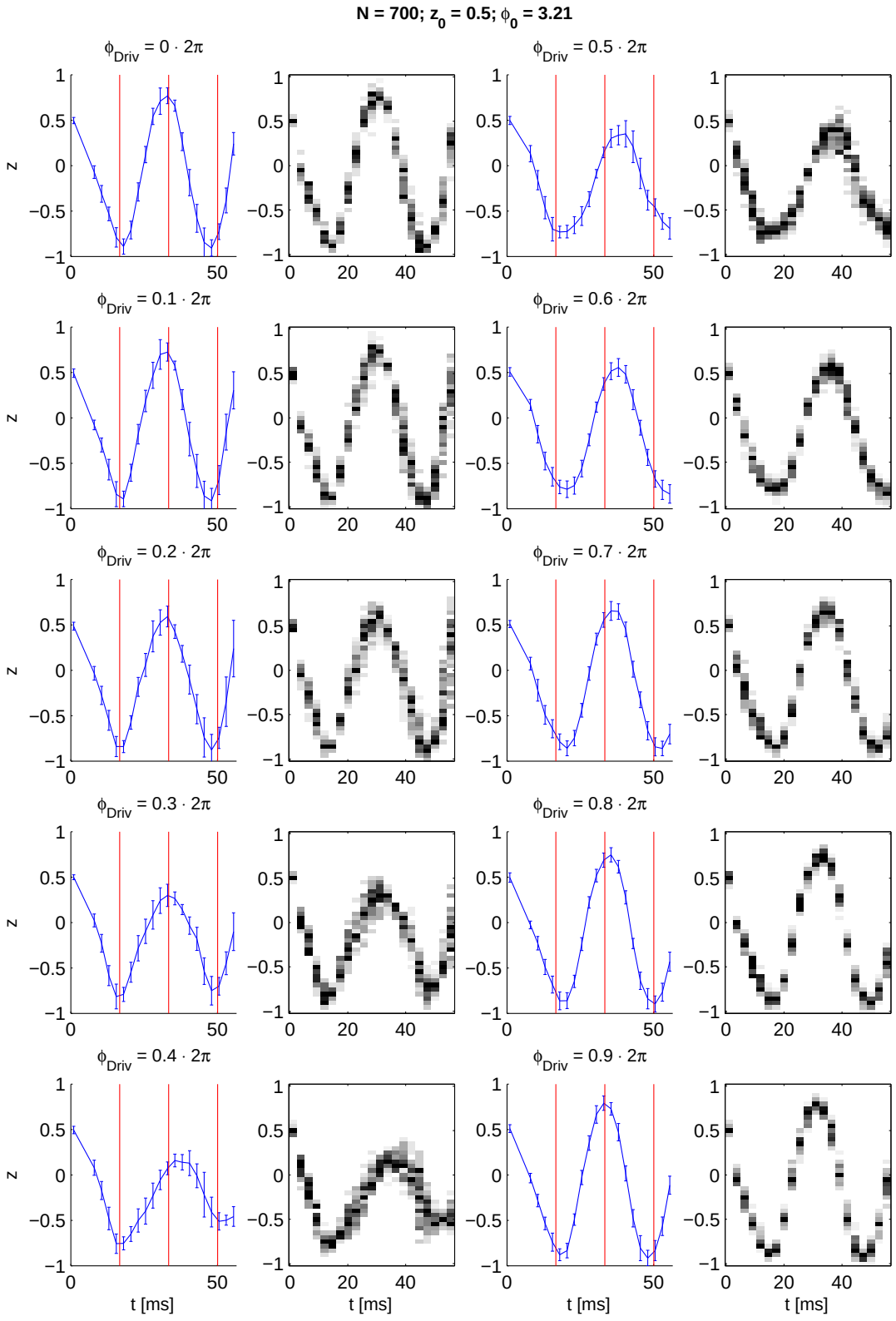
N = 700; z0 = 0.5; ϕ0 = 3.21
ϕDriv = 0 · 2π
ϕDriv = 0.5 · 2π
ϕDriv = 0.1 · 2π
ϕDriv = 0.6 · 2π
ϕDriv = 0.2 · 2π
ϕDriv = 0.7 · 2π
ϕDriv = 0.3 · 2π
ϕDriv = 0.8 · 2π
ϕDriv = 0.4 · 2π
ϕDriv = 0.9 · 2π
z
t [ms]

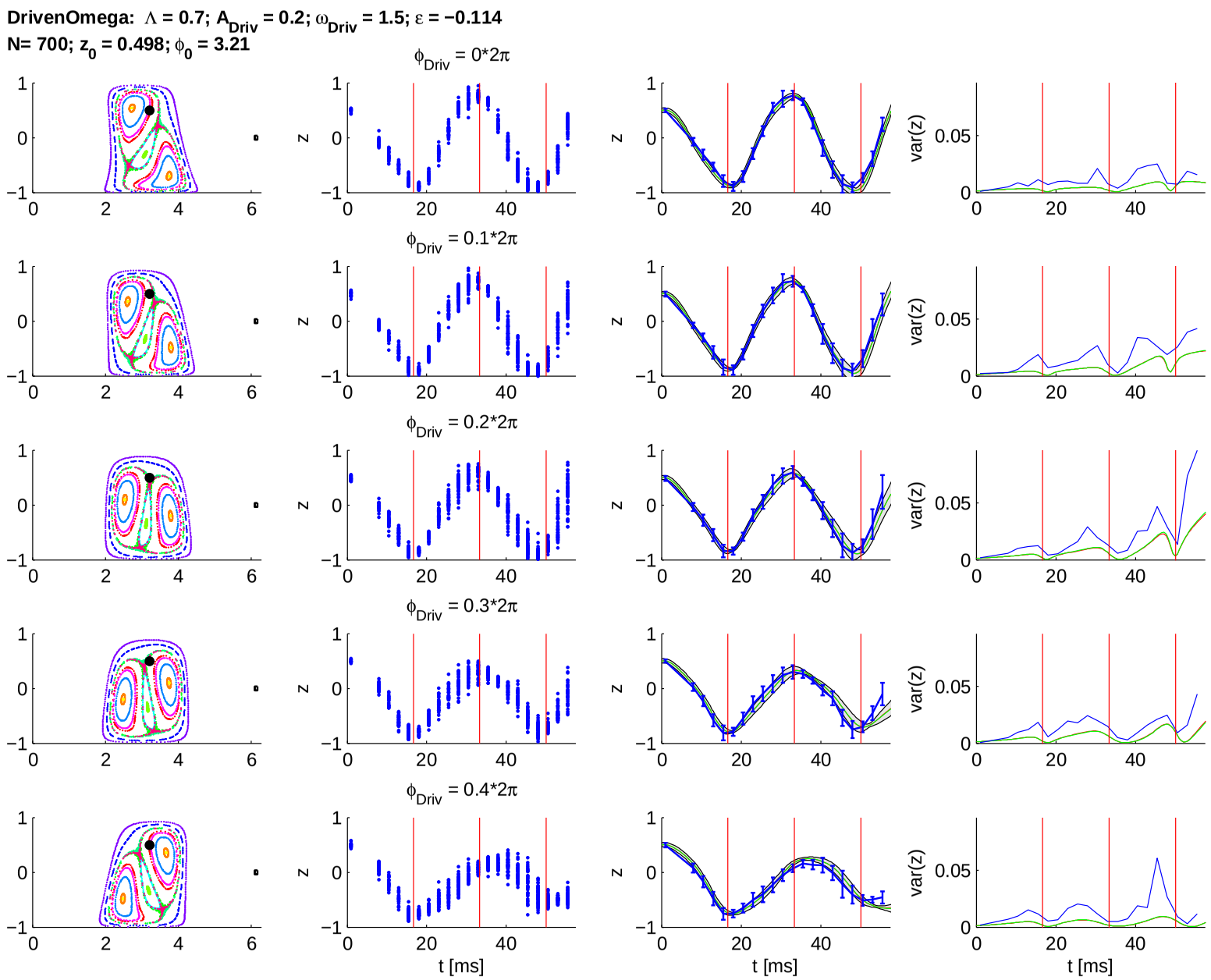
DrivenOmega: Λ = 0.7; A_Driv = 0.2; ω_Driv = 1.5; ε = −0.114
N= 700; z_0 = 0.498; φ_0 = 3.21
φ_Driv = 0*2π
φ_Driv = 0.1*2π
φ_Driv = 0.2*2π
φ_Driv = 0.3*2π
φ_Driv = 0.4*2π
z
var(z)
t [ms]

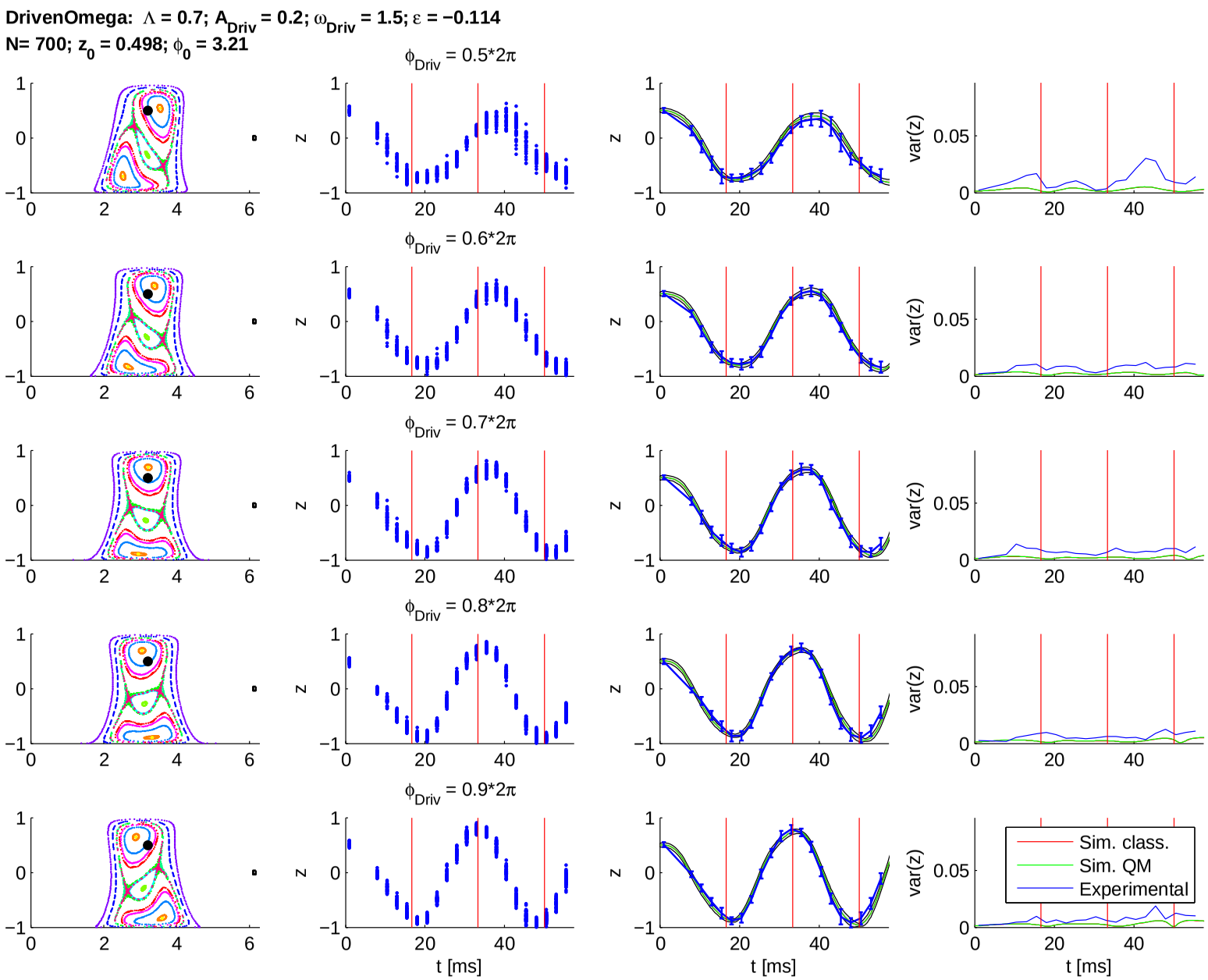
DrivenOmega: Λ = 0.7; A_Driv = 0.2; ω_Driv = 1.5; ε = −0.114
N= 700; z_0 = 0.498; ϕ_0 = 3.21
ϕ_Driv = 0.5*2π
ϕ_Driv = 0.6*2π
ϕ_Driv = 0.7*2π
ϕ_Driv = 0.8*2π
ϕ_Driv = 0.9*2π
z
var(z)
t [ms]
Sim. class.
Sim. QM
Experimental

C.2. Raw-data for measurements at $\Lambda = 1.5$

C.2.1. Reference measurement of the undriven phase space

For a reference measurement, the time evolution for the preparation at different points in phase space is obtained for an undriven system with loss compensation. In addition to the measurement in z also the phase information is obtained by a subsequent tomography pulse (after the time evolution) with $-\pi/2$ around the x axis. Due to too high atom numbers within this experimental run, only few wells were within the desired atom filter.

Parameters:

$$\begin{aligned} \Omega &= 20.7\,Hz\,(*2\pi) \\ \epsilon_{\text{set}} &= -0.1 \\ \epsilon_{\text{fit}} &= -0.07 \end{aligned}$$

Start points:

z_{set}	0	-0.92	-0.61	-0.33	-0.60	0	0.65
z_{fit}	-0.30	-0.87	-0.46	-0.52	-0.68	0.15	0.50
φ_{set}	2.51	3.40	3.96	3.27	3.25	π	π
φ_{fit}	2.68	3.24	3.80	3.32	3.19	3.16	3.34

Loss compensation

$$\begin{aligned} \tau_{Loss} &= 2 \cdot 86\,ms \\ A_{Loss} &= 21.6\,Hz \end{aligned}$$

In the following we plot two graphs for each starting condition (per row): the measured mean with standard deviation as errorbar in z in first column, a histogram vs. time in the second and the same for the phase data (with tomography pulse) in the last two columns. The next graphs shows per line the phase space, the measured points vs time, the mean together with a simulation (the standard deviation is plotted as a gray band) and the variances. In the subsequent line the same is plotted for the tomography data.

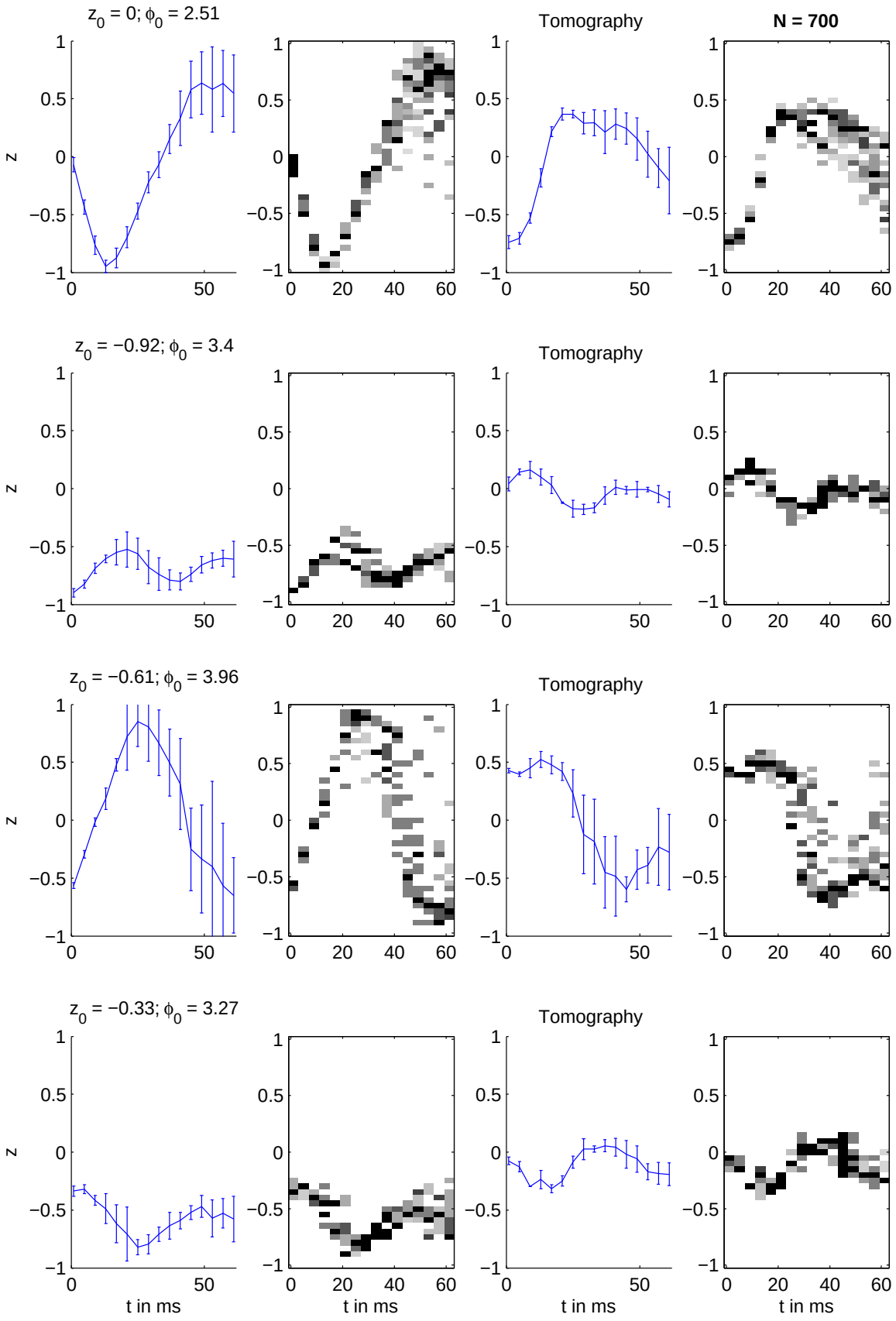
$z_0 = 0; \phi_0 = 2.51$
Tomography
N = 700
$z_0 = -0.92; \phi_0 = 3.4$
Tomography
$z_0 = -0.61; \phi_0 = 3.96$
Tomography
$z_0 = -0.33; \phi_0 = 3.27$
Tomography
z
t in ms

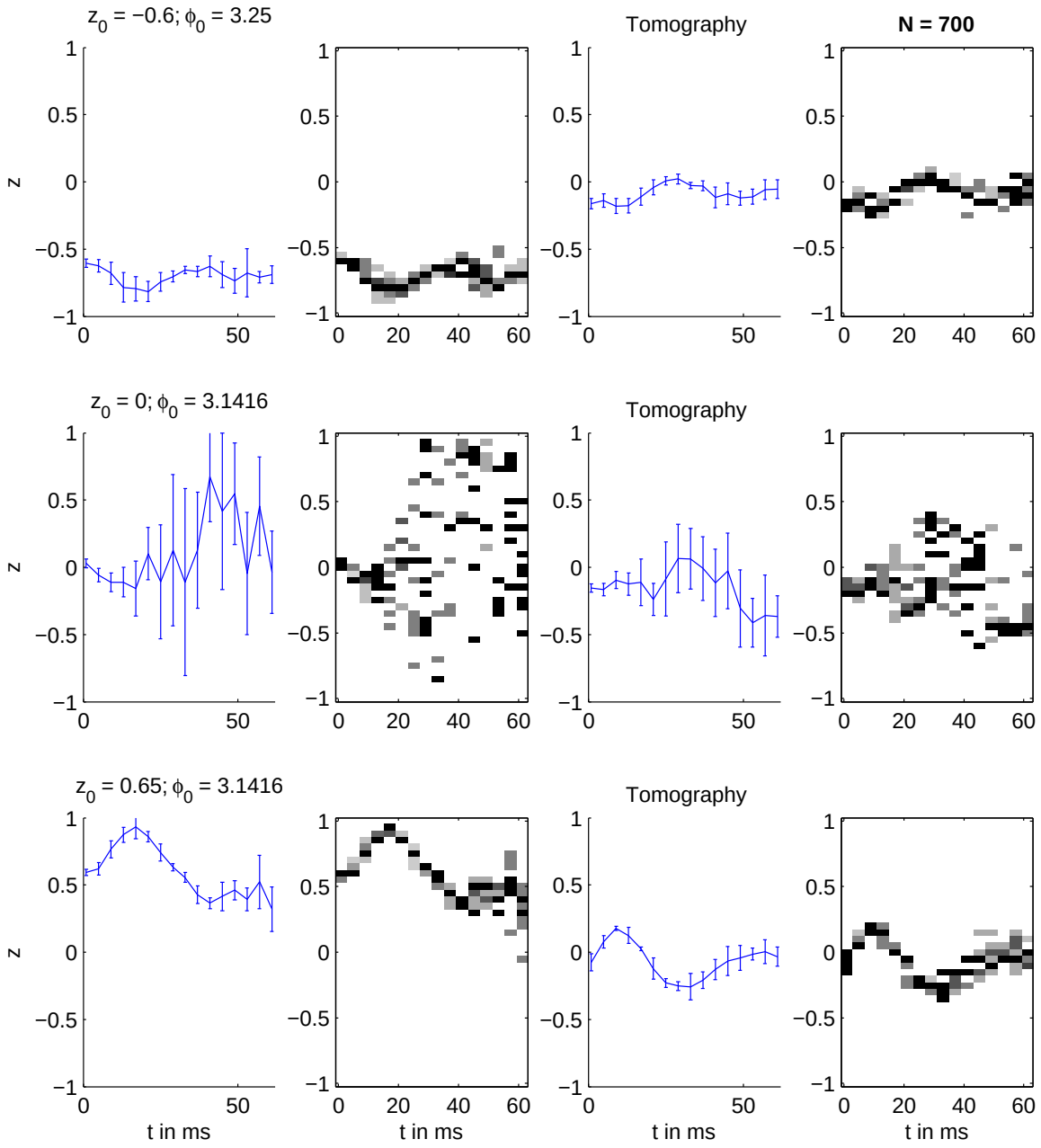
$z_0 = -0.6; \phi_0 = 3.25$
Tomography
N = 700
$z_0 = 0; \phi_0 = 3.1416$
Tomography
$z_0 = 0.65; \phi_0 = 3.1416$
Tomography
z
t in ms

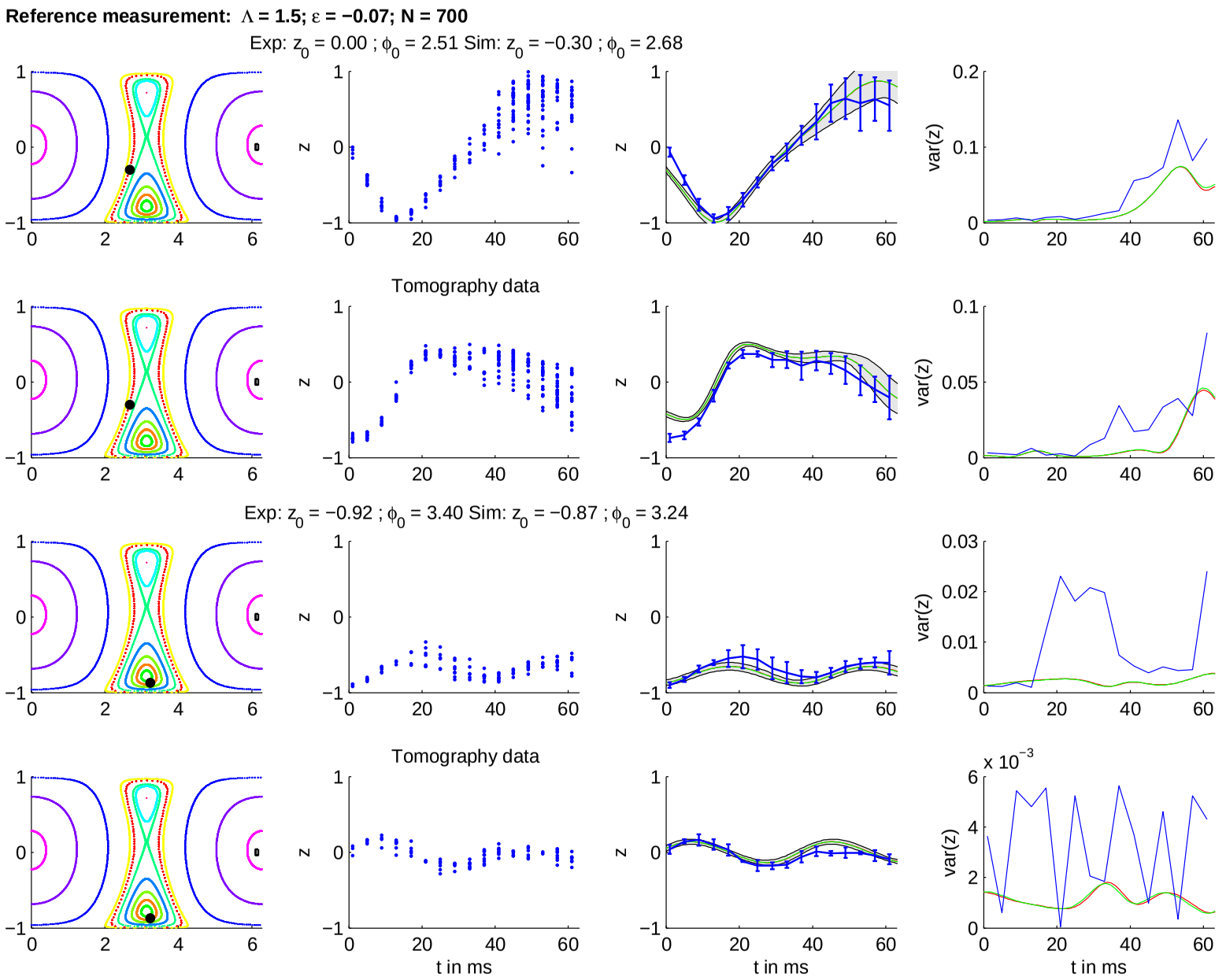
Reference measurement: Λ = 1.5; ε = −0.07; N = 700
Exp: z0 = 0.00 ; ϕ0 = 2.51 Sim: z0 = −0.30 ; ϕ0 = 2.68
Tomography data
Exp: z0 = −0.92 ; ϕ0 = 3.40 Sim: z0 = −0.87 ; ϕ0 = 3.24
Tomography data
z
var(z)
x 10−3
t in ms

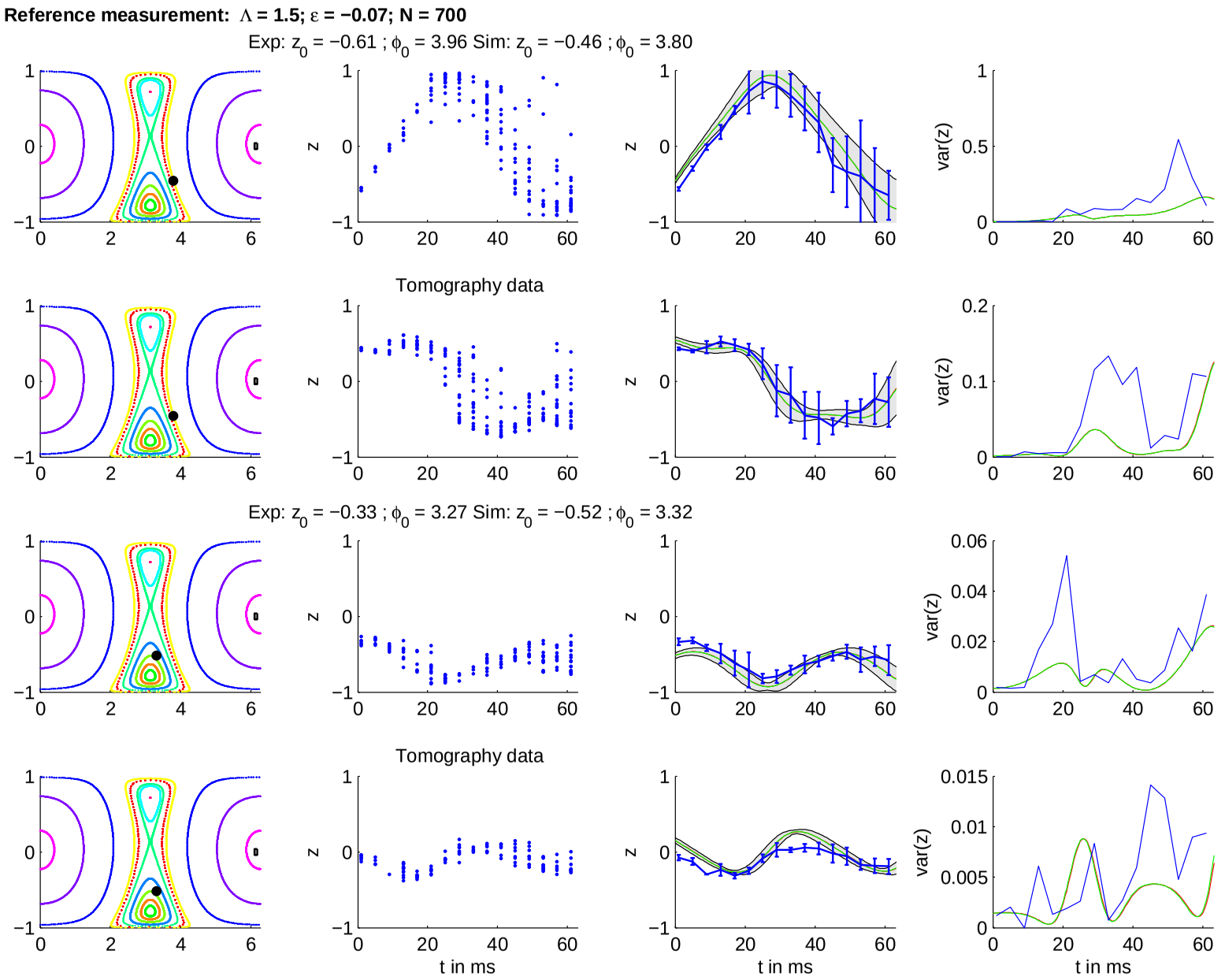
Reference measurement: Λ = 1.5; ε = −0.07; N = 700
Exp: z0 = −0.61 ; ϕ0 = 3.96 Sim: z0 = −0.46 ; ϕ0 = 3.80
Tomography data
Exp: z0 = −0.33 ; ϕ0 = 3.27 Sim: z0 = −0.52 ; ϕ0 = 3.32
Tomography data
z
var(z)
t in ms

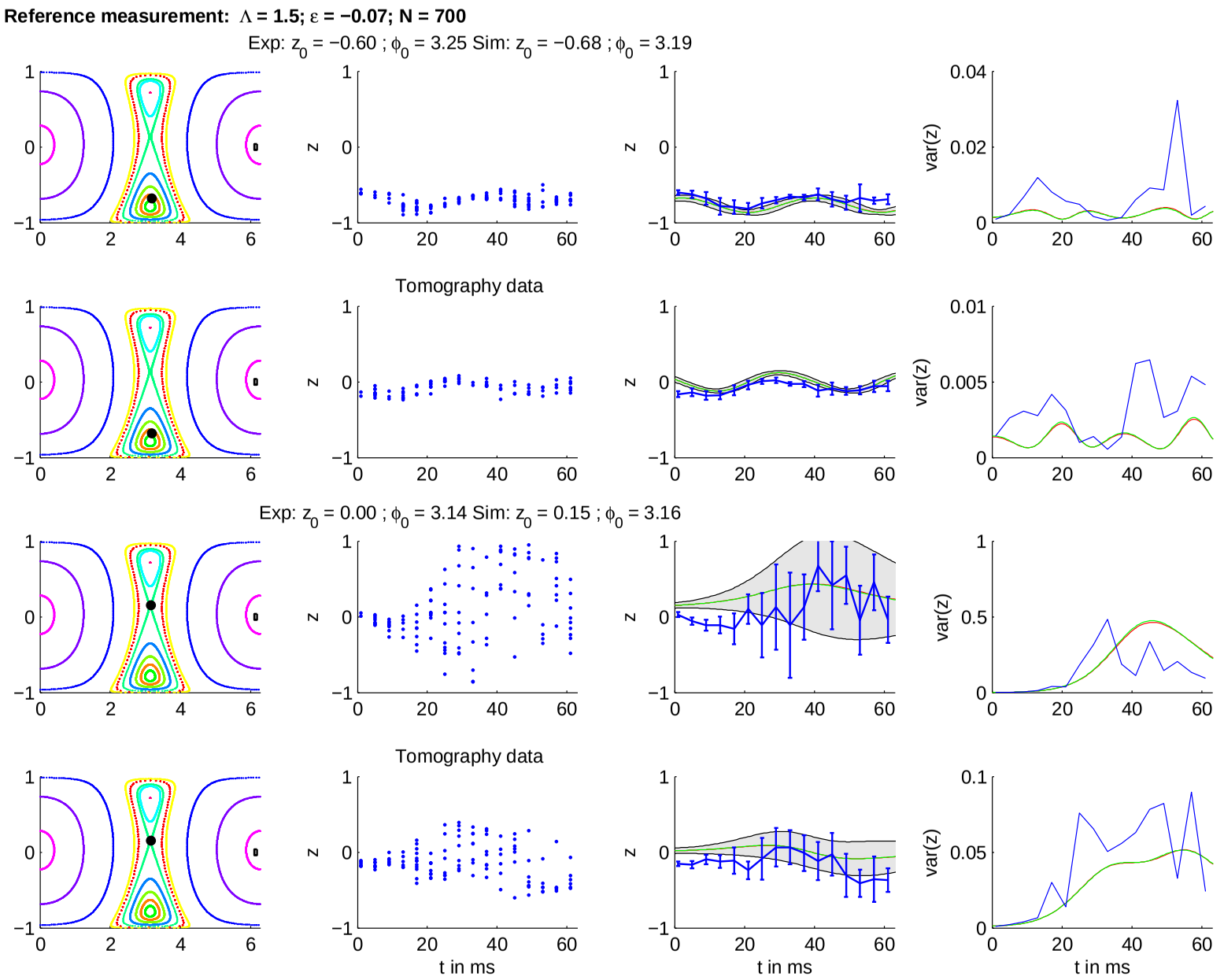
Reference measurement: Λ = 1.5; ε = −0.07; N = 700
Exp: z0 = −0.60 ; ϕ0 = 3.25 Sim: z0 = −0.68 ; ϕ0 = 3.19
Tomography data
Exp: z0 = 0.00 ; ϕ0 = 3.14 Sim: z0 = 0.15 ; ϕ0 = 3.16
Tomography data
z
var(z)
t in ms

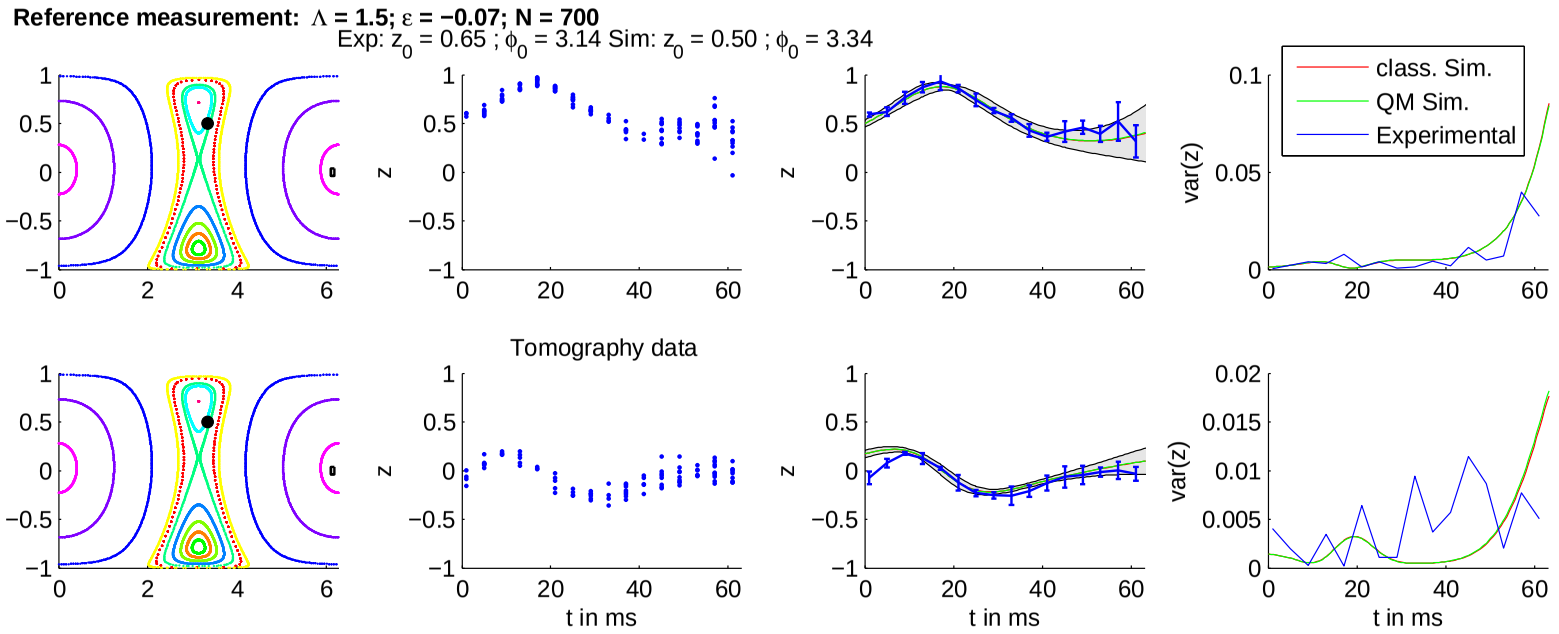
Reference measurement: Λ = 1.5; ε = −0.07; N = 700
Exp: z0 = 0.65 ; ϕ0 = 3.14 Sim: z0 = 0.50 ; ϕ0 = 3.34
Tomography data
class. Sim.
QM Sim.
Experimental
z
var(z)
t in ms

C.2.2. Small driving amplitude $A = 0.035$

Measuring the time evolution of the driven system with small driving amplitude $A_{\mathrm{Driv}} = 0.035$ for a single start point (Exp: $z_0 = 0, \varphi_0 = 2.5$; Fit: $z_0 = -0.3, \varphi_0 = 2.68$) and different driving phases. Due to high atom numbers within this experimental run, the statistics for $N = 700$ atoms is not as well as for other driving amplitudes.

Parameters:

$$\begin{aligned} \Omega &= 20.7\,Hz\,(*2\pi) \\ \epsilon_{\mathrm{set}} &= -0.1 \\ \epsilon_{\mathrm{fit}} &= -0.07 \end{aligned}$$

Driving:

$$\begin{aligned} A_{\mathrm{Driv}} &= 0.035 \\ \omega_{\mathrm{Driv}} &= 33\,Hz \\ \omega^{sc}_{\mathrm{Driv}} &= 1.587 \\ \varphi_{\mathrm{Driv}} &= [0 \quad 0.1 \quad 0.2 \quad 0.3 \quad 0.4 \quad 0.5 \quad 0.6 \quad 0.7 \quad 0.8 \quad 0.9] \cdot 2\pi \end{aligned}$$

Loss compensation

$$\begin{aligned} \tau_{Loss} &= 2 \cdot 86\,ms \\ A_{Loss} &= 21.6\,Hz \end{aligned}$$

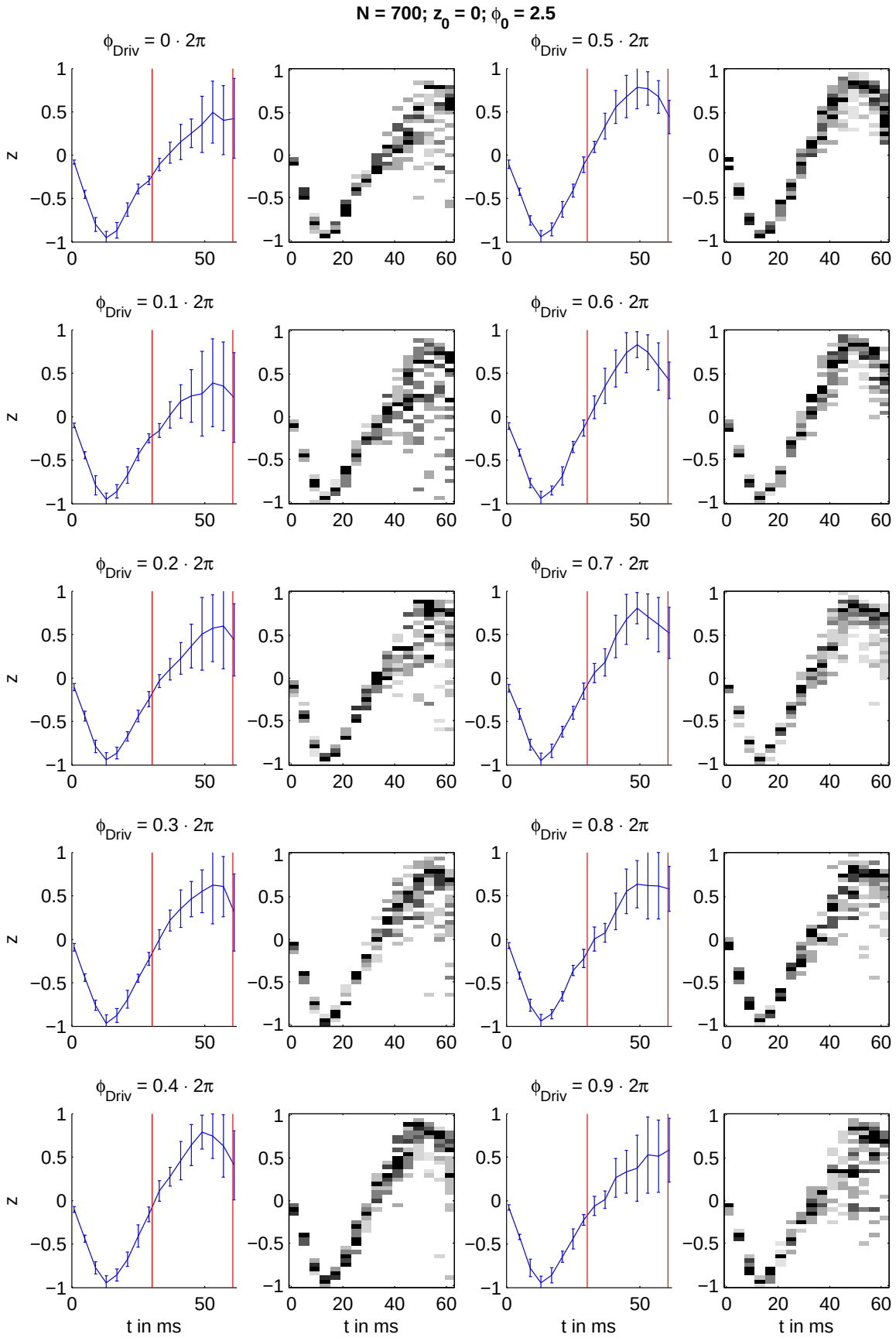
N = 700; z0 = 0; ϕ0 = 2.5
ϕDriv = 0 · 2π
ϕDriv = 0.5 · 2π
ϕDriv = 0.1 · 2π
ϕDriv = 0.6 · 2π
ϕDriv = 0.2 · 2π
ϕDriv = 0.7 · 2π
ϕDriv = 0.3 · 2π
ϕDriv = 0.8 · 2π
ϕDriv = 0.4 · 2π
ϕDriv = 0.9 · 2π
z
t in ms

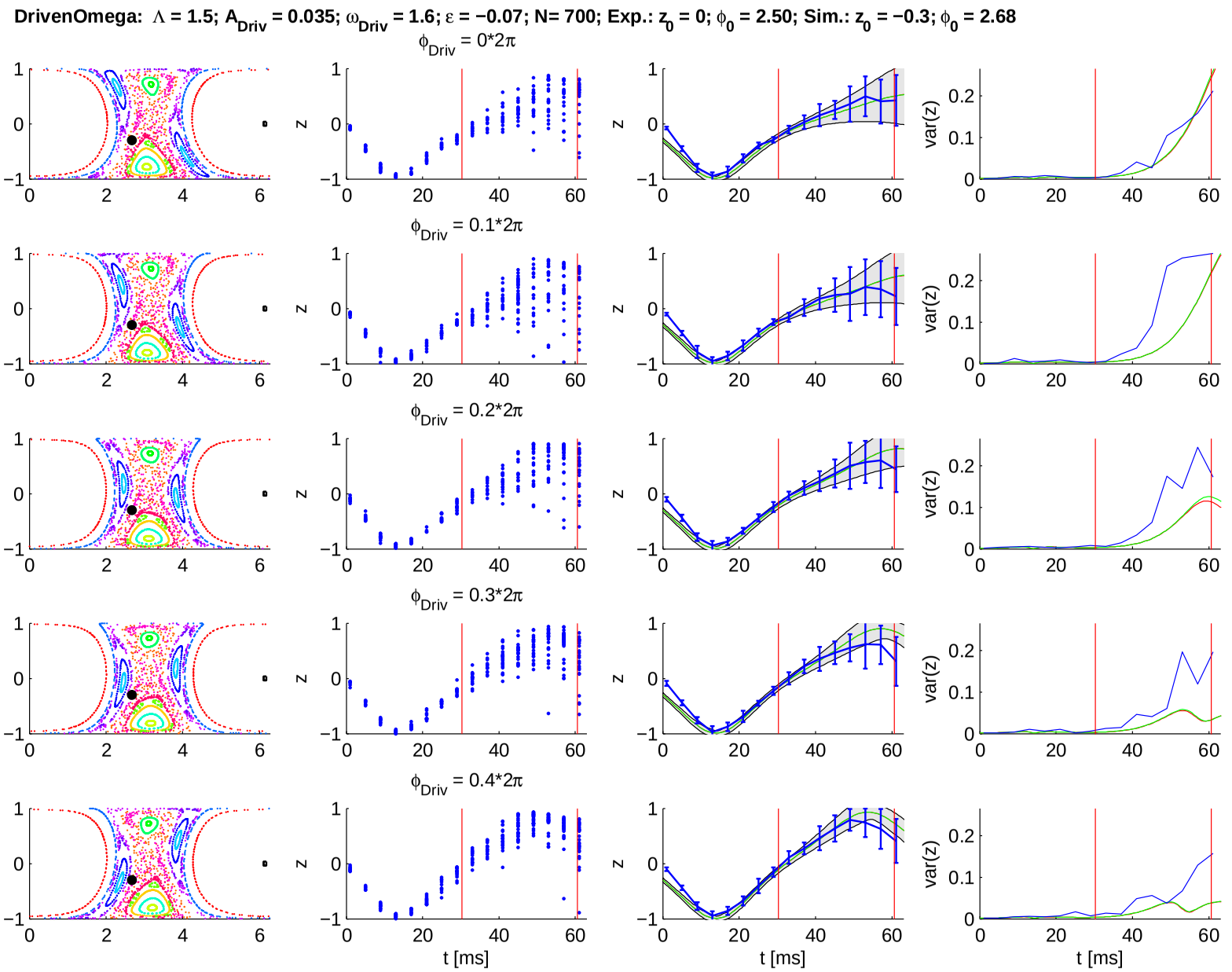
DrivenOmega: Λ = 1.5; A_Driv = 0.035; ω_Driv = 1.6; ε = −0.07; N= 700; Exp.: z_0 = 0; ϕ_0 = 2.50; Sim.: z_0 = −0.3; ϕ_0 = 2.68
ϕ_Driv = 0*2π
ϕ_Driv = 0.1*2π
ϕ_Driv = 0.2*2π
ϕ_Driv = 0.3*2π
ϕ_Driv = 0.4*2π
z
var(z)
t [ms]

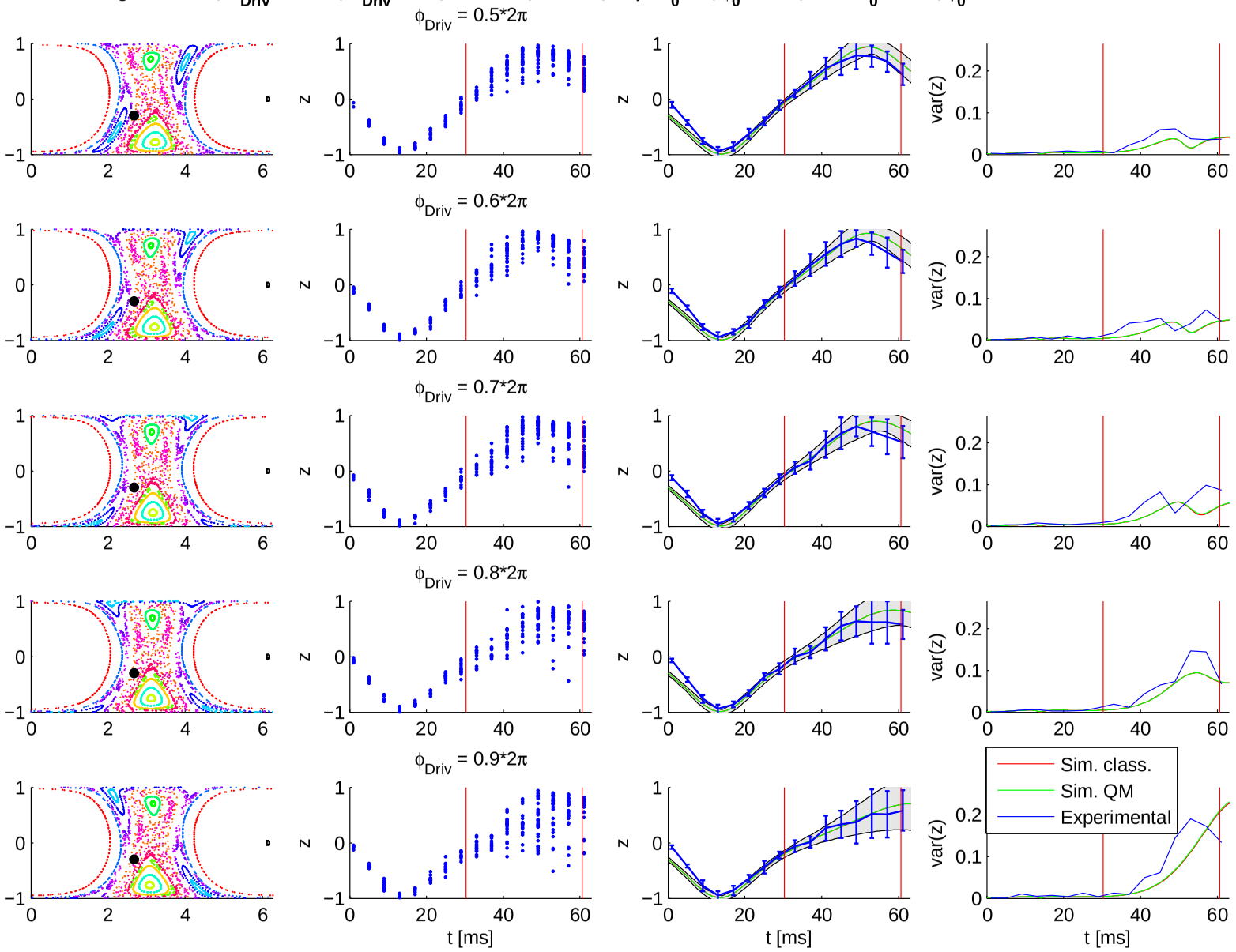
DrivenOmega: Λ = 1.5; A_Driv = 0.035; ω_Driv = 1.6; ε = −0.07; N= 700; Exp.: z_0 = 0; ϕ_0 = 2.50; Sim.: z_0 = −0.3; ϕ_0 = 2.68
ϕ_Driv = 0.5*2π
ϕ_Driv = 0.6*2π
ϕ_Driv = 0.7*2π
ϕ_Driv = 0.8*2π
ϕ_Driv = 0.9*2π
z
var(z)
t [ms]
Sim. class.
Sim. QM
Experimental

C.2.3. Medium driving amplitude $A = 0.07$

Measuring the time evolution of the driven system with a medium driving amplitude $A_{\text{Driv}} = 0.07$ for a single start point (Exp: $z_0 = 0, \varphi_0 = 2.51$; Fit: $z_0 = -0.3, \varphi_0 = 2.68$) and different driving phases.

Parameters:

$$\begin{aligned} \Omega &= 20.7\,Hz\,(*2\pi) \\ \epsilon_{\text{set}} &= -0.1 \\ \epsilon_{\text{fit}} &= -0.07 \end{aligned}$$

Driving:

$$\begin{aligned} A_{\text{Driv}} &= 0.07 \\ \omega_{\text{Driv}} &= 33\,Hz \\ \omega^{sc}_{\text{Driv}} &= 1.587 \\ \varphi_{\text{Driv}} &= [0 \quad 0.1 \quad 0.2 \quad 0.3 \quad 0.4 \quad 0.5 \quad 0.6 \quad 0.7 \quad 0.8 \quad 0.9] \cdot 2\pi \end{aligned}$$

Loss compensation

$$\begin{aligned} \tau_{Loss} &= 2 \cdot 86\,ms \\ A_{Loss} &= 21.6\,Hz \end{aligned}$$

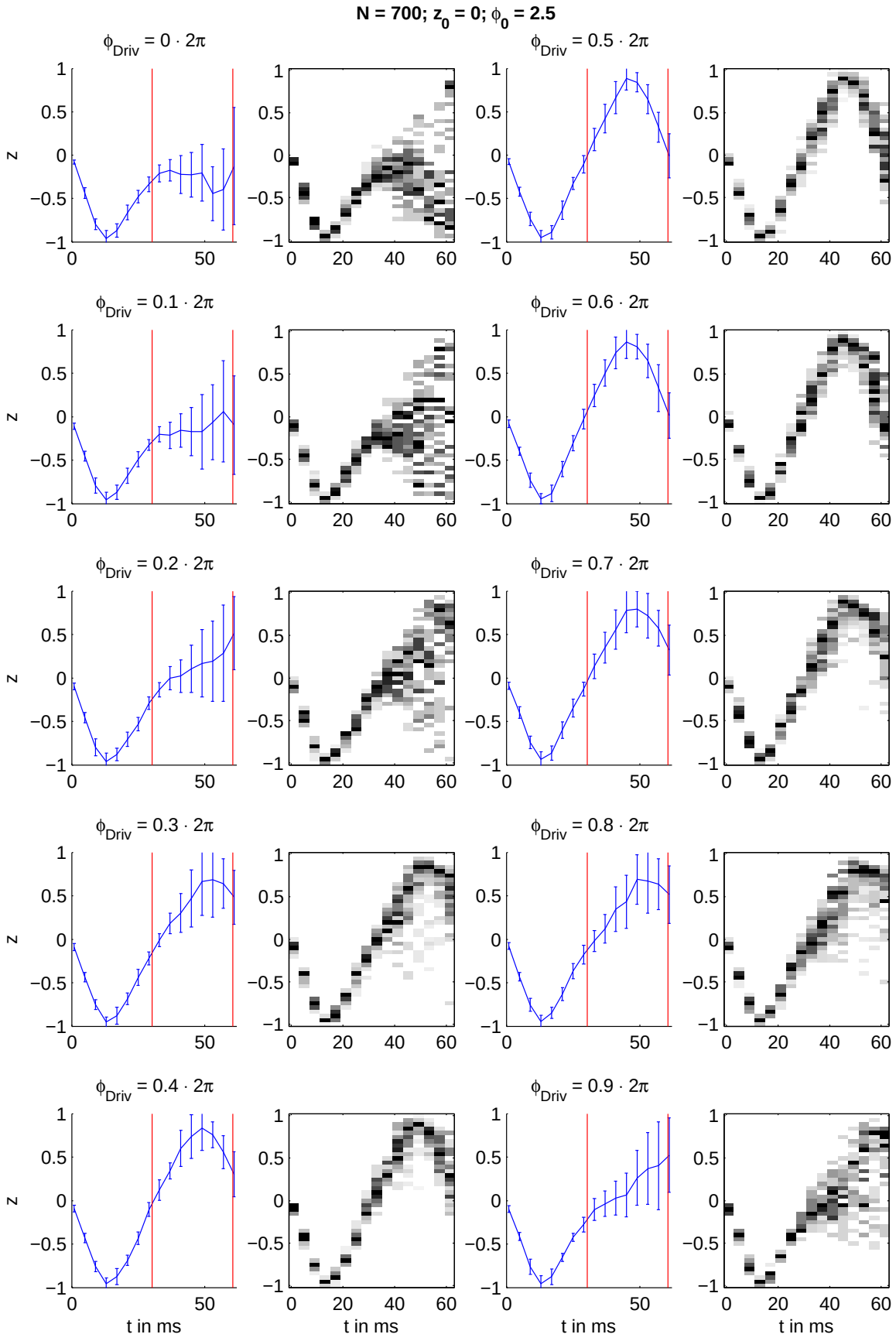
N = 700; z0 = 0; ϕ0 = 2.5
ϕDriv = 0 · 2π
ϕDriv = 0.5 · 2π
ϕDriv = 0.1 · 2π
ϕDriv = 0.6 · 2π
ϕDriv = 0.2 · 2π
ϕDriv = 0.7 · 2π
ϕDriv = 0.3 · 2π
ϕDriv = 0.8 · 2π
ϕDriv = 0.4 · 2π
ϕDriv = 0.9 · 2π
z
t in ms

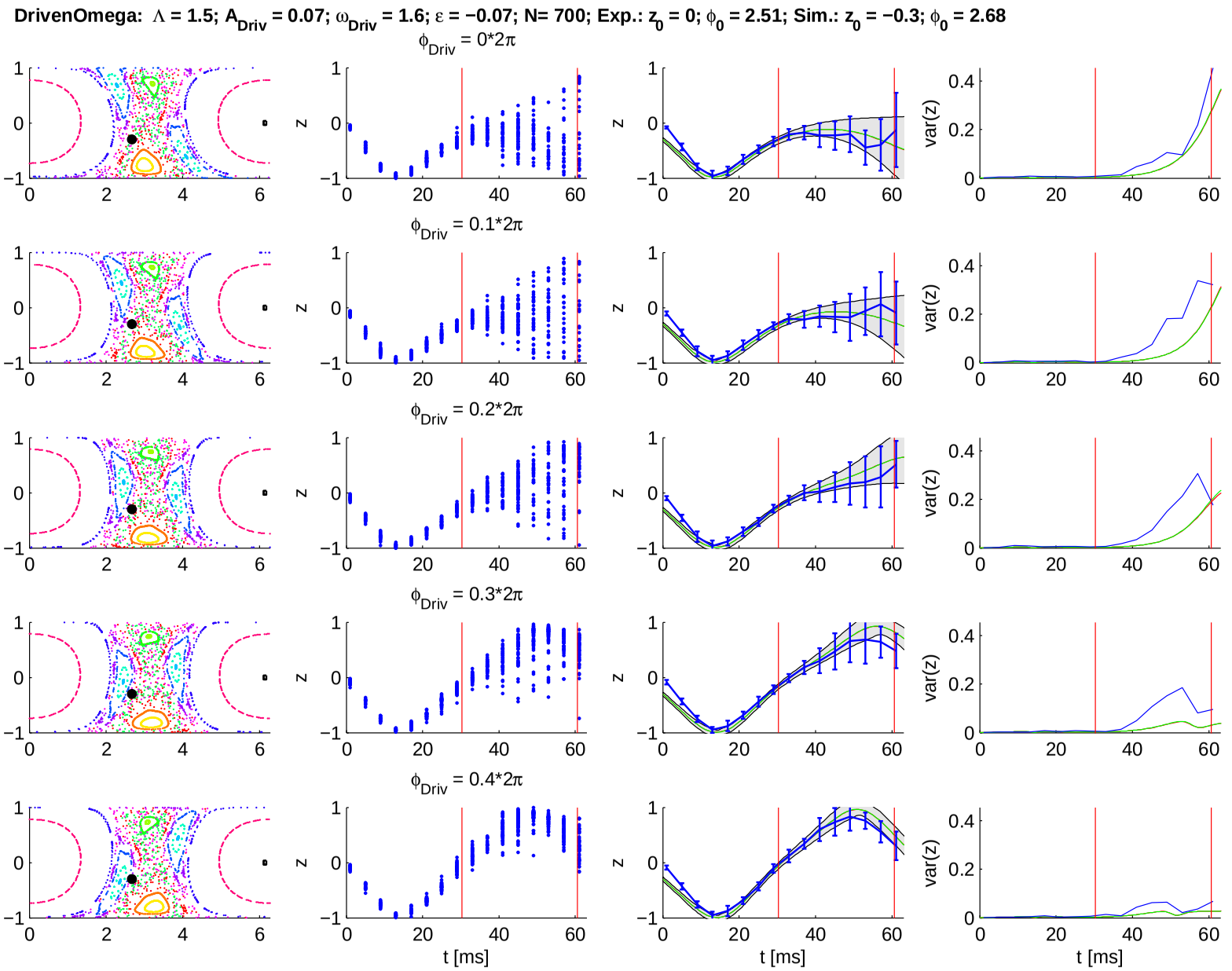
DrivenOmega: Λ = 1.5; A_Driv = 0.07; ω_Driv = 1.6; ε = −0.07; N= 700; Exp.: z_0 = 0; ϕ_0 = 2.51; Sim.: z_0 = −0.3; ϕ_0 = 2.68
ϕ_Driv = 0*2π
ϕ_Driv = 0.1*2π
ϕ_Driv = 0.2*2π
ϕ_Driv = 0.3*2π
ϕ_Driv = 0.4*2π
z
var(z)
t [ms]

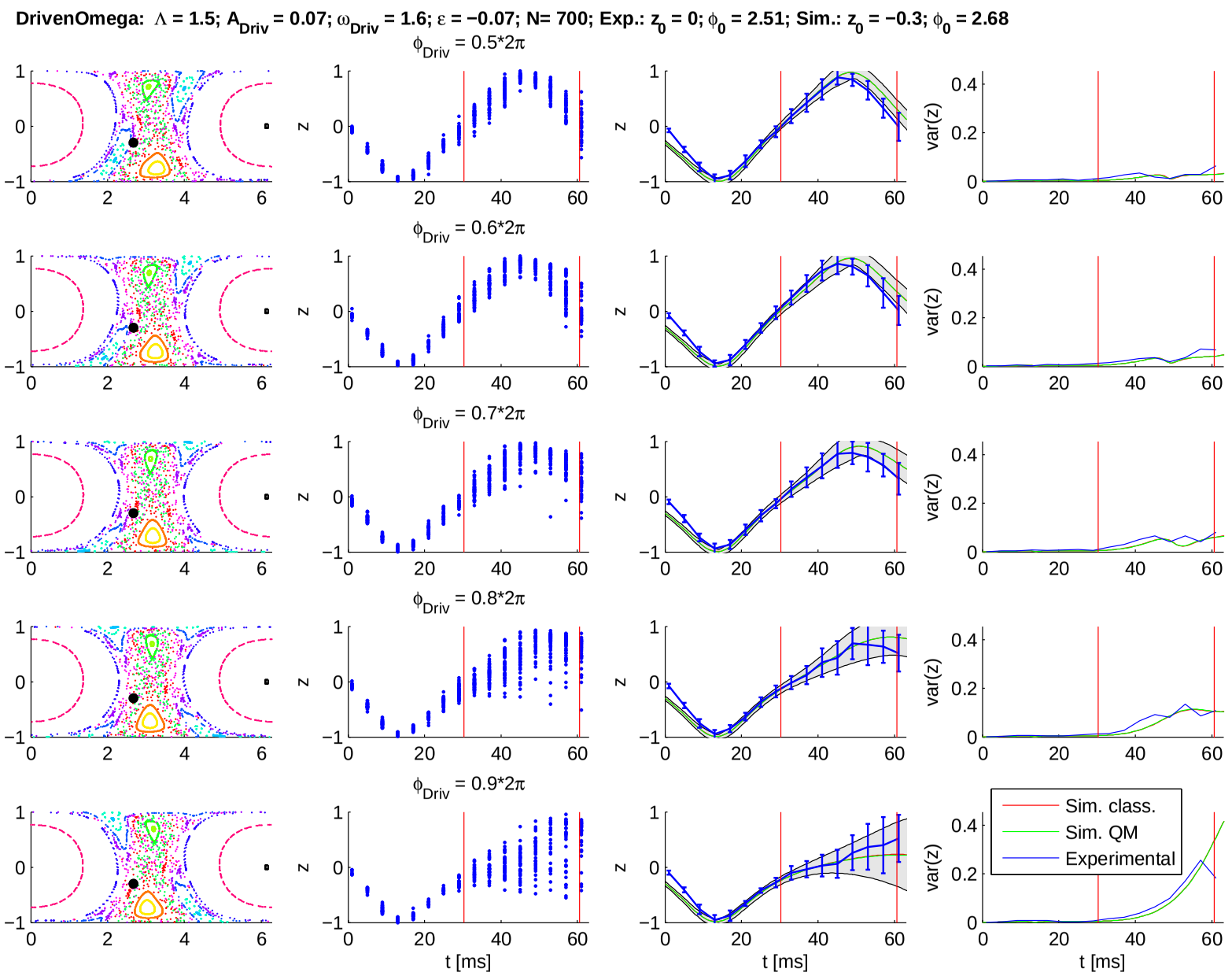
DrivenOmega: Λ = 1.5; A_Driv = 0.07; ω_Driv = 1.6; ε = −0.07; N= 700; Exp.: z_0 = 0; ϕ_0 = 2.51; Sim.: z_0 = −0.3; ϕ_0 = 2.68
ϕ_Driv = 0.5*2π
ϕ_Driv = 0.6*2π
ϕ_Driv = 0.7*2π
ϕ_Driv = 0.8*2π
ϕ_Driv = 0.9*2π
z
var(z)
t [ms]
Sim. class.
Sim. QM
Experimental

C.2.4. Medium driving amplitude $A = 0.07$ including tomography data

Measuring the time evolution of the driven system with a medium driving amplitude $A_{\mathrm{Driv}} = 0.07$ for a single start point (Exp: $z_0 = 0, \varphi_0 = 2.51$; Fit: $z_0 = -0.3, \varphi_0 = 2.68$) and different driving phases. Additionally the phase information is measured by applying a subsequent $\pi/2$ tomography pulse around J_x.

Parameters:

$$\begin{aligned} \Omega &= 20.7\,Hz\,(*2\pi) \\ \epsilon_{\mathrm{set}} &= -0.1 \\ \epsilon_{\mathrm{fit}} &= -0.07 \end{aligned}$$

Driving:

$$\begin{aligned} A_{\mathrm{Driv}} &= 0.07 \\ \omega_{\mathrm{Driv}} &= 33\,Hz \\ \omega^{sc}_{\mathrm{Driv}} &= 1.587 \\ \varphi_{\mathrm{Driv}} &= [0 \quad 0.1 \quad 0.2 \quad 0.3 \quad 0.4 \quad 0.5 \quad 0.6 \quad 0.7 \quad 0.8 \quad 0.9] \cdot 2\pi \end{aligned}$$

Loss compensation

$$\begin{aligned} \tau_{Loss} &= 2 \cdot 86\,ms \\ A_{Loss} &= 21.6\,Hz \end{aligned}$$

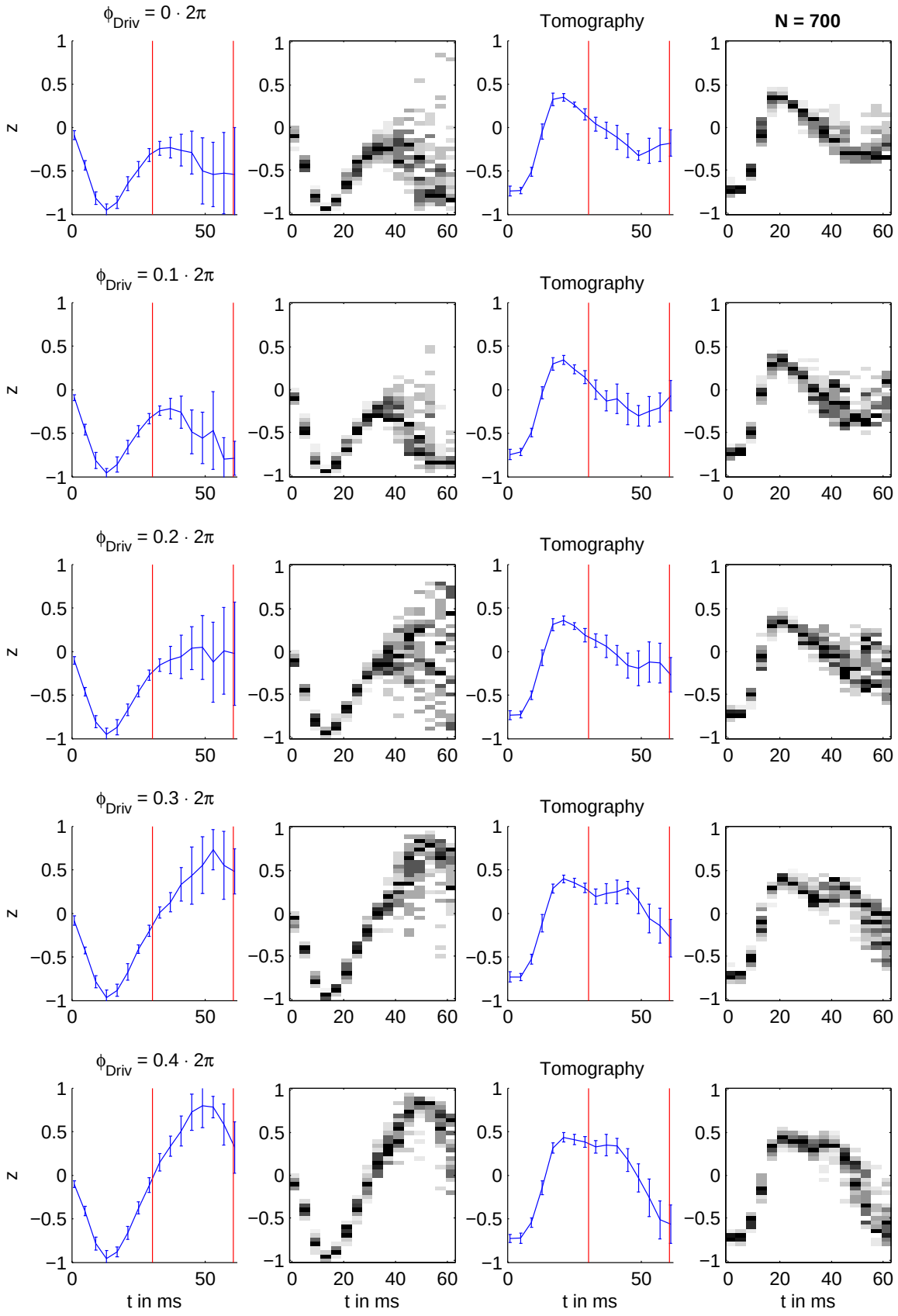
$\phi_{Driv} = 0 \cdot 2\pi$
$\phi_{Driv} = 0.1 \cdot 2\pi$
$\phi_{Driv} = 0.2 \cdot 2\pi$
$\phi_{Driv} = 0.3 \cdot 2\pi$
$\phi_{Driv} = 0.4 \cdot 2\pi$
Tomography
N = 700
z
t in ms

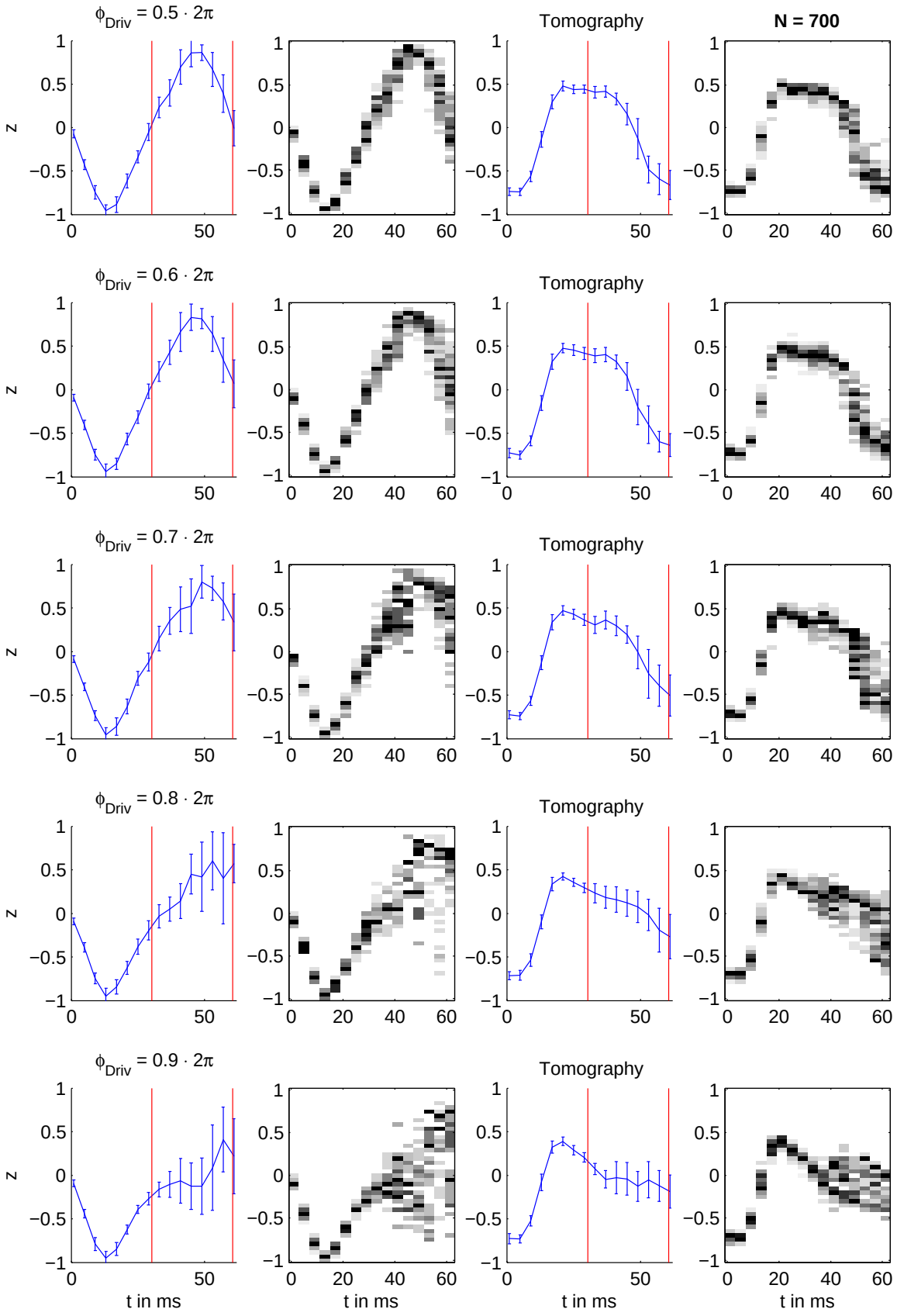
$\phi_{Driv} = 0.5 \cdot 2\pi$
$\phi_{Driv} = 0.6 \cdot 2\pi$
$\phi_{Driv} = 0.7 \cdot 2\pi$
$\phi_{Driv} = 0.8 \cdot 2\pi$
$\phi_{Driv} = 0.9 \cdot 2\pi$
Tomography
N = 700
z
t in ms

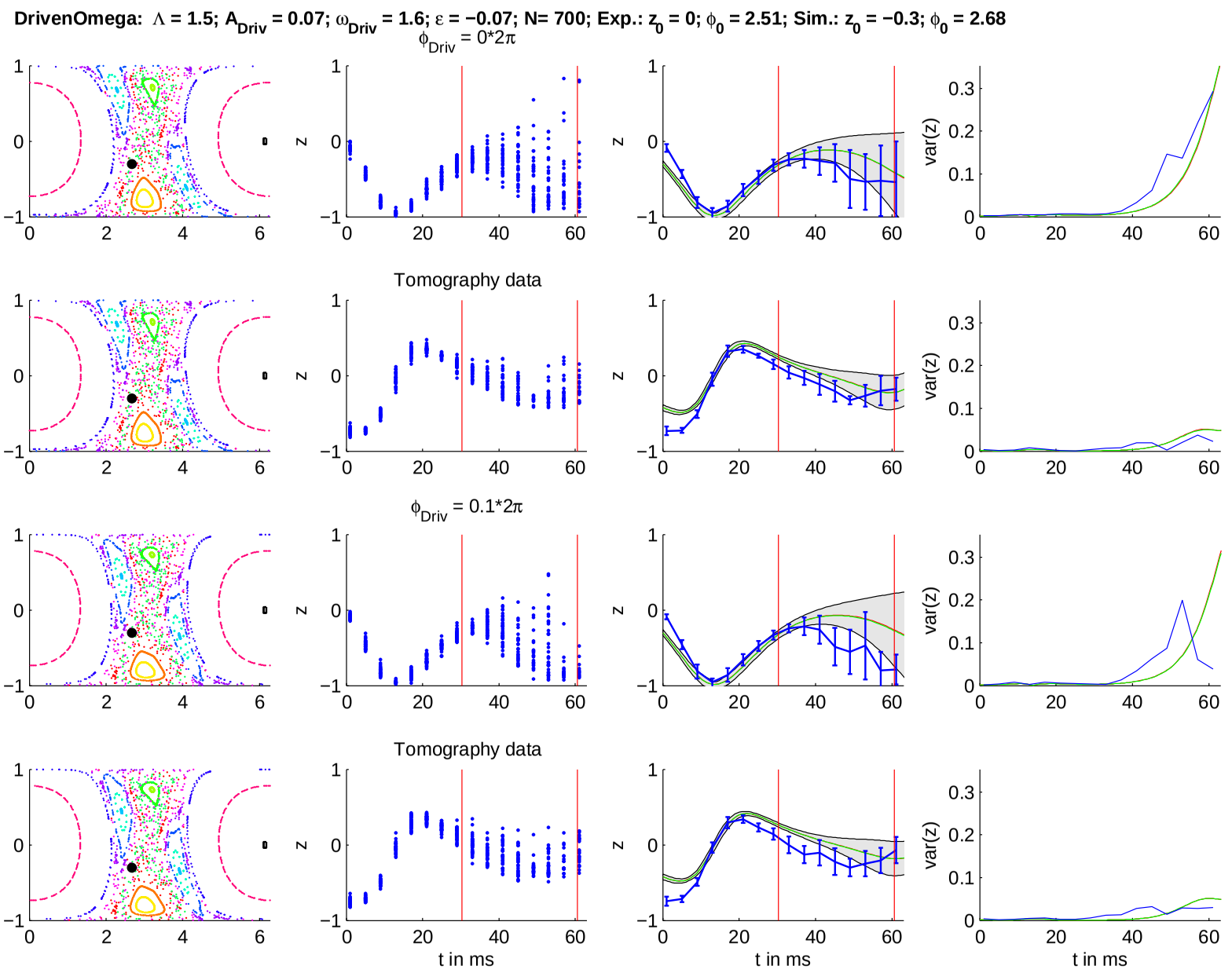
DrivenOmega: Λ = 1.5; A_Driv = 0.07; ω_Driv = 1.6; ε = −0.07; N= 700; Exp.: z_0 = 0; ϕ_0 = 2.51; Sim.: z_0 = −0.3; ϕ_0 = 2.68
ϕ_Driv = 0*2π
Tomography data
ϕ_Driv = 0.1*2π
Tomography data
z
var(z)
t in ms

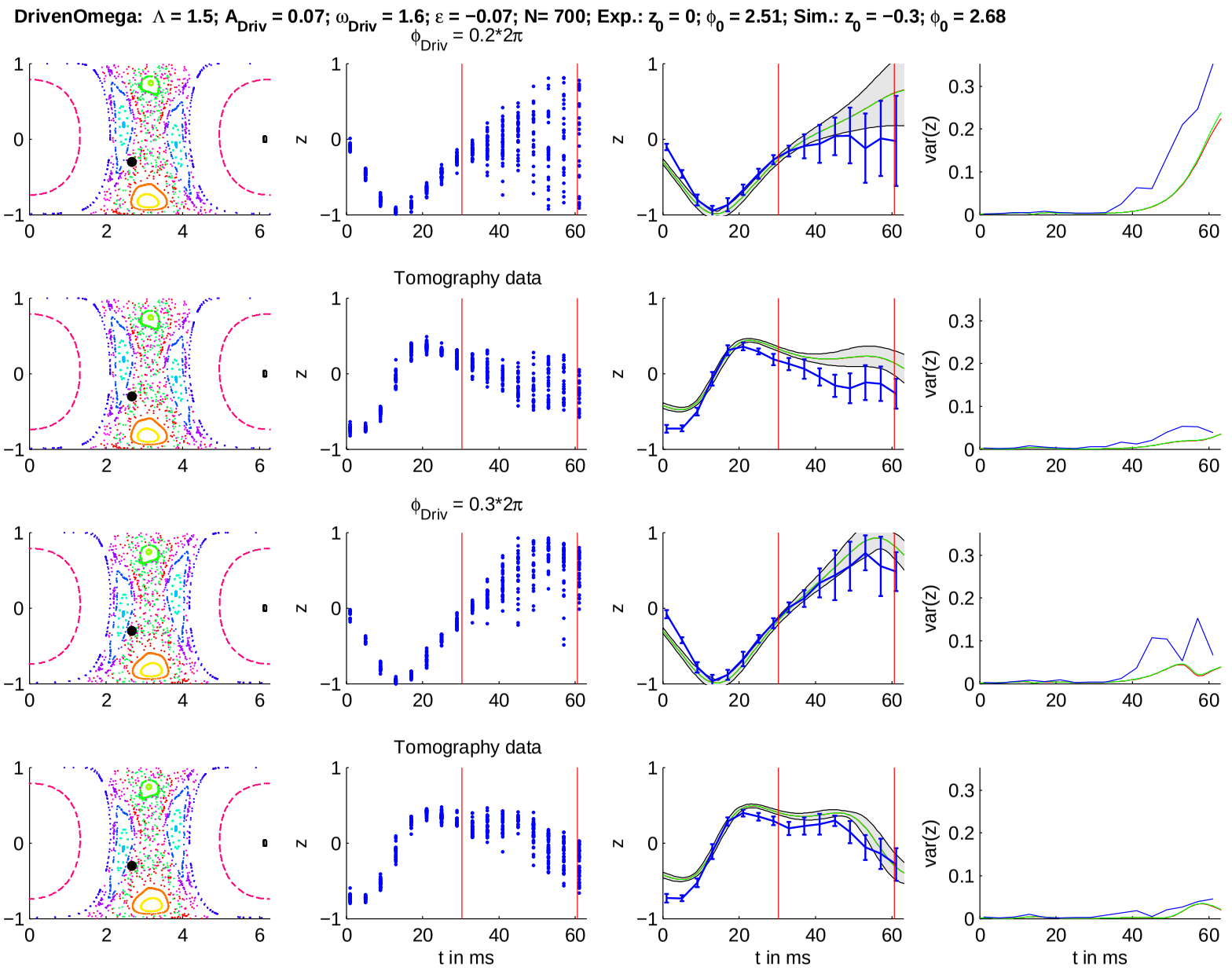
DrivenOmega: Λ = 1.5; A_Driv = 0.07; ω_Driv = 1.6; ε = −0.07; N= 700; Exp.: z_0 = 0; ϕ_0 = 2.51; Sim.: z_0 = −0.3; ϕ_0 = 2.68
ϕ_Driv = 0.2*2π
Tomography data
ϕ_Driv = 0.3*2π
Tomography data
z
var(z)
t in ms

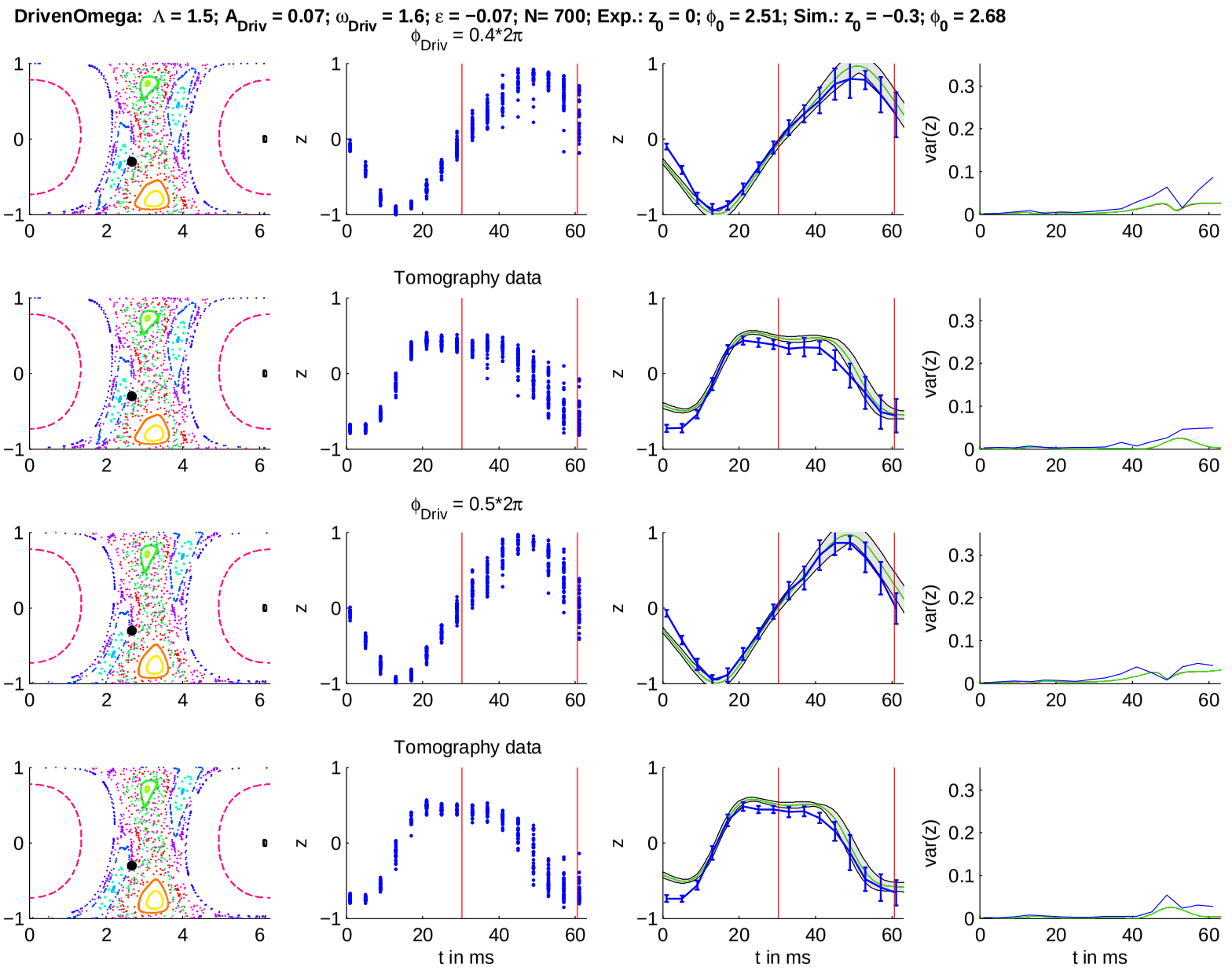
DrivenOmega: Λ = 1.5; A_Driv = 0.07; ω_Driv = 1.6; ε = −0.07; N= 700; Exp.: z_0 = 0; ϕ_0 = 2.51; Sim.: z_0 = −0.3; ϕ_0 = 2.68
ϕ_Driv = 0.4*2π
Tomography data
ϕ_Driv = 0.5*2π
Tomography data
z
var(z)
t in ms

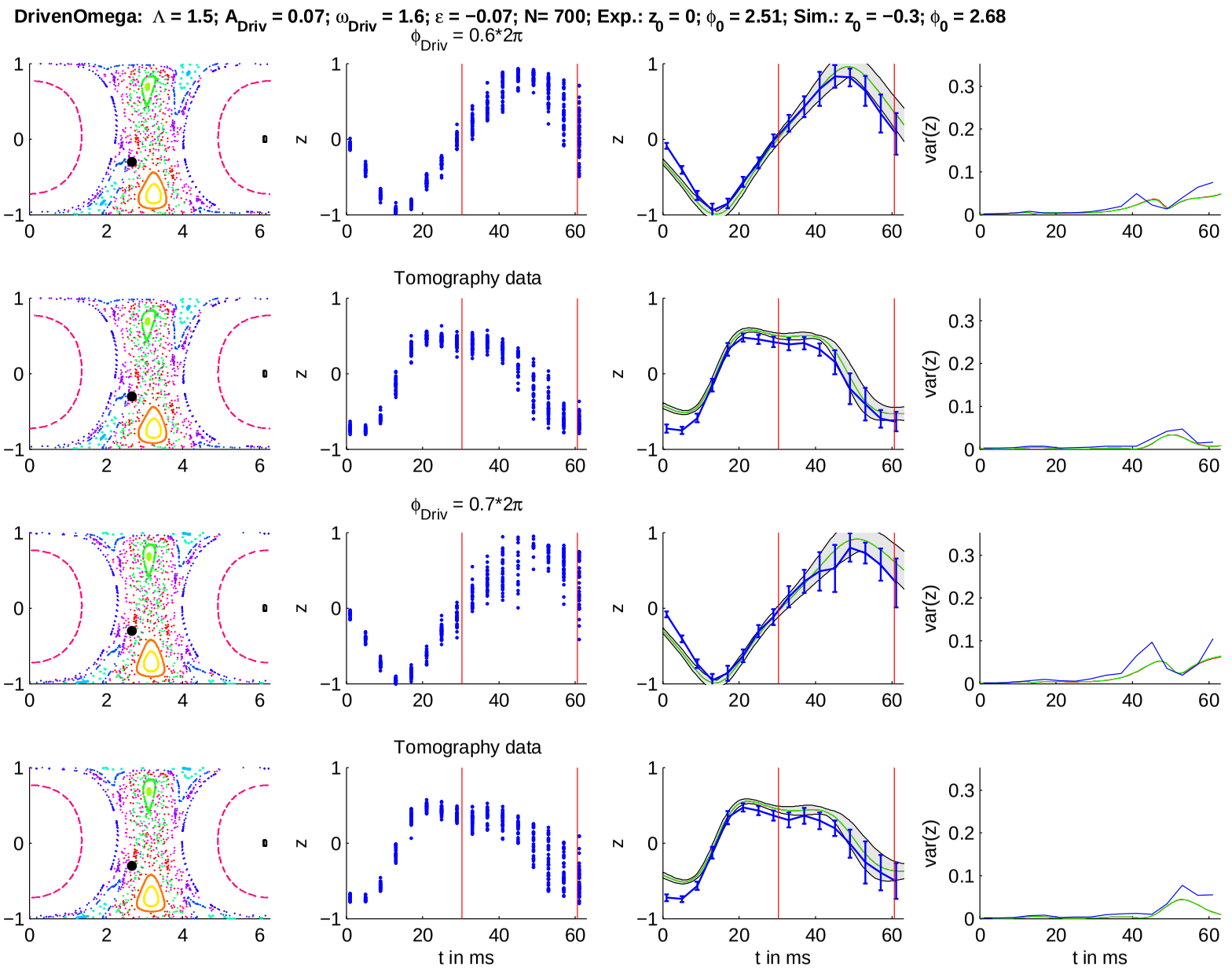
DrivenOmega: Λ = 1.5; A_Driv = 0.07; ω_Driv = 1.6; ε = −0.07; N= 700; Exp.: z_0 = 0; ϕ_0 = 2.51; Sim.: z_0 = −0.3; ϕ_0 = 2.68
ϕ_Driv = 0.6*2π
Tomography data
ϕ_Driv = 0.7*2π
Tomography data
z
var(z)
t in ms

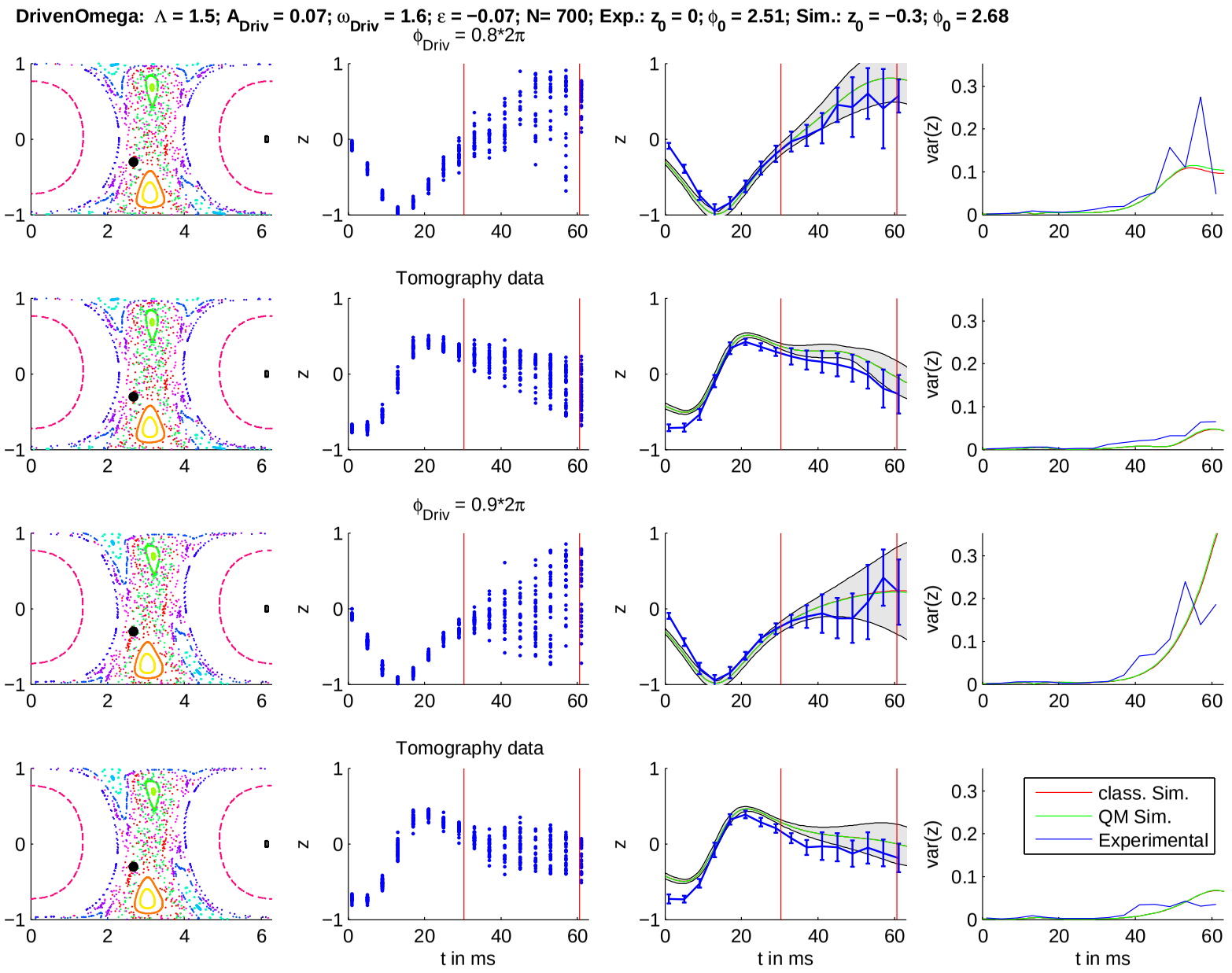
DrivenOmega: Λ = 1.5; A_Driv = 0.07; ω_Driv = 1.6; ε = −0.07; N= 700; Exp.: z_0 = 0; ϕ_0 = 2.51; Sim.: z_0 = −0.3; ϕ_0 = 2.68
ϕ_Driv = 0.8*2π
Tomography data
ϕ_Driv = 0.9*2π
Tomography data
z
var(z)
t in ms
class. Sim.
QM Sim.
Experimental

C.2.5. Strong driving amplitude $A = 0.14$

Measuring the time evolution of the driven system with a strong driving amplitude $A_{\text{Driv}} = 0.14$ for a single start point (Exp: $z_0 = 0, \varphi_0 = 2.51$; Fit: $z_0 = -0.3, \varphi_0 = 2.68$) and different driving phases.

Parameters:

$$\begin{aligned} \Omega &= 20.7\,Hz\,(*2\pi) \\ \epsilon_{\text{set}} &= -0.1 \\ \epsilon_{\text{fit}} &= -0.07 \end{aligned}$$

Driving:

$$\begin{aligned} A_{\text{Driv}} &= 0.07 \\ \omega_{\text{Driv}} &= 33\,Hz \\ \omega^{sc}_{\text{Driv}} &= 1.587 \\ \varphi_{\text{Driv}} &= [2.8\ 5.94] \end{aligned}$$

Loss compensation

$$\begin{aligned} \tau_{Loss} &= 2 \cdot 86\,ms \\ A_{Loss} &= 21.6\,Hz \end{aligned}$$

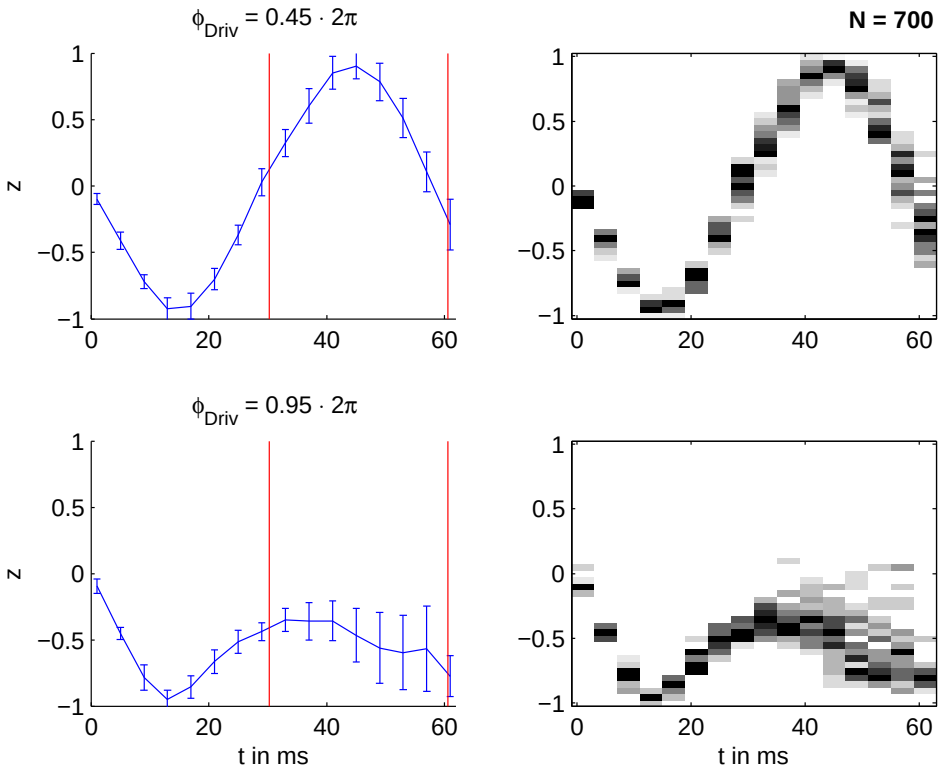
ϕ_{Driv} = 0.45 · 2π
N = 700
ϕ_{Driv} = 0.95 · 2π
z
t in ms

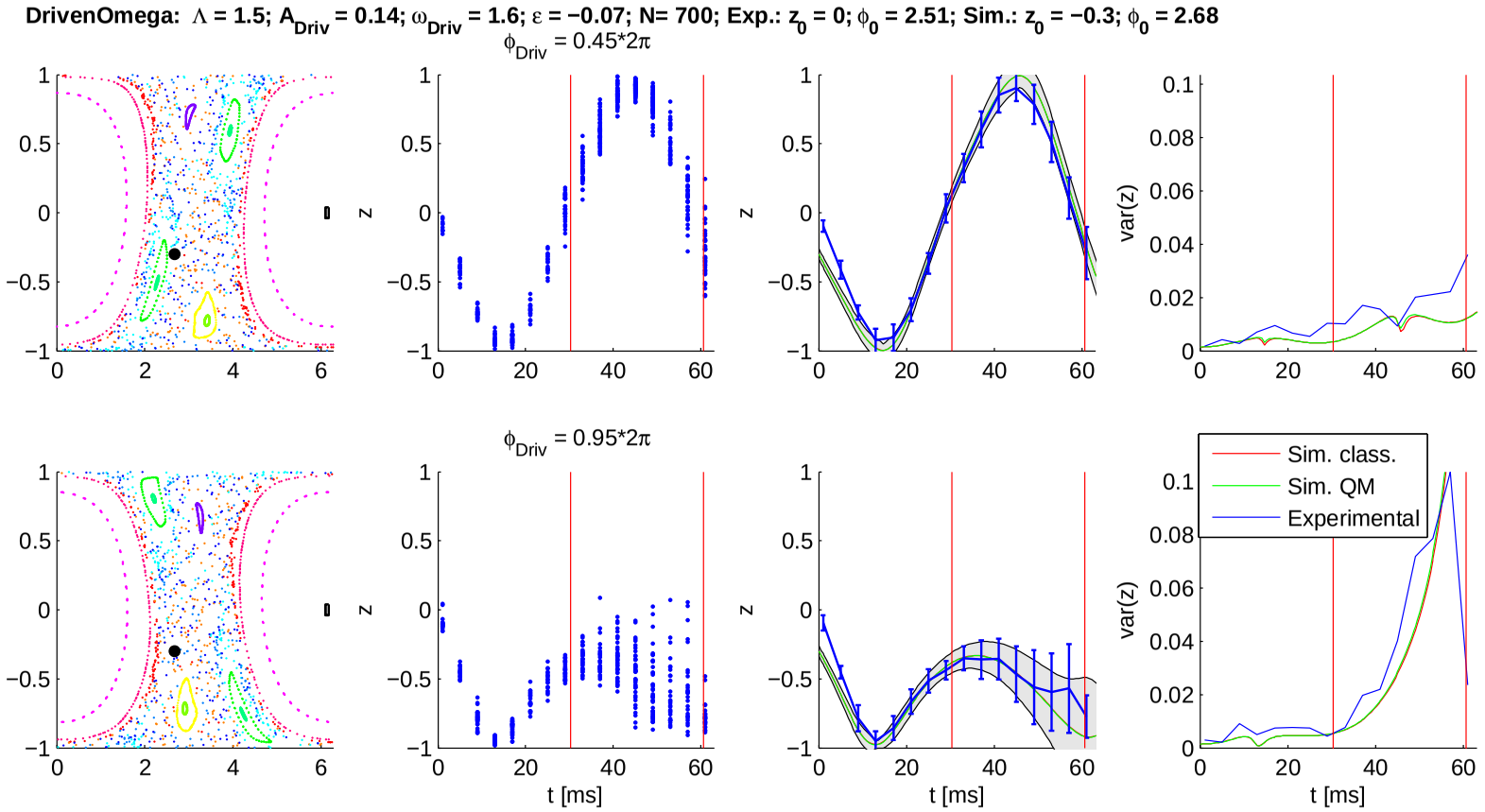
DrivenOmega: Λ = 1.5; A_Driv = 0.14; ω_Driv = 1.6; ε = −0.07; N= 700; Exp.: z_0 = 0; ϕ_0 = 2.51; Sim.: z_0 = −0.3; ϕ_0 = 2.68
ϕ_Driv = 0.45*2π
ϕ_Driv = 0.95*2π
z
var(z)
t [ms]
Sim. class.
Sim. QM
Experimental

C.2.6. Time evolution for different starting points for a medium driving amplitude $A = 0.07$ including tomography data

Measuring the time evolution of the driven system with a medium driving amplitude $A_{\text{Driv}} = 0.07$ for a several start points and one driving phase $\varphi_{\text{Driv}} = 0.3 \cdot 2\pi$. Additionally the phase information is measured by applying a subsequent $\pi/2$ tomography pulse around J_x.

Parameters:

$$\begin{aligned} \Omega &= 20.7\,Hz\,(*2\pi) \\ \epsilon_{\text{set}} &= -0.1 \\ \epsilon_{\text{fit}} &= -0.07 \end{aligned}$$

Driving:

$$\begin{aligned} A_{\text{Driv}} &= 0.07 \\ \omega_{\text{Driv}} &= 33\,Hz \\ \omega^{sc}_{\text{Driv}} &= 1.587 \\ \varphi_{\text{Driv}} &= 0.3 \cdot 2\pi \end{aligned}$$

Loss compensation

$$\begin{aligned} \tau_{Loss} &= 2 \cdot 86\,ms \\ A_{Loss} &= 21.6\,Hz \end{aligned}$$

Start points:

z_{set}	0	-0.92	-0.61	-0.33	-0.60
z_{fit}	-0.29	-0.87	-0.46	-0.52	-0.68
φ_{set}	2.60	3.40	3.96	3.27	3.25
φ_{fit}	2.74	3.24	3.80	3.32	3.19

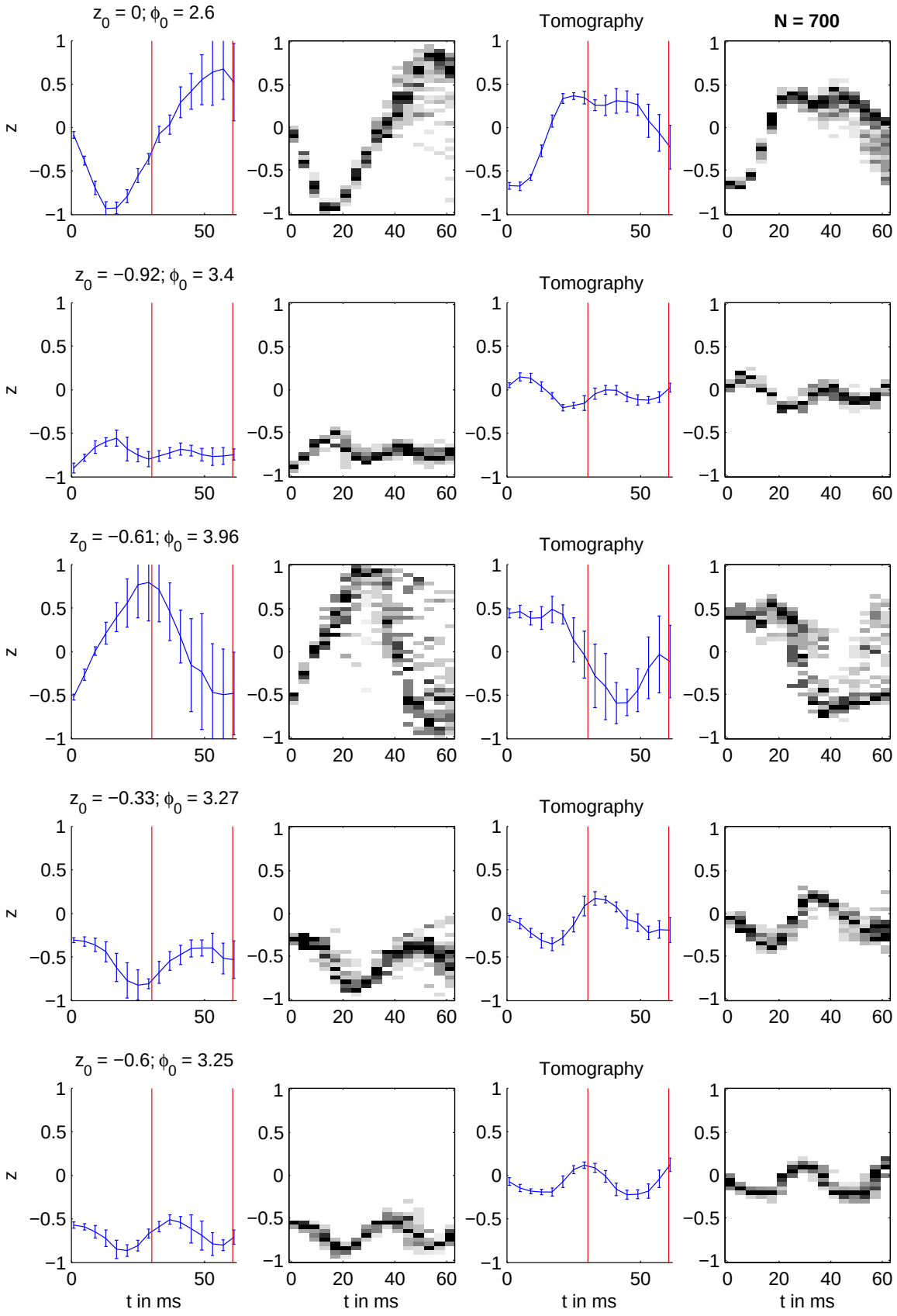
$z_0 = 0; \phi_0 = 2.6$
Tomography
N = 700
$z_0 = -0.92; \phi_0 = 3.4$
Tomography
$z_0 = -0.61; \phi_0 = 3.96$
Tomography
$z_0 = -0.33; \phi_0 = 3.27$
Tomography
$z_0 = -0.6; \phi_0 = 3.25$
Tomography
z
t in ms

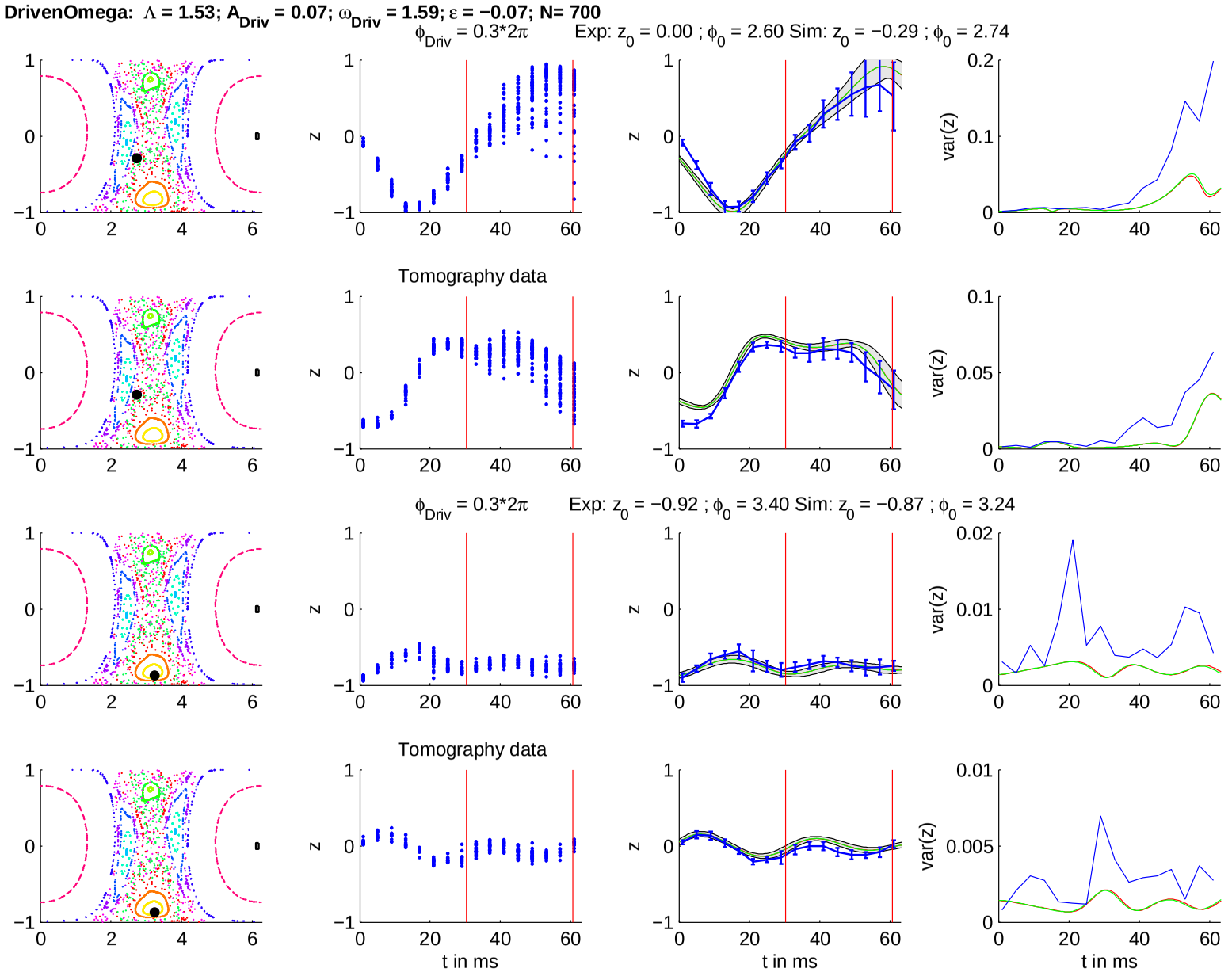
DrivenOmega: Λ = 1.53; A_Driv = 0.07; ω_Driv = 1.59; ε = −0.07; N= 700
ϕ_Driv = 0.3*2π
Exp: z_0 = 0.00 ; ϕ_0 = 2.60 Sim: z_0 = −0.29 ; ϕ_0 = 2.74
Tomography data
ϕ_Driv = 0.3*2π
Exp: z_0 = −0.92 ; ϕ_0 = 3.40 Sim: z_0 = −0.87 ; ϕ_0 = 3.24
Tomography data
z
var(z)
t in ms

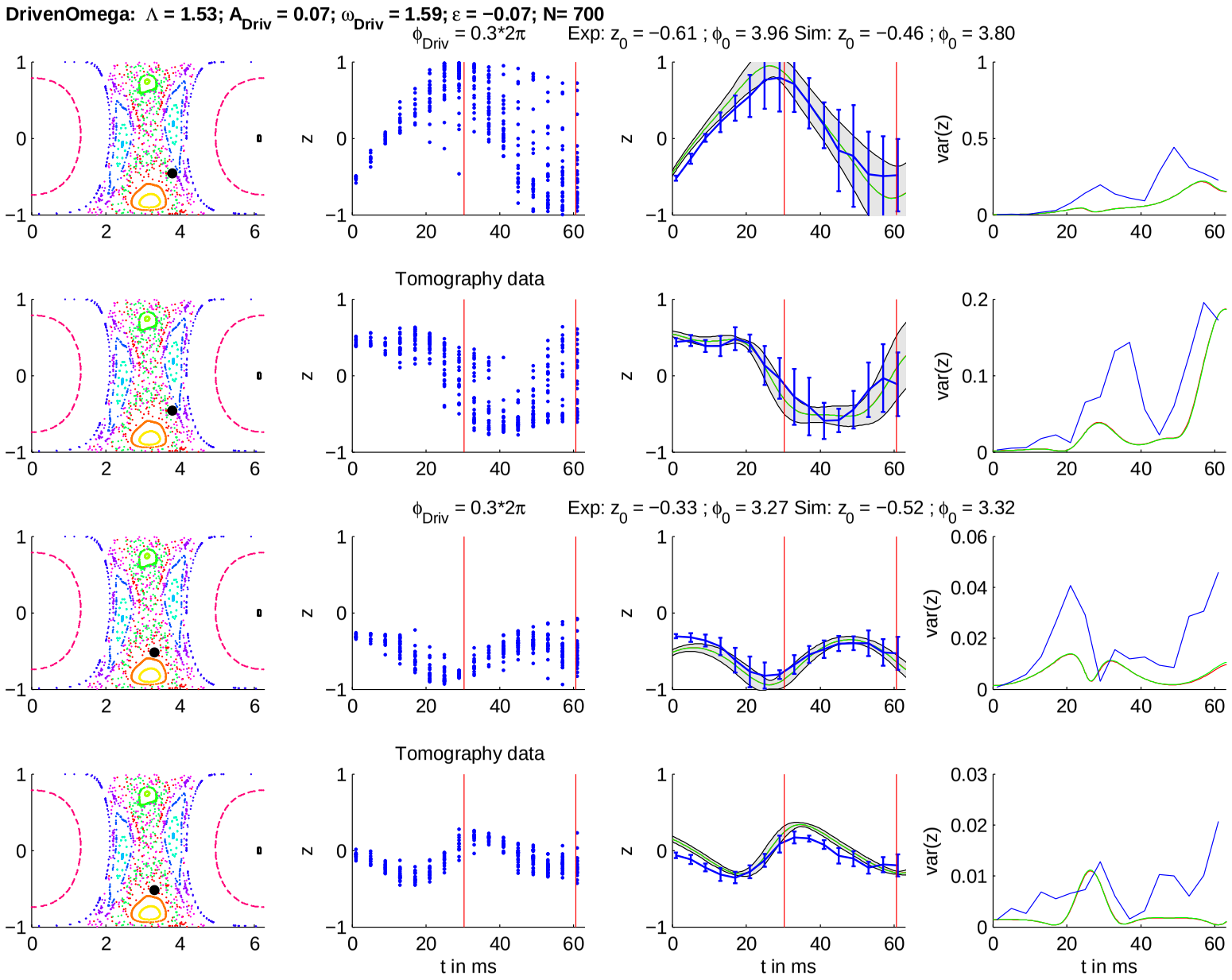
DrivenOmega: Λ = 1.53; A_Driv = 0.07; ω_Driv = 1.59; ε = −0.07; N= 700
ϕ_Driv = 0.3*2π
Exp: z_0 = −0.61 ; ϕ_0 = 3.96 Sim: z_0 = −0.46 ; ϕ_0 = 3.80
Tomography data
ϕ_Driv = 0.3*2π
Exp: z_0 = −0.33 ; ϕ_0 = 3.27 Sim: z_0 = −0.52 ; ϕ_0 = 3.32
Tomography data
z
var(z)
t in ms

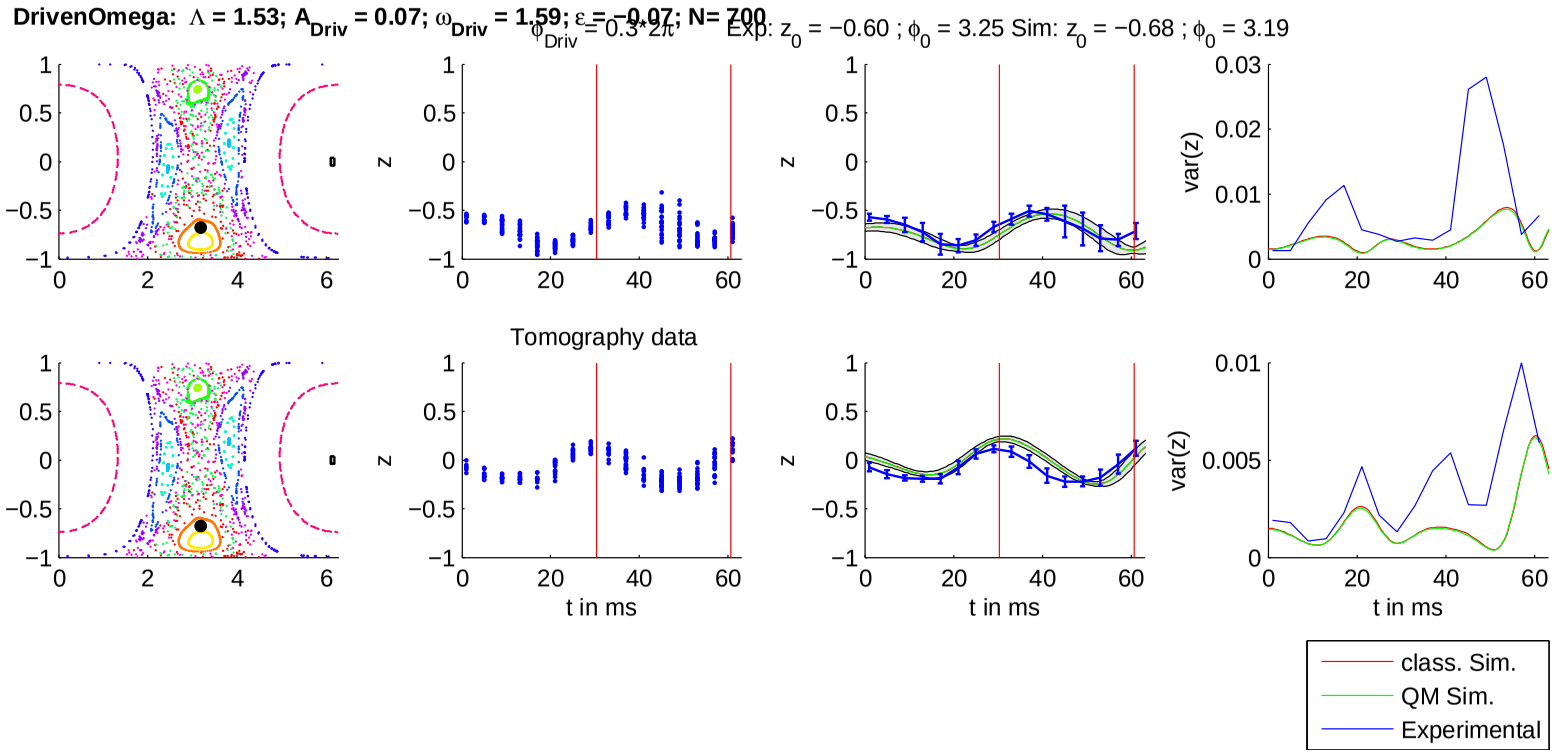
DrivenOmega: Λ = 1.53; A_Driv = 0.07; ω_Driv = 1.59; ε = −0.07; N= 700
φ_Driv = 0.3*2π; Exp: z_0 = −0.60 ; φ_0 = 3.25 Sim: z_0 = −0.68 ; φ_0 = 3.19
Tomography data
z
var(z)
t in ms
class. Sim.
QM Sim.
Experimental

C.2.7. Medium driving amplitude $A = 0.07$ for preparation within the chaotic sea

Measuring the time evolution of the driven system with a medium driving amplitude $A_{\text{Driv}} = 0.07$ for a single start point (Exp: $z_0 = 0, \varphi_0 = 3.14$; Fit: $z_0 = 0.085, \varphi_0 = 3.13$) deep within the chaotic sea and for different driving phases. Due to the tilted system, the preparation is chosen to lie beneath the unstable fixed point of the undriven system at $z_0 = 0.134,\ \varphi_0 = \pi$ to avoid critical dependency of the system on technical noise. This leads to same dynamics for all driving phases for small times, e.g. the distribution starts in $-z$ direction.

Parameters:

$$\begin{aligned} \Omega &= 20.7\,Hz\,(*2\pi) \\ \epsilon_{\text{set}} &= -0.1 \\ \epsilon_{\text{fit}} &= -0.07 \end{aligned}$$

Driving:

$$\begin{aligned} A_{\text{Driv}} &= 0.07 \\ \omega_{\text{Driv}} &= 33\,Hz \\ \omega^{sc}_{\text{Driv}} &= 1.587 \\ \varphi_{\text{Driv}} &= [0 \quad 0.1 \quad 0.2 \quad 0.3 \quad 0.4 \quad 0.5 \quad 0.6 \quad 0.7 \quad 0.8 \quad 0.9] \cdot 2\pi \end{aligned}$$

Loss compensation

$$\begin{aligned} \tau_{Loss} &= 2 \cdot 86\,ms \\ A_{Loss} &= 21.6\,Hz \end{aligned}$$

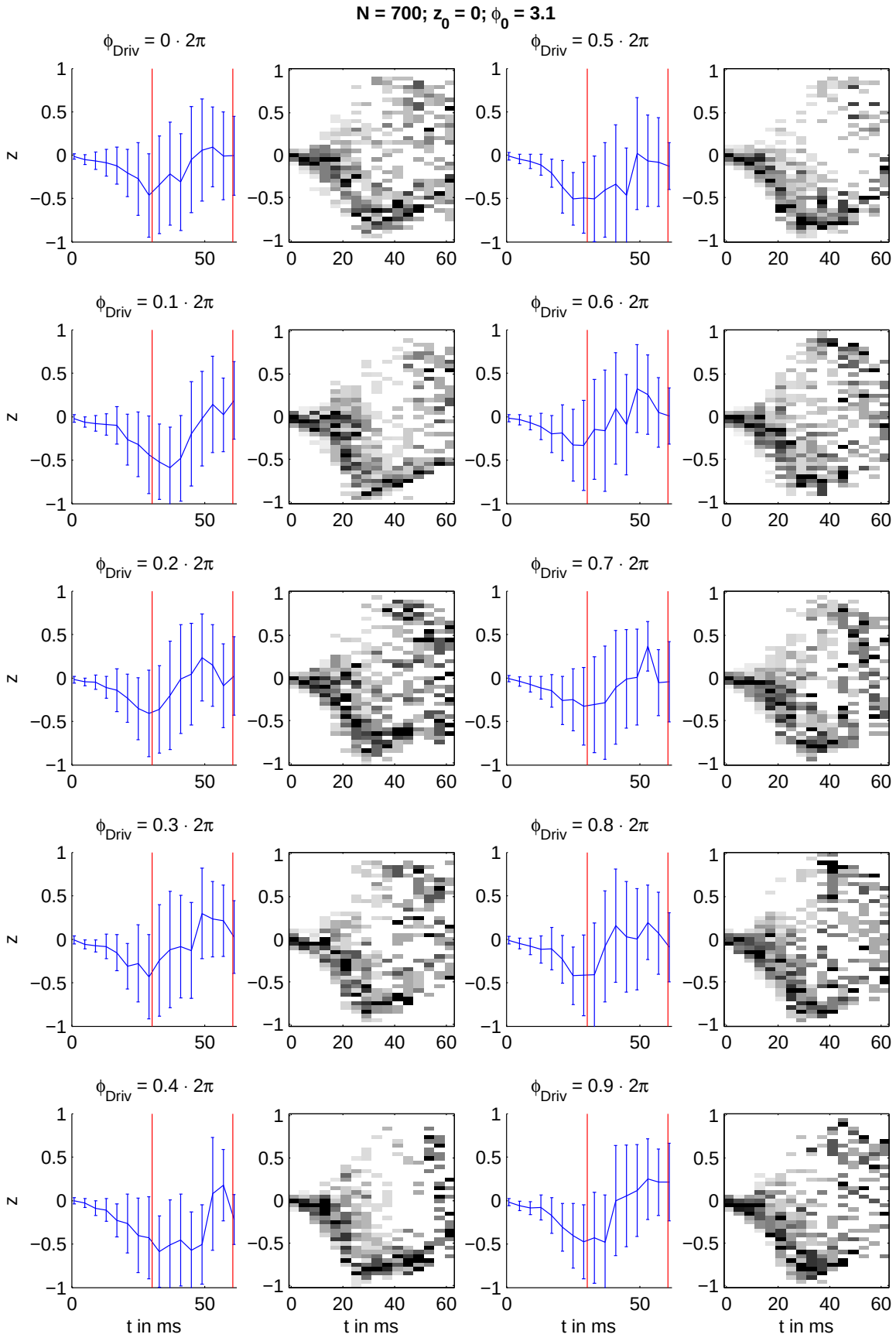
N = 700; z0 = 0; ϕ0 = 3.1
ϕDriv = 0 · 2π
ϕDriv = 0.5 · 2π
ϕDriv = 0.1 · 2π
ϕDriv = 0.6 · 2π
ϕDriv = 0.2 · 2π
ϕDriv = 0.7 · 2π
ϕDriv = 0.3 · 2π
ϕDriv = 0.8 · 2π
ϕDriv = 0.4 · 2π
ϕDriv = 0.9 · 2π
z
t in ms

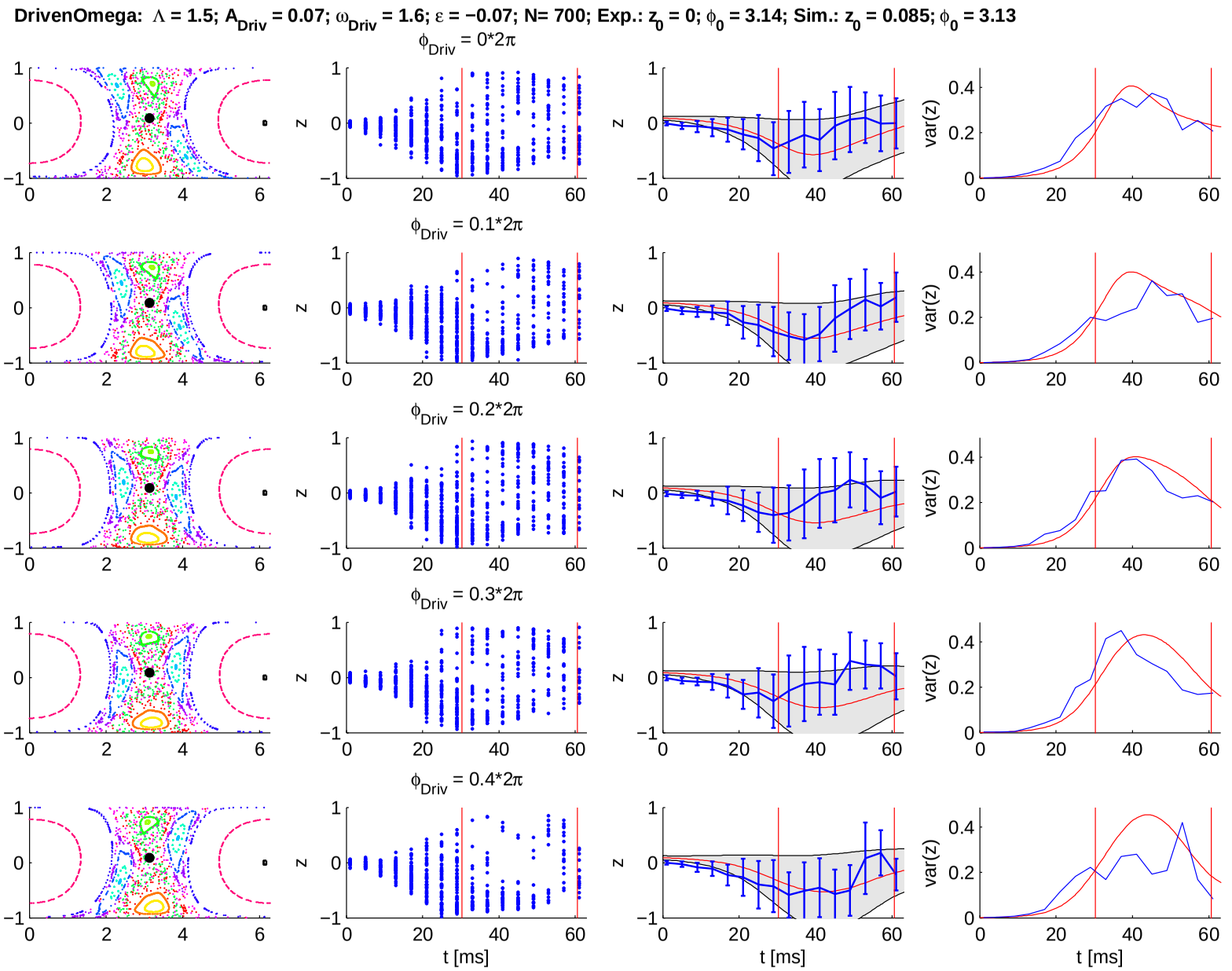
DrivenOmega: Λ = 1.5; A_Driv = 0.07; ω_Driv = 1.6; ε = −0.07; N= 700; Exp.: z_0 = 0; ϕ_0 = 3.14; Sim.: z_0 = 0.085; ϕ_0 = 3.13
ϕ_Driv = 0*2π
ϕ_Driv = 0.1*2π
ϕ_Driv = 0.2*2π
ϕ_Driv = 0.3*2π
ϕ_Driv = 0.4*2π
z
var(z)
t [ms]

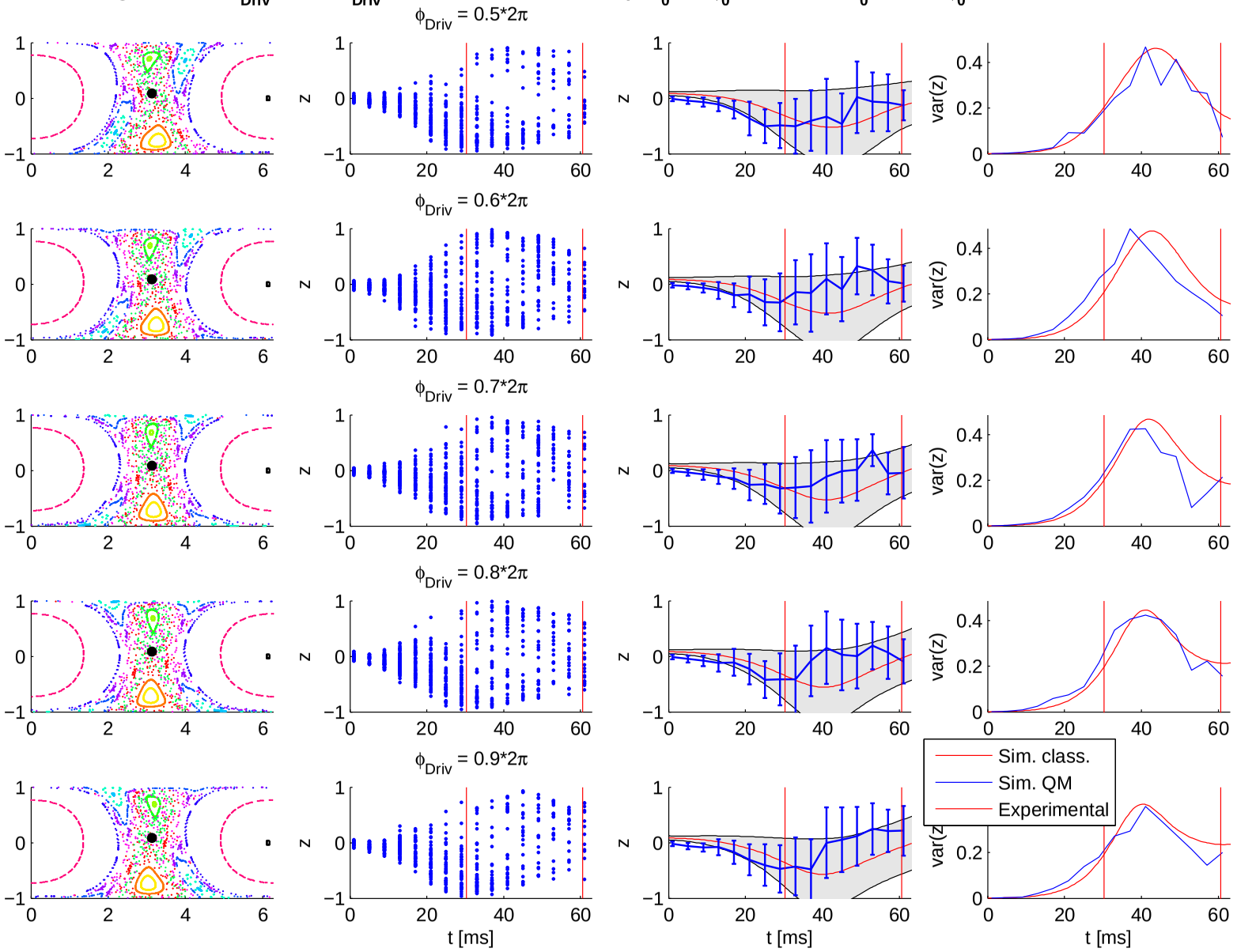
DrivenOmega: Λ = 1.5; A_Driv = 0.07; ω_Driv = 1.6; ε = −0.07; N= 700; Exp.: z_0 = 0; ϕ_0 = 3.14; Sim.: z_0 = 0.085; ϕ_0 = 3.13
ϕ_Driv = 0.5*2π
ϕ_Driv = 0.6*2π
ϕ_Driv = 0.7*2π
ϕ_Driv = 0.8*2π
ϕ_Driv = 0.9*2π
z
var(z)
t [ms]
Sim. class.
Sim. QM
Experimental

Publication List

[1] Kierig, E., Schnorrberger, U., Schietinger, A., Tomkovič, J. & Oberthaler, M. K. Single-particle tunneling in strongly driven double-well potentials. *Phys. Rev. Lett.* **100**, 190405 (2008).

[2] Tomkovič, J., Schreiber, M., Welte, J., Kiffner, M., Schmiedmayer, J. & Oberthaler, M. K. Single spontaneous photon as a coherent beamsplitter for an atomic matter-wave. *Nature Physics* **7**, 379–382 (2011).

[3] Muessel, W., Strobel, H., Joos, M., Nicklas, E., Stroescu, I., Tomkovič, J., Hume, D. B. & Oberthaler, M. K. Optimized absorption imaging of mesoscopic atomic clouds. *Applied Physics B* **113**, 69–73 (2013).

Bibliography

[4] Ott, E. *Chaos in dynamical systems* (Cambridge Univ. Press, Cambridge, 2002), 2. edn.

[5] Cvitanović, P., Artuso, R., Mainieri, R., Tanner, G. & Vattay, G. *Chaos: Classical and Quantum* (Niels Bohr Institute, Copenhagen, 2012).

[6] Moore, F. L., Robinson, J. C., Bharucha, C. F., Sundaram, B. & Raizen, M. G. Atom optics realization of the quantum δ-kicked rotor. *Phys. Rev. Lett.* **75**, 4598–4601 (1995).

[7] Oberthaler, M. K., Godun, R. M., d'Arcy, M. B., Summy, G. S. & Burnett, K. Observation of quantum accelerator modes. *Phys. Rev. Lett.* **83**, 4447–4451 (1999).

[8] Behinaein, G., Ramareddy, V., Ahmadi, P. & Summy, G. S. Exploring the phase space of the quantum δ-kicked accelerator. *Phys. Rev. Lett.* **97**, 244101 (2006).

[9] Ryu, C., Andersen, M. F., Vaziri, A., d'Arcy, M. B., Grossman, J. M., Helmerson, K. & Phillips, W. D. High-order quantum resonances observed in a periodically kicked Bose-Einstein condensate. *Phys. Rev. Lett.* **96**, 160403 (2006).

[10] Fishman, S., Guarneri, I. & Rebuzzini, L. Stable quantum resonances in atom optics. *Phys. Rev. Lett.* **89**, 084101 (2002).

[11] Klappauf, B. G., Oskay, W. H., Steck, D. A. & Raizen, M. G. Quantum chaos with cesium atoms: pushing the boundaries. *Physica D* **131**, 78 – 89 (1999).

[12] Eckardt, A., Holthaus, M., Lignier, H., Zenesini, A., Ciampini, D., Morsch, O. & Arimondo, E. Exploring dynamic localization with a Bose-Einstein condensate. *Phys. Rev. A* **79**, 013611 (2009).

[13] Bodyfelt, J. D., Zheng, M. C., Kottos, T., Kuhl, U. & Stöckmann, H.-J. Probing localization in absorbing systems via Loschmidt Echos. *Phys. Rev. Lett.* **102**, 253901 (2009).

[14] Kondov, S. S., McGehee, W. R., Zirbel, J. J. & DeMarco, B. Three-dimensional Anderson localization of ultracold matter. *Science* **334**, 66–68 (2011).

[15] Jendrzejewski, F., Bernard, A., Muller, K., Cheinet, P., Josse, V., Piraud, M., Pezze, L., Sanchez-Palencia, L., Aspect, A. & Bouyer, P. Three-dimensional localization of ultracold atoms in an optical disordered potential. *Nature Physics* **8**, 398–403 (2012).

[16] Feynman, R. P. *Lectures on physics*, vol. 1 (Pearson Addison Wesley, San Francisco, Calif., 2006).

[17] Schanz, H., Otto, M.-F., Ketzmerick, R. & Dittrich, T. Classical and quantum hamiltonian ratchets. *Phys. Rev. Lett.* **87**, 070601 (2001).

[18] Jones, P. H., Goonasekera, M., Meacher, D. R., Jonckheere, T. & Monteiro, T. S. Directed motion for delta-kicked atoms with broken symmetries: Comparison between theory and experiment. *Phys. Rev. Lett.* **98**, 073002 (2007).

[19] Dana, I., Ramareddy, V., Talukdar, I. & Summy, G. S. Experimental realization of quantum-resonance ratchets at arbitrary quasimomenta. *Phys. Rev. Lett.* **100**, 024103 (2008).

[20] Jones, P. H., Goonasekera, M. & Renzoni, F. Rectifying fluctuations in an optical lattice. *Phys. Rev. Lett.* **93**, 073904 (2004).

[21] Gommers, R., Bergamini, S. & Renzoni, F. Dissipation-induced symmetry breaking in a driven optical lattice. *Phys. Rev. Lett.* **95**, 073003 (2005).

[22] Sjölund, P., Petra, S. J. H., Dion, C. M., Jonsell, S., Nylén, M., Sanchez-Palencia, L. & Kastberg, A. Demonstration of a controllable three-dimensional brownian motor in symmetric potentials. *Phys. Rev. Lett.* **96**, 190602 (2006).

[23] Salger, T., Kling, S., Hecking, T., Geckeler, C., Morales-Molina, L. & Weitz, M. Directed transport of atoms in a hamiltonian quantum ratchet. *Science* **326**, 1241–1243 (2009).

[24] Kierig, E., Schnorrberger, U., Schietinger, A., Tomkovič, J. & Oberthaler, M. K. Single-particle tunneling in strongly driven double-well potentials. *Phys. Rev. Lett.* **100**, 190405 (2008).

[25] Lignier, H., Sias, C., Ciampini, D., Singh, Y., Zenesini, A., Morsch, O. & Arimondo, E. Dynamical control of matter-wave tunneling in periodic potentials. *Phys. Rev. Lett.* **99**, 220403 (2007).

[26] Tomsovic, S. & Ullmo, D. Chaos-assisted tunneling. *Phys. Rev. E* **50**, 145–162 (1994).

[27] Strzys, M., Graefe, E. & Korsch, H. Kicked Bose–Hubbard systems and kicked tops – destruction and stimulation of tunneling. *New Journal of Physics* **10**, 013024 (2008).

[28] Steck, D. A., Oskay, W. H. & Raizen, M. G. Observation of chaos-assisted tunneling between islands of stability. *Science* **293**, 274–278 (2001).

[29] Hensinger, W. K., Haffner, H., Browaeys, A., Heckenberg, N. R., Helmerson, K., McKenzie, C., Milburn, G. J., Phillips, W. D., Rolston, S. L., Rubinsztein-Dunlop, H. & Upcroft, B. Dynamical tunnelling of ultracold atoms. *Nature* **412**, 52–55 (2001).

[30] Salmond, G. L., Holmes, C. A. & Milburn, G. J. Dynamics of a strongly driven two-component Bose-Einstein condensate. *Phys. Rev. A* **65**, 033623 (2002).

[31] Haake, F., Kuś, M. & Scharf, R. Classical and quantum chaos for a kicked top. *Zeitschrift für Physik B* **65**, 381–395 (1987).

[32] Holthaus, M. & Stenholm, S. Coherent control of the self-trapping transition. *The European Physical Journal B* **20**, 451–467 (2001).

[33] Boukobza, E., Moore, M. G., Cohen, D. & Vardi, A. Nonlinear phase dynamics in a driven bosonic Josephson junction. *Phys. Rev. Lett.* **104**, 240402 (2010).

[34] Chaudhury, S., Smith, A., Anderson, B. E., Ghose, S. & Jessen, P. S. Quantum signatures of chaos in a kicked top. *Nature* **461**, 768–771 (2009).

[35] Prosen, T. Chaos and complexity of quantum motion. *Journal of Physics A* **40**, 7881 (2007).

[36] Jacquod, P. & Petitjean, C. Decoherence, entanglement and irreversibility in quantum dynamical systems with few degrees of freedom. *Advances in Physics* **58**, 67–196 (2009).

[37] Gross, C. *Spin squeezing and non-linear atom interferometry with Bose-Einstein condensates*. Ph.D. thesis, Combined Faculties for the Natural Sciences and for Mathematics of the Ruperto-Carola University of Heidelberg, Germany (2010).

[38] Zibold, T. *Classical Bifurcation and Entanglement Generation in an Internal Bosonic Josephson Junction*. Ph.D. thesis, Combined Faculties of the Natural Sciences and Mathematics of the Ruperto-Carola-University of Heidelberg, Germany (2012).

[39] Pitaevskii, L. P. & Stringari, S. *Bose-Einstein condensation*. No. 116 in International series of monographs on physics (Clarendon Press, Oxford, 2008).

[40] Pethick, C. J. & Smith, H. *Bose-Einstein condensation in dilute gases* (Cambridge University Press, Cambridge, 2006).

[41] Leggett, A. J. Bose-Einstein condensation in the alkali gases: Some fundamental concepts. *Rev. Mod. Phys.* **73**, 307–356 (2001).

[42] Gati, R. & Oberthaler, M. K. A bosonic Josephson junction. *J. Phys. B* **40**, R61–R89 (2007).

[43] Meystre, P. *Atom Optics* (Springer, 2001).

[44] Steel, M. J. & Collett, M. J. Quantum state of two trapped Bose-Einstein condensates with a Josephson coupling. *Phys. Rev. A* **57**, 2920–2930 (1998).

[45] Micheli, A., Jaksch, D., Cirac, J. I. & Zoller, P. Many-particle entanglement in two-component Bose-Einstein condensates. *Phys. Rev. A* **67**, 013607 (2003).

[46] Cirac, J. I., Lewenstein, M., Mølmer, K. & Zoller, P. Quantum superposition states of Bose-Einstein condensates. *Phys. Rev. A* **57**, 1208–1218 (1998).

[47] Nicklas, E. *A new tool for miscibility control: Linear coupling*. Ph.D. thesis, Combined Faculties of the Natural Sciences and Mathematics of the Ruperto-Carola-University of Heidelberg, Germany (2013).

[48] Matthews, M. R., Hall, D. S., Jin, D. S., Ensher, J. R., Wieman, C. E., Cornell, E. A., Dalfovo, F., Minniti, C. & Stringari, S. Dynamical response of a Bose-Einstein condensate to a discontinuous change in internal state. *Phys. Rev. Lett.* **81**, 243–247 (1998).

[49] Shchesnovich, V. S. & Trippenbach, M. Fock-space WKB method for the boson Josephson model describing a Bose-Einstein condensate trapped in a double-well potential. *Phys. Rev. A* **78**, 023611 (2008).

[50] Juliá-Díaz, B., Martorell, J. & Polls, A. Bose-Einstein condensates on slightly asymmetric double-well potentials. *Phys. Rev. A* **81**, 063625 (2010).

[51] Reichl, L. E. *The transition to chaos*. Institute for nonlinear science (Springer, New York, Heidelberg, 2004), 2. edn.

[52] Löck, S. private communications (2011).

[53] Arecchi, F. T., Courtens, E., Gilmore, R. & Thomas, H. Atomic coherent states in quantum optics. *Phys. Rev. A* **6**, 2211–2237 (1972).

[54] Gross, C., Zibold, T., Nicklas, E., Esteve, J. & Oberthaler, M. K. Nonlinear atom interferometer surpasses classical precision limit. *Nature* **464**, 1165–1169 (2010).

[55] Juliá-Díaz, B., Zibold, T., Oberthaler, M. K., Melé-Messeguer, M., Martorell, J. & Polls, A. Dynamic generation of spin-squeezed states in bosonic Josephson junctions. *Phys. Rev. A* **86**, 023615 (2012).

[56] Raghavan, S., Smerzi, A., Fantoni, S. & Shenoy, S. R. Coherent oscillations between two weakly coupled Bose-Einstein condensates: Josephson effects, π oscillations, and macroscopic quantum self-trapping. *Phys. Rev. A* **59**, 620–633 (1999).

[57] Albiez, M., Gati, R., Fölling, J., Hunsmann, S., Cristiani, M. & Oberthaler, M. K. Direct observation of tunneling and nonlinear self-trapping in a single bosonic Josephson junction. *Phys. Rev. Lett.* **95**, 010402 (2005).

[58] Zibold, T., Nicklas, E., Gross, C. & Oberthaler, M. K. Classical bifurcation at the transition from Rabi to Josephson dynamics. *Phys. Rev. Lett.* **105**, 204101 (2010).

[59] Hamley, C. D., Gerving, C. S., Hoang, T. M., Bookjans, E. M. & Chapman, M. S. Spin-nematic squeezed vacuum in a quantum gas. *Nature Physics* **8**, 305–308 (2012).

[60] Strogatz, S. H. *Nonlinear dynamics and chaos*. Studies in nonlinearity (Westview, Cambridge, Mass., 2006).

[61] Jin, D. S., Ensher, J. R., Matthews, M. R., Wieman, C. E. & Cornell, E. A. Collective excitations of a Bose-Einstein condensate in a dilute gas. *Phys. Rev. Lett.* **77**, 420–423 (1996).

[62] Orzel, C., Tuchman, A. K., Fenselau, M. L., Yasuda, M. & Kasevich, M. A. Squeezed states in a Bose-Einstein condensate. *Science* **291**, 2386–2389 (2001).

[63] Esteve, J., Gross, C., Weller, A., Giovanazzi, S. & Oberthaler, M. K. Squeezing and entanglement in a Bose-Einstein condensate. *Nature* **455**, 1216–1219 (2008).

[64] Demtröder, W. *Experimentalphysik 1* (Springer, Berlin, Heidelberg, 2013), 6. edn.

[65] Metcalf, H. J. & Straten, P. v. *Laser cooling and trapping* (Springer, New York, Berlin, Heidelberg, 1999).

[66] Böhi, P., Riedel, M. F., Hoffrogge, J., Reichel, J., Hänsch, T. W. & Treutlein, P. Coherent manipulation of Bose-Einstein condensates with state-dependent microwave potentials on an atom chip. *Nature Physics* **5**, 592–597 (2009).

[67] Riedel, M. F., Böhi, P., Li, Y., Hänsch, T. W., Sinatra, A. & Treutlein, P. Atom-chip-based generation of entanglement for quantum metrology. *Nature* **464**, 1170–1173 (2010).

[68] Greiner, M., Mandel, O., Esslinger, T., Hänsch, T. W. & Bloch, I. Quantum phase transition from a superfluid to a Mott insulator in a gas of ultracold atoms. *Nature* **415**, 39–44 (2002).

[69] Eiermann, B. *Kohärente nichtlineare Materiewellendynamik - Helle atomare Solitonen*. Ph.D. thesis, Mathematisch-Naturwissenschaftliche Sektion, Universität Konstanz (2004).

[70] Albiez, M. *Observation of nonlinear tunneling of a Bose-Einstein condensate in a single Josephson junction*. Ph.D. thesis, Combined Faculties for the Natural Sciences and for Mathematics of the Ruperto-Carola University of Heidelberg, Germany (2005).

[71] Gati, R. *Bose-Einstein Condensates in a Single Double Well Potential*. Ph.D. thesis, Combined Faculties for the Natural Sciences and for Mathematics of the Ruperto-Carola University of Heidelberg, Germany (2007).

[72] Weller, A. *Dynamics and Interaction of Dark Solitons in Bose-Einstein Condensates*. Ph.D. thesis, Combined Faculties for the Natural Sciences and for Mathematics of the Ruperto-Carola University of Heidelberg, Germany (2009).

[73] Steck, D. A. Rubidium 87 d line data. Tech. Rep. 2.1.2, University of Oregon (2009). URL `http://steck.us/alkalidata`.

[74] Hertel, I. V. & Schulz, C.-P. *Atome, Moleküle und optische Physik 1* (Springer, Berlin, Heidelberg, 2008).

[75] Cohen-Tannoudji, C. *Quantenmechanik* (de Gruyter, Berlin, 1999).

[76] Anderson, M. H., Ensher, J. R., Matthews, M. R., Wieman, C. E. & Cornell, E. A. Observation of Bose-Einstein condensation in a dilute atomic vapor. *Science* **269**, 198–201 (1995).

[77] Davis, K. B., Mewes, M. O., Andrews, M. R., van Druten, N. J., Durfee, D. S., Kurn, D. M. & Ketterle, W. Bose-Einstein condensation in a gas of sodium atoms. *Phys. Rev. Lett.* **75**, 3969–3973 (1995).

[78] Ketterle, W., Durfee, D. & Stamper-Kurn, D. Making, probing and understanding Bose-Einstein condensates. In Inguscio, M., Stringari, S. & Wieman, C. (eds.) *Proceedings of the International School of Physics "Enrico Fermi"*, vol. 140 of *Bose-Einstein Condensation in Atomic Gases*, 67 – 176 (IOS Press, 1999).

[79] Vitanov, N. V., Halfmann, T., Shore, B. W. & Bergmann, K. Laser-induced population transfer by adiabatic passage techniques. *Annu. Rev. Phys. Chem.* **52**, 763–809 (2001).

[80] Erhard, M., Schmaljohann, H., Kronjäger, J., Bongs, K. & Sengstock, K. Measurement of a mixed-spin-channel feshbach resonance in ^{87}Rb. *Phys. Rev. A* **69**, 032705 (2004).

[81] Chin, C., Grimm, R., Julienne, P. & Tiesinga, E. Feshbach resonances in ultracold gases. *Rev. Mod. Phys.* **82**, 1225–1286 (2010).

[82] Kaufman, A. M., Anderson, R. P., Hanna, T. M., Tiesinga, E., Julienne, P. S. & Hall, D. S. Radio-frequency dressing of multiple feshbach resonances. *Phys. Rev. A* **80**, 050701 (2009).

[83] van Kempen, E. G. M., Kokkelmans, S. J. J. M. F., Heinzen, D. J. & Verhaar, B. J. Interisotope determination of ultracold rubidium interactions from three high-precision experiments. *Phys. Rev. Lett.* **88**, 093201 (2002).

[84] Widera, A., Mandel, O., Greiner, M., Kreim, S., Hänsch, T. W. & Bloch, I. Entanglement interferometry for precision measurement of atomic scattering properties. *Phys. Rev. Lett.* **92**, 160406 (2004).

[85] Smirne, G., Godun, R. M., Cassettari, D., Boyer, V., Foot, C. J., Volz, T., Syassen, N., Dürr, S., Rempe, G., Lee, M. D., Góral, K. & Köhler, T. Collisional relaxation of Feshbach molecules and three-body recombination in ^{87}Rb Bose-Einstein condensates. *Phys. Rev. A* **75**, 020702 (2007).

[86] Cornell, E., Hall, D., Matthews, M. & Wieman, C. Having it both ways: Distinguishable yet phase-coherent mixtures of Bose-Einstein condensates. *J. Low Temp. Phys.* **113**, 151–165 (1998).

[87] Döring, D., Debs, J. E., Robins, N. P., Figl, C., Altin, P. A. & Close, J. D. Ramsey interferometry with an atom laser. *Opt. Express* **17**, 20661–20668 (2009).

[88] Tojo, S., Hayashi, T., Tanabe, T., Hirano, T., Kawaguchi, Y., Saito, H. & Ueda, M. Spin-dependent inelastic collisions in spin-2 Bose-Einstein condensates. *Phys. Rev. A* **80**, 042704 (2009).

[89] Myatt, C. J., Burt, E. A., Ghrist, R. W., Cornell, E. A. & Wieman, C. E. Production of two overlapping Bose-Einstein condensates by sympathetic cooling. *Phys. Rev. Lett.* **78**, 586–589 (1997).

[90] Tommasini, P., de Passos, E. J. V., de Toledo Piza, A. F. R., Hussein, M. S. & Timmermans, E. Bogoliubov theory for mutually coherent condensates. *Phys. Rev. A* **67**, 023606 (2003).

[91] Goldstein, E. V., Moore, M. G., Pu, H. & Meystre, P. Eliminating the mean-field shift in two-component Bose-Einstein condensates. *Phys. Rev. Lett.* **85**, 5030–5033 (2000).

[92] Meystre, P. & Sargent, M. *Elements of quantum optics* (Springer, Berlin, Heidelberg, 2007).

[93] Bergmann, K., Theuer, H. & Shore, B. W. Coherent population transfer among quantum states of atoms and molecules. *Rev. Mod. Phys.* **70**, 1003–1025 (1998).

[94] Stadler, E. *Modulationsverfahren / Modulation und Demodulation in der elektrischen Nachrichtentechnik* (Vogel, Würzburg, 1993), 7. edn.

[95] Reinaudi, G., Lahaye, T., Wang, Z. & Guéry-Odelin, D. Strong saturation absorption imaging of dense clouds of ultracold atoms. *Opt. Lett.* **32**, 3143–3145 (2007).

[96] Muessel, W., Strobel, H., Joos, M., Nicklas, E., Stroescu, I., Tomkovič, J., Hume, D. B. & Oberthaler, M. K. Optimized absorption imaging of mesoscopic atomic clouds. *Applied Physics B* **113**, 69–73 (2013).

[97] Ottenstein, T. B. *A New Objective for High Resolution Imaging of Bose-Einstein Condensates*. Master's thesis, Faculty of Physics and Astronomy, University of Heidelberg (2006).

[98] NIST/SEMATECH. *e-Handbook of Statistical Methods* (2013). URL http://www.itl.nist.gov/div898/handbook/.

[99] Bronstejn, I. N., Semendjaev, K. A. & Musiol, G. *Taschenbuch der Mathematik* (Deutsch, Frankfurt am Main, Thun, 2000).

[100] Arnol'd, V. I. Small denominators and problems of stability of motion in classical and celestial mechanics. *Russian Mathematical Surveys* **18**, 85 (1963).

[101] Moser, J. *Stable and Random Motions in Dynamical Systems: With Special Emphasis on Celestial Mechaniscs*, vol. 1 (Princeton University Press, 1973).

[102] Birkhoff, G. D. On the periodic motions of dynamical systems. *Acta Mathematica* **50**, 359–379 (1927).

[103] Wisniacki, D. A., Saraceno, M., Arranz, F. J., Benito, R. M. & Borondo, F. Poincaré-Birkhoff theorem in quantum mechanics. *Phys. Rev. E* **84**, 026206 (2011).

[104] Arranz, F. J., Seidel, L., Giralda, C. G., Benito, R. M. & Borondo, F. Onset of quantum chaos in molecular systems and the zeros of the husimi function. *Phys. Rev. E* **87**, 062901 (2013).

[105] Hennig, D. & Esser, B. Transfer dynamics of a quasiparticle in a nonlinear dimer coupled to an intersite vibration: Chaos on the bloch sphere. *Phys. Rev. A* **46**, 4569–4576 (1992).

[106] Mackay, R., Meiss, J. & Percival, I. Transport in hamiltonian systems. *Physica D* **13**, 55 – 81 (1984).

[107] Brown, R. C. & Wyatt, R. E. Quantum mechanical manifestation of cantori: Wave-packet localization in stochastic regions. *Phys. Rev. Lett.* **57**, 1–4 (1986).

[108] Tomkovič, J., Schreiber, M., Welte, J., Kiffner, M., Schmiedmayer, J. & Oberthaler, M. K. Single spontaneous photon as a coherent beamsplitter for an atomic matter-wave. *Nature Physics* **7**, 379–382 (2011).

[109] Arndt, M. Quantum optics: Coherence from spontaneity. *Nature Physics* **7**, 375–376 (2011).

[110] Pfau, T., Spälter, S., Kurtsiefer, C., Ekstrom, C. R. & Mlynek, J. Loss of spatial coherence by a single spontaneous emission. *Phys. Rev. Lett.* **73**, 1223–1226 (1994).

[111] Chapman, M. S., Hammond, T. D., Lenef, A., Schmiedmayer, J., Rubenstein, R. A., Smith, E. & Pritchard, D. E. Photon scattering from atoms in an atom interferometer: Coherence lost and regained. *Phys. Rev. Lett.* **75**, 3783–3787 (1995).

[112] Kokorowski, D. A., Cronin, A. D., Roberts, T. D. & Pritchard, D. E. From single- to multiple-photon decoherence in an atom interferometer. *Phys. Rev. Lett.* **86**, 2191–2195 (2001).

[113] Milonni, P. W. *The quantum vacuum* (Academic Press, Boston, 1995).

[114] Milonni, P. W. & Knight, P. L. Spontaneous emission between mirrors. *Opt. Commun.* **9**, 119 – 122 (1973).

[115] Drexhage, K. H. {IV} interaction of light with monomolecular dye layers. vol. 12 of *Progress in Optics*, 163 – 192 (Elsevier, 1974).

[116] Goy, P., Raimond, J., Gross, M. & Haroche, S. Observation of cavity-enhanced single-atom spontaneous emission. *Phys. Rev. Lett.* **50**, 1903 (1983).

[117] Eschner, J., Raab, C., Schmidt-Kaler, F. & Blatt, R. Light interference from single atoms and their mirror images. *Nature* **413**, 495–498 (2001).

[118] Eschner, J. Sub-wavelength resolution of optical fields probed by single trapped ions: Interference, phase modulation, and which-way information. *The European Physical Journal D* **22**, 341–345 (2003).

[119] Oberthaler, M., Abfalterer, R., Bernet, S., Keller, C., Schmiedmayer, J. & Zeilinger, A. Dynamical diffraction of atomic matter waves by crystals of light. *Phys. Rev. A* **60**, 456–472 (1999).

[120] Bohr, N. *Albert Einstein: Philosopher Scientist* (Library of Living Philosophers, Evanston, 1949).

[121] Bertet, P., Osnaghi, S., Rauschenbeutel, A., Nogues, G., Auffeves, A., Brune, M., Raimond, J. M. & Haroche, S. A complementarity experiment with an interferometer at the quantum-classical boundary. *Nature* **411**, 166–170 (2001).

[122] Cronin, A. D., Schmiedmayer, J. & Pritchard, D. E. Optics and interferometry with atoms and molecules. *Rev. Mod. Phys.* **81**, 1051–1129 (2009).

[123] Martin, P., Oldaker, B., Miklich, A. & Pritchard, D. Bragg scattering of atoms from standing light-wave. *Phys. Rev. Lett.* **60**, 515–518 (1988).

[124] Morawitz, H. Self-coupling of a two-level system by a mirror. *Phys. Rev.* **187**, 1792 (1969).

[125] Di Stefano, O., Savasta, S. & Girlanda, R. Three-dimensional electromagnetic field quantization in absorbing and dispersive bounded dielectrics. *Phys. Rev. A* **61**, 023803 (2000).

[126] Aspect, A., Arimondo, E., Kaiser, R., Vansteenkiste, N. & Cohen-Tannoudji, C. Laser cooling below the one-photon recoil energy by velocity-selective coherent population trapping. *Phys. Rev. Lett.* **61**, 826–829 (1988).

[127] Tomkovič, J. *Erzeugung eines kohärenten Zustandes durch spontane Prozesse*. Master's thesis, Institut für Theoretische Physik, Fachrichtung Physik, Fakultät Mathematik und Naturwissenschaften der Technischen Universität Dresden (2008).

[128] Kierig, E. *AC-Control of Single Particle Tunneling*. Ph.D. thesis, Combined Faculties of the Natural Sciences and Mathematics of the Ruperto-Carola-University of Heidelberg, Germany (2008).

[129] Bäcker, A., Ketzmerick, R. & Monastra, A. G. Flooding of chaotic eigenstates into regular phase space islands. *Phys. Rev. Lett.* **94**, 054102 (2005).

[130] Bittrich, L. *Flooding of Regular Phase Space Islands by Chaotic States*. Ph.D. thesis, Institut für Theoretische Physik, Fachrichtung Physik, Fakultät für Mathematik und Naturwissenschaften, Technische Universität Dresden (2010).

[131] Löck, S., Bäcker, A., Ketzmerick, R. & Schlagheck, P. Regular-to-chaotic tunneling rates: From the quantum to the semiclassical regime. *Phys. Rev. Lett.* **104**, 114101 (2010).

[132] Lenz, M., Wüster, S., Vale, C. J., Heckenberg, N. R., Rubinsztein-Dunlop, H., Holmes, C. A., Milburn, G. J. & Davis, M. J. Dynamical tunneling with ultracold atoms in magnetic microtraps. *Phys. Rev. A* **88**, 013635 (2013).

[133] Lin, W. A. & Ballentine, L. E. Quantum tunneling and chaos in a driven anharmonic oscillator. *Phys. Rev. Lett.* **65**, 2927–2930 (1990).

[134] Tomsovic, S. Chaos-assisted tunnelling in the absence of reflexion symmetry. *Journal of Physics A* **31**, 9469 (1998).

[135] Hume, D. B., Stroescu, I., Joos, M., Muessel, W., Strobel, H. & Oberthaler, M. K. Accurate atom counting in mesoscopic ensembles. *Phys. Rev. Lett.* **111**, 253001 (2013).

[136] Landau, R. H., Páez, M. J. & Bordeianu, C. C. *Computational physics* (WILEY-VCH, Weinheim, 2007), 2. edn.

[137] Marsaglia, G. & Bray, T. A. A convenient method for generating normal variables. *SIAM Review* **6**, 260–264 (1964).

[138] Weisstein, E. W. Sphere point picking. MathWorld – A Wolfram Web Resource (2013). URL http://mathworld.wolfram.com/SpherePointPicking.html.

[139] Seaman, D. N-dim spherical random number drawing. Online (1996). URL http://www.math.niu.edu/~rusin/known-math/96/sph.rand.

[140] Jähne, B. *Digitale Bildverarbeitung* (Springer, Berlin, Heidelberg, 2005).

[141] Melé-Messeguer, M., Juliá-Díaz, B., Guilleumas, M., Polls, A. & Sanpera, A. Weakly linked binary mixtures of F = 1 ^{87}Rb Bose-Einstein condensates. *New Journal of Physics* **13**, 033012 (2011).

[142] Schuster, H. G. & Just, W. *Deterministic chaos* (Wiley-VCH, Weinheim, 2005), 4. edn.

[143] Schwabl, F. *Quantenmechanik für Fortgeschrittene (QM II)* (Springer Berlin, Heidelberg, 2008).